



HAL
open science

Evaluating the role of orbitally-induced paleoceanographic changes in subtropical South Atlantic for the global climate over the last 800,000 years

João Marcelo Ballalai

► To cite this version:

João Marcelo Ballalai. Evaluating the role of orbitally-induced paleoceanographic changes in subtropical South Atlantic for the global climate over the last 800,000 years. Earth Sciences. Université de Bretagne occidentale - Brest; Universidade Federal Fluminense (Brésil), 2023. English. NNT : 2023BRES0038 . tel-04261916

HAL Id: tel-04261916

<https://theses.hal.science/tel-04261916>

Submitted on 27 Oct 2023

HAL is a multi-disciplinary open access archive for the deposit and dissemination of scientific research documents, whether they are published or not. The documents may come from teaching and research institutions in France or abroad, or from public or private research centers.

L'archive ouverte pluridisciplinaire **HAL**, est destinée au dépôt et à la diffusion de documents scientifiques de niveau recherche, publiés ou non, émanant des établissements d'enseignement et de recherche français ou étrangers, des laboratoires publics ou privés.

COLLEGE SCIENCES
DOCTORAL DE LA MER
BRETAGNE ET DU LITTORAL

UBO
Université de Bretagne Occidentale

uff Universidade
Federal
Fluminense

THESE DE DOCTORAT EN COTUTELLE INTERNATIONALE DE

L'UNIVERSITE
DE BRETAGNE OCCIDENTALE

ECOLE DOCTORALE N° 598
Sciences de la Mer et du Littoral
Spécialité : Géosciences marines

AVEC UNIVERSIDADE FEDERAL FLUMINENSE
ECOLE DOCTORALE

Spécialité : Géosciences (Géochimie)

Par

João M. BALLALAI

Evaluating the role of Orbitally-Induced Paleoceanographic Changes in Subtropical South Atlantic for the Global Climate over the Last 800,000 Years

Thèse présentée et soutenue à Niterói, Brésil, le 07 juillet 2023

Unité de recherche : Geo-Ocean UMR6538, Ifremer, CNRS, UBO, UBS, F-29280 Plouzané, France

Departamento de Geoquímica, Universidade Federal Fluminense, UFF, Niterói, Brésil

Ifremer

GeoOcean

Rapporteurs avant soutenance :

Claire WAELBROECK
Cristiano CHIESSI

Directeur de recherche, CNRS, France
Professeur, Universidade de São Paulo, Brésil

Composition du Jury :

Président :
Examineurs :

Bruno TURCQ
Stefan MULITZA
Igor VENANCIO
Nicolas STRIKIS

Directeur de recherche, IRD, France
Professeur, MARUM, Allemagne
Professeur, Universidade Federal Fluminense, Brésil
Professeur, Universidade Federal Fluminense, Brésil

Dir. de thèse cotutelle : Ana Luiza ALBUQUERQUE
Dir. de thèse : Stephan JORRY

Professeur, Universidade Federal Fluminense, Brésil
Chercheur, IFREMER, France

Co-encadrant :

Natalia VAZQUEZ RIVEIROS Chercheur, IFREMER, France

INSTITUTO DE QUÍMICA

PROGRAMA DE PÓS-GRADUAÇÃO EM GEOCIÊNCIAS - GEOQUÍMICA

JOÃO MARCELO BALLALAI

**ORBITALLY-INDUCED PALEOCEANOGRAPHIC CHANGES IN SUBTROPICAL
SOUTH ATLANTIC FOR THE GLOBAL CLIMATE OVER THE LAST 800,000
YEARS**

**UNIVERSIDADE
FEDERAL
FLUMINENSE**

NITERÓI

2023

JOÃO MARCELO BALLALAI

**ORBITALLY-INDUCED PALEOCEANOGRAPHIC CHANGES IN SUBTROPICAL
SOUTH ATLANTIC FOR THE GLOBAL CLIMATE OVER THE LAST 800,000
YEARS**

Thesis presented to the Graduate Course in Geosciences at the Fluminense Federal University, as a partial requirement for obtaining the degree of Doctor of Philosophy. Concentration area: Environmental Geochemistry.

Supervisors:

Prof.^a Dr.^a Ana Luiza Spadano Albuquerque

Dr.^a Natalia Vázquez Riveiros

Dr. Stephan Jorry

Co-supervisors:

Prof.^a Dr.^a Karen Badaraco Costa

Prof. Dr. Thiago Pereira dos Santos

NITERÓI

2023

UFF. SDC. Biblioteca de Pós-Graduação em Geoquímica

Ficha catalográfica automática - SDC/BGQ
Gerada com informações fornecidas pelo autor

B188o Ballalai, João Marcelo
Orbitally-induced Paleoceanographic Changes in Subtropical South Atlantic for the Global Climate Over the Last 800,000 Years / João Marcelo Ballalai. - 2023.
216 p.: il.

Orientador: Ana Luiza Spadano Albuquerque.
Coorientador: Natalia Vazquez Riveiros; Stephan Jorry;
Thiago Pereira dos Santos.
Tese (doutorado)-Universidade Federal Fluminense, Instituto de Química, Niterói, 2023.

1. Paleoclimatologia. 2. Paleoceanografia. 3. Foraminíferos planctônicos e bentônicos. 4. Isótopos estáveis. 5. Produção intelectual. I. Albuquerque, Ana Luiza Spadano, orientadora. II. Vazquez Riveiros, Natalia, coorientadora. III. Jorry, Stephan, coorientador. IV. Santos, Thiago Pereira dos, coorientador. V. Universidade Federal Fluminense. Instituto de Química. VI. Título.

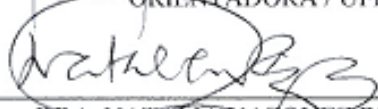
CDD - XXX

APPROVAL SHEET**JOÃO MARCELO BALLALAI****ORBITALLY-INDUCED PALEOCEANOGRAPHIC CHANGES IN SUBTROPICAL
SOUTH ATLANTIC FOR THE GLOBAL CLIMATE OVER THE LAST 800,000 YEARS.**

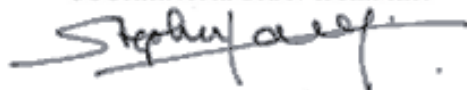
Tese de doutorado apresentada ao Curso de Pós - Graduação
em Geociências da Universidade Federal Fluminense, como
requisito parcial para a obtenção do **Grau de Doutor**. Área de
Concentração: **Geoquímica Ambiental**.

Aprovada em julho de 2023.**BANCA EXAMINADORA**

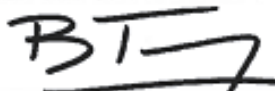
PROFA. DRA. ANA LUÍZA SPADANO ALBUQUERQUE
ORIENTADORA / UFF



DRA. NATALIA VAZQUEZ RIVEIROS
COORIENTADORA / IFREMER



DR. STEPHAN JORRY
COORIENTADOR / IFREMER



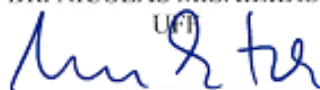
PROF. DR. BRUNO JEAN TURCQ
IRD



PROF. DR. IGOR MARTINS VENANCIO PADILHA DE OLIVEIRA
UFF



PROF. DR. NICOLÁS MISAILIDIS STRÍKIS
UFF



DR. STEFAN MULITZA
MARUM

NITERÓI
2022

ACKNOWLEDGEMENTS

This thesis was not done by just one person or two. Many people had a crucial role in building up what will be presented in the next pages. Because of that, I would like to say really thank you to all who participated during this stage of my life. I would like to express my heartfelt gratitude to the following individuals and groups who have been instrumental in the completion of this thesis:

First, I would like to thank my parents and family for their love, care, and understanding throughout my life. To my sister Cecília and mother, Nazaré, which always supported me in my crazy plans to live abroad. Their support has been invaluable, and I am truly grateful for their constant encouragement. I would like to especially thank my father, who always bet on my academic journey and used to dream of this moment. I know that you are proud.

I would like to thank Letícia Vianna, my partner and life mate, for being my rock and companion throughout this entire process, without you and Ringo, I couldn't do it. We have shared unforgettable moments, and I am eternally grateful for your love and unwavering support. I'm grateful for building a future together and spending many more years by your side. Your presence and support have meant the world to me, and I am incredibly fortunate to have such a loving and supportive partner.

I am deeply indebted to my supervisor, Ana Luiza Albuquerque, whose guidance and support have been invaluable. After "our" interview to get into the master's, you introduced me to the fascinating world of paleoceanography, and I am now a passionate enthusiast thanks to your mentorship. Since there, you have supported, encouraged, and always shown me that it is possible to have a brilliant professional future. I am grateful for the dedication and effort you have put into your research group and for providing me with the great opportunities I have had in my professional life. You are a great reference to me, thank you.

I thank all integrants of Laboratório de Oceanografia Operacional e Paleoceanografia (LOOP; UFF) for your support, once in LOOP, always in LOOP. I also thank Thiago Santos, Igor Venancio, and Douglas Lessa for your help and good work with the students. I can't forget to especially thank Caio Gonçalves, Rodrigo Azevedo, Daniel Tremmel, and Patricia Piacsek, who always helped and tranquilized me during the tough periods of my thesis, both

in our personal and working lives. I sincerely thank all my friends in the Geochemistry department (UFF), my professors, and workers from the department.

I couldn't let to acknowledge all friends I have made during a special period of my life and career during my time in Brest, the city that conquered me. A special thanks to Naoufel Haddam and Anouk Villedieu for your friendship, support, and care for Leticia and me, you were always there for everything. *Merci pour me proportionner le moment "c'est ma première fois" avec des amis en France, un gros merci pour tout !* I also thank Farley and Gabrielle, who were always there sharing friendship, laughs, wine, and much good food. That American Pie still lives in my memory! Also, many thanks to Dani, Rafa, and Biel, with whom I shared great special moments at Brest and who have contributed significantly with nice talks about academia, life, and science, you taught me a lot! You are also part of my development and are references as researchers to me.

I'm thankful to all colleagues I have made from *Geo-Ocean*, thanks to Maryline Moulin, Stelle Eleroux, Philippe Schnurle, and Stephan Jorry whom I shared good talks. A special thanks to Suzana Gonçalves and Anne-Marie Pouliquen, my life at IFREMER would be the same without your friendship, laughs, and coffee time together. Last but not least, I'm thankful to my supervisor Natalia Vazquez, who accepted to work with me, received me at Brest, bet on me, guided me, taught me so much, and made it all possible to improve my scientific skills. You contributed to my professional and personal development, and this year in Brest was successful because of your support.

I thank Claire Waelbroeck and Cristiano Chiessi for accepting to compose my *Comité de Suivi de Thèse*. I'm thankful for all the scientific discussions and suggestions that contributed for improving my work through these years of thesis. I also thank my jury members for accepting the invitation and evaluating my work. I'm sure I will profit from your valuable insides and scientific discussions.

I thank CNPq and CAPES for the financial support granting the scholarship at the beginning of my Ph.D. and over my international experience at IFREMER.

I offer my heartfelt thanks to all those mentioned above and to anyone else who has supported me along this journey. Your contributions have been invaluable, and I am truly grateful for your presence in my life.

ABSTRACT

Anthropogenic greenhouse gas emissions significantly altered the Earth's climate system, particularly in recent decades. This increased atmospheric CO₂ and global warming have been associated with the slowdown in the Atlantic Meridional Overturning Circulation (AMOC). The AMOC regulates climate by distributing heat and carbon throughout the Atlantic, maintaining the inter-hemispheric energy balance with the Intertropical Convergence Zone (ITCZ) and global atmospheric patterns. The wind-driven South Atlantic Subtropical Gyre (SASG), part of the upper limb of the AMOC, transports heat from the subtropics to the North Atlantic. Long-term climate changes are driven by cyclic oscillations in Earth's orbit, resulting in latitudinal and seasonal variations in incoming insolation. To fully comprehend the natural behavior and limitations of the AMOC, it is crucial to examine its dynamics on an orbital scale, considering surface and deep-water perspectives across different climates during the Late Pleistocene. This thesis focuses on the controls that orbital forcing exercises on paleoceanographic processes in the subtropical South Atlantic over the last 800 ka and their implications for global climate. By analyzing oxygen ($\delta^{18}\text{O}$) and carbon ($\delta^{13}\text{C}$) stable isotopes from benthic and planktic foraminiferal species from sediment cores GL-854 (25°12'S, 42°37'W) and MD08-3167 (23°18.91'S, 12°22.61'E), as well as Mg/Ca ratio of planktic species from core MD08-3167, this thesis aims to uncover the intricate relationship between AMOC modes and the set of different climates. The proposed framework provides a comprehensive understanding of deep-water and ocean-atmospheric processes, as well as of controlling mechanisms of the Benguela Upwelling System (BUS), on the orbital scale and their impacts on the global climate. Chapters 1, 2, and 3 are dedicated to the thesis's introduction, objectives, methods, and results. Chapter 4 investigates the deep-water circulation dynamic in the South Atlantic over the last 770 ka, based on the benthic foraminifera $\delta^{13}\text{C}$ record from core GL-854. This record is compared to published $\delta^{13}\text{C}$ data from the eastern South Atlantic to examine the zonal $\delta^{13}\text{C}$ gradient variability ($\Delta\delta^{13}\text{C}_{\text{w-e}}$) of North Atlantic Deep Water (NADW). It is proposed that AMOC oscillated between four modes controlled by orbitally-triggered variations in Antarctic sea ice extent. The orbital forcing is then propagated toward subtropical regions through controls over the deep-water formation. The proposed framework connects sea-ice and ocean-atmosphere dynamics to deep-water geometry within the South Atlantic basin, contributing to modulating the climate during the Late Pleistocene. Chapter 5 focuses on understanding the long-term variability of the BUS over the last 365 ka, based on the reconstruction of upper ocean stratification using the $\delta^{18}\text{O}$ gradient between planktic foraminifera species *Globigerina bulloides* and *G. inflata* ($\Delta\delta^{18}\text{O}$). Precessionally-paced stratification decrease is associated with the intensification and offshore expansion of the upwelling cell during austral summer insolation maxima. It is proposed that intensified deep-water formation in the North Atlantic during positive precession promotes intensified inter-hemispheric heat transfer, resulting in a northward shift of the SASG and enhanced the upwelling at BUS. A robust link is established between the upwelling intensification, the AMOC intensity, global atmospheric patterns, and a decrease in atmospheric CO₂ during positive precession. Chapter 6 presents the protocol for performing Mg/Ca measurements in foraminifera samples using an ICP-MS performed at

IFREMER. The protocol was applied to *Globorotalia inflata* specimens from core MD08-3167 to reconstruct thermocline temperature at the BUS over the last 365 ka. External reproducibility attests to accurate and precise results, allowing the continuous robust reconstruction of the Mg/Ca-based thermocline temperatures. This record contributes to a better understanding of past oceanographic and climatic variability in the BUS and its implications for the carbon cycle. By combining surface and deep-water perspectives, studying ocean-atmospheric dynamics and the carbon cycle, we have gained insight into feedback mechanisms associated with AMOC variability, with important implications for atmospheric CO₂.

Keywords: Atlantic Meridional Overturning Circulation; orbital cycles; South Atlantic Subtropical Gyre, inter-hemispheric heat transfer; South Atlantic controls on climate, Mg/Ca analysis.

RESUMO

As emissões antropogênicas de gases de efeito estufa mudaram significativamente o sistema climático da Terra, particularmente nas últimas décadas. Como resultado, o aumento do CO₂ atmosférico e o aquecimento global tem sido associado a desaceleração da Circulação Meridional do Atlântico (do inglês, Atlantic Meridional Overturning Circulation - AMOC). A AMOC desempenha um papel crítico na regulação do clima, distribuindo calor e carbono em todo o Atlântico, mantendo o balanço energético inter-hemisférico em conjunto com a zona de convergência intertropical (do inglês, Intertropical Convergence Zone - ITCZ) e padrões atmosféricos globais. O giro subtropical do Atlântico Sul (do inglês, South Atlantic Subtropical Gyre - SASG), controlado pelo vento, faz parte do membro superior da AMOC, responsável pelo transporte de calor dos subtrópicos para o Atlântico Norte. As mudanças de longo prazo nesses componentes climáticos são influenciadas por oscilações cíclicas na órbita da Terra, que causam variações na radiação solar em diferentes latitudes e estações. Para compreender totalmente o comportamento natural e os limites da AMOC, é crucial examinar sua dinâmica em uma escala orbital, considerando sua componente de superfície e de águas profundas em diferentes climas durante o Pleistoceno tardio. Esta tese analisa os efeitos da força orbital nos processos paleoceanográficos no Atlântico Sul subtropical nos últimos 800 ka e suas implicações as mudanças climáticas globais no presente e futuro. Utilizando isótopos estáveis de oxigênio ($\delta^{18}\text{O}$) e carbono ($\delta^{13}\text{C}$) em foraminíferos bentônicos e planctônicos nos testemunhos sedimentares GL-854 (25°12'S, 42°37'W) e MD08-3167 (23°18.91'S, 12°22.61'E), bem como a análise de Mg/Ca de espécies planctônicas do testemunho MD08-3167, o objetivo desta tese é compreender a complexa relação entre os modos da AMOC e os diferentes climas. A estrutura proposta busca fornecer uma compreensão abrangente da dinâmica de águas profundas e das interações oceano-atmosférica, assim como os mecanismos que controlam o sistema de ressurgência da Benguela (do inglês, Benguela Upwelling System - BUS) em escala orbital e seus impactos no clima global. Os capítulos 1, 2, e 3 são dedicados a introdução, objetivos, métodos e resultados da tese. O capítulo 4 investiga a dinâmica de circulação de águas profundas no Atlântico Sul nos últimos 770 ka, com base no registro de $\delta^{13}\text{C}$ de foraminífero bentônico *Cibicides wuellerstorfi* do testemunho GL-854. Este registro é comparado a dados publicados de $\delta^{13}\text{C}$ do leste do Atlântico Sul, a fim de examinar a variabilidade do gradiente zonal de $\delta^{13}\text{C}$ ($\Delta\delta^{13}\text{C}_{w-e}$) da Água Profundas do Atlântico Norte (do inglês, North Atlantic Deep Water - NADW). Propomos que a AMOC tenha oscilado entre quatro modos controlados por variações de gelo marinho na Antártica induzidos pelas forçantes orbitais. O efeito do orbital é então propagado para as regiões subtropicais através de controles sobre a formação de águas profundas no Atlântico. A discussão busca estabelecer conexões entre a dinâmica do gelo marinho, da interface oceano-atmosfera e a geometria das águas profundas na bacia do Atlântico Sul, contribuindo para a compreensão da modulação climática durante o Pleistoceno tardio. O capítulo 5 tem como objetivo compreender a variabilidade de longo prazo do BUS nos últimos 365 ka, com base na reconstrução da estratificação de superfície ($\Delta\delta^{18}\text{O}$) utilizando o gradiente de $\delta^{18}\text{O}$ entre as espécies *G. Bulloides* e *G. inflata*. Durante os períodos de máxima insolação de verão austral a estratificação é reduzida, associada à

intensificação e expansão *offshore* da célula de ressurgência. O aumento na formação de águas profundas no Atlântico Norte durante a precessão positiva fortalece a transferência de calor entre os hemisférios, causando o deslocamento do SASG para o norte e um aumento na ressurgência no BUS. É estabelecida uma conexão entre a intensificação da ressurgência, a intensidade da AMOC, padrões atmosféricos globais e uma diminuição no CO₂ atmosférico durante a precessão positiva. O capítulo 6 apresenta o protocolo para analisar as concentrações de Mg/Ca em foraminíferos usando um ICP-MS realizado no IFREMER. Este protocolo foi aplicado à espécie *G. inflata* do testemunho MD08-3167 para reconstruir as temperaturas da termoclina nos últimos 365 ka, o qual demonstrou uma reprodutibilidade externa consistente, o que garante resultados precisos e permite uma reconstrução contínua e confiável das temperaturas com base no Mg/Ca. Esse registro contribui para uma melhor compreensão da variabilidade oceanográfica e climática do passado do BUS e suas implicações para o ciclo do carbono. Ao combinar perspectivas superficiais e de águas profundas, estudando dinâmica oceano-atmosfera e o ciclo do carbono, obtivemos informações sobre mecanismos de feedback associados a variabilidades da AMOC, com implicações importantes para o CO₂ atmosférico.

Palavras-chave: Circulação de Revolvimento Meridional do Atlântico; ciclos orbitais; Giro subtropical do Atlântico Sul; transferência de calor inter-hemisférica; controles do Atlântico Sul no clima, análise de Mg/Ca.

RÉSUMÉ

Les émissions anthropiques de gaz à effet de serre ont considérablement modifié le système climatique de la Terre, en particulier au cours des dernières décennies. En conséquence, l'augmentation de la teneur en CO₂ atmosphérique et du réchauffement climatique sont vraisemblablement en train de mener à un ralentissement de la Circulation Méridienne de l'Atlantique (AMOC, de l'anglais *Atlantic Meridional Overturning Circulation*). L'AMOC joue un rôle critique dans la régulation du climat en distribuant la chaleur et le carbone dans tout l'Atlantique, en maintenant l'équilibre énergétique inter-hémisphérique en conjonction avec la Zone de Convergence Intertropicale (ITCZ, de l'anglais *Intertropical Convergence Zone*) et les schémas atmosphériques globaux. Le gyre subtropical de l'Atlantique Sud (SASG, de l'anglais *South Atlantic Subtropical Gyre*), contrôlé par les vents, fait partie de la branche supérieure de l'AMOC, responsable du transport de chaleur des régions subtropicales vers l'Atlantique Nord. Les changements à long terme de ces composantes climatiques sont influencés par des oscillations cycliques dans l'orbite de la Terre, qui entraînent des variations du rayonnement solaire à différentes latitudes et saisons. Pour comprendre pleinement le comportement naturel et les limites de l'AMOC, il est crucial d'examiner sa dynamique à une échelle orbitale, en tenant compte de la dynamique des eaux de surface et profondes dans différents climats au cours du Pléistocène tardif. Cette thèse analyse les effets du forçage orbital sur les processus paléocéanographiques dans l'Atlantique Sud subtropical au cours des 800 000 dernières années, ainsi que leurs implications pour le climat mondial. En utilisant les isotopes stables de l'oxygène ($\delta^{18}\text{O}$) et du carbone ($\delta^{13}\text{C}$) dans les foraminifères benthiques et planctoniques des carottes sédimentaires GL-854 (25°12'S, 42°37'O) et MD08-3167 (23°18.91'S, 12°22.61'E), ainsi que l'analyse du rapport Mg/Ca des espèces planctoniques dans la carotte MD08-3167, l'objectif de cette thèse est de comprendre la relation complexe entre des états de l'AMOC et les différents climats. La structure du manuscrit proposée vise à fournir une compréhension globale de la dynamique des eaux profondes et des interactions océan-atmosphère, ainsi que des mécanismes qui contrôlent le système de remontée des eaux profondes de Benguela (BUS, de l'anglais *Benguela Upwelling System*) à l'échelle orbitale et de ses impacts sur le climat mondial. Les chapitres 1, 2 et 3 sont dédiés à l'introduction, les objectifs, les méthodes et les résultats de la thèse. Le chapitre 4 examine la dynamique de la circulation des eaux profondes dans l'Atlantique Sud au cours des 770 derniers milliers d'années, à partir de l'enregistrement du $\delta^{13}\text{C}$ des foraminifères benthiques de la carotte GL-854. Cet enregistrement est comparé à des données publiées de $\delta^{13}\text{C}$ de l'est de l'Atlantique Sud afin d'examiner la variabilité du gradient zonal de $\delta^{13}\text{C}$ ($\Delta\delta^{13}\text{C}_{\text{w-e}}$) des Eaux Profondes de l'Atlantique Nord (NADW, de l'anglais *North Atlantic Deep Water*). Je propose que l'AMOC a oscillé entre quatre états ou modes contrôlés par des variations de la glace de mer de l'Antarctique induites par les forçages orbitaux. L'effet orbital est ensuite propagé vers les régions subtropicales par le biais du contrôle de la formation des eaux profondes dans l'Atlantique. La discussion proposée cherche à établir des liens entre la dynamique de la glace de mer, la dynamique océano-atmosphérique et la géométrie des eaux profondes dans le bassin de l'Atlantique Sud, contribuant ainsi à la compréhension de la modulation climatique pendant le Pléistocène tardif. Le chapitre 5 vise à comprendre la variabilité à long terme du BUS au cours des 365 derniers milliers d'années, sur la base de la reconstruction de la stratification des eaux de surface en utilisant le gradient de $\delta^{18}\text{O}$ entre les espèces *Globigerina bulloides* et *G. inflata* ($\Delta\delta^{18}\text{O}$). Pendant les périodes d'insolation de l'été austral maximale, on observe une réduction de la stratification, associée à une intensification et à une expansion du BUS vers le large. L'augmentation de la formation d'eaux profondes dans

l'Atlantique Nord pendant des périodes de précession positive renforce le transfert de chaleur entre les hémisphères, entraînant le déplacement du SASG vers le nord et une augmentation de la résurgence dans le BUS. J'ai ainsi pu établir une connexion entre l'intensification de la résurgence, l'intensité de l'AMOC, la circulation atmosphérique globale et une diminution du CO₂ atmosphérique pendant des phases positives de précession. Le chapitre 6 présente le protocole pour l'analyse des concentrations de Mg/Ca dans les foraminifères à l'aide d'un ICP-MS mis en place à l'IFREMER. Ce protocole a été appliqué à l'espèce *Globorotalia inflata* de la carotte MD08-3167 pour reconstruire les températures de la thermocline au cours des 365 derniers milliers d'années. Les analyses ont montré une reproductibilité externe cohérente, garantissant des résultats précis et permettant une reconstruction continue et fiable des températures basée sur la méthode Mg/Ca. Cet enregistrement contribue à une meilleure compréhension de la variabilité océanographique et climatique passée du BUS et de ses implications pour le cycle du carbone. En combinant ces points de vue des eaux de surface et des eaux profondes, ensemble avec la dynamique océan-atmosphérique et le cycle du carbone, nous avons obtenu des informations sur les mécanismes de rétroaction associés à la variabilité de l'AMOC, avec des implications importantes pour les changements de CO₂ atmosphérique.

Mots-clés: Circulation Méridienne de l'Atlantique; cycles orbitaux; Gyre Subtropical de l'Atlantique Sud; transfert de chaleur inter-hémisphérique; contrôles de l'Atlantique Sud sur le climat; analyses de Mg/Ca.

RÉSUMÉ DÉTAILLÉ EN FRANÇAIS

Le climat de la Terre a changé considérablement au cours du derniers siècles en raison des activités humaines, entraînant une augmentation substantielle des niveaux de CO₂ atmosphérique. Ceci a conduit à une augmentation des températures de surface globale que devrait se poursuivre dans les prochaines décennies. Les impacts de ces changements de température sont déjà évidents, avec des catastrophes climatiques plus fréquentes et intenses survenant dans le monde. L'un des composants clés affectés par le réchauffement climatique est la circulation méridienne de retournement Atlantique (AMOC, de l'anglais *Atlantic Meridional Overturning Circulation*), qui joue un rôle crucial dans la régulation du système climatique. Des études ont montré que l'AMOC ralentit dans les conditions actuelles et futures du réchauffement climatique. Ce ralentissement est attribué à la fonte de la glace dans les régions Arctique et Antarctique, ce qui perturbe l'AMOC et entraîne des changements dans l'étendue de la glace de mer et les températures de la surface de la mer et des eaux profondes, affectant la production en eau profonde et la circulation atmosphérique et les schémas de précipitations. Ces variations ont des conséquences d'une grande portée, notamment des changements dans les conditions météorologiques, une augmentation des sécheresses et des inondations et une augmentation régionale du niveau de la mer. Comprendre les mécanismes stimulant les changements AMOC et leur impact sur le système climatique est essentiel pour prédire et atténuer les effets du changement climatique. Les études paléoclimatologiques, et en particulier ceux basés sur des foraminifères, fournissent des informations précieuses sur le système climatique de la Terre et sa réponse à divers forçages. En examinant la variabilité passée des composants climatiques importants tels que les masses en eau profonde, l'océan supérieur et la dynamique atmosphérique, les scientifiques peuvent améliorer la modélisation du climat et faire des prédictions plus précises sur les changements climatiques futurs.

Le climat de la Terre a connu des transitions climatiques naturelles appelées cycles glaciaires-interglaciaires (G-IG) au cours des 800 000 dernières années. Ces cycles sont principalement entraînés par les changements de paramètres orbitaux de la Terre, tels que l'excentricité, l'inclinaison axiale et le forçage de la précession. Ces changements orbitaux conduisent à des variations du rayonnement solaire atteignant la surface de la Terre, affectant la dynamique climatique et la teneur de CO₂ atmosphérique. L'interaction entre le forçage

orbital, la dynamique de l'AMOC et le CO₂ atmosphérique est complexe et agit à travers des circuits en eau profonde et des interactions océan-atmosphériques.

L'AMOC, caractérisé par un forçage éolien en surface et thermohalin en profondeur, est essentielle pour transporter les masses d'eau à travers l'océan Atlantique et pour le maintien du bilan énergétique mondial. Deux composants clés de l'AMOC, le gyre subtropical de l'Atlantique Sud (SASG, de l'anglais *South Atlantic Subtropical Gyre*) et la position de la zone de convergence intertropicale (ITCZ, de l'anglais *Intertropical Convergence Zone*), ont des impacts significatifs sur le système climatique. Le SASG influence la variabilité du climat mondial par le biais de la dynamique de ses interactions océan-atmosphère dans l'Atlantique Sud, contrôlant le transport de l'énergie vers le nord. Les oscillations latitudinales de l'ITCZ représentent la réponse atmosphérique à ce transport d'énergie, jouant un rôle dans l'équilibrage de la distribution d'énergie à travers l'équateur et influençant les conditions météorologiques et la distribution des précipitations. En plus, le Système de remontes d'eaux profondes (ou "upwelling") du Benguela (BUS, de l'anglais *Benguela Upwelling System*), une cellule de l'upwelling de la marge orientale de l'Atlantique Sud, est influencé par l'étendue spatiale et l'intensification de l'ITCZ et par le transport d'énergie dans les régions subtropicales. Le BUS est crucial pour la pompe biologique, qui élimine le carbone de l'atmosphère et le stocke dans l'océan profond, réduisant les niveaux de CO₂ atmosphériques. La régulation de ces mécanismes dans des états climatiques différents est probablement associée à des modes distincts de l'AMOC, qui sont contrôlés par des réorganisations des interactions océan-atmosphère à l'échelle mondiale.

Cette thèse étudie les mécanismes de contrôle du forçage orbital sur les processus paléocéanographiques dans l'Atlantique Sud au cours des derniers 800 ka. L'accent est mis sur la compréhension du fonctionnement de la dynamique des eaux de surface et des eaux profondes pendant différents climats, et sur leur impact sur les niveaux de CO₂ atmosphérique. L'effort analytique a ciblé la production d'enregistrement des isotopes stables de l'oxygène et du carbone ($\delta^{18}\text{O}$ et $\delta^{13}\text{C}$) des coquilles de foraminifères de surface (planctoniques) et des fonds (benthiques) et de rapports de magnésium/calcium (Mg/Ca) des foraminifères planctoniques de deux carottes de sédiments marins subtropicaux aux deux marges du bassin de l'Atlantique Sud, sur les bords de la SASG : la carotte GL-854 (25°12'S, 42°37'O, 2220 m) est positionnée à la marge brésilienne sur 800 ka, et la carotte MD08-3167 (23°18.91'S, 12°22.61'E, 1948 m) à la marge namibienne et couvre 365 ka. Cette thèse

explore la relation complexe à une échelle de temp orbitale entre la dynamique des eaux profondes atlantiques, les processus océan-atmosphères et l'activité du BUS. Cette perspective de l'Atlantique Sud vise à mettre en évidence l'importance de la mise au point de déplacement de l'Atlantique Nord largement étudié vers l'Atlantique Sud sous-exploré dans la recherche climatique. La thèse est structurée en sept chapitres, avec le Chapitre 1 comme introduction et le Chapitre 2 détaillant les objectifs scientifiques et la structure des discussions scientifiques dans le manuscrit. Le Chapitre 3 se focalise sur la méthodologie, les indicateurs utilisés, le cadre chronologique et les résultats analytiques. Les Chapitres 4, 5 et 6 plongent dans des discussions scientifiques spécifiques sur la variabilité de masses d'eaux profondes, l'activité du BUS, et les reconstructions de la paleotemperature de surface respectivement. En étudiant les interactions de ces mécanismes complexes, j'ai pu obtenir des informations précieuses pour comprendre comment ils réagissent au forçage externe et modulent le climat mondial.

Le chapitre 4 explore les modes de circulation des eaux profondes dans l'océan Atlantique Sud au cours des derniers 800 ka à partir de l'enregistrement de $\delta^{13}\text{C}$ benthique de la carotte GL-854, que représente la variabilité de NADW dans l'Atlantique sud. En analysant le gradient zonale en $\delta^{13}\text{C}$ ($\Delta\delta^{13}\text{C}_{\text{w-e}}$) entre le courant profond de bord ouest (DWBC, de l'anglais *Deep Western Boundary Current*) et le courant de bord est (DEBC, de l'anglais *Deep Eastern Boundary Current*) calculé avec notre enregistrement, j'ai visé la compréhension des fluctuations de NADW dans le bassin sud-atlantique à l'échelle orbitale. Les périodes interglaciaires montrent des valeurs positives de $\Delta\delta^{13}\text{C}_{\text{w-e}}$, suggérant une influence plus forte de NADW, bien ventilée, sur le ouest de l'Atlantique Sud (WSA, de l'anglais *Western South Atlantic*), tandis que pendant les périodes glaciaires le gradient est diminué ou inversé, indiquant une circulation océanique réduite et une portée limitée des eaux bien ventilées. J'ai interprété donc l'indicateur $\Delta\delta^{13}\text{C}_{\text{w-e}}$ comme une réponse aux changements de la profondeur de l'interface entre NADW et Eau de fond de l'Antarctique (AABW, de l'anglais *Antarctic Bottom Water*). Quatre phases de l'AMOC ont été identifiées, oscillant entre des états de circulation plus intense et plus réduite, associés à des variations dans le volume de formation d'eaux profondes NADW ou AABW. Comme indiqué par les phases I et III identifiées sur l'enregistrement $\Delta\delta^{13}\text{C}_{\text{w-e}}$ (Fig. 25), il y a un impact notable sur les profondeurs moyennes de l'Atlantique Sud en raison d'influence accrue d'eaux plus faiblement ventilée. À l'inverse, les phases II et IV montrent que le signal « ventilé » du NADW atteint le WSA plutôt que l'Est de l'Atlantique Sud. Ces modes de

circulation à long terme de l'AMOC, alternant entre des états intenses et faibles, sont donc liés à la réorganisation mondiale de la circulation des eaux profondes et aux changements de ventilation de l'Océan Australe. Nos interprétations suggèrent une amplitude G-IG croissante associée à une formation augmentée d'eaux profondes et à des états vigoureux de l'AMOC après la Mid-Brunhes Transition (MBT).

Il est évident que l'Océan Australe joue un rôle crucial dans le lien entre la production en eau profonde, le réservoir de carbone de l'océan profond et l'atmosphère. Dans ce contexte, la variabilité de la glace de mer de l'Antarctique apparaît comme un facteur clé, contrôlant la stratification des eaux profondes et la formation d'AABW par le processus de rejet de saumure. Nos analyses suggèrent que l'augmentation de l'étendue de la glace de mer est contemporaine du dépôt de matériaux détritiques provenant des débris d'icebergs (IRD, de l'anglais *Ice-rafted Debris*) provenant de l'Antarctique sur le plateau des Agulhas et de la diminution de grande amplitude des valeurs $\Delta\delta^{13}C_{w-e}$. Ces facteurs contribuent à une augmentation de l'influence de l'AABW dans les profondeurs moyennes de l'Atlantique Sud, car l'augmentation de la glace de mer, le dépôt d'icebergs et les conditions glaciaires extrêmes entravent le mélange entre AABW et NADW, provoquant une réduction du NADW et une expansion de l'AABW simultanément avec des phases de $\Delta\delta^{13}C_{w-e}$ réduit. Le schéma opposé est observé pendant les phases de $\Delta\delta^{13}C_{w-e}$ plus élevé en réponse à la réduction de la glace de la mer Antarctique et des dépôts d'IRD. En outre, l'étude a examiné les effets du mécanisme suggéré concernant la glace de mer de l'Antarctique sur le positionnement des vents d'ouest (ou de l'anglais "*westerlies*") et des systèmes frontaux et son impact sur la formation des eaux profondes. Nos conclusions sont basées sur l'analyse de l'influence des altérations du flux de flottabilité dans l'Atlantique Nord, qui ont été causées par la réactivation de la fuite des Aiguilles (AL) après le MIS 12. Ces conclusions clarifient les mécanismes complexes contrôlant les cellules d'eaux profondes de l'AMOC et la dynamique océan-atmosphérique associée pour nous aider à comprendre comment la dynamique de l'Océan Australe impacte le cycle global du carbone à l'échelle orbitale.

J'ai cherché à identifier les forces à l'origine des changements significatifs de la glace de mer qui pourraient conduire à ces seuils de circulation. Les analyses spectrales que j'ai effectué sur plusieurs enregistrements ont fourni des preuves de puissance spectrale orbitale dans les domaines de l'obliquité (~ 40 ka) et de l'excentricité (~ 100 ka), indiquant que ces forçages exercent un contrôle sur la variabilité de la glace de la mer Antarctique et sur

l'enregistrement $\Delta\delta^{13}\text{C}_{\text{w-e}}$. La combinaison de différentes conditions d'insolation aux hautes latitudes méridionales contrôlées par le forçage orbital s'est avérée à l'origine des diverses phases vues dans l'enregistrement $\Delta\delta^{13}\text{C}_{\text{w-e}}$. L'impact de l'obliquité sur la quantité d'énergie d'insolation annuelle reçue dans l'hémisphère sud est un facteur crucial. Les périodes de faible obliquité ont entraîné une diminution de la fonte des glaces et une augmentation de la glace de mer, qu'explique les valeurs élevées de $\Delta\delta^{13}\text{C}_{\text{w-e}}$ pendant ces périodes, et un schéma opposé pendant les périodes de forte obliquité. En outre, l'amplitude croissante du forçage de l'obliquité peut avoir amplifié les cycles G-IG après MIS 12, comme discuté dans la littérature en accord avec notre enregistrement de $\Delta\delta^{13}\text{C}_{\text{w-e}}$. L'excentricité a probablement joué un rôle crucial dans cette transition climatique en modulant l'amplitude de l'insolation aux hautes latitudes, qui contrôle la fonte des glaces de mer, affectant la production en eau profonde. La nature saisonnière de la glace de mer Antarctique a été influencée par les effets de l'excentricité incrémentant ou réduisant les effets de l'obliquité sur l'insolation pendant l'hiver austral, la saison critique de la construction de glace. Dans l'ensemble, cet étude met en lumière le lien entre le forçage orbital, la variabilité de la glace de mer Antarctique, la formation des eaux profondes et les transitions entre les modes de l'AMOC, fournissant des informations précieuses sur la dynamique complexe du système climatique.

Le chapitre 5 se concentre sur la reconstruction de l'activité des BUS au cours des derniers 365 ka, une région de productivité biologique significative dans l'océan, contrôlée par la circulation de surface et l'activité du vent, et est également connectée à l'intensité AMOC. Ce chapitre explore la relation entre les alizés du sud-est (ou de l'anglais "*trade winds*"), le SASG et la variabilité des eaux profondes dans différents états de l'AMOC à l'échelle orbitale. Ces composants climatiques sont modifiés par les émissions de gaz à effet de serre anthropiques sous les changements climatiques actuels, qui devraient provoquer de graves conséquences pour le BUS. L'intensité du BUS est étroitement liée aux modes de circulation atmosphérique à grande échelle et à l'équilibre énergétique entre les hémisphères. Les modèles climatiques projettent un décalage vers le sud de la zone de convergence intertropicale (ITCZ, pour "*Intertropical Convergence Zone*") dans les océans du Pacifique oriental et de l'Atlantique, ce qui aurait un grand impact sur l'activité upwelling. Cependant, les impacts exacts de ces changements atmosphériques sont encore incertains.

Le BUS est bien connu et apprécié pour sa remarquable productivité biologique, attribuable aux eaux riches en nutriments qui sont remonté en surface par le déplacement des

couches superficielles par le vent. Ce phénomène naturel conduit à la mise à disposition en surface d'une abondance de nutriments qui soutient des diverses formes de vie et un écosystème florissant. L'upwelling favorise la croissance du phytoplancton et le transfert de CO₂ de l'atmosphère vers l'océan profond à travers de l'efficacité de la pompe biologique. Cependant, lorsque ces hauts niveaux de nutriments en surface ne sont pas entièrement utilisés par la biota, le BUS peut devenir une source de CO₂ dans l'atmosphère. Le BUS est divisé en deux sous-systèmes: le BUS sud (SBUS) et le BUS nord (NBUS). Le SBUS connaît un forte upwelling pendant l'été austral, tandis que le NBUS connaît un haut niveau de l'upwelling tout au long de l'année, s'intensifiant encore plus en hiver austral; en dessous de 20°S le NBUS agit comme un puits actif de CO₂ atmosphérique. Des études antérieures ont regardé des aspects divers de la dynamique du BUS, notamment le rôle de l'activité du vent, la productivité primaire, le cycle des nutriments et l'assimilation du CO₂. Cependant, il y a toujours un manque d'enregistrements à haute résolution à long terme qui puissent fournir une compréhension complète de la variabilité du BUS à la fin du Pléistocène.

Ce chapitre se concentre donc sur l'étude de la variabilité à long terme du NBUS au cours des quatre derniers cycles glaciaires-interglaciaires. Pour y parvenir, une approche multiproxy a été utilisée à partir de l'analyse réalisée à haute résolution de la carotte de sédiments marins MD08-3167, situé dans la marge de la Namibie. La stratification de l'océan de surface du NBUS a été reconstruite pour suivre la variabilité de la remontée des eaux profonde en calculant le gradient $\delta^{18}\text{O}$ entre deux espèces de foraminifères planctoniques, *Globigerina bulloides*, espèce qui est censée habiter en surface, et de *Globorotalia inflata*, nichant dans la thermocline ($\Delta\delta^{18}\text{O}$). En plus, les gradients de leur $\delta^{13}\text{C}$ ont été calculés entre les mêmes espèces ($\Delta\delta^{13}\text{C}_{\text{upper}}$) et entre *G. inflata* et les foraminifères benthiques *Cibicides wuellerstorfi* ($\Delta\delta^{13}\text{C}_{\text{lower}}$). Ces gradients de $\delta^{13}\text{C}$ aident à vérifier les effets potentiels de l'activité de l'upwelling sur le budget mondial du carbone. Des modes complexes et les changements dans le NBUS à l'échelle orbitale sont vérifiés en combinant ces indicateurs indépendants.

L'enregistrement de $\Delta\delta^{18}\text{O}$ montre une stratification plus poussée pendant les périodes interglaciaires qui diminue systématiquement pendant les périodes glaciaires et les sous périodes froids. Ce compartiment s'est accompagné d'une augmentation rapide des valeurs $\delta^{18}\text{O}$ de *G. bulloides* et de *G. inflata*. La similitude entre les enregistrements isotopiques des deux espèces suggère qu'un forçage commun à leur contrôle, potentiellement

lié à l'intensification du vent et à la pompe d'Ekman. Des vents plus forts favorisent l'upwelling des eaux centrales froides de l'Atlantique Sud (SACW) aux couches supérieures de l'océan, conduisant à une diminution de la stratification et des eaux de surface plus froides, ce qui est reflété par le refroidissement systématique de la température de la surface de la mer (SST) au NBUS. Ces diminutions brusques de $\Delta\delta^{18}\text{O}$ ont coïncidé avec des pics dans l'abondance de *Neogloboquadrina pachyderma* dans des carottes voisines, suggérant une relation entre la diminution de la stratification et l'activité d'upwelling. Ces occurrences ont eu lieu principalement pendant des périodes de précession positive, lorsque les étés de l'hémisphère sud sont intensifiés. L'intensification du NBUS pendant la précession positive a probablement élargi la zone d'upwelling vers l'ouest en raison des alizés du SE intensifiés, jusqu'à atteindre le site MD08-3167. Cela suggère que les contrôles orbitaux, en particulier la précession positive.

L'analyse spectrale des enregistrements $\delta^{18}\text{O}$ et $\Delta\delta^{18}\text{O}$ confirme l'influence des contrôles orbitaux sur le BUS sur les domaines de la précession, de l'obliquité et de l'excentricité. Le rythme de précession s'aligne sur les changements de $\Delta\delta^{18}\text{O}$ dans les maxima d'insolation estivale à 23°S pendant une précession positive, tandis que une stratification accrue est observée pendant la précession négative. L'obliquité influence les latitudes moyennes à élevées en régulant l'insolation et l'intensité des vents d'ouest de l'hémisphère sud et des alizés du sud-est, ce qui contrôle l'activité d'upwelling du NBUS.

L'intensité de l'antiphase entre les zones d'upwelling côtières du nord-ouest et du sud-ouest de l'Afrique est observée en raison de la dynamique asymétrique des alizés entre les hémisphères. Nos résultats indiquent que la diminution de l'activité de mousson de l'hémisphère nord pendant les périodes d'upwelling est intensifiée. De manière opposée, lorsque le Sahara nord-africain subit un réchauffement de surface et des basses pressions, la mousson d'Afrique de l'Ouest s'intensifie. Ceci, à son tour, réduit la zonalité des alizés du sud-est et l'upwelling au NBUS. La reconstruction de la force du vent dans l'Atlantique sud-est corrobore notre interprétation de l'intensification zonale des alizés, qui renforce les connexions subtropicales-tropicales et augmente l'upwelling pendant la précession positive. La connexion subtropicale-tropicale renforcée par la cellule subtropicale et le courant de Benguela explique le schéma de stratification similaire à celui du NBUS dans l'ouest de l'Atlantique Sud tropical. L'enregistrement $\Delta\delta^{18}\text{O}$ fournit un enregistrement à haute

résolution de l'activité d'upwelling du NBUS, montrant une intensification induite par la précession pendant les maxima d'insolation australe.

La formation intensifiée en eau profonde dans l'Atlantique Nord pendant les phases de précession positive entraîne un transfert de chaleur de l'Atlantique Sud vers le nord, accompagné d'un décalage vers le nord des composants SASG et atmosphérique. Ce changement vers le nord est le principal mécanisme qui a favorisé l'intensification des alizés qu'augmentent l'upwelling dans le NBUS. Inversement, les phases de précession négative présentent un schéma opposé. Le rôle du SASG dans la régulation du transport d'énergie interhémisphérique est également lié aux connexions indo-atlantiques, ce qui implique un schéma de bascule entre le NBUS et l'AL. Ces dynamiques océan-atmosphériques sont essentielles pour moduler l'AMOC par des cycles précessionnaires. Pendant la précession négative, la position vers le sud du SASG réduit le transport énergétique interhémisphérique et réactive l'AL, faisant du SASG un réservoir de chaleur pendant ces périodes.

L'efficacité de la pompe biologique associée au transfert de carbone dans l'océan pendant la précession positive a été évaluée via des enregistrements $\Delta\delta^{13}\text{C}_{\text{upper}}$ et $\Delta\delta^{13}\text{C}_{\text{lower}}$. Les enregistrements $\delta^{13}\text{C}$ individuels de *G. bulloides* et *G. inflata* présentent également des valeurs plus élevées pendant activité intense d'upwelling, ce qui suggère que pendant les périodes d'intensification de la productivité primaire, le carbone est transféré verticalement dans la colonne d'eau vers la thermocline. De manière cohérente, les différences en $\delta^{13}\text{C}$ entre les couches de surface et de thermocline sont réduites, comme le montrent l'augmentation de $\Delta\delta^{13}\text{C}_{\text{upper}}$, indiquant une couche supérieure homogène avec une productivité primaire accrue. Le $\Delta\delta^{13}\text{C}_{\text{lower}}$ montre un schéma similaire, suggérant qu'une partie significative de l'absorption de carbone dans la surface est transférée vers le fond, ce qui est corroboré par une augmentation des enregistrements de carbone organique de plusieurs sites dans le NBUS pendant ces périodes. Ces résultats indiquent que le NBUS agissent comme un puits de CO_2 atmosphérique en raison de l'activité biologique dépassant le CO_2 qui dégaze pendant les périodes de précession positive, synchrones avec des réductions de CO_2 atmosphérique enregistrées dans les carottes de glace d'Antarctique. Cela suggère que le CO_2 atmosphérique est capturé et stocké dans l'océan profond. Les températures plus froides de l'Antarctique et une position vers le nord du SASG éloignent les vents de l'ouest de l'Antarctique, réduisant l'upwelling dans l'océan Austral et empêchant le CO_2 de sortir des couches profondes. Cette dynamique, associée à l'upwelling

intensifiée dans le NBUS, contribue à une réduction de la teneur en CO₂ atmosphérique pendant les phases de précession positive. Ce chapitre met l'accent sur le rôle de la modulation précessionnelle sur le transport inter-hémisphérique de l'AMOC, déclenchant des réponses océan-atmosphériques dans l'Atlantique Sud qui contrôlent l'activité des BUS. Les processus en surface et en profondeur fonctionnent ensemble pendant les cycles précessionnaires, exerçant un grand contrôle sur le CO₂ atmosphérique

Le Chapitre 6 présente le protocole d'analyse du rapport Mg/Ca dans les coquilles calcaires des foraminifères à l'aide d'un spectromètre de masse à couplage inductif haute résolution à source plasma (ICP-MS) à l'IFREMER, avec l'intention à mi-terme de mettre en œuvre la même technique analytique à l'Universidade Federal Fluminense (UFF) au Brésil. Bien que l'analyse Mg/Ca ait été largement utilisée dans les laboratoires européens pour des études en paléocéanographie, paléoclimatologie et biogéochimie, elle est moins répandue au Brésil à cause des coûts élevés et des exigences de manutentions. Ce chapitre décrit les matériaux nécessaires, le protocole de nettoyage, la préparation et utilisation de standards internes et internationaux pour calibration des résultats avec la méthode de calibration externe, les étapes analytiques pour la détermination de la concentration des échantillons de foraminifères et les équations pour reconstruire les températures à partir des résultats de mesure.

Le protocole a été appliqué aux échantillons d'espèces de *G. inflata* de la carotte MD08-3167 afin de reconstruire la variabilité de la température de la thermocline dans le BUS au cours des derniers environ 365 ka. La détermination des incertitudes associées aux mesures en évaluant l'analyse répétée des solutions standard a été une priorité. La reproductibilité externe a été évaluée, et la précision des mesures a été trouvée dans les limites acceptables, fournissant des résultats fiables et précis. En calibrant les rapports Mg/Ca avec l'équation que j'ai trouvée la plus adéquate (Groeneveld and Chiessi, 2011, section 6.6), des températures entre 0.4°C et 14°C ont été reconstruites, avec une température moyenne de 9.3°C. L'enregistrement montre une variabilité significative, avec des cycles glaciaires-interglaciaires distincts et des changements superposés à l'échelle de temps millénaire. Les reconstructions de température ont révélé un refroidissement de la thermocline systématique concomitant avec une augmentation des excursions positives de δ¹⁸O en foraminifère planctonique de thermocline au cours de la période d'étude, ce qui implique la grande influence de la température sur les valeurs de δ¹⁸O planctonique à cette

profondeur. Les résultats suggèrent que les changements dans l'intensité de l'upwelling, associée avec du stress du vent et des courants océaniques, ont joué un rôle important dans le refroidissement de la thermocline. Ces résultats contribuent à une meilleure compréhension de la variabilité océanographique et climatique passée dans le BUS, ce qui a des implications pour le cycle du carbone. En outre, ces résultats montrent que cette dynamique mérite d'être explorée et approfondie dans un futur proche en examinant différentes échelles de temps. En outre, la mise en œuvre réussie de la technique Mg/Ca à l'IFREMER représente une étape importante du transfert de technologie entre IFREMER et UFF, avec des plans futurs pour valider la méthode au Brésil.

Comme résumé dans le Chapitre 7, la recherche présentée dans cette thèse a examiné, d'un point de vue autant de la surface que des eaux profondes, les processus océanographiques, leur interaction avec l'atmosphère et leur relation avec le cycle du carbone de l'Atlantique Sud pendant le Quaternaire tardif. Mes résultats ont révélé les connexions complexes et des mécanismes de rétroaction qui régissent la variabilité de l'AMOC et ses implications pour les niveaux de CO₂ atmosphériques. Ils contribuent à notre compréhension plus large de la variabilité du climat à long terme et soulignent le rôle pivot de la région de l'Atlantique Sud dans la modulation du climat globale. Cette thèse invite à une exploration plus approfondie et souligne l'importance de la recherche continue dans l'Atlantique Sud subtropical pour approfondir nos connaissances des changements climatiques passés et leurs implications pour l'avenir.

LIST OF FIGURES

- FIGURE 1** - LOCATION OF THE TWO MARINE SEDIMENT CORES UTILIZED IN THIS THESIS. WESTERN MARGIN: GL-854 AT SANTOS BASIN (BLUE DIAMOND). EASTERN MARGIN: MD08-3167 OFF THE NAMIBIAN MARGIN (GREEN DIAMOND). THE PURPLE DASHED LINE AND ARROWS REPRESENT THE ATMOSPHERIC COMPONENTS: THE INTERTROPICAL CONVERGENCE ZONE (ITCZ) AND TRADE WINDS, RESPECTIVELY. THE SOUTH ATLANTIC WATER GATEWAYS CONNECTING THE INDIAN AND THE PACIFIC OCEANIC BASINS ARE INDICATED: AGULHAS LEAKAGE (AL) AND DRAKE PASSAGE (DP). BLACK ARROWS SCHEMATICALLY REPRESENT THE SOUTH ATLANTIC UPPER CIRCULATION. WHITE ARROWS INDICATE THE POSITION OF THE HIGH-LATITUDE FRONTAL SYSTEM. BACKGROUND COLORS DISPLAY THE SUBSURFACE TEMPERATURE AT 300 M FROM THE DATABASE WORLD OCEAN ATLAS 2018 (WOA 18; LOCARNINI ET AL., 2018). MC: BRAZIL-MAVINAS CONFLUENCE. SEC: SOUTH ATLANTIC EQUATORIAL CURRENT. SECC: SOUTH ATLANTIC EQUATORIAL COUNTER CURRENT. BC: BRAZILIAN CURRENT. SAC: SOUTH ATLANTIC CURRENT. BEC: BENGUELA CURRENT. NBC: NORTH BRAZIL CURRENT. NECC: NORTH BRAZIL COUNTER CURRENT 46
- FIGURE 2** - SCANNING ELECTRON MICROSCOPE (SEM) PHOTOGRAPHY OF THE FORAMINIFERAL SPECIES USED IN THIS THESIS. THE LEFT PANEL PRESENTS THE BENTHIC SPECIES (A) CIBICIDES WUELLERSTORFI AND (B) UVIGERINA PEREGRINA. THE RIGHT PANEL SHOWS THE PLANKTIC SPECIES (C) GLOBIGERINOIDES RUBER, (D) GLOBIGERINA BULLOIDES, AND (E) GLOBOROTALIA INFLATA. IMAGES FROM WORMS EDITORIAL BOARD (2023) 50
- FIGURE 3** - FORAMINIFERA DISTRIBUTION PROVINCES. LATITUDINAL PROVINCES ARE POLAR (P), SUBPOLAR (SUBP), TRANSITIONAL (TRANS), SUBTROPICAL (S), TROPICAL (TR), AND THE UPWELLING AND EUTROPHIC CONDITIONS (U). MODIFIED AFTER HEMLEBEN ET AL. (1989) (SCHIEBEL AND HEMLEBEN, 2017) 51
- FIGURE 4** - TEMPERATURE-RELATED DISTRIBUTION OF PLANKTIC FORAMINIFERA SPECIES AND THEIR RESPECTIVE PROVINCES IN THE ATLANTIC OCEAN (KUCERA ET AL., 2005). THE AVERAGE ABUNDANCES OF THE MAJOR SPECIES OF THE RESPECTIVE ASSEMBLAGES ARE DISPLAYED BY COLORED BARS. MODIFIED AFTER KUCERA (2007) (SCHIEBEL AND HEMLEBEN, 2017) 53
- FIGURE 5** - REFERENCE CURVE AND THE ORIGINAL AGE-DEPTH MODEL OF GL-854 CORE PUBLISHED IN DE ALMEIDA ET AL. (2015). THE LEFT FIGURE DISPLAYS A) C. WUELLERSTORFI $\Delta^{18}\text{O}$ (PERMIL VPDB) VS. DEPTH, B) SAME VS. AGE (KA) PLOTTED AGAINST THE BENTHIC $\Delta^{18}\text{O}$ GLOBAL STACK (LR04, IN PERMIL VPDB; LISIECKI AND RAYMO, 2005), AND C) C. WUELLERSTORFI $\Delta^{13}\text{C}$ (PERMIL VPDB) VS. AGE (KA). BLACK TRIANGLES INDICATE RADIOCARBON AGES. RIGHT FIGURE: D) AGE-DEPTH MODEL BASED ON THE SOFTWARE ANALYSERIES V2.0 (PAILLARD ET AL., 1996) 60
- FIGURE 6** - REFERENCE CURVE AND THE AGE-DEPTH MODEL OF MD08-3167 CORE. THE LEFT FIGURE DISPLAYS A) BENTHIC $\Delta^{18}\text{O}$ (PERMIL VPDB) VS. DEPTH, B) THE SAME VS. AGE (KA) PLOTTED AGAINST THE BENTHIC $\Delta^{18}\text{O}$ GLOBAL STACK (LR04; IN PERMIL VPDB; LISIECKI AND RAYMO, 2005), AND C) BENTHIC $\Delta^{13}\text{C}$ (PERMIL VPDB) VS. AGE (KA). UVIGERINA PEREGRINA DATA (BROWN DATA POINTS) ARE INDICATED IN PANEL C. BLACK TRIANGLES INDICATE THE RADIOCARBON AGES. RIGHT FIGURE D) AGE-DEPTH MODEL BASED ON BACON V2.3 (BLAAUW AND CHRISTEN, 2011) 61
- FIGURE 7** - BENTHIC ISOTOPIC RECORD VERSUS DEPTH (CM) FROM CORE GL-854. CIBICIDES WUELLERSTORFI A) $\delta^{13}\text{C}$ (PERMIL VPDB) AND B) $\delta^{18}\text{O}$ (PERMIL VPDB). VERTICAL DASHED LINES MARK GLACIAL TERMINATIONS, DEFINED BASED ON THE BENTHIC $\delta^{18}\text{O}$ RECORD 63
- FIGURE 8** - PLANKTIC ISOTOPIC RECORD VERSUS DEPTH (CM) FROM CORE GL-854. A) GLOBIGERINOIDES RUBER (RED CURVES) $\delta^{13}\text{C}$ (PERMIL VPDB) AND B) $\delta^{18}\text{O}$ (PERMIL VPDB). C) GLOBOROTALIA INFLATA (BLUE CURVES) $\delta^{13}\text{C}$ (PERMIL VPDB) AND D) $\delta^{18}\text{O}$ (PERMIL VPDB)

RECORDS. VERTICAL DASHED LINES MARK GLACIAL TERMINATIONS, DEFINED BASED ON THE BENTHIC $\delta^{18}\text{O}$ RECORD..... 64

FIGURE 9 - BENTHIC ISOTOPIC RECORD VERSUS DEPTH (CM) FROM CORE MD08-3167. A) CIBICIDES WUELLERSTORFI (DARK GREEN LINE; $\delta^{18}\text{O}$ -CORRECTED VALUES) AND U. PEREGRINA (BROWN DOTS) $\delta^{13}\text{C}$ (PERMIL VPDB) AND B) $\delta^{18}\text{O}$ (PERMIL VPDB) RECORDS. BENTHIC ISOTOPES FROM THE FIRST 700 CM OF THE CORE ARE UNPUBLISHED DATA PREVIOUSLY PRODUCED AT LSCE (LIGHT BLUE LINE). VERTICAL DASHED LINES MARK GLACIAL TERMINATIONS, DEFINED BASED ON THE BENTHIC $\delta^{18}\text{O}$ RECORD 66

FIGURE 10 - PLANKTIC ISOTOPIC RECORD VERSUS DEPTH (CM) FROM CORE MD08-3167. GLOBIGERINA BULLOIDES (RED CURVES) A) $\delta^{13}\text{C}$ (PERMIL VPDB) AND B) $\delta^{18}\text{O}$ (PERMIL VPDB) RECORDS. GLOBOROTALIA INFLATA (DARK BLUE CURVES) C) $\delta^{13}\text{C}$ (PERMIL VPDB) AND D) $\delta^{18}\text{O}$ (PERMIL VPDB) RECORDS. PLANKTIC ISOTOPES FROM THE FIRST 700 CM OF THE CORE ARE UNPUBLISHED DATA PREVIOUSLY PRODUCED IN LSCE (LIGHT BLUE LINE). VERTICAL DASHED LINES MARK GLACIAL TERMINATIONS, DEFINED BASED ON THE BENTHIC $\delta^{18}\text{O}$ RECORD 67

FIGURE 11 - GLOBOROTALIA INFLATA A) MG/CA RATIO (MMOL/MOL), B) $\delta^{18}\text{O}$ (PERMIL VPDB) RECORDS, AND C) BENTHIC FORAMINIFERA $\delta^{18}\text{O}$ (PERMIL VPDB) RECORD VERSUS DEPTH (CM) FROM MD08-3167 CORE BETWEEN 700 AND 3541 CM OF THE CORE. VERTICAL DASHED LINES MARK GLACIAL TERMINATIONS, DEFINED BASED ON THE BENTHIC $\delta^{18}\text{O}$ RECORD 69

FIGURE 12 - INTENSITIES OF SOME XRF-MEASURED MAJOR ELEMENTS AND LIGHTNESS (L^*) MEASURED BY SPECTROPHOTOMETRY IN THE MULTI SENSOR CORE LOGGER (MSCL) ON BOARD, BOTH IN BULK SEDIMENTS FROM MD08-3167. A) TI/CA RATIO; B) CA/FE RATIO; C) L^* ; AND D) BENTHIC FORAMINIFERA $\delta^{18}\text{O}$ (PERMIL VPDB) FOR STRATIGRAPHIC REFERENCE. VERTICAL DASHED LINES MARK GLACIAL TERMINATIONS, DEFINED BASED ON THE BENTHIC $\delta^{18}\text{O}$ RECORD 70

FIGURE 13 - A) POSITION OF CORE GL-854 (RED PIN, THIS STUDY) IN THE WESTERN SOUTH ATLANTIC (WSA) AND OTHER MARINE RECORDS DISCUSSED IN THIS WORK (RED CIRCLES: MID-DEPTH CORE SITE, WHITE CIRCLES: DEEP CORE SITES): NORTH ATLANTIC SITES: ODP SITE 980 (FLOWER ET AL., 2000), IODP SITE U1308 (HODELL AND CHANNELL, 2016), ODP SITES 658, 659 (SARNTHEIN AND TIEDEMANN, 1989), GIK 13519 (SARNTHEIN ET AL., 1984); SOUTH ATLANTIC SITES: ODP SITES 1264, 1267 (BELL ET AL., 2014), AND 704 (HODELL, 1993), MD02-2588 (STARR ET AL., 2021), ODP SITES 1088 AND 1090 (HODELL ET AL., 2003). B) TO F) SECTIONS SHOWING PRE-INDUSTRIAL $\delta^{13}\text{C}$ DISTRIBUTION IN THE WATER COLUMN (EIDE ET AL., 2017). E) MERIDIONAL SECTIONS OF THE B) WESTERN AND C) EASTERN SOUTH ATLANTIC ENCOMPASSING THE SUBTROPICAL SOUTH ATLANTIC SITES; D) SUBTROPICAL SOUTH ATLANTIC ZONAL SECTION. SECTIONS ARE REPRESENTED IN THE MAP BY THE BLUE, RED, AND YELLOW COLORS, RESPECTIVELY. F) PREINDUSTRIAL VERTICAL $\delta^{13}\text{C}$ PROFILES OF THE CLOSEST STATIONS TO GL-854 (BLUE) AND TO ODP SITE 1264 (RED) (EIDE ET AL., 2017). THE BLACK SQUARE AND CIRCLE ARE THE CLOSEST DATA POINTS TO THE DEPTH OF THE CORES. THE FIGURE WAS PRODUCED USING OCEAN DATA VIEW (SCHLITZER, 2021) 74

FIGURE 14 - LONG-TERM RAMPFIT PHASES REVEALED IN THE $\Delta\delta^{13}\text{C}_{\text{W-E}}$ ($\delta^{13}\text{C}_{\text{GL-854}} - \delta^{13}\text{C}_{\text{ODP 1264}}$) RECORD, SHOWING THAT THE SUBTROPICAL ZONAL $\delta^{13}\text{C}$ GRADIENT BETWEEN THE SOUTH ATLANTIC MID-DEPTH SITES INCREASE AFTER THE MID-BRUNHES TRANSITION (MBT). A) $\Delta\delta^{13}\text{C}_{\text{W-E}}$ (LIGHT PURPLE LINE) WITH EIGHT-POINT KNN-SMOOTHED AVERAGE (DARK PURPLE LINE); RAMPFIT RESULTS (SOLID RED LINES) ARE DISPLAYED WITH THEIR RESPECTIVE UNCERTAINTIES (LIGHT BLUE

SHADED AREA). B) LATITUDINAL GRADIENT ($\Delta\delta^{13}\text{C}_{\text{NCW-SCW}}$, THIN LIGHT GREEN LINE) AND THREE-POINT RUNNING AVERAGE (THICK LIGHT GREEN LINE) OF THE DIFFERENCE BETWEEN THE NORTHERN AND SOUTHERN COMPONENT WATER (NCW AND SCW, RESPECTIVELY) STACKS (BARTH ET AL., 2018). C) $\delta^{13}\text{C}$ (‰ VPDB) AND D) $\delta^{18}\text{O}$ (‰ VPDB) OF CORES GL-854 (THIS STUDY; BLUE), ODP SITE 1264 (RED) AND NORTH ATLANTIC ODP SITE 980 (DARK PINK). ODP SITE 980 REPRESENTS THE END-MEMBER OF THE UPPER PORTION OF THE NORTH ATLANTIC DEEP WATER (NADW) IN THE VICINITY OF NORTH ATLANTIC PRODUCTION SITES. THE COMPARISON BETWEEN THEM SHOWS THAT THE NADW SIGNAL IS CARRIED BY THE DEEP WESTERN BOUNDARY CURRENT (DWBC) TO THE WESTERN SOUTH ATLANTIC. RED BARS HIGHLIGHT INTERGLACIAL PERIODS AND DASHED LINES MARK GLACIAL-INTERGLACIAL TRANSITIONS OVER THE LAST CA. 800 KA (TERMINATIONS (T) I TO VIII ARE INDICATED). ALL RECORDS ARE SHOWN AGAINST AGE (KA)..... 84

FIGURE 15 - EVOLUTION OF LONG-TERM OCEANOGRAPHIC AND CLIMATE RECORDS CONTROLLING THE LONG-TERM TREND IN THE DEEP-WATER SEESAW. A) OBLIQUITY ($^\circ$; LASKAR ET AL., 2004). B) $\Delta\delta^{13}\text{C}_{\text{W-E}}$ (LIGHT PURPLE LINE) WITH 8-POINT KNN-SMOOTHED AVERAGE (DARK PURPLE LINE); RAMPFIT RESULTS (SOLID RED LINES) ARE DISPLAYED WITH RESPECTIVE UNCERTAINTIES (LIGHT BLUE SHADED AREA). THE BACKGROUND BLUE, LIGHT YELLOW, GREEN, AND DARK YELLOW BARS INDICATE RAMPFIT PHASES I, II, III, AND IV, RESPECTIVELY. BLACK LINE: ECCENTRICITY LASKAR ET AL., 2004). C) SEA-SALT Na FLUX (YELLOW LINE; WOLFF ET AL., 2006), AGULHAS PLATEAU ICE-RAFTED DEBRIS (IRD) COUNTS (DARK BLUE SHADED LINE; STARR ET AL., 2021), AND ODP SITE 1090 Fe MAR (DARK PINK LINE; (MARTÍNEZ-GARCIA ET AL., 2011) RECORDS. D) EPICA DOME C δD AND ATMOSPHERIC CO_2 (BLACK AND PURPLE LINES, RESPECTIVELY; JOUZEL ET AL., 2007; LÜTHI ET AL., 2008). E) ODP SITE 1090 SEA-SURFACE TEMPERATURE (SST) (ORANGE LINE; (MARTÍNEZ-GARCIA ET AL., 2009) AND ACCUMULATION RATE (AR) OF TYPICAL AGULHAS LEAKAGE FAUNA (GLOROBOTALIA MERNARDII) FROM ODP SITE 1087 (GREEN FILLED CURVE; CALEY ET AL., 2012). DASHED LINES REPRESENT THE GLACIAL-INTERGLACIAL TERMINATIONS. ALL RECORDS ARE PRESENTED AGAINST AGE (KA) 89

FIGURE 16 - REDFIT SPECTRAL ANALYSIS RESULTS PERFORMED IN A) GL-854 $\delta^{13}\text{C}$, B) DOME C SSNa, C) $\Delta\delta^{13}\text{C}_{\text{W-E}}$, AND D) AGULHAS PLATEAU IRD RECORDS REVEAL RELEVANT SPECTRAL POWER (Y AXES) ABOVE THE 90% CONFIDENCE INTERVALS IN THE OBLIQUITY AND ECCENTRICITY FREQUENCY DOMAINS (X AXES). CONFIDENCE LEVEL BASE LINES (GREEN AND ORANGE) AND SIGNIFICANT SPECTRAL PERIODICITIES ARE INDICATED..... 92

FIGURE 17 - SCHEMATIC REPRESENTATION OF THE MAIN PROCESSES RESULTANT OF ANTARCTIC SEA ICE EXTENT VARIABILITY THROUGH RAMPFIT PHASES A) I, B) II, C) III, AND D) IV. PHASES II AND IV SHOW SIMILAR SCENARIOS WITH REDUCED SEA ICE EXTENT, DECREASED BRINE REJECTION, AND HENCE REDUCED ANTARCTIC BOTTOM WATER (AABW) FORMATION. REDUCED SEA ICE EXTENT ALSO PROMOTES THE SOUTHWARD LATITUDINAL DISPLACEMENT OF THE WESTERLIES AND SUBTROPICAL FRONT, INCREASING AGULHAS LEAKAGE (AL) THAT CONTRIBUTES TO INCREASING NORTH ATLANTIC DEEP WATER (NADW) PRODUCTION. HIGHER INTERGLACIAL SEA-ICE MELTING AND THE AL REACTIVATION AFTER MIS 12 WOULD EXPLAIN THE MAIN DIFFERENCE BETWEEN PHASES II AND IV THAT LED TO MORE EXTENDED NADW SOUTHWARD PENETRATION DURING PHASE IV. RAMPFIT PHASES I AND III SHOW INCREASED GLACIAL SEA ICE EXTENT, ENHANCED BRINE REJECTION AND INCREASED ANTARCTIC BOTTOM WATER (AABW) FORMATION. DURING THESE PHASES, VERY LOW AABW $\delta^{13}\text{C}$ VALUES ARE DUE TO THE ENHANCED BIOLOGICAL PUMP, AND AABW PENETRATES FURTHER NORTH, REACHING UP TO 2200 M DEPTH, REDUCING $\Delta\delta^{13}\text{C}_{\text{W-E}}$. THE MAIN DIFFERENCE BETWEEN PHASES I AND III IS RELATED TO THE AL INTENSIFICATION DURING PHASE III. IN THIS PHASE, THE AL EFFECT ON NADW DURING MIS 11 AND MIS 9 MAY HAVE BEEN COMPENSATED BY THE INTENSE GLACIAL STAGES AT MIS 12 AND MIS 10. THE VERTICAL

MOVEMENTS OF THE BOUNDARY BETWEEN NADW AND AABW ARE REPRESENTED. COMBINED, THESE PROCESSES DRIVE SUBSTANTIAL CHANGES IN DEEP-WATER PROPERTIES AND FORMATION, AFFECTING ATLANTIC MERIDIONAL OVERTURNING CIRCULATION. DIAGRAMS AND SYMBOLS ARE DESCRIBED IN THE FIGURE. DARKER AND LIGHTER BACKGROUND COLORS REPRESENT DENSER AND LESS DENSE DEEP-WATER CELLS, RESPECTIVELY OF AABW AND NADW 93

FIGURE 18 - A) SOUTH ATLANTIC UPPER CIRCULATION AND ATMOSPHERIC COMPONENTS: THE INTERTROPICAL CONVERGENCE ZONE (ITCZ), TRADE WINDS (BLUE DASHED LINE AND ORANGE ARROWS REPRESENTATION, RESPECTIVELY), AND THE SOUTH ATLANTIC HADLEY CELL (3D BLUE AND RED ARROWS AND CLOUD). BACKGROUND COLORS REPRESENT INTERPOLATED PHOSPHATE DISTRIBUTION AT 300 M DEPTH (MMOL/L) FROM THE WORLD OCEAN ATLAS 2018 (WOA 18; GARCIA ET AL., 2018) DATABASE. DASHED WHITE SQUARES INDICATE THE GEOGRAPHIC AREA REFERENT TO B) EASTERN SOUTH ATLANTIC (ESA) AND C) WESTERN SOUTH ATLANTIC (WSA). POSITION OF SEDIMENT CORE MD08-3167 (GREEN DIAMOND PIN, THIS STUDY) AND OTHER MARINE RECORDS DISCUSSED IN THIS WORK (WHITE CIRCLES) IN A) WSA: GL-1180 (NASCIMENTO ET AL., 2021); M125-55-7 (HOU ET AL., 2020); AND IN B) ESA: MD96-2094 (STUUT ET AL., 2002); GEOB 1712-4; GEOB 1711-4; GEOB 1710-3 (LITTLE ET AL., 1997; VOLBERS ET AL., 2003; WEST ET AL., 2004); GEOB 1028 (SCHNEIDER ET AL., 1995); ODP SITE 1083 (WEST ET AL., 2004); CAPE BASIN RECORD (PEETERS ET AL., 2004). BACKGROUND COLORS ON B) AND C) INDICATE THE PHOSPHATE DISTRIBUTION AT SURFACE. SOUTH ATLANTIC CENTRAL WATER (SACW) FORMATION ZONES ARE INDICATED ON B) BRAZIL-MALVINAS CONFLUENCE (BMC) AND C) AGULHAS LEAKAGE (AL). THE FIGURE WAS PRODUCED USING OCEAN DATA VIEW (SCHLITZER, 2021) 112

FIGURE 19 - RECORDS FROM CORE MD08-3167 LOCATED AT THE NORTHERN BENGUELA UPWELLING SYSTEM (NBUS). A) GLOBIGERINA BULLOIDES (RED LINE) AND GLOBOROTALIA INFLATA (BLUE LINE) $\delta^{18}\text{O}$ RECORDS (‰ VPDB). B) UPPER-OCEAN STRATIFICATION RECORD (TRANSPARENT PURPLE LINE WITH CIRCLES; $\Delta\delta^{18}\text{O} = \delta^{18}\text{O}_{\text{G.INFLATA}} - \delta^{18}\text{O}_{\text{G.BULLOIDES}}$; ‰ VPDB) WITH THREE-POINT RUNNING AVERAGE (SOLID PURPLE LINE). C) UPPER-VERTICAL $\delta^{13}\text{C}$ GRADIENT BETWEEN SURFACE AND THERMOCLINE LAYERS ($\Delta\delta^{13}\text{C}_{\text{UPPER}} = \delta^{13}\text{C}_{\text{G.BULLOIDES}} - \delta^{13}\text{C}_{\text{G.INFLATA}}$; ‰ VPDB; TRANSPARENT GREEN LINE WITH CIRCLES) WITH THREE-POINT RUNNING AVERAGE (SOLID GREEN LINE). D) GLOBIGERINA BULLOIDES (RED LINE) AND GLOBOROTALIA INFLATA (BLUE LINE) $\delta^{13}\text{C}$ RECORDS (‰ VPDB). E) CIBICIDES WUELLERSTORFI $\delta^{13}\text{C}$ (PINK LINE; ‰ VPDB). F) LOWER-VERTICAL $\delta^{13}\text{C}$ GRADIENT BETWEEN THERMOCLINE AND BENTHIC LAYERS ($\Delta\delta^{13}\text{C}_{\text{LOWER}} = \delta^{13}\text{C}_{\text{G.INFLATA}} - \delta^{13}\text{C}_{\text{C.WUELLERSTORFI}}$; ‰ VPDB; BLACK LINE). G) BENTHIC FORAMINIFERA $\delta^{18}\text{O}$ COMPOSITE RECORD COMPOSED BY C. WUELLERSTORFI (CORRECTED BY A FACTOR OF PLUS 0.64 ‰) AND U. PEREGRINA $\delta^{18}\text{O}$ VALUES (PINK LINE; ‰ VPDB). VERTICAL BLUE BARS MARK GLACIAL PERIODS AND COLD INTERGLACIAL SUBSTAGES. VERTICAL DASHED LINES MARK GLACIAL TERMINATIONS. ALL RECORDS ARE PLOTTED AGAINST AGE (KA) 119

FIGURE 20 - PRECESSIONALLY-PACED STRATIFICATION RECORDS REGISTER NBUS UPWELLING ACTIVITY, SHOWING UPWELLING INTENSIFICATION DURING AUSTRAL SUMMER INSOLATION MAXIMA DURING POSITIVE PRECESSION PERIODS. A) ECCENTRICITY (PURPLE DASHED LINE) AND PRECESSION (BLACK LINE) FORCING (LASKAR ET AL., 2004). B) UPPER-OCEAN STRATIFICATION RECORD (PURPLE LINE WITH TRANSPARENCY; $\Delta\delta^{18}\text{O}$; ‰ VPDB) WITH THREE-POINT RUNNING AVERAGE (PURPLE LINE); AND FEBRUARY INSOLATION AT 23°S (RED DASHED LINE). C) ALKENONE-BASED SEA SURFACE TEMPERATURE RECORDS (SST; °C) FROM GEOB1712-4 (LIGHT ORANGE LINE), GEOB 1711-4 (DARK ORANGE LINE), GEOB 1710-3 (DARK YELLOW LINE) (KIRST ET AL., 1999). D) GLOBIGERINA BULLOIDES $\delta^{18}\text{O}$ (LIGHT RED LINE; ‰ VPDB) FROM CORE MD08-3167. E)

NEOGLOBOQUADRINA PACHYDERMA ABUNDANCE RECORDS (%) FROM ODP SITE 1083 (LIGHT GREEN LINE; WEST ET AL., 2004); GEOB 1711-4 (DARK GREEN LINE; LITTLE ET AL., 1997); GEOB 1710-3 (NEON-LIKE GREEN LINE; VOLBERS ET AL., 2003). VERTICAL BARS HIGHLIGHT PERIODS OF UPWELLING INTENSIFICATION AT NBUS FOLLOWING AUSTRAL SUMMER INSOLATION MAXIMA. VERTICAL DASHED LINES MARK GLACIAL TERMINATIONS. ALL RECORDS ARE PLOTTED AGAINST AGE (KA)..... 122

FIGURE 21 - REDFIT SPECTRAL ANALYSIS (SCHULZ AND MUDELSEE, 2002) RESULTS PERFORMED IN MD08-3167 RECORDS. A) $\Delta\delta^{18}\text{O}$ RECORD, B) GLOBIGERINA BULLOIDES $\delta^{18}\text{O}$ RECORD, C) GLOBOROTALIA INFLATA $\delta^{18}\text{O}$ RECORD. RESULTS REVEAL RELEVANT SPECTRAL POWER (Y AXES) ABOVE THE 90% CONFIDENCE INTERVALS IN THE PRECESSION, OBLIQUITY, AND ECCENTRICITY FREQUENCY DOMAINS (X AXES). CONFIDENCE LEVEL BASELINES (GREEN AND ORANGE) AND SIGNIFICANT SPECTRAL PERIODICITIES ARE INDICATED..... 124

FIGURE 22 - TRADE WINDS INTENSIFICATION IN RESPONSE TO DECREASED NORTHERN HEMISPHERE MONSOON SYSTEMS DURING PERIODS OF REDUCED UPPER-OCEAN STRATIFICATION AND RELATED UPWELLING INTENSIFICATION AT NBUS. A) UPPER-OCEAN STRATIFICATION RECORD (PURPLE LINE WITH TRANSPARENCY; $\Delta\delta^{18}\text{O}$; ‰ VPDB) WITH THREE-POINT RUNNING AVERAGE (PURPLE LINE); AND FEBRUARY INSOLATION AT 23°S (RED DASHED LINE). B) THREE-POINT RUNNING AVERAGE ^{230}Th -NORMALIZED SAHARA DUST FLUXES FROM SEDIMENT CORE MD03-2705 (LIGHT GREEN LINE; $\text{G CM}^{-2} \text{ KYR}^{-1}$; SKONIECZNY ET AL., 2019). C) SPELEOTHEM $\delta^{18}\text{O}$ RECORD OF ASIAN MONSOON SYSTEM (DARK GREEN LINE; ‰ VPDB; CHENG ET AL., 2016). D) WIND STRENGTH PROXY FROM THE EASTERN SUBTROPICAL SOUTH ATLANTIC (BROWN LINE; STUUT ET AL., 2002). VERTICAL BARS HIGHLIGHT PERIODS OF UPWELLING INTENSIFICATION AT NBUS FOLLOWING AUSTRAL SUMMER INSOLATION MAXIMA. VERTICAL DASHED LINES MARK GLACIAL TERMINATIONS. ALL RECORDS ARE PLOTTED AGAINST AGE (KA) 125

FIGURE 23 - MECHANISM CONTROLLING UPWELLING INTENSIFICATION AT NBUS. A) THREE-POINT RUNNING AVERAGE OF $\Delta\delta^{18}\text{O}$ (‰ VPDB) RECORD FROM TROPICAL SOUTH ATLANTIC (PINK LINE; NASCIMENTO ET AL., 2021) AND PRECESSION (BLACK LINE; LASKAR ET AL., 2004). B) THREE-POINT RUNNING AVERAGE OF $\Delta\delta^{18}\text{O}$ (‰ VPDB) RECORD (DARK PURPLE LINE) AND RESPECTIVE 23-KA LOESS FILTER (YELLOW LINE). C) SEA SURFACE TEMPERATURE (SST) GRADIENT BETWEEN CORES M125-55-7 AND ODP SITE 999 ($\Delta\text{SST}_{\text{ODP 999} - \text{M125-55-7}}$, BLUE LINE; °C), AND RESPECTIVE 23-KA LOESS FILTER (VIOLET LINE) (SCHMIDT ET AL., 2006; HOU ET AL., 2020). D) AGULHAS LEAKAGE FAUNA RECORD (TRANSPARENT ORANGE LINE; PEETERS ET AL., 2004) AND RESPECTIVE THREE-POINT RUNNING AVERAGE (SOLID ORANGE LINE). E) SOUTHERN TROPICAL SOUTH ATLANTIC SST FROM CORE M125-55-7 (TRANSPARENT GREEN LINE; HOU ET AL., 2020; °C) AND RESPECTIVE THREE-POINT RUNNING AVERAGE (SOLID GREEN LINE). VERTICAL BARS HIGHLIGHT PERIODS OF UPWELLING INTENSIFICATION AT NBUS. VERTICAL DASHED LINES MARK GLACIAL TERMINATIONS. ALL RECORDS ARE PLOTTED AGAINST AGE (KA)..... 129

FIGURE 24 - VERTICAL CARBON TRANSFER DURING UPWELLING INTENSIFICATION AT NBUS BASED ON MD08-3167 ISOTOPIC RECORDS. A) THREE-POINT RUNNING AVERAGE OF $\Delta\delta^{18}\text{O}$ (‰ VPDB) RECORD (DARK PURPLE LINE) AND RESPECTIVE 23-KA LOESS FILTER (YELLOW LINE). B) VERTICAL $\delta^{13}\text{C}$ GRADIENT BETWEEN SURFACE AND THERMOCLINE LAYERS ($\Delta\delta^{13}\text{C}_{\text{SURFACE-THERMOCLINE}}$, DARK GREEN LINE; ‰ VPDB), AND RESPECTIVE 23-KA LOESS FILTER (DARK VIOLET LINE). C) VERTICAL $\delta^{13}\text{C}$ GRADIENT BETWEEN THERMOCLINE AND BOTTOM LAYERS ($\Delta\delta^{13}\text{C}_{\text{THERMOCLINE-BOTTOM}}$, BLACK LINE; ‰ VPDB), AND RESPECTIVE 23-KA LOESS FILTER (LIGHT VIOLET LINE). D) TOTAL ORGANIC CARBON (TOC) FROM GEOB 1028, GEOB 1712-4, GEOB 1711-4, AND GEOB 1710-3 (%; DARK BLUE, LIGHT BROWN, DARK BROWN, AND GOLD YELLOW, RESPECTIVELY; SCHNEIDER ET AL., 1996; KIRST

ET AL., 1999). D) ATMOSPHERIC CO ₂ RECORD FROM THE EUROPEAN PROJECT FOR ICE CORING IN ANTARCTICA (EPICA) DOME C ICE CORE (PPMV; LIGHT GREEN LINE; JOUZEL ET AL., 2007). VERTICAL BARS HIGHLIGHT PERIODS OF UPWELLING INTENSIFICATION AT NBUS FOLLOWING AUSTRAL SUMMER INSOLATION MAXIMA. VERTICAL DASHED LINES MARK GLACIAL TERMINATIONS. ALL RECORDS ARE PLOTTED AGAINST AGE (KA).....	133
FIGURE 25 - PERIODIC TABLE HIGHLIGHTING DETECTABLE ELEMENTS BY ICP-MS, SUCH AS METALS, METALLOIDS, SEMIMETALS, NON-METALS, OR HALOGENS (MODIFIED FROM PRÖFROCK AND PRANGE, 2012).....	149
FIGURE 26 - SCHEMATIC REPRESENTATION OF AN INDUCTIVELY COUPLED PLASMA MASS SPECTROMETRY (ICP-MS) (WILSCHEFSKI AND BAXTER, 2019); ADAPTED FROM KOŠLER AND SYLVESTER (2003).....	150
FIGURE 27 - A) ELEMENT XR HIGH-RESOLUTION MULTI-COLLECTOR ICP-MS FROM THE PÔLE SPECTROMÉTRIE OCÉAN (PSO) AT L'INSTITUT FRANÇAIS DE RECHERCHE POUR L'EXPLOITATION DE LA MER (IFREMER). B) ICP-MS AUTOSAMPLER, CARRYING SAMPLES AND SOLUTIONS USED FOR MEASUREMENTS.....	151
FIGURE 28 - A) CLEAN ROOM LABORATORY AT THE PÔLE SPECTROMÉTRIE OCÉAN (PSO), IFREMER. B) LAMINAR FLOW HOOD FROM THE CLEAN ROOM WHERE ALL Mg/CA CLEANING PROTOCOL WAS PERFORMED.....	154
FIGURE 29 - EQUIPMENT NEEDED FOR ROUTINELY CLEANING FORAMINIFERA SAMPLES FOR Mg/CA ANALYSIS IN A CLEAN LABORATORY, AS LISTED IN TABLE 4. A) SET OF SOLUTIONS; B) EQUIPMENT: ULTRASOUND, MICROCENTRIFUGE, AND LAB DANCER.....	156
FIGURE 30 - DILUTION STEPS PERFORMED ON A CLEAN ROOM FROM PSO. A) DILUTION PREPARATION FOR THE FIRST MEASUREMENTS RUN (DILUTION FACTOR = 5). B) ADS LAMINAIRE STERILE HOOD FROM THE ICP-MS LABORATORY WHERE DILUTIONS FOR THE SECOND MEASUREMENTS RUN, AND ALL STANDARDS USED FOR EXTERNAL CALIBRATION WERE PREPARED.....	156
FIGURE 31 - SCHEMATIC EXAMPLE OF BRACKETING METHOD CONCENTRATION DETERMINATION CALCULATED FROM THE TWO KNOWN CONCENTRATION STANDARDS (MODIFIED FROM KETRIN ET AL., 2017). C1 AND Y1 REPRESENT THE CONCENTRATION AND INTENSITY OF STANDARD 1; SAME FOR C2 AND Y2 BUT RELATIVE TO STANDARD 2; CX AND YX ARE THE CONCENTRATION AND INTENSITY OF THE ANALYTE IN THE SAMPLE. THE ANALYTE CONCENTRATION CX IS DETERMINED FROM LINEAR INTERPOLATION BETWEEN TWO KNOWN INTENSITIES-CONCENTRATION VALUES OF THE STANDARDS (I.E., THE HYPOTENUSE LINE ON THE BLUE TRIANGLE).....	168
FIGURE 32 - GLOBOROTALIA INFLATA TE/CA RATIOS FROM CORE MD08-3167 USED FOR TRACKING CONTAMINATION (TE/CA _{CONTAMINANTS}) IN THE MEASURED SAMPLES. A) AL/CA RATIO. B) MN/CA RATIO. C) FE/CA RATIO. D) XRF TI/CA USED AS A REFERENCE OF DETRITAL MATERIAL PRESENCE AT THE SITE. E) BENTHIC δ ¹⁸ O (PERMIL, VPDB) AS A TIME REFERENCE. ALL CURVES PLOTTED AGAINST AGE (KA).....	175
FIGURE 33 - EVALUATION OF CONTAMINANT CONTRIBUTION TO Mg/CA VALUES BASED ON TE/CA RATIOS. A) AL/CA vs. Mg/CA, R ² = 0.003. B) MN/CA vs. Mg/CA, R ² = 0.005. C) FE/CA vs. Mg/CA, R ² = 0.52. AL/CA AND FE/CA PRESENT EXTREMELY LOW R ² , INDICATING A NEGLIGIBLE CORRELATION WITH Mg/CA DATA. HOWEVER, MN/CA CORRELATES WITH Mg/CA (R ² = 0.52). ALTHOUGH THIS CORRELATION SEEMS RELEVANT, THE AVERAGE VALUE OF MN/CA VALUES LETS US ASSUME THEY ARE NEGLIGIBLE SINCE ABSOLUTE VALUES ARE LOWER THAN DESCRIBED IN THE LITERATURE SHOWING NO CONTAMINATION.....	176
FIGURE 34 - ANNUAL MEAN TEMPERATURE CONDITIONS AT SITE MD08-3167 A) VERTICAL TEMPERATURE PROFILE AND B) TEMPERATURE AT 300M IN THE NAMIBIA MARGIN. DATA FROM BOTH PLOTS ARE FROM THE WORLD OCEAN ATLAS 2018 (WOA18) DATABASE (LOCARNINI ET AL., 2018). ALL TEMPERATURE VALUES ARE REPORTED IN °C.....	178

FIGURE 35 - EVALUATION OF MG/CA-TEMPERATURE EQUATIONS DEVELOPED FOR *G. INFLATA* (TABLE 10). A) COMPARISON OF RECONSTRUCTED THERMOCLINE TEMPERATURE FROM THE EIGHT DIFFERENT EQUATIONS ($^{\circ}\text{C}$). B) RECONSTRUCTED THERMOCLINE TEMPERATURE ($^{\circ}\text{C}$) EQUATIONS FROM THORNALLEY ET AL. (2009) AND GROENEVELD AND CHIESSI (2011), WHICH ARE THE MOST PLAUSIBLE EQUATIONS FOR THE MD08-3167 SITE. C) MG/CA RECORD (MMOL/MOL) AND D) $\delta^{18}\text{O}$ (PERMIL, VPDB) FROM MD08-3167 CORE..... 182

FIGURE 36 - COMPARISON BETWEEN ASTERN AND WESTERN UPPER-OCEAN STRATIFICATION RECORDS. A) MD08-3167 THREE-POINT RUNNING AVERAGE OF $\Delta\delta^{18}\text{O}$ (‰ VPDB) RECORD (DARK PURPLE LINE) AND RESPECTIVE 23-KA LOESS FILTER (YELLOW LINE). B) GL-854 UPPER-OCEAN STRATIFICATION RECORD (BLUE LINE; $\Delta\delta^{18}\text{O}$; ‰ VPDB) AND RESPECTIVE 100-KA LOESS FILTER (DARK ORANGE LINE). C) WIND STRENGTH PROXY FROM THE EASTERN SUBTROPICAL SOUTH ATLANTIC (BROWN LINE; STUUT ET AL., 2002). D) GL-854 (LIGHT GREEN LINE) AND GL-852 (DARK GREEN LINE) *G. BULLOIDES* RELATIVE ABUNDANCE ($\%$; LESSA ET AL., 2019). E) GL-854 (LIGHT GREEN LINE) AND GL-852 (DARK GREEN LINE) RELATIVE ABUNDANCE RATIO BETWEEN *G. BULLOIDES* AND *GLOBIGERINOIDES RUBER* (GB/GR) SPECIES (LESSA ET AL., 2019)..... 191

LIST OF TABLES

TABLE 1 - LOCATION AND CORING INFORMATION FOR THE MARINE SEDIMENT CORES USED IN THIS THESIS	45
TABLE 2 - MEASUREMENT SUMMARY. PICKED SPECIES, SIEVE SIZE, TYPE OF ANALYSIS, EQUIPMENT, LABORATORY, AND PRODUCED PROXY RECORDS ARE ADDRESSED FOR EACH INVESTIGATED MATERIAL, AS WELL AS A REFERENCE TO THE CHAPTER OF THIS THESIS WHERE THE RECORDS ARE DISCUSSED. UAB: <i>UNIVERSITAT AUTONOMA DE BARCELONA</i> . PSO: <i>POLE SPECTROMETRIE OCEAN</i> . LSCE: <i>LABORATOIRE DES SCIENCES DU CLIMAT ET DE L'ENVIRONNEMENT</i>	48
TABLE 3 - QUANTIFICATION OF THE ANALYTICAL MEASUREMENTS PERFORMED DURING THIS THESIS. MEASUREMENTS ARE DETAILED BY CORE, FORAMINIFERA SPECIES, AND ANALYSIS TYPE	62
TABLE 4 - LIST OF THE MATERIALS USED FOR Mg/Ca ANALYSIS	155
TABLE 5 - ELEMENT RATIO CONCENTRATIONS OF USED STANDARDS FOR THE ELEMENTS OF INTEREST IN THIS THESIS	162
TABLE 6 - EXAMPLE OF A TABLE USED TO APPLY ALL POST-ANALYSIS CORRECTIONS. ELEMENTS WERE ORGANIZED FOLLOWING THEIR RESOLUTION RANGE (I.E., LOW RESOLUTION (LR), MEDIUM RESOLUTION (MR), AND HIGH RESOLUTION (HR)). COLOR CODES WERE DETERMINED FOR EACH SAMPLE IN THE SEQUENCE OF MEASUREMENTS ON THE ICP-MS SESSION. YELLOW: MACHINE BLANKS; BLUE: FOREXRB IN-HOUSE STANDARD; GREEN: NIST 8301 (FORAMS) INTERNATIONAL STANDARD; RED: NIST 8301 DILUTIONS; NO FILL: FORAMINIFERA SAMPLES, IDENTIFIED BY CORE NAME, SP, AND DEPTH	164
TABLE 7 - EXAMPLE OF A) NIST 8301 INTERNATIONAL REFERENCE MATERIAL AND B) FOREXRB IN-HOUSE STANDARD STATISTICS CALCULATIONS ROUTINELY DONE ON EACH ICP-MS MEASUREMENT SESSION. THE MEAN AND STANDARD DEVIATION OF THE STANDARD MEASUREMENT INTENSITIES FOR EACH TE/CA RATIO OF INTEREST WERE USED TO DETERMINE FOREXRB CONCENTRATIONS AND SAMPLE CONCENTRATIONS (I.E., IN MMOL/MOL).....	169
TABLE 8 - STANDARD STATISTICS FOR A) NIST 8301 AND B) FOREXRB	173
TABLE 9 - SAMPLE MEASUREMENTS STATISTICS: MINIMUM, MAXIMUM, MEAN, STANDARD DEVIATION. DIFFERENT FROM RAW DATA PRESENTED FOR NIST 8301 AND FOREXRB, ALL RATIOS ARE REPORTED IN MMOL/MOL SINCE THESE RATIOS A COMMONLY REPORTED ON THIS UNIT	174
TABLE 10 - LIST OF Mg/Ca-TEMPERATURE EQUATIONS SPECIFICALLY DEVELOPED FOR <i>G. INFLATA</i> SPECIES EVALUATED IN THIS THESIS	180

TABLE OF CONTENTS

1 THESIS PRESENTATION	34
1.1 CONTEXT: CURRENT CLIMATE CHANGES AND OCEAN CIRCULATION	34
1.2 INTRODUCTION	35
2 OBJECTIVES AND OUTCOMES	43
2.1 INTRODUCTION TO THE SCIENTIFIC ARTICLES MANUSCRIPTS	43
3 METHODS AND DATA	45
3.1 SEDIMENTAL ARCHIVES AND SAMPLING	45
3.2 GEOCHEMICAL PROXIES AND ANALYTICAL EFFORT	48
3.2.1 <i>Foraminifera: a vital tool for paleoceanographic reconstructions</i>	48
3.2.2 <i>Stable isotopes</i>	53
3.2.3 <i>X-Ray Fluorescence (XRF)</i>	56
3.2.4 <i>Mg/Ca paleothermometry and $\delta^{18}O_{sw}$</i>	57
3.3 CHRONOLOGICAL APPROACH: GL-854 AND MD08-3167	58
3.4 GEOCHEMICAL DATA	61
3.4.1 <i>Stable isotopes</i>	62
3.4.2 <i>Mg/Ca</i>	67
3.4.3 <i>X-Ray fluorescence</i>	70
4 ATLANTIC $\delta^{13}C$ DEEP-WATER SEESAW CONTROLLED BY ANTARCTIC SEA ICE OVER THE LAST 800 KA	71
4.1 MATERIAL AND METHODS	75
4.1.1 <i>Sediment cores</i>	75
4.1.2 <i>Study area</i>	76
4.1.3 <i>Stable isotopic carbon composition</i>	77
4.1.4 <i>GL-854 age model</i>	77
4.1.5 <i>RAMPFIT and spectral analysis</i>	78
4.2 RESULTS	79
4.2.1 <i>Benthic $\delta^{13}C$ and zonal $\delta^{13}C$ gradient evolution</i>	79
4.3 DISCUSSION	80
4.3.1 <i>Atlantic deep-water seesaw: long-term trends in AMOC strength</i>	80
4.3.2 <i>Antarctic sea-ice controls on Atlantic deep-water geometry</i>	85
4.3.3 <i>Orbital controls over the Antarctic sea ice</i>	90
4.4 CONCLUSIONS	93
4.5 SUPPORTING INFORMATION	105
5 PRECESSIONALLY-DRIVEN UPWELLING STRENGTH AT NORTHERN BENGUELA UPWELLING SYSTEM	109
5.1 MATERIAL AND METHODS	113
5.1.1 <i>Sediment core and study area</i>	113
5.1.2 <i>Age model</i>	114
5.1.3 <i>Stable isotopes and gradients</i>	115
5.1.4 <i>Spectral analysis</i>	116
5.2 RESULTS	116

5.2.1	<i>Stable isotopes</i>	116
5.2.2	<i>Time-series analysis</i>	118
5.3	DISCUSSION	120
5.3.1	<i>Upper ocean stratification tracks northern NBUS activity</i>	120
5.3.2	<i>The mechanism behind precessionally-paced NBUS intensification</i>	125
5.3.3	<i>Implications for global atmospheric CO₂</i>	130
5.4	CONCLUSIONS	134
5.5	SUPPORTING INFORMATION	146
6	IMPLEMENTING FORAMINIFERA MG/CA ANALYSIS TECHNIQUE ON IFREMER ICP-MS	147
6.1	ELEMENTARY ANALYSIS ON ICP-MS: FORAMINIFERA TE/CA RATIOS	147
6.2	MATERIALS, REAGENTS, AND FACILITY STRUCTURE: PROTOCOL PREPARATION 153	
6.2.1	<i>Cleaning protocol</i>	157
6.3	WALKING THROUGH THE ANALYTICAL STEPS	160
6.3.1	<i>Pre-analysis: standard preparations</i>	160
6.3.2	<i>The routine of measurements: ICP-MS sessions</i>	162
6.3.3	<i>Post-analysis: data treatment</i>	164
6.3.4	<i>Determination of element concentrations</i>	167
6.4	MEASUREMENT RESULTS	172
6.5	TRACKING CONTAMINATION: EVALUATING THE EFFICACY OF THE CLEANING PROTOCOL	174
6.6	EVALUATION OF MG/CA-TEMPERATURE EQUATIONS	177
6.7	CONCLUSIONS AND PERSPECTIVES	183
7	CONCLUSIONS AND FUTURE STEPS	185
7.1	FUTURE STEPS	188
	REFERENCES	192
	ANNEX A	210
	ANNEX B	216

1 THESIS PRESENTATION

1.1 Context: current climate changes and ocean circulation

Over the last century, Earth's climate has experienced considerable changes attributed to human activities, such as deforestation and burning of fossil fuels, resulting in a significant increase in atmospheric CO₂ (IPCC, 2022). Based on the historical CO₂ data from the period between 1850 and 2019, it has been observed that 62% of CO₂ emissions happened after 1970, 42% after 1990, and roughly 17% after 2010, thus temperature anomalies show a steep increase in global surface temperatures, reaching 415 ppm in 2019, and very recently in 2023 up to 425 ppm (IPCC, 2022; NOAA, 2022). It is now known that anthropogenic impact on atmospheric CO₂ has caused global temperatures to increase by 1.2°C above the industrial period relative to the period between 1850 and 1900. According to climate modeling predictions, even if we achieve net zero CO₂ emissions globally, the temperature increase will likely reach 2°C of positive anomaly between 2030 and 2052 (IPCC, 2022). However, if we follow other climate model scenarios such as RCP2.6, RCP4.5, RCP7.0, or RCP8.5, temperatures could increase by more than 4°C until 2100 (IPCC, 2022). This sharp increase in global temperatures associated with the increasing atmospheric CO₂ concentration has greatly impacted the global climate with severe consequences for society, resulting in more frequent and intense climate-related disasters (e.g., Beniston and Stephenson, 2004; Planton *et al.*, 2008; Marengo *et al.*, 2012; Liu *et al.*, 2020; da Fonseca Aguiar; Cataldi, 2021; Alifu *et al.*, 2022).

Studies have demonstrated that the increase in temperature in regions close to the poles causes significant effects on critical climate components (Dai *et al.*, 2019; Rantanen *et al.*, 2022; Purich; England, 2023). These effects include the melting of ice in the Arctic and Antarctic, which leads to substantial impacts on the thermohaline circulation and the Atlantic Meridional Overturning Circulation (AMOC) (Gilbert; Kittel, 2021; Li *et al.*, 2023; Liu *et al.*, 2020; Purich; England, 2023). Different climate models and proxy-based reconstruction outcomes have shown similar results: under current and future global warming conditions, the AMOC is very likely slowing down (Thornalley *et al.*, 2018; Caesar *et al.*, 2018, 2021; IPCC 2022; Li *et al.*, 2023). The AMOC impacts multiple key components in the climate system, changing the extent of Antarctic and Arctic sea ice, the patterns of sea-surface and deep-water temperatures, and atmospheric temperature and circulation,

altering precipitation patterns. This significantly impacts the climate, including changes in weather, such as droughts and floods, and regional sea level increases (Caesar *et al.*, 2018; Liu *et al.*, 2020; IPCC 2022). Understanding the mechanisms driving AMOC changes and how the climatic system responds to them is crucial for predicting and mitigating the effects of climate change.

An approach that studies AMOC dynamics from the surface to deep water is paramount since it allows full comprehension of the dynamic of two important components of the climatic system: the oceans and the atmosphere. Investigating a long range of periods provides a unique opportunity to understand the different responses of the components mentioned above to different initial forcings and the climate system's response. Through the last 800 ka, the Earth's climate has undergone important natural climatic transitions that involve critical processes in regulating atmospheric CO₂. Although immediate impacts of climate changes can already be seen on a seasonal/annual scale, the magnitude and the extent of future AMOC changes and the impacts of rising CO₂ on the climate and its components on relatively longer scales are still debatable. In this regard, paleoclimatological studies and foraminifera research play a crucial role in understanding the Earth's climatic system and its responses to various forcings. Paleoceanographic and paleoclimatological research offers a long-term natural variability approach that can help us better understand the AMOC dynamics and the response of the climatic system to different forcings. Specifically, investigating past variability of deep-water masses, the upper ocean and atmospheric dynamics provide insights into mechanisms associated with CO₂ sea-air exchange and the burial of carbon in the deep ocean through different time scales, which is valuable to improving climate modeling and predictions of future climate changes.

1.2 Introduction

Over the past 800,000 years, the Earth has undergone a series of dramatic climatic oscillations known as glacial-interglacial (G-IG) cycles (Imbrie *et al.*, 1993; Lisiecki; Raymo, 2005). The primary drivers of these cycles are thought to be changes in the Earth's orbital parameters, specifically its eccentricity, axial tilt, and precession forcing. Eccentricity refers to the shape of the Earth's orbit, obliquity refers to the angle at which the Earth's axis is tilted, and precession refers to the gradual wobbling motion of the Earth's rotational axis

(Imbrie *et al.*, 1984; Berger; Loutre, 2006). Orbital changes lead to variations in the amount and distribution of solar radiation reaching the Earth's surface, directly impacting the climate component dynamics. The precession cycle governs the timing and intensity of the seasons; the 65°N insolation is considered a critical component of the Milankovitch theory of the Quaternary glaciations due to its controls on the growth and retreat of the Northern Hemisphere ice sheets. Insolation changes trigger feedback mechanisms that amplify or dampen the initial climate forcing, ultimately impacting the atmospheric CO₂ oscillations between G-IG of approximately 180 and 280 ppm (Petit *et al.*, 1999; Siegenthaler *et al.*, 2005; Lüthi *et al.*, 2008). The interplay between orbital forcing, AMOC dynamics, and atmospheric CO₂ is complex and operates through deep-water and ocean-atmospheric dynamics.

The AMOC results from wind-driven currents and thermohaline circulation, encompassing surface and deep-water dynamics responsible for mass transport across the hemispheres within the Atlantic (Rahmstorf, 2006). Deep-water circulation is characterized by two overturning cells overlaying each other. Warm and salty waters are carried toward the North Atlantic high latitudes to deep-water formation regions at the Labrador and Nordic Seas, where they gradually cool and become denser, sinking carbon-rich waters into the deep ocean (Rahmstorf, 2006). When these waters sink, they form the North Atlantic Deep Water (NADW) that flows through the Deep Western Boundary Current (DWBC) until south of the Southern Hemisphere Polar Front in the Antarctic Divergence zone, where it mixes with Circumpolar Deep Water (CDW) and is pushed to the surface by the wind-driven upwelling. In the Southern Ocean (SO), the freezing of sea ice causes bottom water formation in the Antarctic continental shelf. This process increases the salinity of the water due to the salt rejected by the newly formed ice (a.k.a. the brine rejection process), resulting in higher water density levels on the shelves. As the salty water accumulates, salinity reaches a critical value that makes it dense enough to sink over the shelf edges and flow into the deep basins. Antarctic Bottom Water (AABW) is then formed in the South Atlantic sector on deep-water formation site at the Weddell Sea, flowing northward as a characteristic older, denser, and colder water throughout the deep Atlantic below NADW (Curry; Oppo, 2005; Rahmstorf, 2006). The dynamics of the deep-water cell is imposed by the production rate and ventilation of each of these water masses, which are compensated by each other within the ocean's interior, promoting different circulation states.

An important component of the AMOC upper limb of circulation in the South Atlantic is the South Atlantic Subtropical Gyre (SASG) (Fig. 1). The SASG is the wind-driven circulation pattern at mid-latitudes, critical in modulating global climate variability (Peterson; Stramma, 1991). The surface current system flowing anti-clockwise is composed of the Brazil Current (BC) flowing southward along the South American coast until 33-38°S, meeting the northeastward extension of the Antarctic Circumpolar Current (ACC) into the Atlantic, and the Malvinas Current, known as the Brazil-Malvinas Confluence (BMC), the most energetic region in the southern Atlantic Ocean (Gordon, 1985, 1989; Garzoli, 1993). The eastward flow from this point forms the South Atlantic Current (SAC), the southern boundary of the STG (Olson *et al.*, 1988; R. G. Peterson; Stramma, 1991; Silveira *et al.*, 2000). The SAC encounters the Benguela Current (BeC) flowing northward along the African continent, until it turns west into the southern branch of the South Equatorial Current (SEC), the current that forms the northern edge of the subtropical gyre (Peterson; Stramma, 1991; Goni *et al.*, 2011). The bifurcation of the SEC around 10°S originates two western boundary currents: the BC flowing south and the northward flow crossing the equator, the North Brazil Current (NBC) (Silveira *et al.*, 2000). Flowing through NBC, waters reach the North Atlantic Subtropical and Subpolar Gyres, feeding the North Atlantic deep-water production sites and closing the upper-ocean overturning circulation.

The BC and NBC are crucial in transferring energy between the southern and northern hemispheres (Peterson; Stramma, 1991; Rodrigues *et al.*, 2007) and between the ocean and the atmosphere (Cronin *et al.*, 2010). Thus, the SEC bifurcation determines whether South Atlantic upper ocean layers become part of the continuous northward flow of the AMOC towards the Northern Hemisphere or recirculate in the South Atlantic subtropical gyre, seasonally favoring NBC or BC transport, respectively (Rodrigues *et al.*, 2007; Marcello *et al.*, 2018). The energy repartition between these branches responds to the asymmetric energy balance between the hemispheres, further influenced by seasonal insolation (Rodrigues *et al.*, 2007). This promotes a dynamic circulation pattern of energy transport from the tropics toward high latitudes (Fasullo; Trenberth, 2008; Garzoli; Matano, 2011; Garzoli *et al.*, 2013). Throughout their pathway in the SASG, the transported waters suffer changes through air-sea interactions, mixing, subduction, and advection processes, making the South Atlantic not only a passive conduit for water masses but actively influencing them (Garzoli; Matano, 2011). Thus, the SASG plays a crucial role in regulating the AMOC intensity and in maintaining the global energy system balanced, which promotes

atmospheric responses associated with the Intertropical Convergence Zone (ITCZ) (Garzoli *et al.*, 2013; Marcello *et al.*, 2018).

The ITCZ is a region near the Earth's equator characterized by low atmospheric pressure. It represents the ascending branch of lower atmospheric circulations and has a significant impact on global weather patterns and precipitation distribution (Green; Marshall, 2017). The position of the ITCZ is determined by the amount of energy flowing across the equator through the atmosphere and oppositely to the amount of net energy input at the equator (Broccoli *et al.*, 2006; Adam *et al.*, 2016). This energy flow is primarily driven by temperature and pressure differences between the hemispheres, which can be influenced by factors such as seasonal insolation (McGee *et al.*, 2018). Due to the continuous energy flux at a constant rate of 0.4 petawatts by the AMOC, the ITCZ is positioned to the north of equator at an annual mean position of 5°N latitude. However, the ITCZ undergoes a seasonal movement pattern primarily influenced by the Northern and Southern Hemispheres' atmospheric and sea surface temperature gradients (Marshall *et al.*, 2014). This atmospheric feature remains above the warmest sea surface water temperature in tropical regions, where it plays a significant role in shaping weather patterns and rainfall distribution (Broccoli *et al.*, 2006; Marshall *et al.*, 2014). When ITCZ is in a northward position, the South Atlantic Hadley Cell expands, intensifying the atmospheric ascendent branch of the ITCZ, and the southeastern trade winds that blow close to the ocean (Broccoli *et al.*, 2006; Marshall *et al.*, 2014). This atmospheric response compensates the inter-hemispheric energy transfer realized by the AMOC with southward atmospheric heat transport realized by the Hadley Cells (Marshall *et al.*, 2014). The Hadley Cells and trade winds thus vary in response to seasonality, creating an asymmetrical pattern of these atmospheric components between the hemispheres (McGee *et al.*, 2018).

An important ocean-surface process related to the northward shift of the ITCZ in response to intensified AMOC inter-hemispheric energy transfer is the control of the intensity and spatial extent of the South Atlantic eastern boundary upwelling cells from subtropical latitudes (Emeis *et al.*, 2009; Shannon, 1985). The Benguela Upwelling System (BUS) is located off the coast of southwestern Africa, driven by strong northward alongshore winds and the interaction of the prevailing ocean currents (Shannon, 1985; Hutchings *et al.*, 2009). The coastal southeast winds push warm surface water northward, and due to the Coriolis effect, it is redirected westward, bringing cold and nutrient-rich South Atlantic

Central Waters (SACW) to the surface (Emeis *et al.*, 2009). Although stronger trade winds prevail all year in this region, BUS is characterized by a seasonal regime that is intensified during austral winter and supports the highest levels of biological productivity and organic carbon flux of the eastern upwelling systems (Carr, 2002; Carr; Kearns, 2003). As photosynthetic organisms die and sink to the ocean floor, they transport carbon from the atmosphere to be stored in the deep ocean, increasing the biological pump's efficiency. Increased energy transport toward North Atlantic and intensified South Atlantic Hadley Cell increases the zonality of the trade winds, strengthening the SEC transport (e.g., Johns *et al.*, 1998). These surface ocean dynamics promote changes in the SASG dynamics that directly impact BUS variability and the efficiency of the biological pump, which is important in regulating atmospheric CO₂.

Kim *et al.* (2003) reconstructed the trade wind intensity based on the sea surface temperature (SST) gradients between the Angola-Benguela Front and the northern BUS over the last 25 ka. They argue that when trade winds and SEC are intensified, they enhance the SEC countercurrent and the intrusion of warm equatorial waters into the Angola-Benguela Front through the Angola Current. Meanwhile, trade winds intensification would have increased the upwelling, which decreased SST at northern BUS. Their findings show that during the Last Glacial Maximum, Younger Dryas and mid-to-late Holocene, trade winds were strong. Oppositely, evidence from the last deglaciation and cold millennial-scale events, such as Dansgaard–Oeschger (DO) stadials and Heinrich events (HS), suggest that the southward movement of the ITCZ is caused by North Atlantic cooling and South Atlantic warming in response to the bipolar seesaw (Crowley, 1992; Stocker, 1998; Pedro *et al.*, 2018). This results in the reorganization of the thermohaline deep ocean circulation due to freshwater input at high northern latitudes promoting AMOC slowdown (Broecker, 2003; Barker *et al.*, 2009; Shakun *et al.*, 2012; Henry *et al.*, 2016). Reduced AMOC, in turn, increases Southern Atlantic SST, promoting a southward shift in tropical precipitation. Reduced cross-equatorial temperature gradients decrease the trade winds intensity, which reduces the BUS activity (Peterson, 2000; Kim *et al.*, 2003; Wang *et al.*, 2004). On longer time scales, BUS activity has been reconstructed using planktonic foraminifera assemblages during the last 450 ka, showing a consistent upwelling intensification during glacial and precession maxima periods with good agreement with G-IG scale trade wind intensity reconstruction (Stuut *et al.*, 2002; West *et al.*, 2004). It is hypothesized that increased temperature gradients in the Southern Hemisphere during glacial stages strengthened the

trade winds and related upwelling, while during precession maxima episodes, increased zonality of the Benguela Current would have favored the upwelling (Schneider; Müller, 1996; West *et al.*, 2004).

The rising temperatures in the Southern Hemisphere and the southward shift of the ITCZ also impacts deep-water ventilation by increasing the rate of deep-water upwelling in the SO. The upwelling can be attributed to the stronger winds at Drake Passage, which are a direct result of the intensified westerly winds that occur due to the interaction between low and high latitudes (a.k.a., atmospheric teleconnections) (Toggweiler *et al.*, 2006; Toggweiler; Lea, 2010). As a result, it increases deep-water ventilation, augmenting the sea-air exchange that increases CO₂ outgassing from the deep ocean, which is also expected to be compensated by the enhanced deep-water formation in the North Atlantic (Anderson *et al.*, 2009a; Lee *et al.*, 2011; Marshall; Speer, 2012; Toggweiler; Lea, 2010; Toggweiler; Samuels, 1995) (Anderson *et al.*, 2009; Toggweiler; Lea, 2010; Lee *et al.*, 2011; Marshall; Speer, 2012). Applied to the G-IG time scale, the SO warming during interglacial periods decreases Antarctic sea-ice extent during interglacial periods, which would have promoted the southward position of westerly winds (Wolff *et al.*, 2006, 2010). On the other hand, expanded SO glacial conditions and sea ice act as a physical barrier preventing CDW from upwelling to the surface and would have pushed the Southern Hemisphere westerlies northward, preventing CO₂ outgassing from the deep ocean (Sigman; Boyle, 2000; Toggweiler *et al.*, 2006; Ferrari *et al.*, 2014). Expanded sea ice also affects deep-water formation by increasing SO stratification and AABW formation, which is expanded northward in the deep Atlantic resulting in a weak mixing with NADW that altered the deep-water distribution in the Atlantic. These deep water mass dynamics may also have contributed to the carbon storage in the ocean and reduced atmospheric CO₂ (Curry; Oppo, 2005; Bouttes *et al.*, 2010; Jansen; Nadeau, 2016; Jansen, 2017; Marzocchi; Jansen, 2019; Sigman; Boyle, 2000).

On an orbital scale, different insolation configurations driven by orbital forcing play a role in controlling Antarctic temperatures and expanding sea ice, which must influence or even control some of the abovementioned mechanisms (Yin; Berger, 2012; Yin, 2013). The received annual insolation energy is primarily driven by the obliquity forcing that significantly impacts high latitudes, especially prominent in the Southern Hemisphere due to the greater ocean area and their greater thermal potential (Yin; Berger, 2012; Wu *et al.*,

2020). Therefore, it is highly likely that the amount of sea ice increases during low-obliquity periods and decreases during high-obliquity periods, conversely and proportionally to decreasing/increasing insolation (Paillard, 2021). The timing and amplitude of changes in obliquity have been linked to G-IG amplitude and the timing of glacial terminations through their impact on the seasonal and latitudinal distribution of solar radiation, particularly in the southern high latitudes (Huybers; Wunsch, 2005; Riechers *et al.*, 2021; Mitsui *et al.*, 2022; Mitsui; Boers, 2022). It is crucial to consider this orbital influence when examining the deep-water formation, ventilation, and associated AMOC variability across G-IG cycles over longer time scales.

The main objective of this thesis is to investigate the impact of orbital forcing on the paleoceanography processes of the South Atlantic during the last 800 ka. The study will particularly focus on how these processes affect atmospheric CO₂ levels, impacting the global climate. This will be achieved by analyzing proxy records based on foraminifera found in marine sediment cores from the subtropical South Atlantic. The regulation of atmospheric CO₂ requires careful consideration of processes such as, the interaction between Southern Hemisphere and SO temperatures, the dynamics of Antarctic sea ice, and the resulting deep-water stratification and ventilation in the SO. Additionally, AMOC intensity variability and the ocean-atmospheric dynamics that drive teleconnections between tropical, mid-latitude, and high-latitude regions are also important mechanisms (Sigman; Boyle, 2000; Stephens; Keeling, 2000; Ferrari *et al.*, 2014; Jansen; Nadeau, 2016; Marzocchi; Jansen, 2019). By doing so, the research presented in this thesis aims to better understand the complex dynamics of ocean-atmospheric processes related to BUS activity and the deep water system oscillations from the South Atlantic region.

Historically, paleoclimatological research has predominantly concentrated on the North Atlantic region. Extensive research expeditions have led to the acquisition of a large number of marine cores, resulting in a wealth of records. This focus on the North Atlantic has led to the perception that variations in this region drive major global climate changes. However, considering the factors mentioned above, it is important to recognize the significance of possibly shifting our attention from the well-studied North Atlantic to the underexploited South Atlantic (Imbrie *et al.*, 1992; Huybers, 2009; Shakun *et al.*, 2012; Timmermann *et al.*, 2009).

The thesis is organized into seven chapters, with Chapter 1 is dedicated to the thesis presentation. Chapter 2 is dedicated to the description of the general objectives of the thesis and introduces the scientific discussions and related articles. Chapter 3 presents the methodological and analytical approach, the utilized proxies, the chronological framework, and a summary of the results and produced data, providing the foundation for the scientific discussions and investigative processes detailed in Chapters 4, 5, and 6.

The scientific results presented in this thesis cover three main discussions: Chapter 4 presents the first research paper under review on *Global and Planetary Changes* (Ballalai *et al.*, 2023). Its discussion aims to understand how the long-term deep-water mass variability in the South Atlantic responded to Antarctic sea-ice variability over the last 800 ka. We investigate the relation between different AMOC modes before and after the Mid-Brunhes Transition, an important climatic transition that marks an increasing G-IG and atmospheric CO₂ amplitude. Chapter 5 presents a research article draft, currently undergoing internal revision and intended to be submitted shortly to *Earth and Planetary Science Letters*. Chapter 6 provides technical details about the Mg/Ca analysis protocol conducted on inductively coupled plasma mass spectrometry (ICP-MS) that allows paleotemperature reconstructions of surface and thermocline layers. This manuscript focuses on reconstructing the BUS activity over the last 400 ka, exploring the implications for the carbon cycle and global climate.

Chapter 7 summarizes the main conclusions of the scientific discussions conducted throughout this thesis and presents topics related to possible future discussions developed from the generated data only partially explored in this thesis.

2 OBJECTIVES AND OUTCOMES

The main objective of this thesis is to provide insights into how variations in the orbital parameters and the interplay between them control paleoceanographic processes in the South Atlantic and are tied to oscillations in AMOC stability and the global climate over the Late Pleistocene. This general objective will be achieved by exploring both surface and deep-water paleoceanographic dynamics in the South Atlantic as follows:

- 1) To investigate the influence of orbital forcing in long-term deep water dynamics in the South Atlantic and their mechanisms. Benthic foraminifera $\delta^{13}\text{C}$ record were used to reconstruct the $\delta^{13}\text{C}$ the dissolved inorganic carbon along the Deep Western Boundary Current at the western South Atlantic in the Brazilian margin over the last 770 ka. This study specifically investigate the links between distinct patterns of deep water formation and distribution with different AMOC states and their climatic transitions over the Late Pleistocene.
- 2) To investigate the orbital modulation of the Benguela Upwelling System, the mechanisms operating the upwelling, and its impacts on the carbon cycle and global climate. The upper ocean stratification and vertical carbon transport in this region are reconstructed over the last 365 ka using $\delta^{18}\text{O}$ and $\delta^{13}\text{C}$ records from planktic and benthic foraminifera.
- 3) Implementing a protocol for Mg/Ca analysis performed in foraminiferal species at IFREMER. Mg/Ca ratios of deep-dwelling planktonic foraminifera *G. inflata* allow us to reconstruct and investigate the thermocline temperature variability in the eastern subtropical South Atlantic over the last 365 ka.

2.1 Introduction to the scientific articles manuscripts

Chapter 4: the main objective of this paper is to investigate past NADW variability in the South Atlantic, exploring how it has been zonally distributed within the basin on an orbital scale over the last ca. 800 ka. We propose a reconstruction of the Atlantic deep-water seesaw to investigate long-term patterns on AMOC, which are crucial in propagating orbital effects on the climate. We explored the mechanisms behind orbitally-controlled changes in the deep-water seesaw. With this paper, I address these questions:

- **Through which mechanisms do orbital parameters control long-term variations in AMOC strength?**
- **What are their role in the global carbon cycle and climatic transitions over the Late Pleistocene?**

Chapter 4 concerns the first manuscript of the thesis, submitted to *Global and Planetary Changes*:

Paper I: João M. Ballalai, Natalia Vázquez Riveiros, Thiago P. Santos, Rodrigo A. Nascimento, Manfred Mudelsee, Patrícia Piacsek, Igor M. Venancio, Bruna B. Dias, André Belem, Karen B. Costa, Felipe Toledo, Ana Luiza S. Albuquerque (under review). *Atlantic $\delta^{13}C$ Deep-water Seesaw Controlled by Antarctic Sea Ice Over the Last 800 ka*. *Global and Planetary Changes*.

Chapter 5: the main objective of this paper is to reconstruct the upwelling dynamics in the northern BUS on an orbital scale over the last 400 ka to evaluate its impact on the ocean carbon cycle through its influences on atmospheric CO₂. We explore a stratification proxy derived from the planktic foraminifera $\delta^{18}O$ gradient between the surface and thermocline layers to reconstruct the past NBUS variability. With this paper, I address these questions:

- **What are the main drivers of the BUS activity on an orbital scale?**
- **What are its implications for the carbon cycle and the global climate?**

Chapter 5 concerns the second article of the thesis, currently passing through an intern revision and intended to be submitted to *Earth and Planetary Science Letters*:

Paper II: João M. Ballalai, Natalia Vázquez Riveiros, Thiago P. Santos, Rodrigo A. Nascimento, Tainã Pinho, Patrícia Piacsek, Ana Luiza S. Albuquerque. *Precessionally-driven Upwelling Strength at Northern Benguela Upwelling System*. *Earth and Planetary Science Letters*.

Chapter 6: the main objective of this section is to present detailed technical information on the analytical approach implemented to perform Mg/Ca measurements on ICP-MS at IFREMER. I implemented a routine elementary analysis on foraminifera shells in the Geo-Ocean laboratory to generate Mg/Ca-based surface and subsurface temperatures from the eastern edge of the SASG. Unlike the other discussions, I do not present this section in an article manuscript format but report-like form.

3 METHODS AND DATA

This chapter introduces the two marine sediment cores I investigated, which form the basis of this thesis. In the following sections, I will describe the main analyses performed on them, associated proxies applicability, and produced data.

3.1 Sedimental archives and sampling

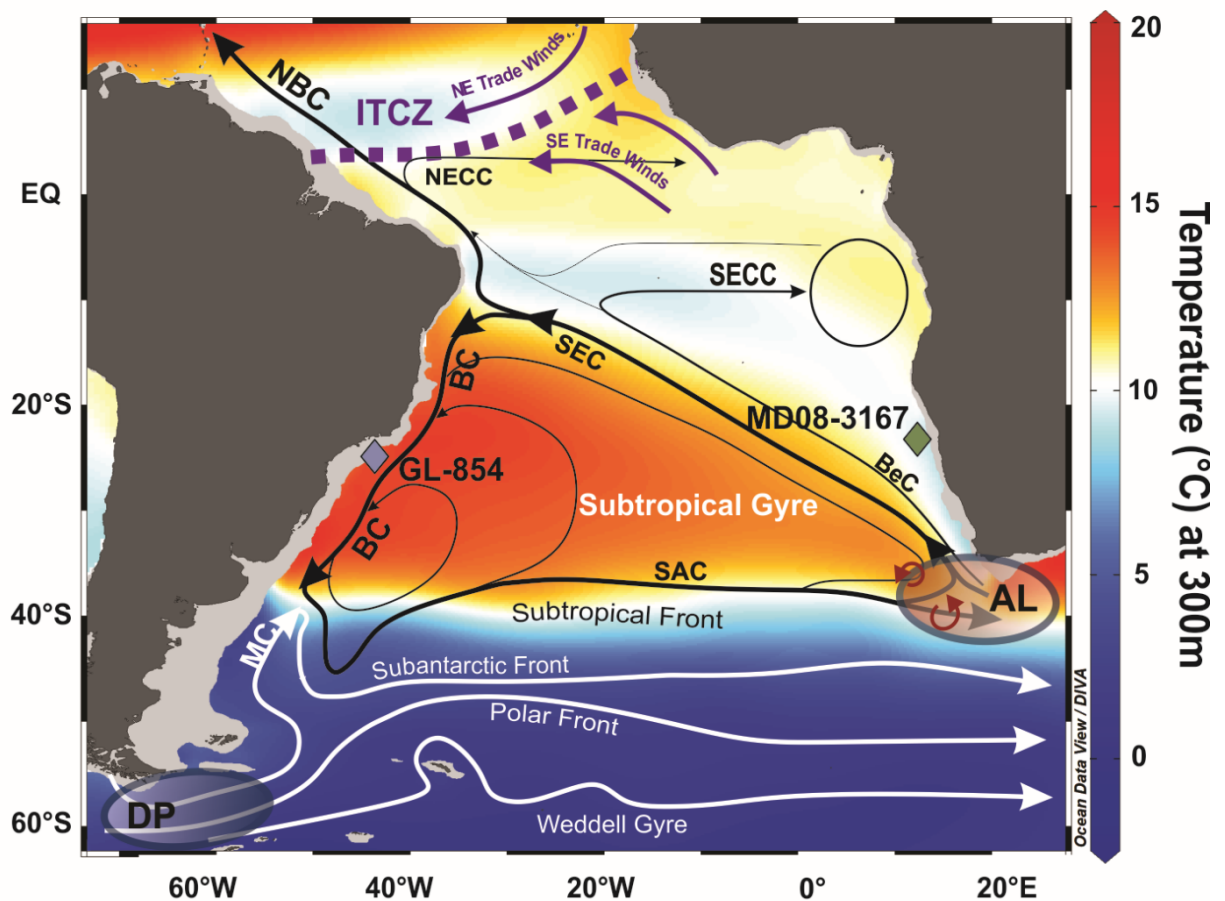
Two sediment cores have been selected for this thesis to reconstruct past oceanographic and climate variability from both sides of the South Atlantic basin over the Late Pleistocene period (Fig. 1). Additional sediment cores are used in the discussions from Chapters 4, 5, and 6, but those will be described in the methods section from that chapter.

Table 1 - Location and coring information for the marine sediment cores used in this thesis

Core site	Latitude	Longitude	Study area	Water depth (m)	Lenght (m)	Cruise campaign	Year
GL-854	25°12'S	42°37'W	Western South Atlantic	2220	20,38	Fugro Explorer Campaign	2007
MD08-3167	23°18.91'S	12°22.61'E	Eastern South Atlantic	1948	35,45	IMAGES XVI - MD167/RETR O	2008

The piston core GL-854 (20.38 m-long) was recovered at 2220 m water depth in the southwestern Atlantic Ocean at the Brazilian margin (25°12'S, 42°37'W). It was collected from the continental slope of Santos Basin in the Santos Drift by Petrobras oil company during the Fugro Explorer Campaign in 2007. The core lithology is composed of carbonate-rich mud (CaCO₃ content 18-30 %), intercalated by carbonate-poor mud (CaCO₃ content 5-18 %) and marl (de Almeida *et al.*, 2015), and does not present any hiatus. Two cm-thick samples were taken every 5 cm interval throughout the core, totalizing 409 sediment samples destined for isotopic, geochemical, and micropaleontological analysis. GL-854 location is ideally positioned to monitor the orbital scale variability of the oceanography of the western South Atlantic margin through the Late Pleistocene period.

Figure 1 - Location of the two marine sediment cores utilized in this thesis. Western margin: GL-854 at Santos basin (blue diamond). Eastern margin: MD08-3167 off the Namibian margin (green diamond). The purple dashed line and arrows represent the atmospheric components: the Intertropical Convergence Zone (ITCZ) and trade winds, respectively. The South Atlantic water gateways connecting the Indian and the Pacific Oceanic basins are indicated: Agulhas Leakage (AL) and Drake Passage (DP). Black arrows schematically represent the South Atlantic upper circulation. White arrows indicate the position of the high-latitude frontal system. Background colors display the subsurface temperature at 300 m from the database World Ocean Atlas 2018 (WOA 18; Locarnini et al., 2018). MC: Brazil-Mavinas confluence. SEC: South Atlantic Equatorial Current. SECC: South Atlantic Equatorial Counter Current. BC: Brazilian Current. SAC: South Atlantic Current. BeC: Benguela Current. NBC: North Brazil Current. NECC: North Brazil Counter Current



The 35.24 m-long Calypso core MD08-3167 was recovered at 1948 m water depth in the southeastern Atlantic Ocean at the African margin (23.3152°S; 12.3768°E), collected from the continental slope off Namibia during the IMAGES MD167/RETRO cruise (Waelbroeck *et al.*, 2008). Continuous high-resolution sediment physical properties

measurements were performed at 2 cm onboard the Marion Dufresne Research Vessel using a Geotek Multi-Sensor Core Logger (MSCL). Parameters measured encompass P-wave velocity (i.e., thickness), magnetic susceptibility, natural gamma (i.e., bulk density), electrical resistivity, digital photographs, and color spectrophotometry (i.e., reflectance; L^*).

One-cm thick core samples were taken every 4 cm throughout the first 700 cm and every 8 cm interval from this level toward the bottom of the core, totaling 534 sediment samples destined for isotopic, geochemical, and micropaleontological analysis. Site MD08-3167 is located off the coast of Namibia in the eastern South Atlantic margin, in the strong Benguela Upwelling System close to the Walvis Bay cell. This location is ideal for reconstructing upwelling variability, and since it is on the eastern border of the SASG, to track possible gyre lateral movements or expansion/contraction.

Samples from the GL-854 core were previously washed and already available at *Laboratório de Paleoceanografia do Atlântico Sul* (LaPAS) in São Paulo, Brazil, where I sieved all samples destined for foraminiferal picking in the *Laboratório de Oceanografia e Paleoceanografia* (LOOP) from the *Universidade Federal Fluminense*, Niterói, Brazil. The MD08-3167 core was stored at the *Laboratoire des Sciences du Climat et de l'Environnement* (LSCE), Gif-sur-Yvette, France. The first 700 cm of the core were previously explored in the framework of the RETRO and ACCLIMATE projects (Collins *et al.*, 2013; Collins *et al.*, 2014; Waelbroeck *et al.*, 2019), and later within Angelique Roubi's master's thesis from the *Université de Bretagne Occidentale* (UBO), Plouzané, France, (Roubi, 2017) focusing on isotopic, Mg/Ca, and foraminifera assemblage analyses. The rest of the core was sampled by Natalia Vázquez Riveiros (Geo-Ocean) and sent to Brazil to the LOOP, where I washed and sieved all samples destined for foraminiferal picking.

Approximately 10 cm³ of each sample of both cores were washed over a 63 μm mesh sieve, oven-dried for 24 h at 60°C, and stored in acrylic flasks where foraminifera shells were handpicked using a binocular microscope. The overview of each sediment core, the analyses information performed on them, picked species and shell numbers destined for each analysis, and related produced proxy records are summarized in Tables 1 and 2 and will be presented in the following method sections.

3.2 Geochemical Proxies and Analytical Effort

This section will describe all measurements ($n = 2964$) I performed in this thesis, summarized in Tables 2 and 3.

Table 2 - Measurement summary. Picked species, sieve size, type of analysis, equipment, laboratory, and produced proxy records are addressed for each investigated material, as well as a reference to the chapter of this thesis where the records are discussed. UAB: *Universitat Autònoma de Barcelona*. PSO: *Pôle Spectrométrie Océan*. LSCE: *Laboratoire des Sciences du Climat et de l'Environnement*

Core	XRF-bulk scanner	Water column layer	Foraminifera species	Mesh size (μm)	Equipment	Laboratory of analysis	Produced proxy records	Discussion chapters
GL-854		Surface	<i>Globigerinoides ruber</i>	250-300	IR-MS	UAB	$\delta^{18}\text{O}$, $\delta^{13}\text{C}$	-
		Thermocline	<i>Globorotalia inflata</i>	250-300		PSO	$\delta^{18}\text{O}$, $\delta^{13}\text{C}$	-
		Deep	<i>Cibicides wuellerstorfi</i>	> 150		UAB	$\delta^{18}\text{O}$, $\delta^{13}\text{C}$	4
MD08-3167	X	Surface	<i>Globorotalia bulloides</i>	250-300	IR-MS / ICP-MS	PSO / LSCE	$\delta^{18}\text{O}$, $\delta^{13}\text{C}$, Mg/Ca, $\delta^{18}\text{O}_{\text{sw}}$	6; 4
		Thermocline	<i>Globorotalia inflata</i>	250-300		PSO / PSO	$\delta^{18}\text{O}$, $\delta^{13}\text{C}$, Mg/Ca, $\delta^{18}\text{O}_{\text{sw}}$	6; 4
		Deep	<i>Uvigerina peregrina</i>	250-355	IR-MS	PSO	$\delta^{18}\text{O}$, $\delta^{13}\text{C}$	6; 4
			<i>Cibicides wuellerstorfi</i>	250-355			$\delta^{18}\text{O}$, $\delta^{13}\text{C}$	6; 4

3.2.1 Foraminifera: a vital tool for paleoceanographic reconstructions

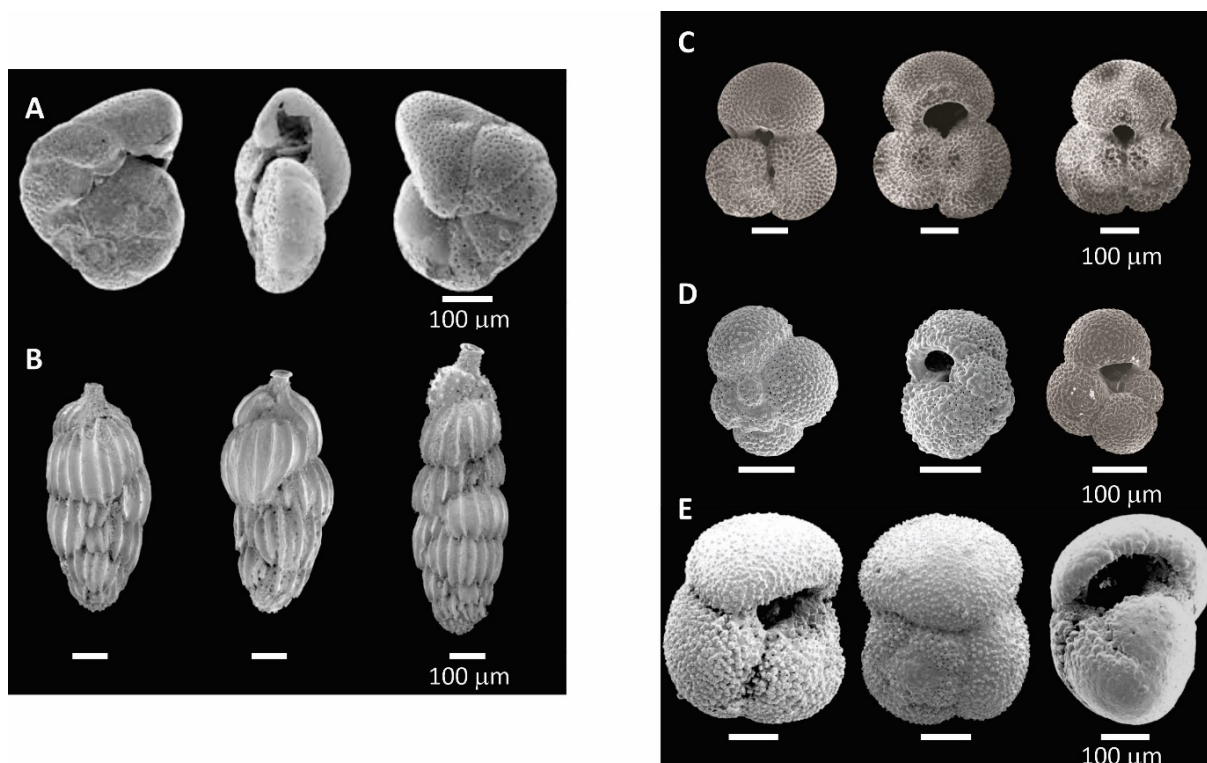
For many decades, the microorganisms called foraminifera have been widely employed to reconstruct past oceanographic conditions from the surface layers through the top of the water column and the deep ocean. Applicability improvements and the development of a wide variety of proxies based on analytical measurements of the calcitic shell of different species might arguably be significantly responsible for advances in the climatology and oceanography sciences, crucial for a better understanding of the Earth's system. Foraminifera are marine heterotrophic protists, in which the majority of the species diversity belongs to the benthos (i.e., living on the surface or deep in sediment), while a

minority are planktonic (i.e., live and vertically migrate through the top of the water column). Outside their unicellular body, most foraminifera species precipitate calcium carbonate in equilibrium with the surrounding water, constructing shells to protect the cytoplasm (i.e., *tests*) composed mostly of calcium carbonate and on a tiny proportion of silica or agglutinating minerals or biogenic fragments from the environment. The broad biogeographic distribution and excellent preservation of foraminifera fossil shells in marine sediment deposits make them a reliable “fingerprint” of the water masses from their habitat, providing an ideal fossil record on Earth for environmental reconstructions (Kucera, 2007).

Benthic foraminiferal species were used in this thesis (Fig. 2; left panel) to perform carbon and isotopic measurements and construct a robust age model for both sediment cores (see sections 3.2.2 and 3.3). *Cibicides wuellerstorfi* (Schwager, 1866) lives at the surface of marine sediments (i.e., epifaunal), usually attached to hard substrates in the upper 14 cm above the sediments (Lutze; Thiel, 1989; Gooday, 2003; Murray, 2006). The other benthic foraminifera utilized in this thesis is the species *Uvigerina peregrina*, a shallow infaunal species most abundant where there is a rich supply of organic matter (Fontanier *et al.*, 2002; Murray, 2006). *Uvigerina peregrina* precipitates its shell $\delta^{18}\text{O}$ in equilibrium with bottom water, while *C. wuellerstorfi* $\delta^{18}\text{O}$ is shifted by 0.64 ‰. After corrections are applied, both species provide a reliable record of bottom water $\delta^{18}\text{O}$. On the other hand, only *C. wuellerstorfi* $\delta^{13}\text{C}$ is registered in equilibrium with bottom water $\delta^{13}\text{C}_{\text{DIC}}$, while *U. peregrina* $\delta^{13}\text{C}$ is recorded in equilibrium with porewater $\delta^{13}\text{C}$ (Shackleton, 1974; Duplessy *et al.*, 1984). These are the most commonly used benthic species for stable isotope-based studies.

Uvigerina peregrina O and C stable isotopes were measured in the MD08-3167 core levels where *C. wuellerstorfi* was absent. Isotopic measurements of both species on this core were used to compose a single high-resolution benthic $\delta^{18}\text{O}$ curve for each core, crucial for the implemented chronological framework. Besides, *C. wuellerstorfi* isotopes from GL-854 were used in the first submitted manuscript, where we investigated the Deep Western Boundary Current at the Santos basin, exploring deep-water variability across different climate states over the last ca. 800 ka (see Chapter 4)

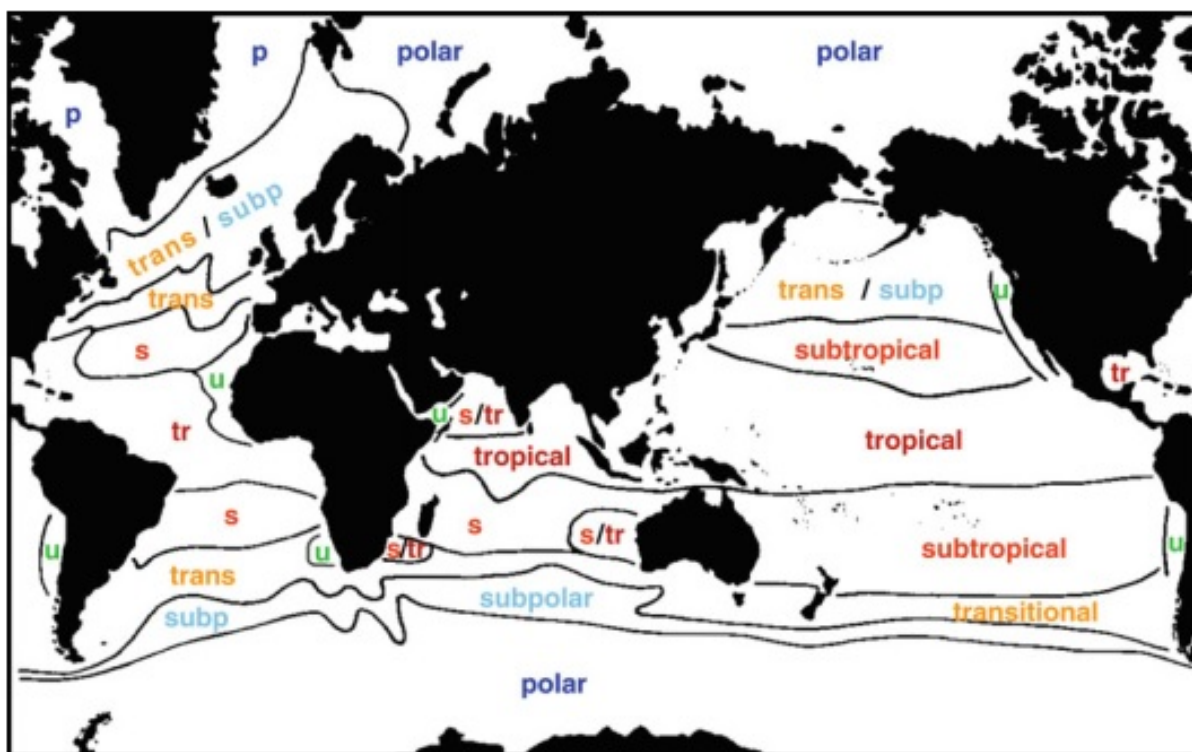
Figure 2 - Scanning electron microscope (SEM) photography of the foraminiferal species used in this thesis. The left panel presents the benthic species (a) *Cibicides wuellerstorfi* and (b) *Uvigerina peregrina*. The right panel shows the planktic species (c) *Globigerinoides ruber*, (d) *Globigerina bulloides*, and (e) *Globorotalia inflata*. Images from WoRMS Editorial Board (2023)



The geochemical analysis and isotopic measurements in this thesis mainly focus on planktic species from both cores (Fig. 2, right panel). During their life cycle, planktic foraminifera species migrate seasonally vertically within the water column to reproduce, mostly in pace with the lunar cycle (Spindler *et al.*, 1979; Gupta, 2003). Species can also have a half lunar life-cycle, such as *Globigerinoides ruber*, or an annual cycle for species habiting in thermocline layers (Bé, 1977; Kucera, 2007). Their distribution follows distinct oceanic provinces, as illustrated in Fig. 3. Upwelling regions have specific conditions defined by eutrophic and cold environments. Foraminiferal abundances are strongly temperature-dependent, this variable regulating assemblage composition, diversity, and size (Bé, 1977; Morey *et al.*, 2005). In addition, planktic foraminifera also responds to other environmental parameters, such as nutrient availability, light intensity, and salinity, that limit species distribution (Bé, 1977; Little *et al.*, 1997; Arz *et al.*, 1999; Volbers *et al.*, 2003; Al-Sabouni *et al.*, 2007). Therefore, it is essential to fully understand the species-specific life cycles characteristics, such as living-habitat preferences, calcification depth, seasonality,

and vital effects of used species, in order to use planktic foraminifera to reconstruct past environments (Schiebel; Hemleben, 2017).

Figure 3 - Foraminifera distribution provinces. Latitudinal provinces are polar (p), subpolar (subp), transitional (trans), subtropical (s), tropical (tr), and the upwelling and eutrophic conditions (u). Modified after Hemleben et al. (1989) (Schiebel and Hemleben, 2017)



Geochemical analyses were performed on planktic foraminifera picked from both GL-854 and MD08-3167 cores, specifically on the species *G. ruber* (Orbigny, 1839), *Globigerina bulloides* (Orbigny, 1826), and *Globorotalia inflata* (Orbigny, 1839) (Table 2; Fig. 4). These species were selected because of their respective abundance on each site, feasible for picking throughout the core samples, and commonly used for paleoceanographic reconstructions (e.g., Chiessi *et al.*, 2008; Cl  roux *et al.*, 2008; Cl  roux *et al.*, 2013; V  zquez Riveiros *et al.*, 2016). Furthermore, the different living habitats allow comparison between surface-dwelling (*G. bulloides* and *G. ruber*) and deep-dwelling species (*G. inflata*) that calcify in the permanent thermocline. Besides, using these species will permit discussing the evolution and the comparison of these water column layers from each side of the South Atlantic basin.

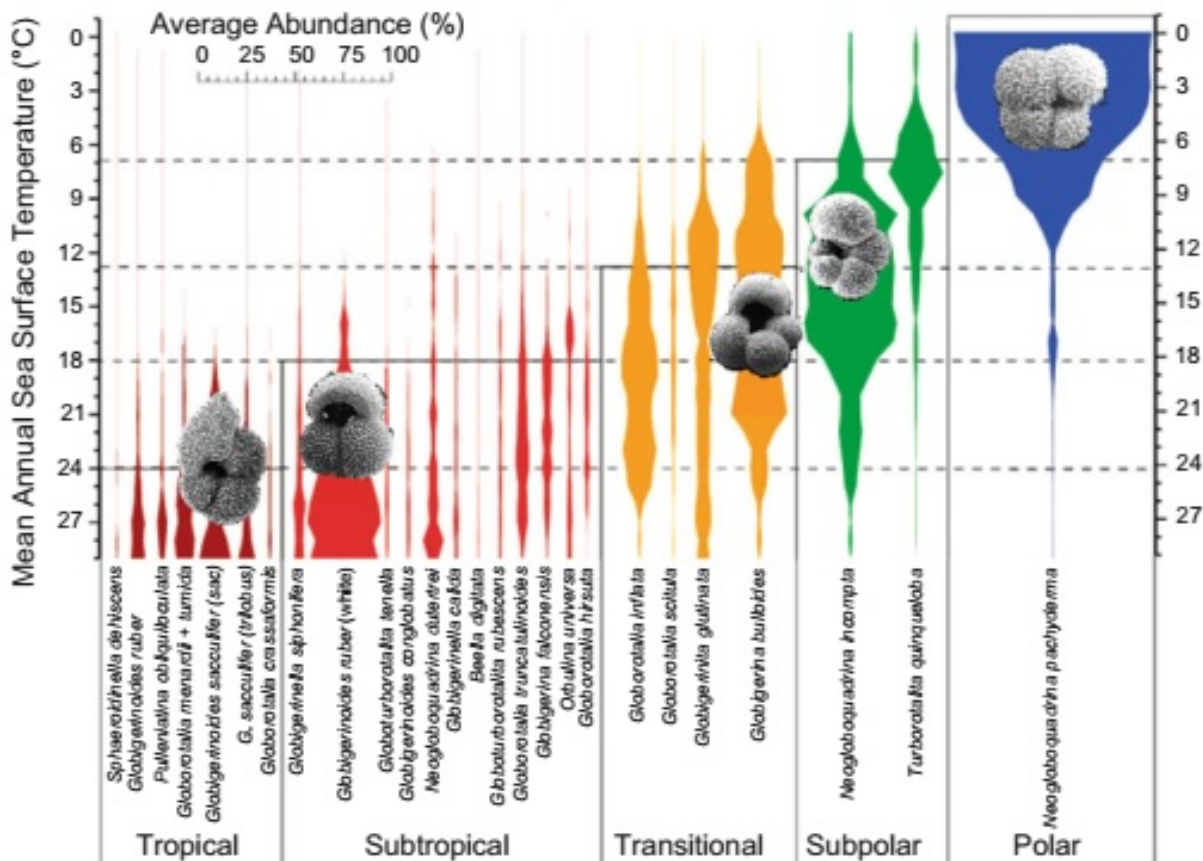
Globigerinoides ruber (white) has a preferential habitat in warm tropical and subtropical shallow waters (0-50 m), usually abundant in low turbidity oligotrophic regions

(Schiebel *et al.*, 2004). It reproduces all year (i.e., reproduction is not seasonal) and its biogeographic distribution has limitations in the South Atlantic. At the Brazilian margin, it prefers waters as far south as 25 °S, but only until 13 °S in the African margin (Bé, 1977; Schiebel; Hemleben, 2017). Thus, this species is more abundant on warm subtropical water in the western South Atlantic than in the eastern margin, and for this reason, *G. ruber* was chosen as representative of near-surface layer species in the GL-854 core. *Globigerinoides ruber* is one of the most tolerant species to low sea surface salinity (22-49 PSU) and presents in wide temperature range (14-31°C).

Globigerina bulloides is characteristic of transitional environmental conditions (i.e., mixing zones), preferring relatively cold nutrient-rich waters, usually associated with temperate to sub-polar water masses. It lives above the thermocline in the upper water column (0-60 m) without significant migration toward greater depths, so calcification occurs within the first 100 m (Schiebel *et al.*, 1997). It is abundant in subtropical-subpolar upwelling regions with episodic phytoplankton bloom (Schiebel *et al.*, 2004), where its high abundance in sediment archives makes this species one of the most analyzed planktic foraminifera in paleoceanographic studies. Thus, it is a key species that can also be used as a tracer for upwelling activity depending on the oceanic region (e.g., western South Atlantic, Lessa *et al.*, 2015; eastern South Atlantic, Little *et al.*, 1997; West *et al.*, 2004) (Giraudeau, 1993; Schiebel; Hemleben, 2017). *Globigerina bulloides* was chosen as representative of near-surface layer species in the MD08-3167 core.

Globorotalia inflata is a deep-dwelling species usually living in subtropical to subpolar regions at subsurface layers (40-100 m). It preferentially lives in relatively deep cold waters (1-27°C) compared to *G. ruber* and *G. bulloides*. This species migrates through the first few hundred meters in the water column, thus calcification may take place in a wide depth range between 50-500 m, but in the South Atlantic is representative of the permanent thermocline (Elderfield; Ganssen, 2000; Lončarić *et al.*, 2006; Groeneveld; Chiessi, 2011). It is one of the most abundant deep-dwelling transitional water species, with higher abundances found in subtropical regions such as the SASG between 30 – 50 °S through the South Atlantic Subtropical, Subantarctic, and Polar Frontal systems (Bé, 1977; Groeneveld; Chiessi, 2011; Schiebel; Hemleben, 2017).

Figure 4 - Temperature-related distribution of planktic foraminifera species and their respective provinces in the Atlantic Ocean (Kucera et al., 2005). The average abundances of the major species of the respective assemblages are displayed by colored bars. Modified after Kucera (2007) (Schiebel and Hemleben, 2017)



3.2.2 Stable isotopes

Oxygen and carbon stable isotopes of the CaCO_3 shell of foraminifera species have been traditionally applied in paleoenvironmental studies. The isotopic composition of their shells is assumed to be in equilibrium and then to register the signal of the surrounding waters during calcite precipitation (Ravelo; Hillaire-Marcel, 2007; Steph *et al.*, 2009; Katz *et al.*, 2010). The relative abundance between stable isotopic species is represented by the δ notation (in per thousand, ‰, units), which quantifies the difference between isotopic ratios from a sample minus a reference material (i.e., the difference between the ratios of the least abundant isotope over the most abundant), all normalized in relation to the standard value multiplied by 1000 (Eq. 1). The international standard used as a reference for foraminifera is the Vienna Pee Dee Belemnite (VPDB), which was calibrated with the isotopic composition of a marine carbonate fossil from the Cretaceous Pee Dee Formation,

Belemnitella americana. The isotopic composition of seawater is measured against another standard (Standard Mean Ocean Water, SMOW) expressed in ‰ SMOW. The main calcite isotopic ratios measured are $^{18}\text{O}/^{16}\text{O}$ ($\delta^{18}\text{O}_c$) and $^{13}\text{C}/^{12}\text{C}$ ($\delta^{13}\text{C}_c$), described by the formulas below:

$$\delta^{18}\text{O}_c = (\delta^{18}\text{O}_{\text{sample}}/\delta^{18}\text{O}_{\text{standard}} - 1) * 1000 \quad (\text{Eq. 1})$$

$$\delta^{13}\text{C}_c = (\delta^{13}\text{C}_{\text{sample}}/\delta^{13}\text{C}_{\text{standard}} - 1) * 1000 \quad (\text{Eq. 2})$$

$\delta^{18}\text{O}_c$ can be influenced by the foraminifera biological effects, calcification temperature, sea-water $\delta^{18}\text{O}$ ($\delta^{18}\text{O}_{\text{sw}}$), and the global ice volume (Emiliani, 1955). $\delta^{18}\text{O}_c$ can be interpreted as a conservative and qualitative density proxy, changing only by mixing different water masses with different isotopic compositions.

The oxygen isotopic fractionation in carbonate is temperature-dependent, with higher (lower) fractionation occurring under lower (higher) temperatures. It has been widely applied in oceanic circulation (Lynch-Stieglitz *et al.*, 2007), continental ice volume (Waelbroeck *et al.*, 2002), sea-water salinity (Adkins *et al.*, 2002), and temperature (Emiliani, 1955) reconstructions. Due to its relation with global ice volume, benthic foraminifera $\delta^{18}\text{O}_c$ values are used to define the stratigraphy system based on the Marine Isotopic Stages (MIS), in which in longer time-scales ^{18}O -enriched (-poor) $\delta^{18}\text{O}_c$ is observed during glacial (interglacial) and cold (warm) substages when a great (little) amount of ^{16}O is preferentially trapped in the ice-sheets. In this way, global ice volume generally affects the $\delta^{18}\text{O}_c$ proportionally, decreasing by $\sim 0.008 - 0.01$ ‰ per each meter of sea-level rise (Spratt; Lisiecki, 2016). The benthic foraminifera $\delta^{18}\text{O}_c$ composition reflects global ice-volume variations and can be used to construct the chronology for sedimentary archives beyond the 14C-absolute age range (see description in section 3.3). $\delta^{18}\text{O}_{\text{sw}}$ depends on local effects such as evaporation, precipitation, freshwater input, and mixing between different water masses (Duplessy *et al.*, 1988). The relation between $\delta^{18}\text{O}_c$, $\delta^{18}\text{O}_{\text{sw}}$, and temperature predicts ~ 0.23 ‰ per °C, expressed as Eq. 3 (Shackleton, 1974).

$$T = 16.9 - 4.38 * (\delta^{18}\text{O}_c - \delta^{18}\text{O}_{\text{sw}}) + 0.10 * (\delta^{18}\text{O}_c - \delta^{18}\text{O}_{\text{sw}})^2 \quad (\text{Eq. 3})$$

$\delta^{13}\text{C}_c$ registers the $\delta^{13}\text{C}$ signal from the dissolved inorganic carbon (DIC) from seawater ($\delta^{13}\text{C}_{\text{DIC}}$) during foraminifera growth and has been widely used to reconstruct primary productivity and ocean circulation (Duplessy *et al.*, 1988; Lea, 1995; Curry; Oppo,

2005). Interferences promoting differences between the $\delta^{13}\text{C}_c$ and $\delta^{13}\text{C}_{\text{DIC}}$ might be caused by foraminifera biological effects and ocean carbonate ion concentration. Multiple sources affecting the $\delta^{13}\text{C}_{\text{DIC}}$ challenge its interpretation, especially in surface waters. Global changes in $\delta^{13}\text{C}$ due to changes in the terrestrial biosphere also affects ocean's $\delta^{13}\text{C}$ signature. The vertical $\delta^{13}\text{C}_c$ profile reflects the primary productivity, which during the photosynthesis preferentially uptakes ^{12}C and leaves ^{13}C -enriched waters on the surface. At the same time, remineralization of sinking low- $\delta^{13}\text{C}$ organic matter leads to isotopic fractionation leaving the water depleted in ^{13}C , lowering $\delta^{13}\text{C}_{\text{DIC}}$ values at the bottom of the ocean (Duplessy *et al.*, 1984). The directly proportional relation with productivity leads to higher (lower) $\delta^{13}\text{C}_c$ values when there is higher (lower) primary productivity in the water column. Therefore, increased upper ocean productivity directly affects the $\delta^{13}\text{C}_{\text{DIC}}$ from the surface and deep waters, enhancing the gradient between these layers. Ocean circulation also influences $\delta^{13}\text{C}_{\text{DIC}}$ vertical distribution. In deep-water formation regions, ^{13}C -enriched surface waters quickly sink, lowering $\delta^{13}\text{C}_{\text{DIC}}$ at depth. Subsequently, the deep-water flow through the thermohaline circulation promotes the accumulation of low $\delta^{13}\text{C}$ organic carbon, decreasing $\delta^{13}\text{C}_{\text{DIC}}$ as it gets far from the formation zone. Therefore, ventilated (younger) water masses have higher $\delta^{13}\text{C}_{\text{DIC}}$, while less ventilated (older) waters have lower $\delta^{13}\text{C}_{\text{DIC}}$ (Kroopnick, 1985). Other factors can influence $\delta^{13}\text{C}_{\text{DIC}}$, such as (1) end-member variability; (2) pre-formed $\delta^{13}\text{C}$ linked to CO_2 sea-air exchanges and local primary productivity during water mass formation; (3) local nutrient distribution and export to the ocean floor, known as the “phytodetritus effect” (Mackensen *et al.*, 1993; Lynch-Stieglitz *et al.*, 1995; Mackensen; Schmiedl, 2019).

Therefore, planktonic foraminifera $\delta^{13}\text{C}_c$ from the surface layers has a high potential variability due to regional effects, suffering interferences from multiple sources, mainly by continuous sea-air exchanges (i.e., due to fluctuations in atmospheric $\delta^{13}\text{C}$). In contrast, benthic foraminifera $\delta^{13}\text{C}$ records represent long-term stabilized properties from the deep ocean and global oceanic circulation since sea-air exchanges only happen punctually at deep-water formation. Although productivity effects on benthic $\delta^{13}\text{C}$ can not be completely discarded, enhanced G-IG benthic $\delta^{13}\text{C}$ amplitudes are observed independently of local effects, suggesting that water mass dynamics overwhelm local photosynthesis and respiration, imposing vertical $\delta^{13}\text{C}$ distribution according to different water mass signatures.

For an extended explanation of ocean circulation and vertical $\delta^{13}\text{C}_{\text{DIC}}$ distribution, see Chapter 4.

3.2.3 X-Ray Fluorescence (XRF)

X-ray fluorescence (XRF) is a method of elemental analysis based on continuous core-scanning of marine sedimentary archives, analyzing the chemical composition of the total sediment (i.e., bulk) in a non-destructive way. Cores may be measured at mm resolution directly at the surface of a split core section, with minimized sample preparation and relatively low cost compared to other chemical analyses. The increased presence of terrigenous element-rich layers in marine cores might be connected to periods of enhanced erosion and transport of siliciclastic sediments towards the ocean, which may be related to periods of increased moisture in the continent, precipitation and/or lower sea level. Several studies have used data based on XRF analysis to reconstruct the main patterns of precipitation and terrigenous input to the ocean (Arz *et al.*, 1999; Adegbeie *et al.*, 2003; Mulitza *et al.*, 2008; Govin *et al.*, 2012; Hou *et al.*, 2022).

Before the analysis, the core needs to be prepared to smooth the sediment surface to enable complete contact of the sensor with the sediment, ensuring good measurement results. The measured sediment is covered with a 4 μm thin Ultralene film, with high transmission even with very low fluorescence energies, to avoid sample contamination by the equipment (Richter *et al.*, 2006). It is also essential to avoid other possible interferences, such as air bubbles and wrinkles under the film and possible water condensation due to warm temperatures during the scanner measurements. The fluorescent X-ray penetrates the sediment and ionizes the elements, firstly excited by the equipment emissions, and the emitted energy from each element is measured. Heavier elements emit relatively high energies, and the outgoing fluorescence radiation is linked to the element's atomic number. Measurements can be done in any given position over the core length, usually irradiating the sediment surface area of 1 cm x 1 cm at every 1 cm, but can also be adjusted to increase the resolution, for example, at every 0.2 cm (Tjallingii, 2007). The emitted energy irradiated by the samples and their frequencies over a predefined measure time is detected, and element intensities are quantified as counts proportional to the element concentrations. The time required for analysis is relatively reduced by measuring the intensity of larger elements than

minor elements, with analytical precision being best for higher intensities (Govin *et al.*, 2012).

3.2.4 Mg/Ca paleothermometry and $\delta^{18}\text{O}_{\text{sw}}$

The magnesium to calcium ratio (Mg/Ca) measured in planktonic foraminifera shells is widely used to reconstitute paleotemperatures such as sea surface temperature and from thermocline layers (Anand *et al.*, 2003; Ircali *et al.*, 2016; Lessa *et al.*, 2016; Ballalai *et al.*, 2019; Nascimento *et al.*, 2022, 2021). Mg from seawater is incorporated into calcite, replacing Ca through an endothermic reaction, which is directly proportional and dependent on the calcification temperature of the microorganism. Mg/Ca concentration (expressed in mmol/mol) increases with increasing temperature at an average of 10 % per 1°C (Anand *et al.*, 2003; Barker *et al.*, 2003; Cl eroux *et al.*, 2008). The relation between Mg/Ca and temperature is exponential (Elderfield; Ganssen, 2000), expressed as Eq. 4:

$$\text{Mg/Ca} = B \exp(A \cdot T) \quad (\text{Eq. 4})$$

Where Mg/Ca concentration is expressed in mmol/mol; T, the temperature in °C; and A and B are calculated empirically. Many Mg/Ca-temperature calibrations are developed through foraminiferal cultures (i.e., *in vitro*) or calibrated through core tops, which are highly dependent on the region and species they are based on. Since species living preferences might influence the calcification depth, and thus, the temperature registered in calcite, the recommended equation to apply would be species-specific, allowing appropriate temperature reconstructions at the site.

Other factors that can affect Mg/Ca concentration include the partial dissolution of Mg-rich shell parts in waters undersaturated with respect to calcite (Dekens *et al.*, 2002; Regenberg *et al.*, 2009), strong salinity gradients (Lea *et al.*, 1999), pH (i.e., linked to the CO_3^{2-} ; Lea *et al.*, 1999), and individual size and weight (Anand *et al.*, 2003). Despite the challenges associated with measuring Mg/Ca concentrations in foraminifera, the near-constant ratio of Mg/Ca throughout the ocean is an asset for investigating past temperature variability over the Late Pleistocene glacial-interglacial cycles. This is because the residence time for both elements is longer than a million years, making it an ideal proxy for this purpose. Complementary information on the Mg/Ca measurement method can be found in Chapter 6.

The main advantage over other marine paleothermometry proxies is that the estimated temperature can be obtained from the same biotic carrier from which $\delta^{18}\text{O}$ is obtained (Schmidt *et al.*, 2004; Rosenthal, 2007). Mg/Ca analyses are a powerful tool to deconvolve the effect of temperature and salinity on $\delta^{18}\text{O}_c$ analyses by using paleotemperature equations such as equation 4 (Shackleton, 1974; Groeneveld; Chiessi, 2011). Paired Mg/Ca and $\delta^{18}\text{O}_c$ measurements on the same foraminifera population are often used to reconstruct $\delta^{18}\text{O}_{sw}$, an indirect proxy for salinity (Eq. 3). However, $\delta^{18}\text{O}_{sw}$ is affected by regional evaporation and precipitation, among other hydrological dynamics. On a glacial-interglacial scale, it also depends on global changes in ice volume (Cléroux *et al.*, 2008). Therefore, Mg/Ca ratios coupled with $\delta^{18}\text{O}_c$ can ensure a common signal source, averaging the same local environmental conditions, seasonality, and geographic habitat, minimizing errors and uncertainties for these water column reconstructions.

3.3 Chronological approach: GL-854 and MD08-3167

Radiocarbon dating is the most used tool for building chronologies in paleoceanographic and paleoclimate studies, providing absolute ages to construct a reliable age-depth model for the last ca. 45 ka. Ages from a fossil sample are determined by measuring its ^{14}C content, assuming that the initial concentration and the half-life of ^{14}C are known. Analytical results provided by the laboratory will be corrected for reservoir effect (Bard, 1988) and calibrated due to variations in the initial ^{14}C concentration in the atmosphere in the past (Reimer *et al.*, 2013) to accurately constrain the age model from sedimentary sequences and the sedimentation rate (Blaauw; Christen, 2011).

For records that reach further back in time than radiocarbon dating, the orbital tuning of foraminiferal $\delta^{18}\text{O}$ records has been widely accepted for many decades (Imbrie *et al.*, 1984), in particular from benthics, as it can be used as a global ice volume proxy. However, benthic $\delta^{18}\text{O}$ also varies in function of local $\delta^{18}\text{O}_{sw}$ and temperature. Hence, matching different benthic $\delta^{18}\text{O}$ records might obscure timing differences among different locations and depths, artificially generating global $\delta^{18}\text{O}$ changes that might be out of phase by several thousand years (Duplessy *et al.*, 1991). This characteristic is crucial for understanding the limitation of the chronological framework implemented in paleoceanographic studies, which has a precision limitation not better than a few millennia. The age model uncertainties from

marine cores dated by orbital tuning for the last million years is about 5 ka (Lisiecki; Raymo, 2005), which must be considered when investigating quicker circulation changes transmitted across ocean basins.

The chronology for both GL-854 and MD08-3167 cores is constrained by a combination of accelerator mass spectrometry (AMS) ^{14}C dating from foraminifera shells and the alignment of the benthic $\delta^{18}\text{O}$ from each core with the global benthic foraminifera $\delta^{18}\text{O}$ stack LR04 (Lisiecki; Raymo, 2005) for ages beyond ^{14}C range, following the recommendations of (Blaauw *et al.*, 2018) and (Lacourse; Gajewski, 2020). The published age model of the GL-854 is based on three calibrated AMS ^{14}C ages (de Almeida *et al.*, 2015) measured in *Globigerinoides ruber* (white) shells and performed at the National Ocean Science AMS Facility (NOSAMS) at Woods Hole Oceanographic Institution (WHOI), United States. The radiocarbon ages were recalibrated using an estimated reservoir age of 271 years (Butzin *et al.*, 2005; de Almeida *et al.*, 2015) using software available at <http://radiocarbon.LDEO.columbia.edu/> and by applying the Fairbanks *et al.* (2005) calibration curve. The benthic $\delta^{18}\text{O}$ alignment was performed with the software AnalySeries v2.0 (Paillard *et al.*, 1996). See Chapter 4 and the original publication from de Almeida *et al.* (2015) for a detailed description of the age modeling of GL-854.

The age model from the MD08-3167 core is based on 8 radiocarbon dates measured on *G. bulloides* species analyzed at the Poznan Radiocarbon Laboratory, Pologne (Collins *et al.*, 2013). The radiocarbon ages published by Collins *et al.* (2013) for the MD08-3167 core were calibrated using the Marine20 calibration curve (Heaton *et al.*, 2020). No additional reservoir effect was applied. Beyond radiocarbon ages, the benthic $\delta^{18}\text{O}$ was aligned to the LR04 benthic $\delta^{18}\text{O}$ stack with the software QAnalySeries (Kotov; Paelike, 2018), and the complete age-depth model was built within the software Bacon v. 2.3 to reconstruct Bayesian accumulation histories (Blaauw; Christen, 2011). Error estimations of $\delta^{18}\text{O}$ tie-points consider the mean resolution of the benthic $\delta^{18}\text{O}$ record, the mean resolution of the reference curve, a matching error visually estimated when defining the tie points, and the absolute age error of the time scale used for the reference record. The age model calculated with Bacon also provides the maximum and minimum error estimations of the interpolation over the core. The age model built for GL-854 indicates that it spans from 4.4 to 772 ka BP, with a temporal resolution of approximately 1.92 kyr and an average sedimentation rate of 4.3 cm/kyr. For MD08-3167, the age model indicates that the core

covers between 1.1 and 367 ka BP with a temporal resolution of 0.68 kyr and an average sedimentation rate of 12.3 cm/kyr.

Figure 5 - Reference curve and the original age-depth model of GL-854 core published in de Almeida *et al.* (2015). The left figure displays a) *C. wuellerstorfi* $\delta^{18}\text{O}$ (permil VPDB) vs. depth, b) same vs. age (ka) plotted against the benthic $\delta^{18}\text{O}$ global stack (LR04, in permil VPDB; Lisiecki and Raymo, 2005), and c) *C. wuellerstorfi* $\delta^{13}\text{C}$ (permil VPDB) vs. age (ka). Black triangles indicate radiocarbon ages. Right figure: d) Age-depth model based on the software AnalySeries v2.0 (Paillard *et al.*, 1996)

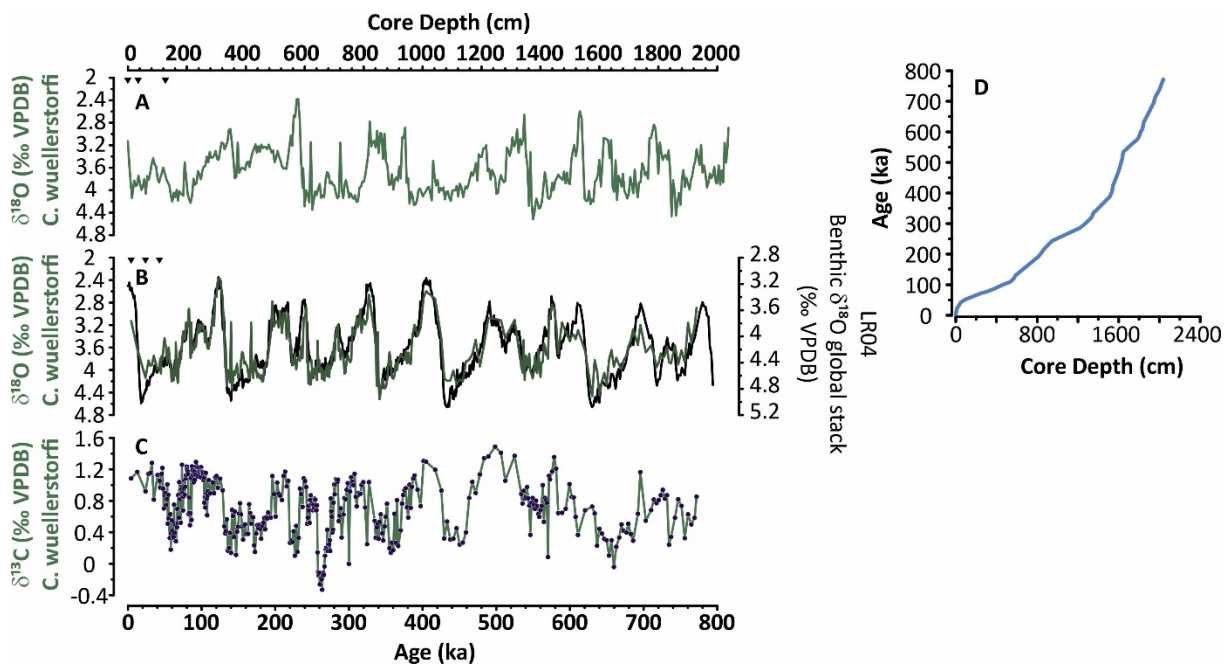
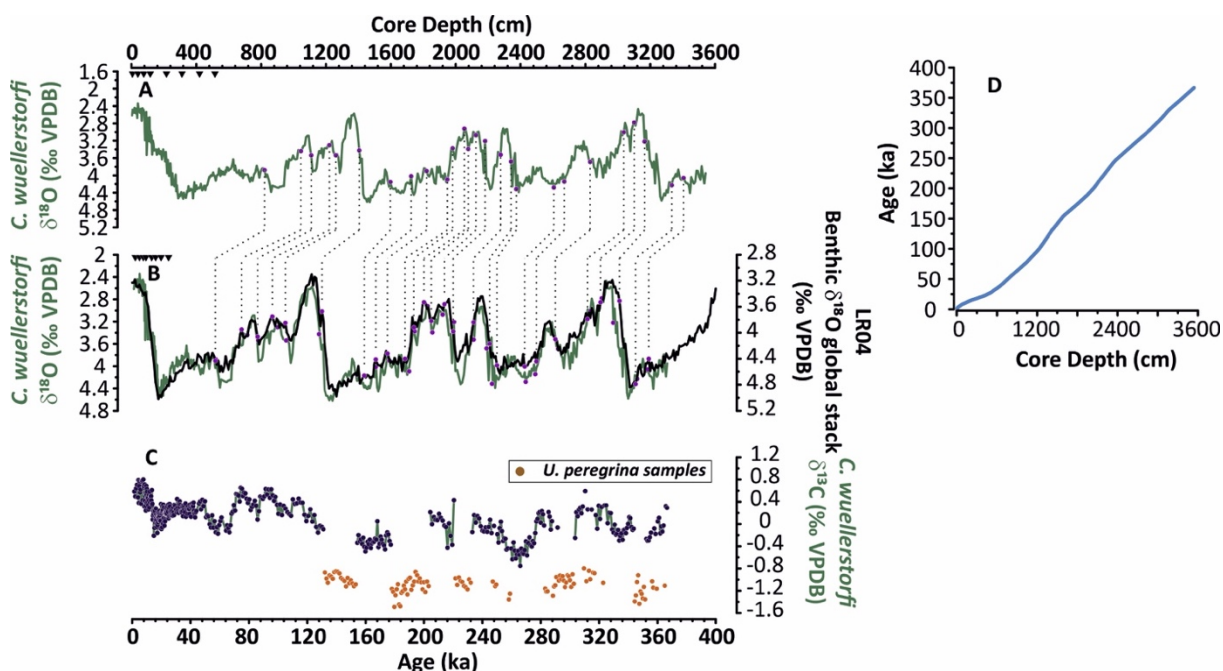


Figure 6 - Reference curve and the age-depth model of MD08-3167 core. The left figure displays a) benthic $\delta^{18}\text{O}$ (permil VPDB) vs. depth, b) the same vs. age (ka) plotted against the benthic $\delta^{18}\text{O}$ global stack (LR04; in permil VPDB; Lisiecki and Raymo, 2005), and c) benthic $\delta^{13}\text{C}$ (permil VPDB) vs. age (ka). *Uvigerina peregrina* data (brown data points) are indicated in panel c. Black triangles indicate the radiocarbon ages. Right figure d) Age-depth model based on Bacon v2.3 (Blaauw and Christen, 2011)



3.4 Geochemical data

A significant part of this thesis was focused on generating high-resolution, good-quality records from marine sediment cores GL-854 and MD08-3167, with the production of almost 3000 measurements (Table 3, Fig. 1). As briefly explained throughout the methods section, my analytical effort was mostly directed at producing oxygen and carbon isotopic and Mg/Ca records from surface and thermocline layers in both sides of the South Atlantic, as well as the benthic isotope records from the two cores that are the basis of our chronological framework. I have reconstructed the long-term upper ocean and deep-water variability over the last ca. 800 ka and ca. 400 ka, respectively, from the western and eastern margins of the South Atlantic basin.

In this section, I will present the protocols, methods implemented for each type of analysis performed, and results. All produced data presented in this section back up the discussions of Chapters 4, 5, and 6.

Table 3 - Quantification of the analytical measurements performed during this thesis. Measurements are detailed by core, foraminifera species, and analysis type

Core site	Foraminifera species	Type of analyses	n° of measurements
GL-854	<i>Globigerinoides ruber</i>	Stable isotopes	406
	<i>Globorotalia inflata</i>		418
	<i>Cibicides wuellerstorfi</i>		398
MD08-3167	<i>Globorotalia bulloides</i>	Stable isotopes	346
		Mg/Ca	351
	<i>Globorotalia inflata</i>	Stable isotopes	334
		Mg/Ca	322
	<i>Uvigerina peregrina</i> <i>Cibicides wuellerstorfi</i>	Stable isotopes	112 261
Total			2948

3.4.1 Stable isotopes

GL-854

Stable isotopic analysis in GL-854 was performed continuously throughout the entire 2038 m of the core. I handpicked the most abundant species, almost constantly present throughout the samples. The average sampling resolution is 5 cm, and measurements were performed on *G. ruber* ($n = 406$), *G. inflata* ($n = 418$), and *C. wuellerstorfi* ($n = 398$) (Table 3). About 30 individuals of each planktic species were picked from a narrow size fraction between 250-300 μm to minimize size effects on isotopic ratios. At least three benthic foraminifera shells were picked from the size fraction $>150 \mu\text{m}$. Before the analysis, foraminiferal samples were dissolved with strong phosphoric acid to transform calcite into gas CO_2 , and a total of 1222 samples were analyzed on an isotope ratio mass spectrometer.

Measurements of *G. ruber* and *C. wuellerstorfi* were performed at the *Universitat Autònoma de Barcelona* by Fabiana de Almeida (LaPAS) on a Finnigan MAT252 mass spectrometer coupled with a carbonate device Carbo Kiel IV, with an averaged reproducibility (1σ) of $\pm 0.03 \text{‰}$ for $\delta^{18}\text{O}$. *Globorotalia inflata* measurements from GL-854 core were performed by Fabien Dewilde using a Thermo Finnigan MAT 353 mass spectrometer equipped with a Carbo Kiel IV carbonate device at the *Pôle Spectrométrie*

Océan (PSO) from Université de Bretagne Occidentale (UBO), Plouzané, France. PSO results were calibrated using the international calibration standards NBS-18 and NBS-19. Measured $\delta^{18}\text{O}$ and $\delta^{13}\text{C}$ values for the NBS-19 standard were -2.20‰ and 1.95‰ , respectively. Measured $\delta^{18}\text{O}$ and $\delta^{13}\text{C}$ values for the in-house carbonate standard were -1.93‰ and 2.10‰ , respectively. The VPDB was calibrated against the NBS-19 standard with an external average reproducibility (1σ) of $\pm 0.03\text{‰}$ and 0.02‰ , respectively, for $\delta^{18}\text{O}$ and $\delta^{13}\text{C}$ values.

Figure 7 - Benthic isotopic record versus depth (cm) from core GL-854. *Cibicides wuellerstorfi* a) $\delta^{13}\text{C}$ (permil VPDB) and b) $\delta^{18}\text{O}$ (permil VPDB). Vertical dashed lines mark glacial Terminations, defined based on the benthic $\delta^{18}\text{O}$ record

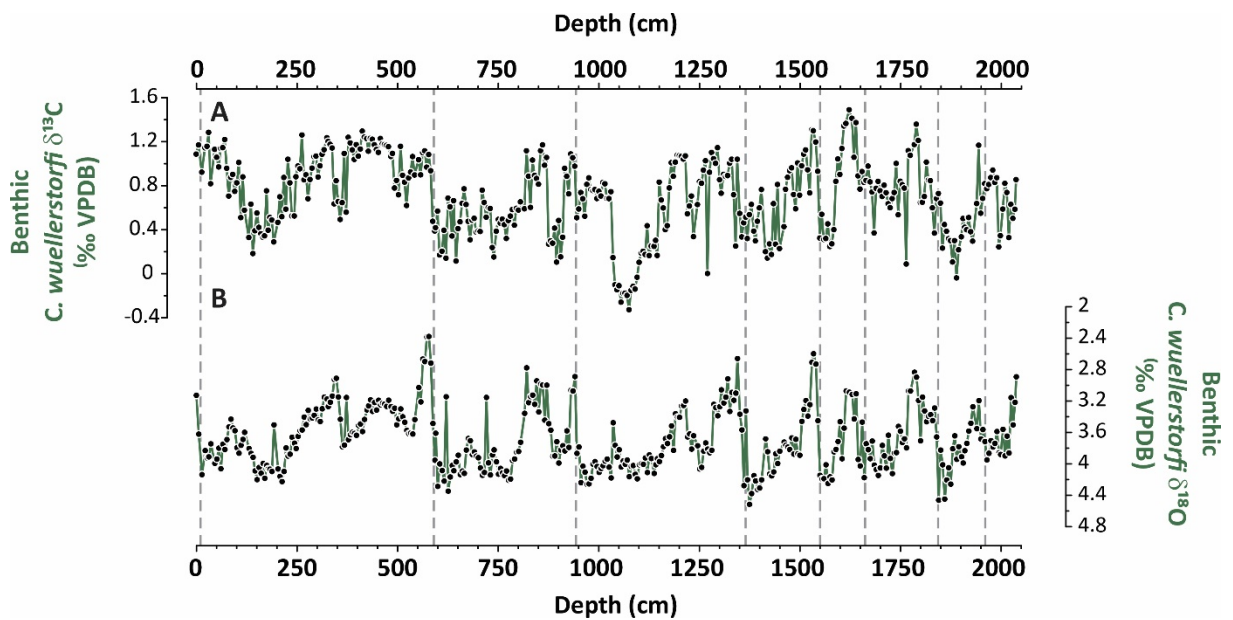
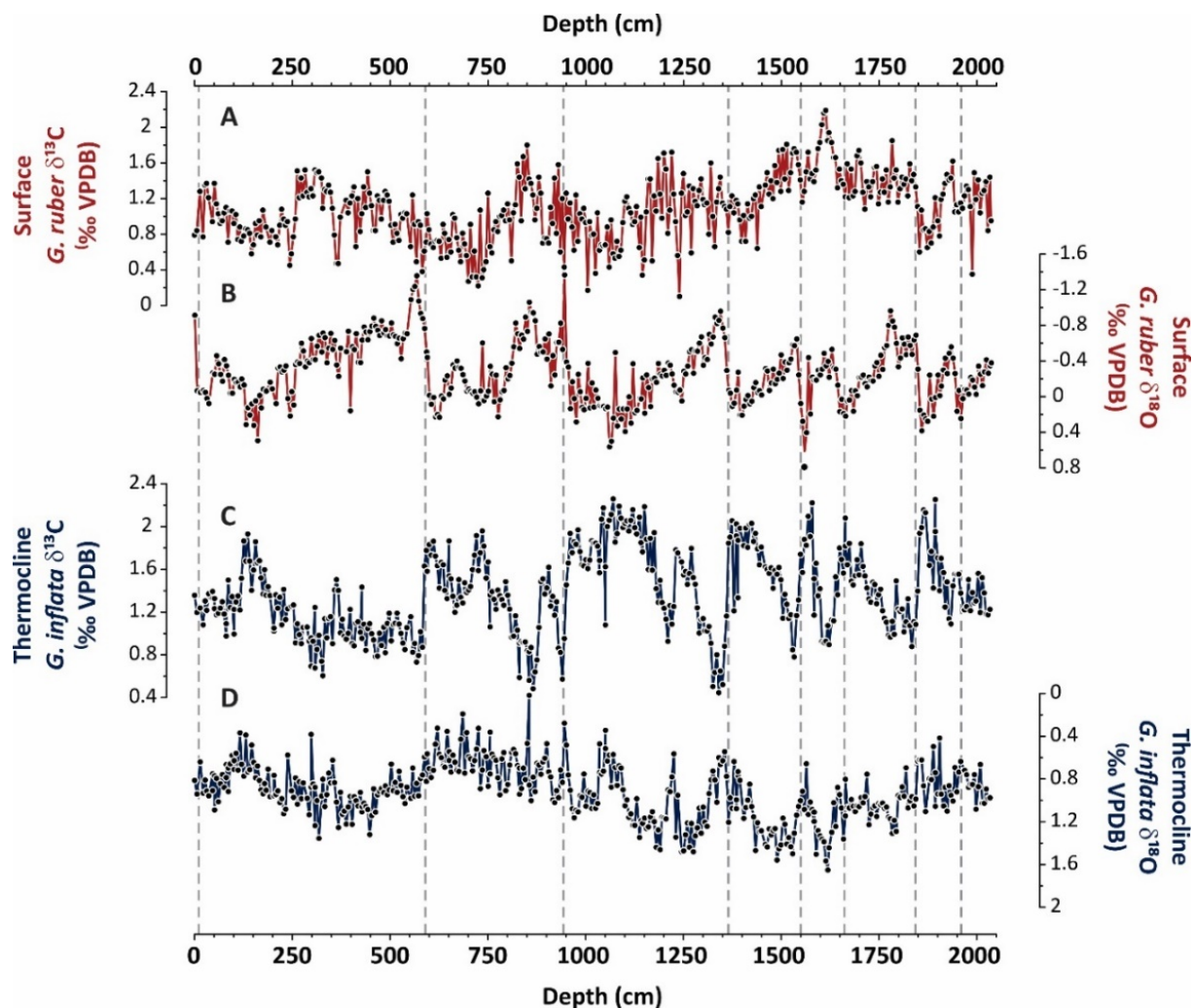


Figure 8 - Planktic isotopic record versus depth (cm) from core GL-854. a) *Globigerinoides ruber* (red curves) $\delta^{13}\text{C}$ (permil VPDB) and b) $\delta^{18}\text{O}$ (permil VPDB). c) *Globorotalia inflata* (blue curves) $\delta^{13}\text{C}$ (permil VPDB) and d) $\delta^{18}\text{O}$ (permil VPDB) records. Vertical dashed lines mark glacial Terminations, defined based on the benthic $\delta^{18}\text{O}$ record



MD08-3167

Stable isotopic analyses were performed between 700-3541 cm of the core, where I handpicked abundant species, almost constantly present throughout the samples. The average sampling resolution is 8 cm, and measurements were performed on *G. bulloides* ($n = 330$), *G. inflata* ($n = 330$), *C. wuellerstorfi* ($n = 246$), and *U. peregrina* ($n = 105$), totalizing 1011 isotopic measurements on core MD08-3167. About 30 individuals of each planktic species were picked from a narrow size fraction between 250-300 μm to minimize size effects on isotopic ratios. At least three benthic foraminifera shells were picked from a size fraction between 250-355 μm . During the analysis, foraminiferal samples were dissolved

with phosphoric acid to transform calcite into gas CO₂, and the samples were analyzed on an isotope ratio mass spectrometer.

For the first 700 cm of the MD08-3167 core, planktonic foraminifera shells were analyzed using a Finnigan $\Delta+$ and Elementar Isoprime mass spectrometer at the LSCE. The VPDB was calibrated against the NBS-19 standard ($\delta^{18}\text{O} = -2.20 \text{ ‰}$), with an external average reproducibility (1σ) of $\pm 0.05 \text{ ‰}$. The measured NBS-18 standard has a $\delta^{18}\text{O}$ value of $-23.20 \pm 0.20 \text{ ‰}$. *Globigerina bulloides*, *G. inflata*, and benthic foraminifera measurements from the 700 – 3541 cm interval of the MD08-3167 and through all GL-854 core were performed using a Thermo Finnigan MAT 353 mass spectrometer equipped with a Carbo Kiel IV carbonate device at PSO by Fabien Dewilde. Measured $\delta^{18}\text{O}$ and $\delta^{13}\text{C}$ values for the NBS-18 standard were -23.20 ‰ and -5.01 ‰ , respectively. Measured $\delta^{18}\text{O}$ and $\delta^{13}\text{C}$ values for the NBS-19 standard were -2.20 ‰ and 1.95 ‰ , respectively. The long-term precision for the in-house standard (CAMIL-21) measured at PSO is $\pm 0.03 \text{ ‰}$ and $\pm 0.01 \text{ ‰}$ for *G. bulloides*, $\pm 0.03 \text{ ‰}$ and $\pm 0.02 \text{ ‰}$ for *G. inflata*, $\pm 0.03 \text{ ‰}$ and $\pm 0.02 \text{ ‰}$ for *C. wuellerstorfi* and *U. peregrina*; respectively for $\delta^{18}\text{O}$ and $\delta^{13}\text{C}$ measurements used as reference material for normalization and evaluate the reproducibility of the measurements. The *Cibicides wuellerstorfi* $\delta^{18}\text{O}$ record was corrected by a factor of plus 0.64 ‰ and plotted together with *U. peregrina* $\delta^{18}\text{O}$ values to produce a unique and reliable curve for bottom water $\delta^{18}\text{O}$ (Duplessy *et al.*, 1984).

Figure 9 - Benthic isotopic record versus depth (cm) from core MD08-3167. a) *Cibicides wuellerstorfi* (dark green line; $\delta^{18}\text{O}$ -corrected values) and *U. peregrina* (brown dots) $\delta^{13}\text{C}$ (permil VPDB) and b) $\delta^{18}\text{O}$ (permil VPDB) records. Benthic isotopes from the first 700 cm of the core are unpublished data previously produced at LSCE (light blue line). Vertical dashed lines mark glacial Terminations, defined based on the benthic $\delta^{18}\text{O}$ record

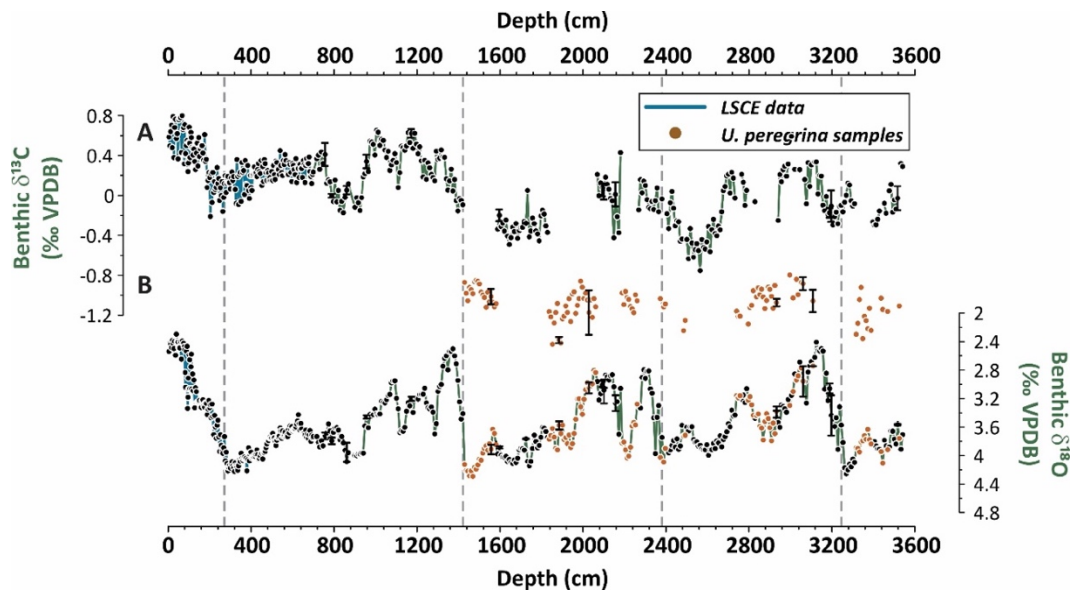
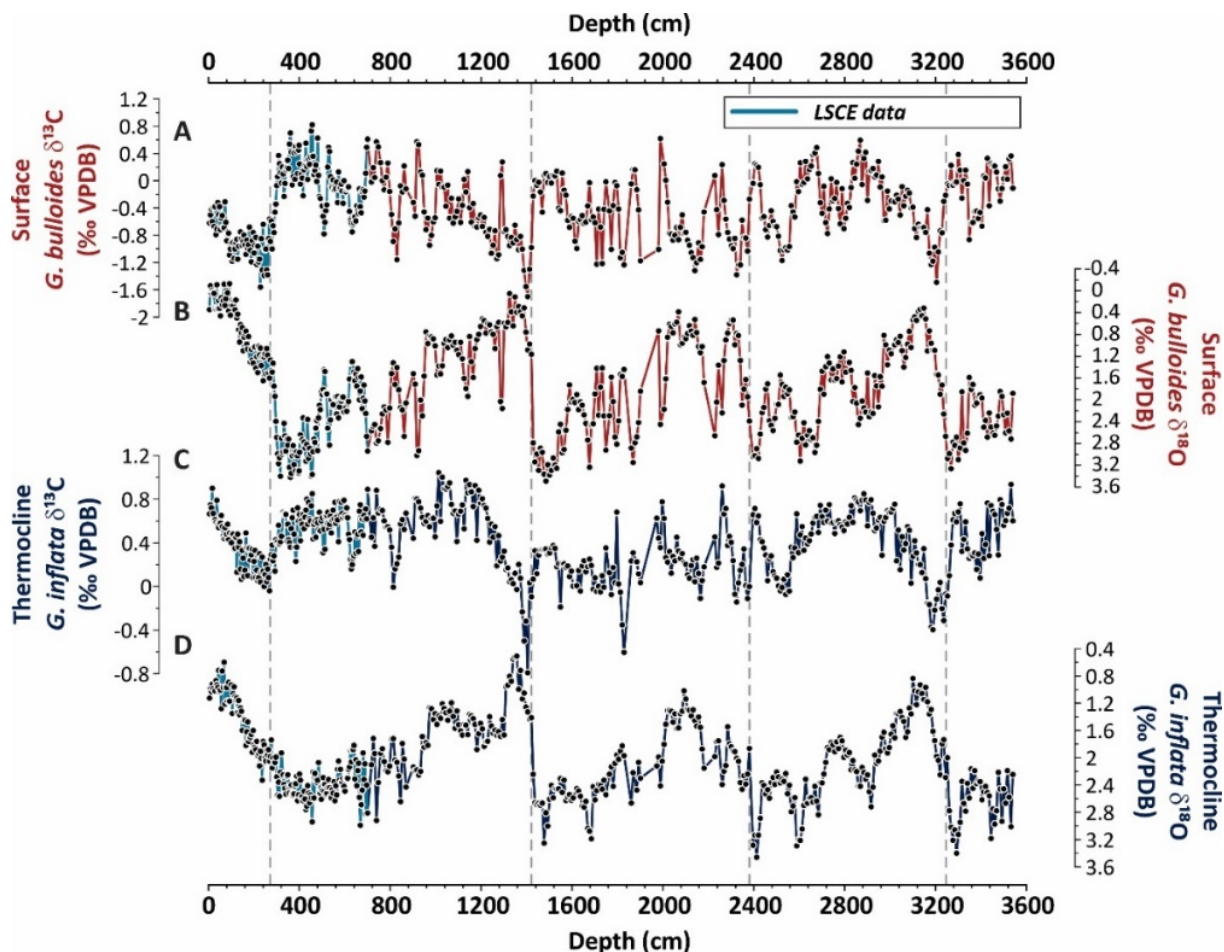


Figure 10 - Planktic isotopic record versus depth (cm) from core MD08-3167. *Globigerina bulloides* (red curves) a) $\delta^{13}\text{C}$ (permil VPDB) and b) $\delta^{18}\text{O}$ (permil VPDB) records. *Globorotalia inflata* (dark blue curves) c) $\delta^{13}\text{C}$ (permil VPDB) and d) $\delta^{18}\text{O}$ (permil VPDB) records. Planktic isotopes from the first 700 cm of the core are unpublished data previously produced in LSCE (light blue line). Vertical dashed lines mark glacial Terminations, defined based on the benthic $\delta^{18}\text{O}$ record



3.4.2 Mg/Ca

MD08-3167

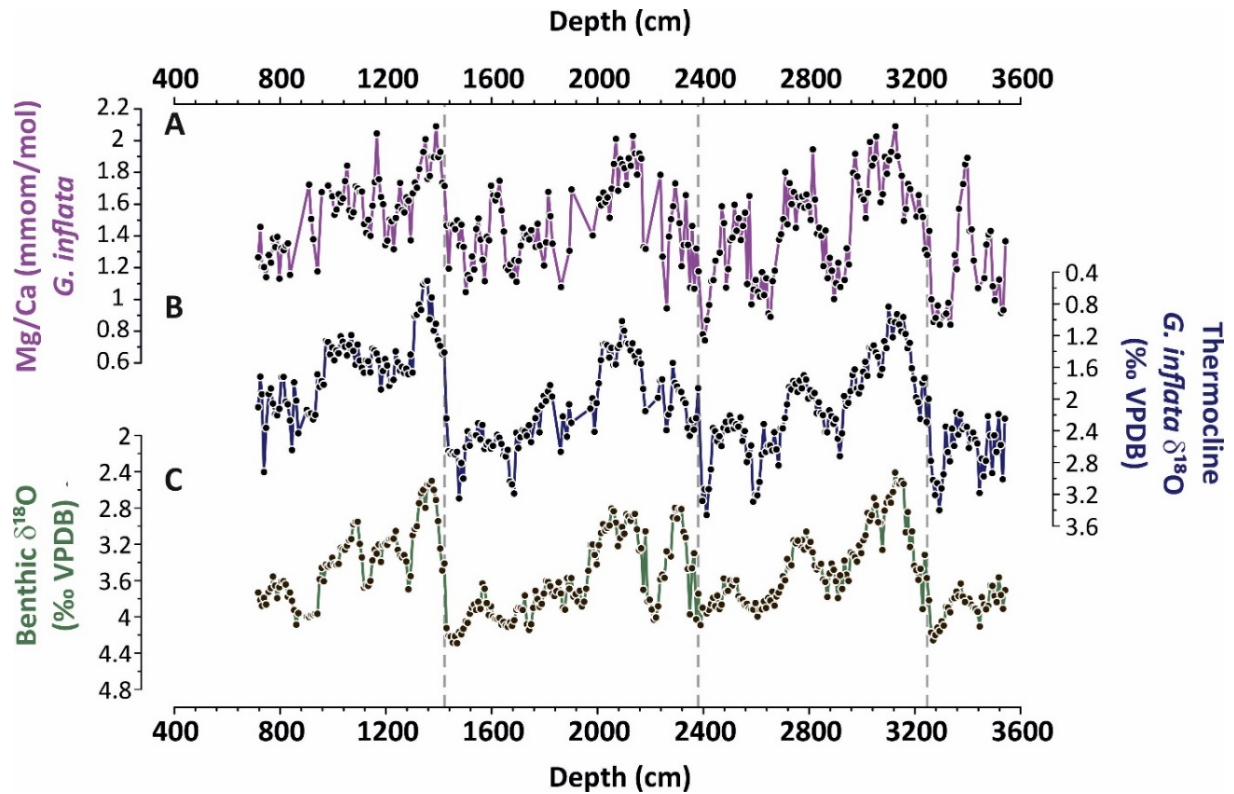
I performed Mg/Ca measurements on *G. bulloides* ($n = 351$) and *G. inflata* ($n = 322$) species. I picked around 30 well-preserved planktonic foraminifera shells from the 250-300 μm size fraction through the core, totalizing 694 measurements. I gently crushed samples between glass plates, transferred them to clean plastic vials, and carefully cleaned them according to the cleaning protocol developed for Mg/Ca analysis without a reductive step (Barker *et al.*, 2003). Briefly, repetitive rinses with Milli-Q water removed clays and detrital material, then samples were oxidatively cleaned for organic matter in a 2% H_2O_2 , lightly

leached with 0.001 M HNO₃, and transferred to clean vials for dissolution and dilution with 0.075 M HNO₃ on the day of analysis.

Globigerina bulloides ($n = 174$; not included in the Mg/Ca measurements of Table 3) species for the first 700 cm of the core were previously analyzed using a Varian Vista Pro ICP-OES at LSCE following the procedure described in (de Villiers *et al.*, 2002). The remaining *G. bulloides* samples between 700-3541 cm are being measured at the LSCE to avoid potential machine biases.

I performed all *G. inflata* measurements ($n = 322$) analyzed using ThermoFisher Scientific's ELEMENT XR High-resolution Multi-collector ICP-MS at the PSO from IFREMER with the help of Yoan Germain. Blanks were regularly measured, one every 15 samples to detect potential contamination during the cleaning process. Standard and replicates were measured on each ICP-MS-session day to monitor equipment drifts or possible biases in the results that might be caused by contamination or equipment instabilities, as well as to assess the precision and accuracy of the equipment, and the reproducibility of the measurements. Al, Mn, Fe, and Zn concentrations were used to monitor for contamination and evaluate the cleaning protocol efficiency performed in samples, showing no contamination. A significant part of my thesis was committed to implementing the Mg/Ca technique at IFREMER. For this reason, Chapter 6 provides detailed information on the *G. inflata* measurements in core MD08-3167, including more technical information as to the used materials and infrastructure facilities (section 6.2) up to preliminary scientific discussions about the generated Mg/Ca-temperature thermocline temperature (section 6.6).

Figure 11 - *Globorotalia inflata* a) Mg/Ca ratio (mmol/mol), b) $\delta^{18}\text{O}$ (permil VPDB) records, and c) benthic foraminifera $\delta^{18}\text{O}$ (permil VPDB) record versus depth (cm) from MD08-3167 core between 700 and 3541 cm of the core. Vertical dashed lines mark glacial Terminations, defined based on the benthic $\delta^{18}\text{O}$ record



GL-854

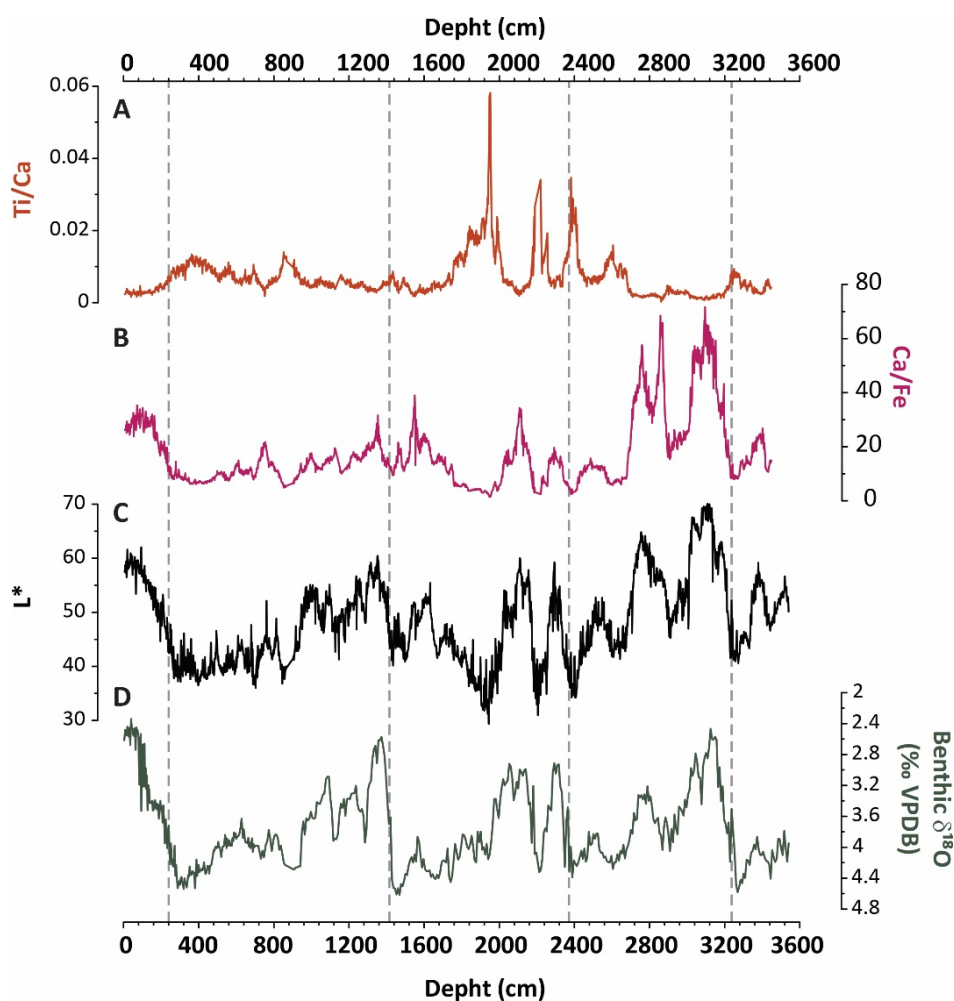
Mg/Ca measurements on this core will be performed on *G. ruber* ($n = 388$) and *G. inflata* ($n = 394$) species. I have already picked around 30 well-preserved planktonic foraminifera shells from the 250-300 μm size fraction through the core, totalizing extra 782 samples to be measured. All foraminifera shells are ready to be crushed and cleaned with the protocol described in this section. This core will be measured in the already purchased ICP-OES machine from LOOP. Future Mg/Ca measurements on this core are important for my scientific perspectives, and very complementary to the measurements performed during this thesis. Although these results will no longer be part of this thesis, I aim to implement at UFF the analytical expertise developed at IFREMER by setting the new equipment dedicated to analyzing foraminifera samples, representing the further step in the international collaboration and technology transfer between IFREMER and LOOP. Besides, I intend to produce an inter-laboratory calibration for Mg/Ca analysis.

3.4.3 X-Ray fluorescence

MD08-3167

Continuously XRF scanner measurements were performed in the MD08-3167 marine core with the Avaatech XRF scanner at the Center for Marine and Environmental Sciences (MARUM), Bremen, Germany. Measurements were performed every 2 cm by irradiating a surface of about 10 mm × 12 mm with a count time of 30 s on the X-ray tube. Each section was scanned at 10 kilovolts (kV) to measure minor elements from Al to Fe and 30 kV for major elements. Ca counts were used as a common denominator to normalize a few used elements. Ratios are presented as natural logarithms (i.e., ln) of the Element / Ca ratio.

Figure 12 - Intensities of some XRF-measured major elements and Lightness (L^*) measured by spectrophotometry in the Multi Sensor Core Logger (MSCL) on board, both in bulk sediments from MD08-3167. A) Ti/Ca ratio; b) Ca/Fe ratio; c) L^* ; and d) benthic foraminifera $\delta^{18}\text{O}$ (permil VPDB) for stratigraphic reference. Vertical dashed lines mark glacial Terminations, defined based on the benthic $\delta^{18}\text{O}$ record



4 ATLANTIC $\delta^{13}\text{C}$ DEEP-WATER SEESAW CONTROLLED BY ANTARCTIC SEA ICE OVER THE LAST 800 ka

Through the last ca. 800 ka, periodic ~ 100 ka oscillations of the climate system named glacial-interglacial (G-IG) cycles have been imprinted on paleoclimate records, such as those of oxygen isotope ratios of benthic foraminifera reflecting the variability of global ice volume (Imbrie *et al.*, 1993; Lisiecki and Raymo, 2005). It is commonly assumed that the pacing of these cycles is controlled by summer insolation forcing at high latitudes of the Northern Hemisphere (Hays *et al.*, 1976) and that mechanisms controlling atmospheric carbon dioxide play a vital role in modulating the amplitude of G-IG cycles. Ice core records reveal that atmospheric CO_2 has varied between 180 and 280 ppm following a G-IG variability (Petit *et al.*, 1999; Siegenthaler *et al.*, 2005; Lüthi *et al.*, 2008). Several distinct mechanisms have been proposed to explain the observed 100 ppm glacial atmospheric CO_2 drawdown, mainly connected to glacial carbon storage in the deep ocean and a corresponding reduction of ocean-atmosphere fluxes in the Southern Ocean (Sigman and Boyle, 2000; Yu *et al.*, 2016).

The Atlantic Meridional Overturning Circulation (AMOC) has undergone significant long-term trends characterized by periods of stability and instability, fluctuations in strength and geometry. On G-IG time scales, changes in deep-water distribution alter the large-scale patterns of the carbon cycle by regulating global atmospheric CO_2 (Toggweiler, 1999; Sigman and Boyle, 2000; Toggweiler *et al.*, 2006). During the last glacial period, fresher and less dense surface waters would have reduced the formation and the extension of the glacial version of North Atlantic Deep Water (NADW), the Glacial North Atlantic Deep/Intermediate Water (GNAIW) (Curry and Oppo, 2005). Reduced production in NADW during glacial periods may have been balanced by increased Antarctic Bottom Water (AABW) formation driven by stronger winds and enhanced sea-ice formation, establishing a deep-water seesaw between NADW/GNAIW and AABW (Broecker, 1998; Buizert and Schmittner, 2015).

Water mass geometry and mixing across the Atlantic basin during different states of the AMOC have been investigated using the $\delta^{13}\text{C}$ proxy (Schmiedl and Mackensen, 1997; Duplessy *et al.*, 1988; Curry and Oppo, 2005; Lund *et al.*, 2015; Peterson and Lisiecki, 2018; Voigt *et al.*, 2017). Benthic foraminifera $\delta^{13}\text{C}$ measurements on *Cibicidoides wuellerstorfi*

species are considered to record deep-water dissolved inorganic carbon isotopic values ($\delta^{13}\text{C}_{\text{DIC}}$) (Duplessy *et al.*, 1988; Lea, 1995; Oppo and Horowitz, 2000). The oceanic vertical $\delta^{13}\text{C}_{\text{DIC}}$ profile mirrors upper ocean biological productivity. During photosynthesis, ^{12}C from surface waters is preferentially removed leaving surrounding waters ^{13}C -enriched, while remineralization leaves the deep ocean ^{13}C -depleted. However, other factors can influence $\delta^{13}\text{C}_{\text{DIC}}$, including nutrient distribution, CO_2 air-sea exchanges during water mass formation, end-member changes, and, particularly, the redistribution of seawater $\delta^{13}\text{C}$ by ocean circulation.

AMOC intensity is coupled to the NADW formation rate (Rahmstorf, 2006), which is connected to the Southern Hemisphere climate via NADW upwelling in the Southern Ocean (Marshall and Speer, 2012; Talley, 2013). Variations in the upwelling rate around Antarctica would, in turn, affect deep-water convection in the North Atlantic by regulating the return flow of circulation. Reduced NADW formation enhances the formation and expansion of nutrient- and respired carbon-enriched AABW, which is believed to have helped to reduce atmospheric CO_2 critically due to increased deep-water stratification and diminished ocean-atmosphere exchange that reduced CO_2 outgassing from the Southern Ocean (Stephens and Keeling, 2000; Ferrari *et al.*, 2014; Nadeau *et al.*, 2019). Therefore, modifications in the balance between NADW and AABW (i.e., the “deep-water seesaw”) are critical for long-term climate changes, playing an important role in climatic transition such as the Mid-Brunhes Transition (MBT; Jansen *et al.*, 1986; Yin, 2013; Barth *et al.*, 2018).

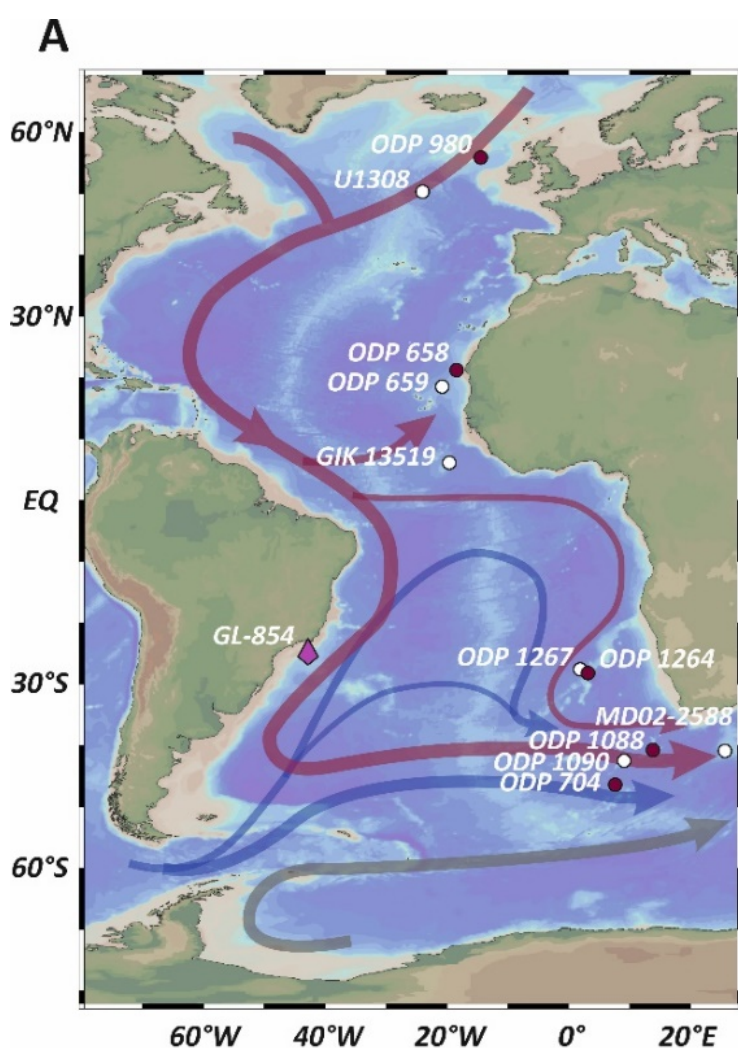
The MBT marks the shift between two different climatic states defined by an increasing amplitude of G-IG cycles; orbital parameters are also thought to play a key role in this transition (Jansen *et al.*, 1986; Yin and Berger, 2010; Yin, 2013). During the more recent Marine Isotope Stages (MIS) (430-0 ka), both Antarctic temperatures and atmospheric CO_2 concentrations were significantly higher than before in the previous “lukewarm interglacials” (800-430 ka) (Jouzel *et al.*, 2007; Lüthi *et al.*, 2008).

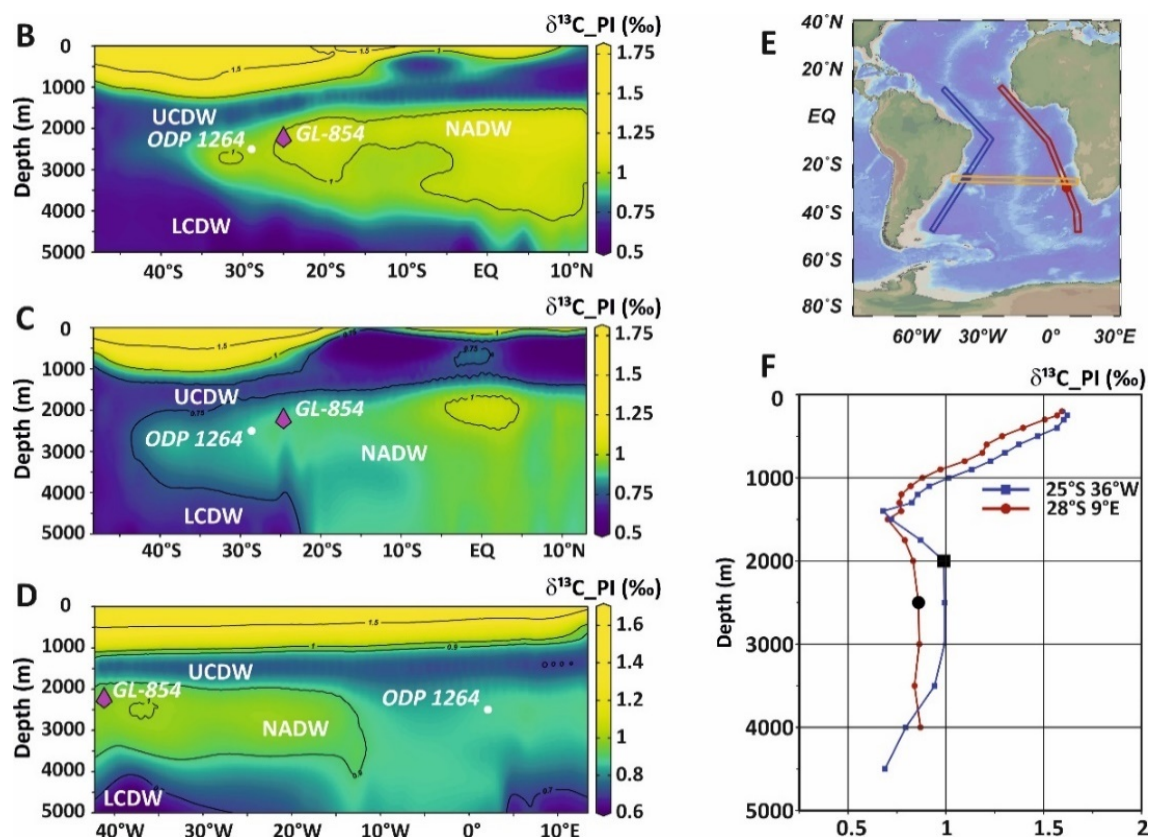
Long-term AMOC variations might have played a critical role in providing positive feedbacks that magnify the orbital effects on climate (Kemp *et al.*, 2010; Holden *et al.*, 2011; Barth *et al.*, 2018). Understanding these mechanisms is essential for deciphering the climate response to both external and internal forcings. In particular, reconstructions of the South Atlantic Deep Western Boundary Current (DWBC) variability and geometry, a critical

component of AMOC for inter-hemispheric heat fluxes exchange, are needed to understand how transitions between distinct modes of circulation affected the carbon cycle during the Late Pleistocene. The water mass dynamics at mid-depths (i.e., 2000 – 2500 m) are particularly interesting since they mark the boundary between northern- and southern-sourced deep-water masses (Curry and Oppo, 2005; Muglia and Schmittner, 2021). However, their accurate evaluation has been hampered by the lack of continuous long-term records in the western South Atlantic (WSA).

Here, we present a new 770 ka $\delta^{13}\text{C}$ record based on the benthic foraminifera species *Cibicidoides wuellerstorfi* from sediment core GL-854 retrieved from the WSA (25°12'S, 42°37'W) at 2200 m water depth (Fig. 13). We compare our record with published $\delta^{13}\text{C}$ data from the Deep Eastern Boundary Current (DEBC) to investigate the zonal $\delta^{13}\text{C}$ gradient variability ($\Delta\delta^{13}\text{C}_{\text{w-e}} = \delta^{13}\text{C}_{\text{GL-854}} - \delta^{13}\text{C}_{\text{ODP 1264}}$) of NADW over the last ca. 800 ka. Our $\Delta\delta^{13}\text{C}_{\text{w-e}}$ record reveals oscillations between distinct modes of AMOC controlled by the orbitally-triggered Antarctic sea-ice variability. We establish the connection between long-term trends in AMOC, sea ice, and orbital forcing over the Late Pleistocene, elucidating the role of AMOC on the climate transition across the MBT.

Figure 13 - A) Position of core GL-854 (red pin, this study) in the western South Atlantic (WSA) and other marine records discussed in this work (red circles: mid-depth core site, white circles: deep core sites): North Atlantic sites: ODP Site 980 (Flower *et al.*, 2000), IODP Site U1308 (Hodell and Channell, 2016), ODP Sites 658, 659 (Sarnthein and Tiedemann, 1989), GIK 13519 (Sarnthein *et al.*, 1984); South Atlantic sites: ODP Sites 1264, 1267 (Bell *et al.*, 2014), and 704 (Hodell, 1993), MD02-2588 (Starr *et al.*, 2021), ODP Sites 1088 and 1090 (Hodell *et al.*, 2003). B) to F) sections showing pre-industrial $\delta^{13}\text{C}$ distribution in the water column (Eide *et al.*, 2017). E) Meridional sections of the B) western and C) eastern South Atlantic encompassing the subtropical South Atlantic sites; D) subtropical South Atlantic zonal section. Sections are represented in the map by the blue, red, and yellow colors, respectively. F) Preindustrial vertical $\delta^{13}\text{C}$ profiles of the closest stations to GL-854 (blue) and to ODP Site 1264 (red) (Eide *et al.*, 2017). The black square and circle are the closest data points to the depth of the cores. The figure was produced using Ocean Data View (Schlitzer, 2021)





4.1 Material and Methods

4.1.1 Sediment cores

We conducted an analysis of marine sediment core GL-854, collected by Petrobras (Rio de Janeiro, Brazil) in the subtropical western South Atlantic (25°12'S, 42°37'W, 2220 m water depth, 20.38 m long; Fig. 13) during the Fugro Explorer Campaign in 2007. Ten cm³ of sediment were collected at 5 cm intervals through the entire core and disaggregated by soaking in distilled water in an orbital shaker. Samples were washed over a 63 μm mesh sieve, oven-dried for 24 h at 60 °C, and stored in acrylic flasks.

Our main interpretations are based on direct comparison to records from the sediment core at ODP Site 1264 (28°31.95'S, 2°50.73'W, 2505 m water depth and 283 m long; Zachos *et al.*, 2004), retrieved at similar water depth in the Walvis Ridge, on the subtropical eastern South Atlantic, to calculate zonal $\delta^{13}\text{C}$ gradient (i.e., $\Delta\delta^{13}\text{C}_{\text{w-e}}$, Fig. 14B).

4.1.2 Study area

Core GL-854 site is located off the Brazilian coast at the Santos Basin continental slope (SE Brazilian margin) in the subtropical WSA (Fig. 13). The uppermost (0–600 m) wind-driven circulation at this site is dominated by the southward-flowing Brazil Current (BC), which is the surface WBC of the South Atlantic Subtropical Gyre (Stramma and England, 1999). The site of GL-854 presents punctually seasonal vertical carbon export to the bottom in some periods throughout the core, but the phytodetritus effect does not significantly affect benthic $\delta^{13}\text{C}$ (Mackensen *et al.*, 1993; de Almeida *et al.*, 2015). This region is a low-latitude oligotrophic area without large river influence, so the supply of terrigenous sediments to the slope is limited, implicating that ocean currents are probably the primary driver for the sedimentary dynamics at the core site (Razik *et al.*, 2015).

In contrast, the subtropical eastern South Atlantic hosts one of the most intense upwelling zones in the world, the Benguela Upwelling System (BUS). At present, the northern BUS presents relatively higher productivity at the surface layers only near the coast (Siegfried *et al.*, 2019). The lower rate of nutrient flux to the euphotic zone farther offshore promotes considerably reduced surface primary productivity and lower vertical transport of carbon to the sea floor, reducing the impact on carbon benthic $\delta^{13}\text{C}$ (Mackensen *et al.*, 1993; Bordbar *et al.*, 2021). ODP Site 1264 was drilled in Walvis Ridge, chosen during Leg 208 as a promising site to record global ocean carbon chemistry and circulation changes without significant BUS influences (Zachos *et al.*, 2004).

The modern ocean circulation structure of the western and eastern sectors of the South Atlantic have quite similar deep water masses distributions (Fig. 13). At present, high $\delta^{13}\text{C}$ NADW is present between 1200 and 4000 m, and lower $\delta^{13}\text{C}$ AABW occupies abyssal depths below 4000 m (Stramma and England, 1999). At higher southern latitudes, NADW splits CDW into two parts: an upper (UCDW) and a lower (LCDW) branch (Stramma and England, 1999; Piola and Matano, 2019). During the last glacial period, high $\delta^{13}\text{C}$ values (~ 1.5 ‰) were centered at 1500 m, corresponding to the well-ventilated and shallower GNAIW (Duplessy *et al.*, 1988; Curry and Oppo, 2005; Lynch-Stieglitz *et al.*, 2007). Below (i.e., at depths > 2000 m), a pool of "old" and isotopically light carbon was present due to increased deep-water isolation and the accumulation of respired carbon (Curry and Oppo, 2005; Skinner *et al.*, 2010; Schmittner and Lund, 2015). The commonly termed Southern Component Water (SCW) has low $\delta^{13}\text{C}$ (~ -0.9 ‰) and occupies deeper South Atlantic layers

because of intensified export of AABW from the Southern Ocean (Curry and Oppo, 2005). Focusing on the western South Atlantic sector, (Curry and Oppo, 2005) suggest that GNAIW penetrated southward as far as 30°S latitude, while deeper SCW may have penetrated as far north as 60°N. These findings are consistent with previous nutrient reconstructions at 28°S, showing that a relative nutrient-depleted water mass was present during the LGM at 1500 m, above expanded, more nutrient-rich SCW (Oppo and Horowitz, 2000).

The glacial shoaling of this boundary between NADW and AABW might correspond to the vertical chemocline at depths of 2000 - 2500 m, a persistent feature of glacial water mass architecture in the Atlantic sector of the Southern Ocean during Pleistocene glacial periods (Hodell *et al.*, 2003) that can also be seen on the Southeastern Atlantic (Marchitto and Broecker, 2006).

4.1.3 Stable isotopic carbon composition

In this work, we present a new benthic $\delta^{13}\text{C}$ record combined with the published benthic oxygen isotope ($\delta^{18}\text{O}$) (de Almeida *et al.*, 2015) of piston core GL-854 (Fig. 14C and D). At least three shells of the epibenthic foraminifera *Cibicidoides wuellerstorfi* (> 150 μm) were handpicked using a binocular microscope and analyzed at the *Universitat Autònoma de Barcelona*, Spain, on a Finnigan MAT252 mass spectrometer with an automated carbonate device. Results are presented in parts per thousand versus the Vienna Pee Dee Belemnite (VPDB) scale. The $\delta^{13}\text{C}$ record of ODP Site 1264 is also based on *C. wuellerstorfi* (Bell *et al.*, 2014), which avoids biases due to distinct vital effects of different species.

4.1.4 GL-854 age model

The age model of the GL-854 core was obtained through a combination of three calibrated AMS ^{14}C ages (de Almeida *et al.*, 2015) and the visual alignment of our benthic $\delta^{18}\text{O}$ record to the global LR04 $\delta^{18}\text{O}$ stack (Lisiecki and Raymo, 2005) following the recommendations of Blaauw *et al.* (2018) and Lacourse and Gajewski (2020). Radiocarbon dating were measured on *Globigerinoides ruber* (white) shells at the National Ocean Science Accelerator Mass Spectrometer Facility (NOSAMS) at Woods Hole Oceanographic Institution (WHOI). The radiocarbon ages calibration is detailed in de Almeida *et al.* (2015).

The benthic $\delta^{18}\text{O}$ alignment was performed with the software AnalySeries (Paillard *et al.*, 1996). The age model allowed the estimation of a mean sedimentation rate of 4.3 cm/ka throughout the core, which therefore covers the period between ca. 4 and 772 kyr (Supplementary Fig. 1).

The age model for ODP Site 1264 is based on the *Cibicides* spp. $\delta^{18}\text{O}$ records are primarily used to map the mcd scale of Site 1267 onto Site 1264 to combine data to form a single continuous record based on the Site 1264 depth scale (Walvis Stack). The Walvis Stack $\delta^{18}\text{O}$ and Site 1264 were stratigraphically aligned to the LR04 benthic stack (Lisiecki and Raymo, 2005). Age controls from calcareous nannofossil and paleomagnetic reversal were used, producing an excellent general agreement with the $\delta^{18}\text{O}$ -derived age model. The original benthic isotopic data have a mean temporal resolution of approximately 5.15 kyr (Bell *et al.*, 2014). More details about ODP Site 1264 age model can be found in Bell *et al.* (2014).

4.1.5 RAMPFIT and spectral analysis

Quantitative time-series analyses are critical to support interpretations of long-term time-series data statistically. RAMPFIT is a statistical software valuable for quantifying and describing past climate transitions accurately in paleoclimatic records that are usually done visually (Mudelsee, 2000). It is based on the weighted least-squares method, and produces a ramp fitting to the record by estimating levels before and after a transition assuming a linear change between two change points in time and delivering a measure of their uncertainties (1 s.d.) based on bootstrap simulations. Each of the 10000 moving block bootstrap simulations (Mudelsee, 2014) uses randomly selected blocks of ramp regression residuals and assures robustness against (1) the presence of non-normal distributions and (2) the existence of serial dependence; both are typical paleoclimatic features that "plague" conventional climate time series analysis. This technique provides one ramp by each performed analysis giving two change points that occurred from a constant level before towards new constant values (i.e., in the y-axis) after the transition. However, oceanographic and climatic records do not necessarily follow this simplistic pattern and might contain multiple transitions, in which level changes across change points are out of the uncertainties and thus statistically relevant (Röthlisberger *et al.*, 2008). Therefore, the subjective selection of the search window for the

fit interval is relevant and might influence the result. Mean Knn-smoothing is a non-parametric trend estimation that calculates the mean over the k nearest neighbors by shifting a window across the time axis. Analyzing the knn-smoothed trend in our $\Delta\delta^{13}\text{C}_{\text{w-e}}$ record allows a first estimation of its general variability, providing a starting point to determine periods for brute-force inspection and search of transitions and ultimately define possible statistically-based change point locations.

We performed RAMPFIT analysis three times in our $\Delta\delta^{13}\text{C}_{\text{w-e}}$ record, applying a full search range each time over three subsections. It revealed a younger transition from the search range between 2.3 to 458 ka, a transition interval from the search range between 257 to 640 ka, and an older transition from the search range between 464 to 771 ka. These three ramps and six change points best fit the trends observed in our record, which can therefore be subdivided into four different phases (Fig. 14A). Changing the selected boundaries of the transition intervals did not lead to significantly altered change-point estimation results, confirming the robustness of the change-point regression model.

REDFIT spectral analysis (Schulz and Mudelsee, 2002) was performed to identify statistically significant periodicities on the GL-854 $\delta^{13}\text{C}$ and $\Delta\delta^{13}\text{C}_{\text{w-e}}$, Dome C Antarctic ice core sea-salt Na (ssNa; (Wolff *et al.*, 2006) and core MD08-2588 IRD count (Starr *et al.*, 2021) records (Fig. 15). We used the software PAST v4.03 (Hammer *et al.*, 2001). Setting different segment values for the analysis did not alter the significance of the main frequencies, suggesting robust spectral power (Fig. 16).

4.2 Results

4.2.1 Benthic $\delta^{13}\text{C}$ and zonal $\delta^{13}\text{C}$ gradient evolution

Our $\delta^{13}\text{C}$ record ranges from -0.33‰ to 1.49‰ , with the most depleted isotopic composition at ca. 263 ka (MIS 8) and most enriched at ca. 499 ka (MIS 13) (Fig. 14C). The average value is 0.7‰ . The $\delta^{13}\text{C}$ value at the top of the core is 1.1‰ , in good agreement with the modern NADW $\delta^{13}\text{C}$ end-member value (Kroopnick, 1985). The largest variation present in our record corresponds to the enrichment of $\sim 1.4\text{‰}$ during the MIS 8/7 transition. Similarly, the end of the MIS 9 toward glacial minima during MIS 8 displays a drastic reduction in the $\delta^{13}\text{C}$ values from 1.1‰ to -0.33‰ , also shifting by $\sim 1.4\text{‰}$. The $\delta^{13}\text{C}$

transitions during glacial Terminations are more abrupt and have higher amplitude after the MBT than before. The isotopic shift through Termination V (MIS 12/11, ~ 1.0 ‰) marks the transition toward the first intense interglacial after the MBT and corresponds to the first abrupt G-IG $\delta^{13}\text{C}$ shift. However, the $\delta^{13}\text{C}$ differences between glacial minima and interglacial maxima are generally higher before the MBT.

The benthic zonal $\delta^{13}\text{C}$ gradient between both sides of the South Atlantic basin was calculated by (1) interpolating the highly resolved series (GL-854; Fig. 14C) to the time scale of the more coarsely resolved series (ODP Site 1264; Fig. 14C) and then by (2) subtracting the isotopic values of the interpolated GL-854 record from the ODP 1264 series, that is, $\Delta\delta^{13}\text{C}_{\text{w-e}} = \delta^{13}\text{C}_{\text{GL-854}} - \delta^{13}\text{C}_{\text{ODP 1264}}$ (Fig. 14A).

The $\Delta\delta^{13}\text{C}_{\text{w-e}}$ (Fig. 14A) record ranges from -0.66 ‰ to 0.84 ‰, with the lowest isotopic gradient at ca. 300 ka (MIS 8) and the highest at ca. 252 ka (MIS 7). The average of the $\Delta\delta^{13}\text{C}_{\text{w-e}}$ record is 0.16 ‰. G-IG variability is well marked in the record; minimum $\Delta\delta^{13}\text{C}_{\text{w-e}}$ values (i.e., reduced western-eastern $\delta^{13}\text{C}$ gradient) seem to be a persistent feature when fully cold glacial conditions are established. Through most of the $\Delta\delta^{13}\text{C}_{\text{w-e}}$ record, the gradient is higher during interglacial periods, with an amplitude closely matching the modern gradient of 0.13 ‰ between these sites. The gradient between both margins is inverted during cold glacial stages (e.g., MIS 12 and MIS 8), driven by ^{13}C -depleted excursions in the GL-854 $\delta^{13}\text{C}$ record. RAMPFIT-calculated change points identify the transitions that separate the long-term $\Delta\delta^{13}\text{C}_{\text{w-e}}$ variability into four main phases: (I) ca. 800-630 ka, with low $\Delta\delta^{13}\text{C}_{\text{w-e}}$ average values of 0.01 ± 0.06 ‰; (II) ca. 630-465 ka, with intermediate values of 0.23 ± 0.054 ‰, (III) ca. 460-300 ka, with low $\Delta\delta^{13}\text{C}_{\text{w-e}}$ values of 0.00 ± 0.08 ‰; (IV) ca. 300 ka to 4.4 ka, with the highest level of 0.31 ± 0.06 ‰.

4.3 Discussion

4.3.1 Atlantic deep-water seesaw: long-term trends in AMOC strength

Past variations in AMOC strength would have substantially affected sites between 1000 and 2500 m water depth, increasing the $\delta^{13}\text{C}$ values due to pronounced southward penetration of isotopically heavier NADW (Muglia and Schmittner, 2021). In order to verify if the site of core GL-854 does register variations on NADW, we have compared its benthic

$\delta^{13}\text{C}$ record to that of ODP Site 980, at 2180 m water depth and 55°N, in the vicinity of the production sites, and commonly used to represent the end-member value of mid-depth NADW (Flower *et al.*, 2000). The GL-854 $\delta^{13}\text{C}$ record shows similar downcore variability and absolute values to ODP Site 980, including similar Holocene $\delta^{13}\text{C}$ values (Fig. 14C). Punctual discrepancies (i.e., lower isotopic values during MIS 5 off Brazil) are likely related to differences in temporal resolution between the records and to short-lived local effects. This suggests that the NADW signal has been carried to the Brazilian site throughout the last ca. 800 ka and allows us to assume that our $\delta^{13}\text{C}$ record represents NADW variability in the South Atlantic.

To investigate the NADW zonal distribution within the South Atlantic, we look at the zonal $\delta^{13}\text{C}$ gradient between the DWBC and DEBC (i.e., $\Delta\delta^{13}\text{C}_{\text{w-e}}$, Fig. 14A) calculated from the GL-854 $\delta^{13}\text{C}$ record minus that of ODP Site 1264 (Fig. 14C). The DWBC in the WSA bifurcates twice, once near the equator and afterward at 22°S, forming NADW eastward zonal flows (Stramma and England, 1999). In present-day conditions, the DWBD presents a slightly ^{13}C -enriched NADW signal than at the eastern margin, characteristic of more ventilated waters (Fig. 13B and C). Also, there is no vertical change in the $\delta^{13}\text{C}$ profiles from both sides of the basin between 2000 and 3000 m water depth (Fig. 13F), which implies that the 300-m depth difference between the two cores is inferred to be irrelevant to explain the discrepancies between the records, in particular during interglacial periods. Therefore, positive values in $\Delta\delta^{13}\text{C}_{\text{w-e}}$ during interglacial periods must represent an enhanced influence of better-ventilated waters of higher NADW $\delta^{13}\text{C}$ on the WSA. Hence, changes in our $\Delta\delta^{13}\text{C}_{\text{w-e}}$ record are assumed to result from changes in the zonal $\delta^{13}\text{C}$ distributions within the same water mass between both margins of the South Atlantic.

The $\Delta\delta^{13}\text{C}_{\text{w-e}}$ record shows a drastically reduced gradient consistently during glacial stages, to the point that it is reversed during fully glacial conditions throughout most of the record (e.g., MIS 4, MIS 8, MIS 10, MIS 12, MIS 16, and MIS 18), except during MIS 6 and MIS 14 (Fig. 14B). This pattern likely responds to a configuration of reduced ocean circulation state during glacial periods, with less well-ventilated waters reaching both sites, decreasing the $\Delta\delta^{13}\text{C}_{\text{w-e}}$ record. Although the first negative excursion in the record appears during the glacial stage MIS 16, this glacial dynamic becomes more marked and regular from the super-glacial stage MIS 12. The low $\Delta\delta^{13}\text{C}_{\text{w-e}}$ values during MIS 16 may represent

the early deep-water response to the first manifestation of the 100-ky cycle pacing of G-IG transitions (Hays *et al.*, 1976; Imbrie *et al.*, 1993; Mudelsee and Schulz, 1997; Diekmann and Kuhn, 2002), which reached its full strength after MIS 12 (Berger and Wefer, 2003). The decrease in NADW production expected during extremely cold climates such as MIS 12 might have promoted a particularly marked AMOC slowdown (Droxler *et al.*, 2003; Vázquez Riveiros *et al.*, 2013), which promoted a shallower boundary between NCW and SCW and increased the SCW influence up to ~ 2200 m depths. A similar pattern is present in the following glacial periods, MIS 10 and MIS 8.

Therefore, we interpret our $\Delta\delta^{13}\text{C}_{\text{w-e}}$ G-IG variability as a deep-water response sensitive to depth variability of the interface between the shallow and deep cells of the AMOC related to different oceanic circulation states. However, since $\Delta\delta^{13}\text{C}_{\text{w-e}}$ is based on a gradient, dependent on the resolution, interpolation methods, and age model construction of each $\delta^{13}\text{C}$ record, care must be taken to avoid over-interpretation of the signals.

RAMPFIT results reveal longer-term trends in the $\Delta\delta^{13}\text{C}_{\text{w-e}}$ record beyond G-IG variability. Six change points subdivided our record into four distinct statistically significant phases (Fig. 15A); the transitions between them are out of the error bars, attesting to the high sensibility of our record to east-west asymmetry in the deep ocean ventilation. Relatively higher $\Delta\delta^{13}\text{C}_{\text{w-e}}$ values respond to a more pronounced ^{13}C -enriched NADW signal delivered to the WSA rather than to the eastern margin. Therefore, we interpret the gradient increase after ca. 300 ka (phase IV, with the highest gradient values) as NADW intensification probably associated with the onset of vigorous AMOC after the MBT (Caley *et al.*, 2012).

The latitudinal gradient based on the $\delta^{13}\text{C}_{\text{DIC}}$ of stack representative of northern and southern component waters (Barth *et al.*, 2018) composed of several marine cores decreases around 500 ka (Fig. 14B). A low latitudinal gradient implies enhanced southward penetration of NADW, while high values indicate enhanced northward penetration of AABW (Barth *et al.*, 2018). The RAMPFIT analysis reveals a change point on this record at the end of MIS 13, which agrees with a change point on the $\Delta\delta^{13}\text{C}_{\text{w-e}}$ record between phases II and III (Fig. 14A and B). However, the zonal gradient only intensifies after 300 ka, probably because RAMPFIT phase III is driven by very low glacial gradient levels during MIS 12, MIS 10, and MIS 8, as will be discussed below. Benthic foraminifera assemblage data from GL-854 indicate a major deep-water condition change occurred after MIS 8 (de Almeida *et al.*, 2015).

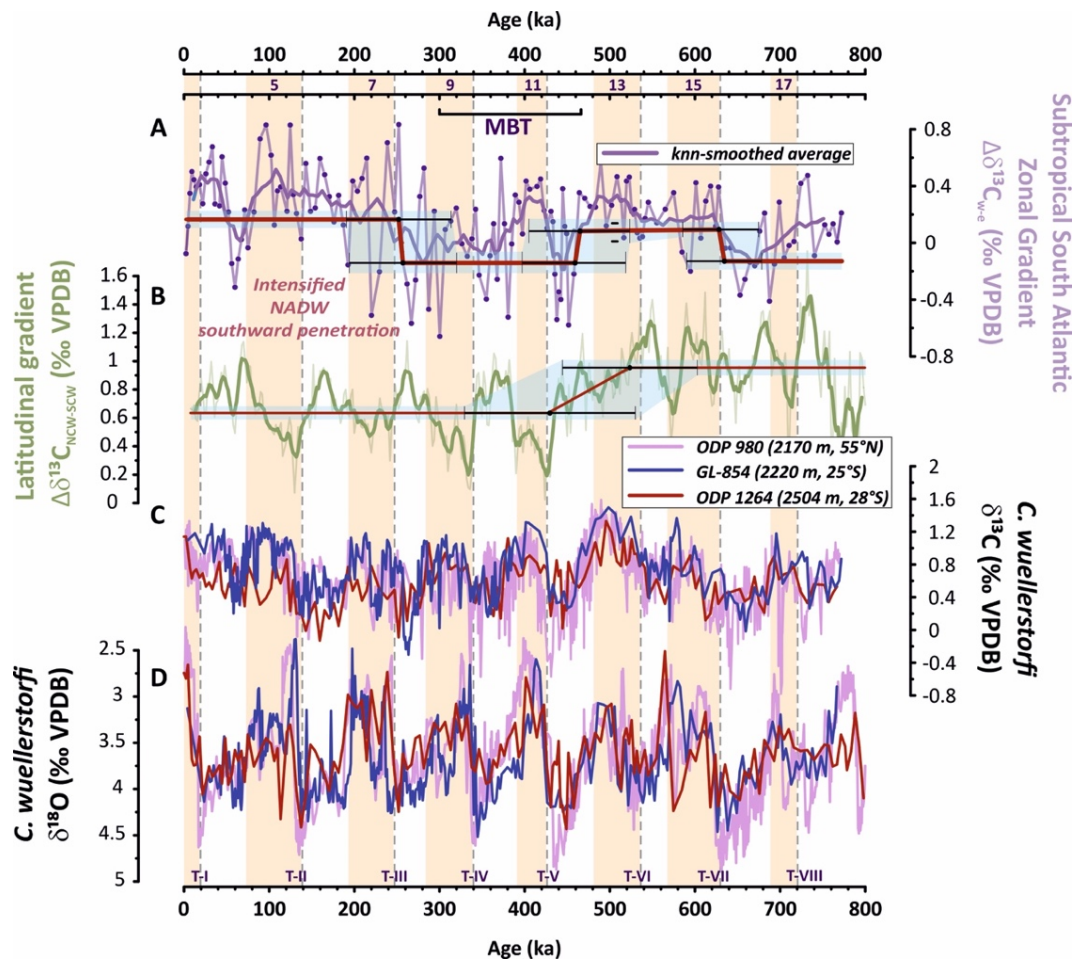
Declining abundances of *Bolivina* spp. coincide with an abrupt increase in *Globocassidulina crassa*, suggesting a transition from reduced bottom-water oxygenation towards stronger bottom currents of more oxygenated waters delivered to the site when $\Delta\delta^{13}\text{C}_{\text{w-e}}$ reaches its maximum absolute value of 0.84 ‰. In addition, the $\delta^{13}\text{C}$ gradient between the Atlantic and Pacific oceans, usually interpreted as an indicator of overturning strength, also intensifies after ca. 300 ka (Bard and Rickaby, 2009; Caley *et al.*, 2012). Moreover, our interpretation that the North Atlantic WBC intensified during phase IV is also supported by surface data evidence that indicates increased cross-equatorial energy transport, with more stable WBC after ca. 300 ka (Billups *et al.*, 2020).

The other identified phases can be related to previous studies discussing long-term circulation patterns oscillating between strong and weak states of AMOC throughout the last ca. 1200 ka, roughly across the MPT and the MBT. For example, Raymo *et al.* (1997) showed a relatively weaker NADW production and AMOC from 900 ka that intensified after MIS 12. Moreover, an increased vertical $\delta^{13}\text{C}$ gradient between the intermediate and deep ocean in the North Atlantic has been found during the same interval, which supports the hypothesis that the deep-water cells shoaled and mixed less in a weak circulation state (Hodell and Channell, 2016), with weaker NADW production and the northward expansion of the AABW (Pena and Goldstein, 2014). Although these findings agree with our phase I, phase II would correspond to an identified transitional period of global circulation reorganization after 650 ka (Schmieder *et al.*, 2000) that we associated with a relatively increased influence of better-ventilated NADW on the WSA. Evidence from modeling studies argues that the period corresponding to our phase III marks the transition after MIS 12 toward the post-MBT world with reduced AABW and enhanced NADW formation during interglacial periods associated with changes in Southern Ocean ventilation (Yin, 2013; Barth *et al.*, 2018). However, it is also related to intensified glacial conditions, which would have reduced our trend estimation to its lower value (see next discussion topic). Therefore, the zonal gradient dynamics proposed here are coherent with these findings regarding long-term trends in AMOC intensity over the last 800 ka, in the scope of circulation changes across the MBT (e.g., Schmieder *et al.*, 2000; Caley *et al.*, 2012; Barth *et al.*, 2018).

It is noteworthy that the phases of different AMOC modes in this study show features of the deep ocean circulation from the middle to late Pleistocene in unprecedented detail

from the WSA. The interpretation of this gradient contributes to our understanding of the transition between long-term AMOC modes, presenting oscillations of the deep-water seesaw that would explain the different transition timings reported in the literature of important climatic events such as the MBT. Still, a question remains: Which mechanism controlled the ocean dynamics that drove the long-term trends in the deep-water seesaw?

Figure 14 - Long-term RAMPFIT phases revealed in the $\Delta\delta^{13}C_{w-e}$ ($\delta^{13}C_{GL-854} - \delta^{13}C_{ODP\ 1264}$) record, showing that the subtropical zonal $\delta^{13}C$ gradient between the South Atlantic mid-depth sites increase after the Mid-Brunhes Transition (MBT). A) $\Delta\delta^{13}C_{w-e}$ (light purple line) with eight-point knn-smoothed average (dark purple line); RAMPFIT results (solid red lines) are displayed with their respective uncertainties (light blue shaded area). B) Latitudinal gradient ($\Delta\delta^{13}C_{NCW-SCW}$, thin light green line) and three-point running average (thick light green line) of the difference between the Northern and Southern Component Water (NCW and SCW, respectively) stacks (Barth *et al.*, 2018). C) $\delta^{13}C$ (‰ VPDB) and D) $\delta^{18}O$ (‰ VPDB) of cores GL-854 (this study; blue), ODP Site 1264 (red) and North Atlantic ODP Site 980 (dark pink). ODP Site 980 represents the end-member of the upper portion of the North Atlantic Deep Water (NADW) in the vicinity of North Atlantic production sites. The comparison between them shows that the NADW signal is carried by the Deep Western Boundary Current (DWBC) to the western South Atlantic. Red bars highlight interglacial periods and dashed lines mark glacial-interglacial transitions over the last ca. 800 ka (Terminations (T) I to VIII are indicated). All records are shown against age (ka)



4.3.2 Antarctic sea-ice controls on Atlantic deep-water geometry

The Southern Ocean is an essential climate system component as it connects the deep ocean carbon pool with the atmosphere, hosting critical mechanisms acting on G-IG time scales (Sigman and Boyle, 2000; Sigman *et al.*, 2010). Numerical climate model simulations have shown that the expansion of Antarctic sea ice enhanced deep-water stratification during glacial periods, which could have contributed to glacial CO₂ drawdown (Marzocchi and Jansen, 2019). Extended sea ice is thought to have enhanced the formation of denser AABW by intensified salt rejection during sea-ice formation, hindering the mixing with NADW (Paillard and Parrenin, 2004; Bouttes *et al.*, 2010; Jansen and Nadeau, 2016; Jansen, 2017). In addition, the sea ice acted as a lid, reducing air-sea exchange and isolating deep waters (Stephens and Keeling, 2000), thus controlling CO₂ outgassing. The impact of the latitudinal advance of the sea ice on deep-water cells can effectively decouple AABW and NADW, promoting the aging of abyssal water masses due to a drastic reduction in deep-water ventilation that alters the deep-water seesaw (Ferrari *et al.*, 2014; Nadeau *et al.*, 2019). In this context, we consider the Antarctic sea ice as the primary driver controlling the deep-water seesaw in the Atlantic that governs our $\Delta\delta^{13}\text{C}_{\text{w-e}}$ record, promoting the observed long-term trends in AMOC.

Relatively colder temperatures were registered in the Antarctic EPICA Dome C δD record during the lukewarm interglacials, which may have allowed pronounced sea ice build-up due to reduced interglacial melting (Fig. 15C and d; Jouzel *et al.*, 2007; Wolff *et al.*, 2006). Consequently, the sea-salt-related Na (ssNa) levels, a proxy for Antarctic sea-ice extent, indicate a higher extension during cold G-IG periods before the MBT, leading to a relatively greater volume of AABW formation (Fig. 15C; Ferrari *et al.*, 2014; Barth *et al.*, 2018). Notably, this pattern is particularly evident during RAMPFIT phase I, characterized by a reduced zonal gradient. Furthermore, ssNa glacial levels decrease from enhanced interglacial melting during MIS 15, which results in intermediate G-IG sea ice coverage throughout phase II. Although these changes in sea ice coverage are subtle, they could explain the observed $\Delta\delta^{13}\text{C}_{\text{w-e}}$ differences between phases I and II. It is worth noting that the transition toward increased NADW influence in the deep Atlantic after the MBT is associated with the change point in the $\Delta\delta^{13}\text{C}_{\text{w-e}}$ record during MIS 12 and in the meridional gradient (Fig. 14B and C). However, reduced glacial sea ice extent and enhanced interglacial melting can be observed only later at phase IV after ssNa reached the largest extent at the

end of phase III (at MIS 8), followed by $\Delta\delta^{13}\text{C}_{\text{w-e}}$ higher values. Although the relation between ssNa and $\Delta\delta^{13}\text{C}_{\text{w-e}}$ record can be established and provide insights to explain our RAMPFIT phases, it is difficult to fully interpret due to ssNa proxy limitations and perhaps due to the high-frequency variability of the record.

ssNa mostly originated from winter sea ice formation rather than from open ocean waters (Wolff *et al.*, 2003), and therefore, we would expect a coupled response between Antarctic temperatures and sea-ice extension (Fig. 15C and D). However, this relation is reduced under maximum glacial conditions due to a declining proxy response to the increased distance from the source, making sea-salt aerosol concentration decay when carried by wind through higher distances (Röthlisberger *et al.*, 2008, 2010). Thus, the ssNa proxy becomes saturated due to the limited sea salt input when sea ice extent continuously expands and only a small fraction of extra salt reaches the Dome C site. The ssNa aerosol also changes its residence time in response to the hydrological cycle variations, which reduces its fluxes particularly during interglacial periods (Petit and Delmonte, 2009). All these factors limit our interpretation of extreme G-IG values of ssNa, challenging the establishment of an accurate relationship between our zonal gradient and sea ice.

However, the oscillatory behavior of the RAMPFIT phases, particularly phases III and IV, also corresponds well with detrital ice-rafted debris (IRD) particle deposition variability sourced from Antarctica in the Agulhas Plateau region over the studied period (Fig. 15C; Starr *et al.*, 2021). Increased icebergs appearing at this location, far from the source, would demand the expansion of colder atmospheric and sea surface temperatures (SST) and favorable oceanographic conditions for transport and deposition at this latitude (Starr *et al.*, 2021). High IRD counts agree with high ssNa values showing that higher IRD deposition and sea ice are coupled to extreme full glacial conditions (Fig. 15C). There is a remarkable fit between periods of higher IRD and ssNa with periods of negative excursions present in our $\Delta\delta^{13}\text{C}_{\text{w-e}}$ record. The low $\Delta\delta^{13}\text{C}_{\text{w-e}}$ phases I ($0.01 \pm 0.06 \text{ ‰}$) and III ($0.00 \pm 0.08 \text{ ‰}$) are coeval with periods of relatively larger IRD deposition, which is related to the increased influence of AABW to shallower depths (Fig. 17A and C). Intermediate phase II ($0.23 \pm 0.054 \text{ ‰}$) is coeval with periods of intermediate levels of IRD, associated with a relatively increasing influence of NADW toward intermediate levels and reduced influence of AABW (Fig. 17B). The enhanced gradient during RAMPFIT phase IV ($0.31 \pm 0.06 \text{ ‰}$)

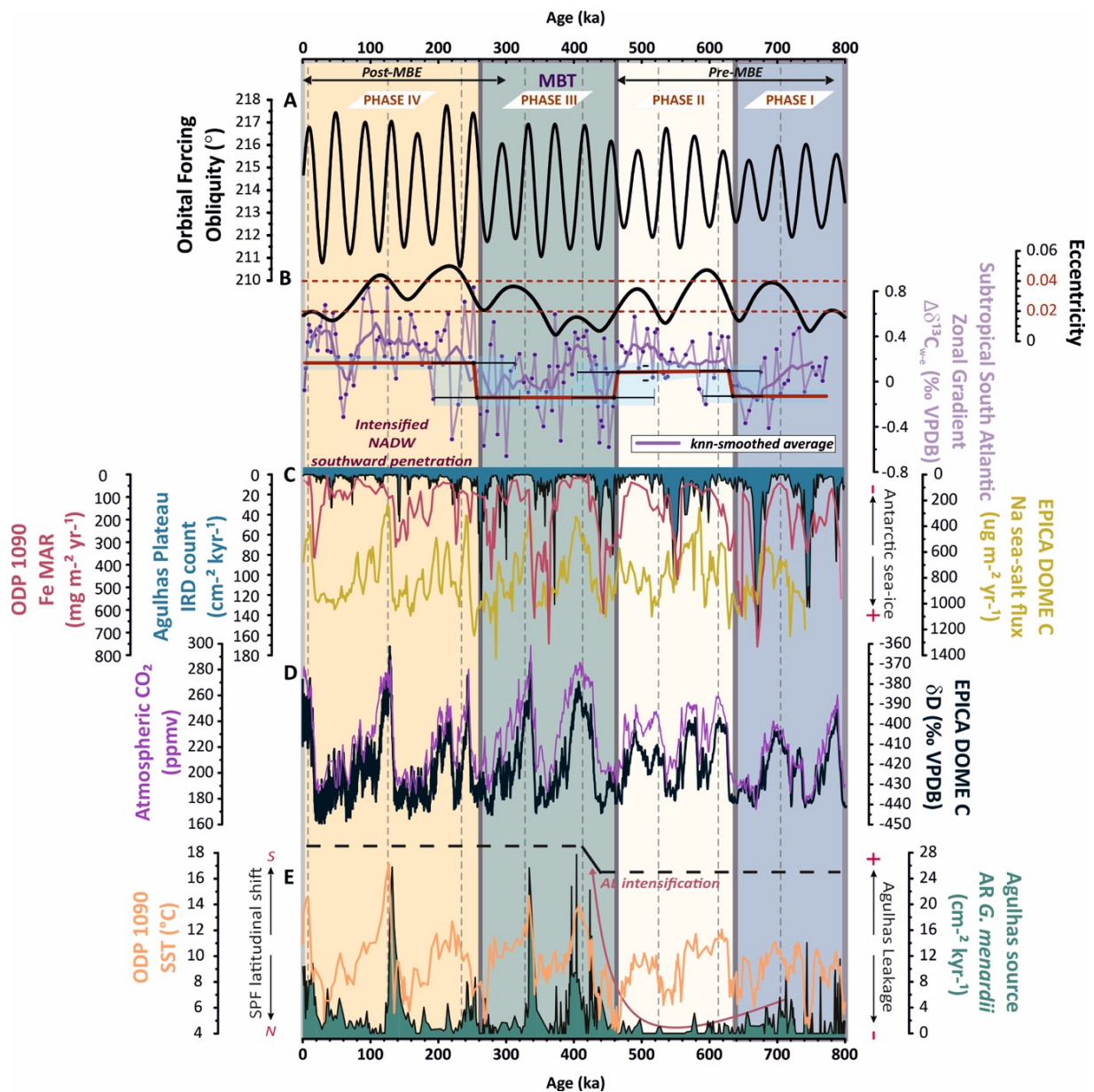
is coeval with periods of drastic reduction IRD deposition, which decreased AABW formation that promoted the NADW intensification (Fig. 17D).

The persistence of the extremely colder glacial Southern Ocean during MIS 12, MIS 10 and MIS 8 may have increased AABW production, promoting negative excursions in the $\Delta\delta^{13}\text{C}_{\text{w-e}}$ record that explain the lowest values of phase III (Fig. 17C). Enhanced surface productivity by increased iron deposition in the Southern Ocean during these glacial periods intensified the biological pump (Fig. 15C; Martin, 1990; Martínez-García *et al.*, 2011). It increased vertical transport from the surface to the bottom of ^{13}C -depleted carbon, lowering the AABW $\delta^{13}\text{C}$ end member signature. Increased AABW production reduced the mixing with NADW, shallowing the boundary between the AMOC cells to depths close to GL-854 and ODP Site 1264, decreasing the $\Delta\delta^{13}\text{C}_{\text{w-e}}$ seen in RAMPFIT phase III. A similar scenario may have occurred during MIS 16 and MIS 18, explaining RAMPFIT phase I. We, therefore, assume that enhanced low- $\delta^{13}\text{C}$ AABW influence reaching shallower depths promoted a larger decrease in the $\Delta\delta^{13}\text{C}_{\text{w-e}}$ during intense glacial stages than expected if its variability was exclusively responding to the NADW end member influence.

The influence of buoyancy flux variations in the North Atlantic also needs to be accounted for since it might contribute to increase NADW production (Caley *et al.*, 2014; Weijer *et al.*, 2002). The rate of Indo-Atlantic water exchanges, namely the Agulhas Leakage (AL), contributes to salt build-up in the Atlantic that strengthens the AMOC (Gordon, 1986; Broecker *et al.*, 1990; Biastoch *et al.*, 2015; Beal and Elipot, 2016). The salty warm waters from the Indian Ocean enter the South Atlantic through the tip of Africa and are transported by the upper limb of the AMOC toward the North Atlantic, ultimately favoring the formation of NADW (Beal *et al.*, 2011; Caley *et al.*, 2014). The extremely reduced accumulation rate of *G. menardii* in the Southeastern Atlantic is one evidence of the decreased influence of the AL between ca. 800-430 ka (phases I and II; Fig. 15E), which also supports our previous interpretations (Caley *et al.*, 2012). After ca. 430 ka, the AL reactivation is thought to have boosted NADW formation, peaking during glacial Terminations of the last four G-IG cycles (Peeters *et al.*, 2004; Caley *et al.*, 2012). However, the northward advances of the STF during cold MIS 12 and to its lowest latitude of the past 800 ka during MIS 10 (Bard and Rickaby, 2009) might have compensated for the AL contribution to NADW intensification during MIS 11 and MIS 9, which would explain the strong glacial characteristic present in our record during phase III. The AL intensification would explain the differences between

RAMPFIT phases I and III (Fig. 15A and C). A diminished Antarctic sea ice surface would regulate both the deep-water seesaw through the decreased formation of AABW (and thus increased NADW volume) and the AL through a more southward position of the STF (and thus increased NADW formation) (Becquey and Gersonde, 2002; Toggweiler *et al.*, 2006; Martínez-García *et al.*, 2009; Kemp *et al.*, 2010; Beal *et al.*, 2011; Caley *et al.*, 2012, 2014).

Figure 15 - Evolution of long-term oceanographic and climate records controlling the long-term trend in the deep-water seesaw. A) Obliquity ($^{\circ}$; Laskar *et al.*, 2004). B) $\Delta\delta^{13}\text{C}_{\text{w-e}}$ (light purple line) with 8-point knn-smoothed average (dark purple line); RAMPFIT results (solid red lines) are displayed with respective uncertainties (light blue shaded area). The background blue, light yellow, green, and dark yellow bars indicate RAMPFIT phases I, II, III, and IV, respectively. Black line: eccentricity Laskar *et al.*, 2004). C) Sea-salt Na flux (yellow line; Wolff *et al.*, 2006), Agulhas Plateau Ice-Rafted Debris (IRD) counts (dark blue shaded line; Starr *et al.*, 2021), and ODP Site 1090 Fe MAR (dark pink line; (Martínez-García *et al.*, 2011) records. D) EPICA Dome C δD and atmospheric CO_2 (black and purple lines, respectively; Jouzel *et al.*, 2007; Lüthi *et al.*, 2008). E) ODP Site 1090 sea-surface temperature (SST) (orange line; (Martínez-García *et al.*, 2009) and accumulation rate (AR) of typical Agulhas Leakage fauna (*Glorobotalia mernardii*) from ODP Site 1087 (green filled curve; Caley *et al.*, 2012). Dashed lines represent the glacial-interglacial Terminations. All records are presented against age (ka)



4.3.3 Orbital controls over the Antarctic sea ice

After exploring the mechanism connecting Antarctic sea-ice variability and the transitions between different phases of AMOC intensity, a question follows: which forcing is driving the substantial changes on sea ice capable of promoting these thresholds on circulation? We explore the effects of orbital forcing on promoting a combination of different insolation conditions at southern high-latitudes on the different phase intervals (Supplementary Fig. 3). The REDFIT spectral analyses (Schulz and Mudelsee, 2002) performed on GL-854 $\delta^{13}\text{C}$ and $\Delta\delta^{13}\text{C}_{\text{w-e}}$, Dome C ssNa and Agulhas Plateau IRD records reveal orbital spectral power in the obliquity (~ 40 ka) and eccentricity (~ 100 ka) domains with 90% of confidence level (Fig. 16), leading to the assumption that the combined effect of these forcings is influencing the Antarctic sea-ice variability.

Obliquity forcing exerts a predominant role in the high latitudes by controlling the received annual insolation energy, which has a particularly strong effect in the Southern Hemisphere due to the higher thermal capacity of larger ocean areas (Yin and Berger, 2012; Wu *et al.*, 2020). The insolation decreases (increases) under low-obliquity (high-obliquity) periods, decreasing (increasing) ice melting, which likely increases (reduces) the amount of sea ice (Paillard, 2021). This would explain why most negative excursions throughout the $\Delta\delta^{13}\text{C}_{\text{w-e}}$ record occurred under low obliquity (Fig. 15; Supplementary Figure 3). Mitsui and Boers (2022) discussed the obliquity effects on the climate system over the last 800 ka in the context of the MBT. They propose that the increasing amplitude of obliquity forcing might be responsible for enhancing the amplitude of G-IG cycles after 450 ka. We agree with this hypothesis, but we further suggest that eccentricity might have played an important role in this climate transition by modulating the high-latitude insolation.

Antarctic sea ice dynamics have a strong seasonal character, with a maximum extent during winter months (Wolff *et al.*, 2006). Obliquity drives seasonality, which varies in function of summer insolation at Southern high latitudes, and eccentricity controls the intensity and duration of the summer and winter seasons by modulation of precession (Hays *et al.*, 1976; Imbrie *et al.*, 1984; Paillard, 2021). Therefore, the eccentricity might have enhanced (reduced) the effect of obliquity during austral winter, regulating Antarctic sea ice (Yin, 2013). Similar spectral power between eccentricity and obliquity in both REDFIT results from $\Delta\delta^{13}\text{C}_{\text{w-e}}$ and IRD records support our assumption of the combined effect of these two forcings on sea ice (Fig. 16C and D). Our analysis further suggests that the impact

of obliquity on South Atlantic paleoceanography is intensified or weakened proportionally to the eccentricity value. Specifically, when eccentricity surpasses a threshold of 0.04 (or 0.02), the effects of obliquity on insolation are amplified (or reduced), which intensifies (reduces) winter insolation that reduces (enhances) sea ice extent (Supplementary Fig. 3). These findings are consistent with previous research by Lessa *et al.* (2019), who identified similar thresholds from surface water observations on core GL-854.

RAMPFIT phases II and IV occur when eccentricity values are above the threshold of 0.04, which boosts seasonal insolation, reducing the sea ice. On the other hand, RAMPFIT phases I and III occur when eccentricity reaches below the threshold of 0.02. It is important to consider the transience of the climate system associated with the accumulated energy over time, particularly in the Southern Hemisphere. Even though low $\Delta\delta^{13}\text{C}_{\text{w-e}}$ phases I and III comprise intervals in which eccentricity levels were above 0.02 (730-660 ka and 350-260 ka), they occurred after an interval with nearly two eccentricity cycles of values lower than 0.02 (800-730 ka and 460-350 ka). In this scenario, longer periods of low eccentricity values may have dampened the effect of increasing eccentricity to values above 0.02 on insolation, which did not add enough energy to cause substantial changes in sea ice. Only when eccentricity crosses the threshold of 0.04, it enhances insolation adding enough energy to cause changes at high latitudes to promote phases II and IV. Eccentricity values below 0.02 also occur during the major decrease in $\Delta\delta^{13}\text{C}_{\text{w-e}}$ during MIS 4 when average $\Delta\delta^{13}\text{C}_{\text{w-e}}$ values are high through phase IV. From MIS 4 toward the Holocene, eccentricity values are below 0.02, hence we expect decreased insolation received at high latitudes through the added effect of amplified low obliquity forcing at MIS 4. This orbital configuration at MIS 4 could have promoted another change point on circulation to reduced AMOC toward the present day, although our record cannot confirm it.

Figure 16 - REDFIT spectral analysis results performed in A) GL-854 $\delta^{13}\text{C}$, B) Dome C ssNa, C) $\Delta\delta^{13}\text{C}_{\text{w-e}}$, and D) Agulhas Plateau IRD records reveal relevant spectral power (Y axes) above the 90% confidence intervals in the obliquity and eccentricity frequency domains (X axes). Confidence level base lines (green and orange) and significant spectral periodicities are indicated

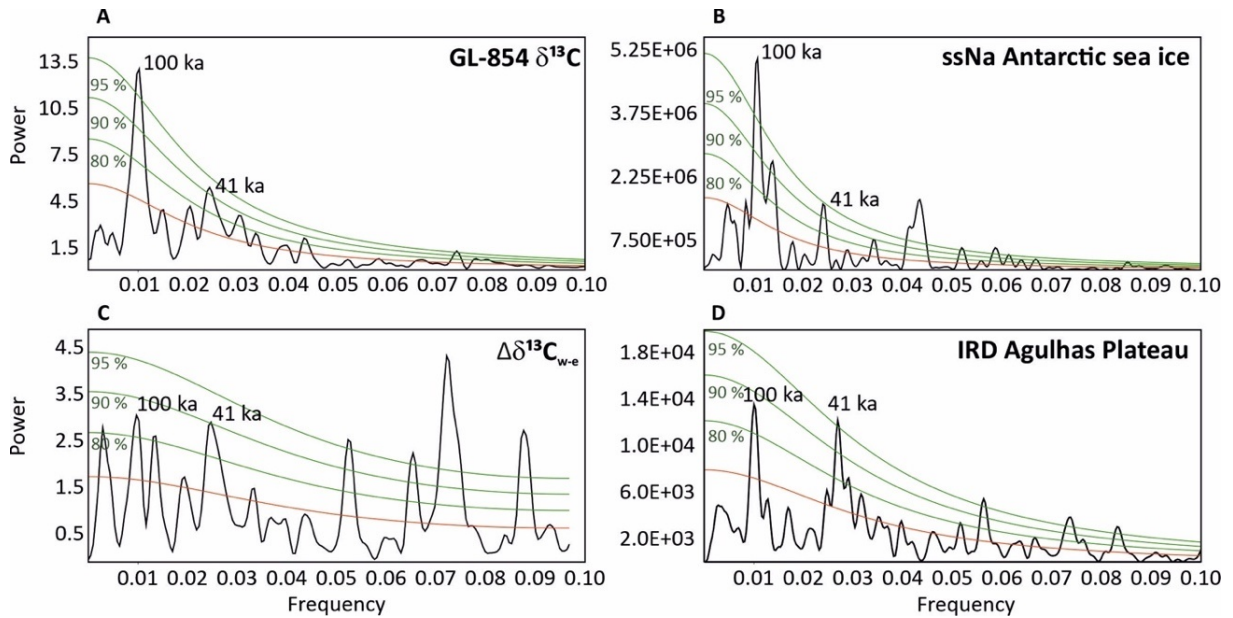
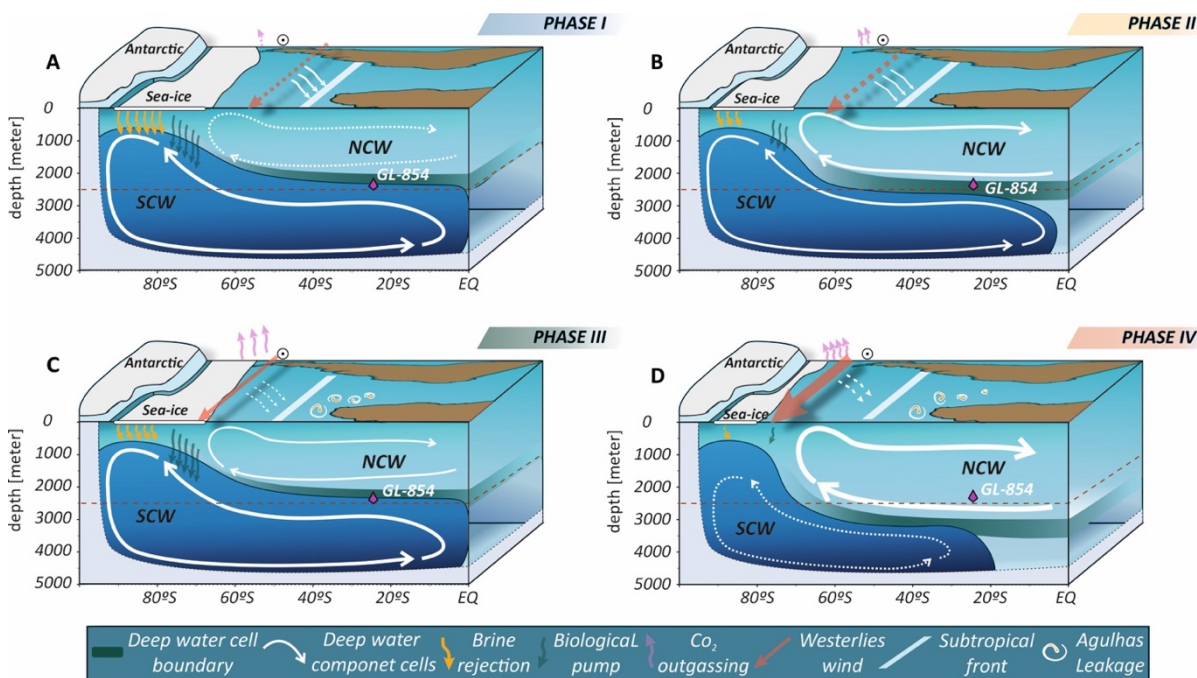


Figure 17 - Schematic representation of the main processes resultant of Antarctic sea ice extent variability through RAMPFIT phases A) I, B) II, C) III, and D) IV. Phases II and IV show similar scenarios with reduced sea ice extent, decreased brine rejection, and hence reduced Antarctic Bottom Water (AABW) formation. Reduced sea ice extent also promotes the southward latitudinal displacement of the Westerlies and subtropical front, increasing Agulhas Leakage (AL) that contributes to increasing North Atlantic Deep Water (NADW) production. Higher interglacial sea-ice melting and the AL reactivation after MIS 12 would explain the main difference between phases II and IV that led to more extended NADW southward penetration during phase IV. RAMPFIT phases I and III show increased glacial sea ice extent, enhanced brine rejection and increased Antarctic Bottom Water (AABW) formation. During these phases, very low AABW $\delta^{13}\text{C}$ values are due to the enhanced biological pump, and AABW penetrates further north, reaching up to 2200 m depth, reducing $\Delta\delta^{13}\text{C}_{\text{w-e}}$. The main difference between phases I and III is related to the AL intensification during phase III. In this phase, the AL effect on NADW during MIS 11 and MIS 9 may have been compensated by the intense glacial stages at MIS 12 and MIS 10. The vertical movements of the boundary between NADW and AABW are represented. Combined, these processes drive substantial changes in deep-water properties and formation, affecting Atlantic Meridional Overturning Circulation. Diagrams and symbols are described in the figure. Darker and lighter background colors represent denser and less dense deep-water cells, respectively of AABW and NADW



4.4 Conclusions

Our study presents a new subtropical benthic foraminiferal $\delta^{13}\text{C}$ record from sediment core GL-854 collected from the Brazilian margin at mid-depth (2200 m), covering the last ca. 800 ka. Core GL-854 is ideally located for investigating past G-IG NADW variability in the South Atlantic basin. We compare this record to ODP Site 1264 $\delta^{13}\text{C}$ to calculate a zonal benthic foraminifera gradient ($\Delta\delta^{13}\text{C}_{\text{w-e}}$) record between DWBC and

DEBC, providing insights into past NADW variability in the South Atlantic. Our zonal gradient increases (decreases) in response to the increased influence of NADW (AABW), recording variations between different AMOC states.

RAMPFIT trend estimations reveal an oscillatory behavior between weak and strong AMOC modes, highlighting the sensibility of our proxy to vertical movements of the boundary between NADW and AABW. The $\Delta\delta^{13}\text{C}_{\text{w-e}}$ increase after ca. 300 ka (phase IV) points to enhanced southward penetration of NADW that preferentially carries a modified signal through the DWBC towards the WSA instead of towards the eastern side of the basin. We attribute it to the AMOC intensification after the MBT, which does not exclusively respond to the NADW, but the enhanced contribution of low glacial AABW $\delta^{13}\text{C}$ to depths close to 2200 m between MIS 12 and MIS 8 likely also played a role. This suggests that both AMOC cells were more intense after the MBT. The contribution of AL reactivation after the MBT (our phase III) is possibly compensated by the strong glacial character of the $\Delta\delta^{13}\text{C}_{\text{w-e}}$ record, which prevented the expression of enhanced NADW production in our gradient during MIS 11 and MIS 9, and might have promoted the aforementioned later response after ca. 300 ka. Our $\Delta\delta^{13}\text{C}_{\text{w-e}}$ record mainly responds to the long-term patterns in the deep-water seesaw, revealing different AMOC states over the last ca. 800 ka, driven by variations in the AABW formation rate, ultimately affecting the NADW and the $\delta^{13}\text{C}$ distribution in the Atlantic (Buizert and Schmittner, 2015).

The major control behind the deep-water seesaw dynamic is ascribed to Antarctic sea-ice variability. During periods of lower (higher) sea ice, reduced (enhanced) brine rejection diminished (intensified) AABW formation, decreasing (increasing) deep stratification (Paillard and Parrenin, 2004; Bouttes *et al.*, 2010). This has a direct impact on AABW and NADW mixing within the Atlantic, enhancing (reducing) the southward penetration of NADW that boosted (reduced) AMOC intensity and deepened (shallowed) the boundary between these deep-water cells. Therefore, expansion and contractions in sea ice allowed the establishment of four different AMOC phases due to its controls in the deep-water seesaw that changed Atlantic water mass geometry. We agree with the hypothesis that in the G-IG time scale, a vigorous AMOC state would demand reduced Southern Ocean sea ice (Ferrari *et al.*, 2014; Nadeau *et al.*, 2019).

Spectral analysis supports an orbital influence over the Antarctic sea ice propagated from high latitudes toward South Atlantic subtropical regions by exercising controls over the deep-water seesaw. The orbitally triggered mechanism is controlled by the combined effects of obliquity and eccentricity forcing the seasonal insolation, mainly regulating the build-up of sea ice during austral winter. Minimum (0.02) and maximum (0.04) threshold values of eccentricity are critical in amplifying or diminishing the obliquity effects at high latitudes. The synergic effect of the obliquity when eccentricity crosses these thresholds establishes specific insolation configurations that regulate the sea ice extent and promote the transitions between our RAMPFIT phases. Lower $\Delta\delta^{13}\text{C}_{\text{w-e}}$ phases I and III are established under low obliquity when eccentricity is maintained below the threshold of 0.02, while higher phases II and IV are established under high obliquity when eccentricity crosses values of 0.04. We argue that these phases refer to discrete states of the Late Pleistocene deep-water circulation and climate system (Schmieder *et al.*, 2000; Barth *et al.*, 2018), driven by the transitions among the various combinations of insolation conditions (Yin, 2013).

Near-200 ka cycles have been previously documented in paleoclimate records, usually ascribed to a 173-ka modulation of the obliquity cycle (Westerhold *et al.*, 2005; Boulila *et al.*, 2011; Huang *et al.*, 2021) or interpreted either as a harmonic frequency of the 400-ka cycle or as a double 100-ka cycle (Hilgen *et al.*, 2015). Considering the eccentricity variations over the last 800 ka, major transitions should occur nearly every two eccentricity cycles, i.e., related to long-term increasing trends from minimum to maximum eccentricity and vice versa. Although these low frequencies are relatively too weak to be identified by spectral analysis under untreated data, the periodicity of the RAMPFIT phases is close to a 200-ka-like cycle. It would agree with recent findings revealing a ~ 200 ka eccentricity cycle for the first time accounting for it as a component of the eccentricity forcing (Hilgen *et al.*, 2020). Therefore, our orbital hypothesis and related periodic oscillations between different AMOC modes would be coherent with the 200-ka cycle eccentricity component despite the relation being speculative.

We have proposed a framework exploring the role of the deep-water seesaw in sustaining orbitally-triggered variations on Antarctic sea ice that significantly impact the oceanic carbon cycle. Our proposed mechanism connects the sea ice and ocean-atmosphere dynamics to deep-water geometry within the South Atlantic basin, which ultimately may have contributed to climate change across the MBT. Despite these AMOC modes and

transitions probably having an orbital nature, the internal mechanisms in response to insolation forcing play a crucial role in propagating orbital effects on the climate (Caley *et al.*, 2012; Yin, 2013; Barth *et al.*, 2018). The explored South Atlantic controls on deep-water circulation might be responsible for an unclear MBT signal in North Atlantic climate records (Candy and McClymont, 2013). We further suggest that our RAMPFIT phases could possibly be related to the paleoceanographic changes throughout the shift from dominant 41-ka glacial-interglacial cycles to longer 100-ka cycles across the Mid-Pleistocene Transition (MPT; Hays *et al.*, 1976; Pisias and Moore, 1981). Although longer records need to be used to establish a better relation with the MPT, our interpretations would also converge with interpretations showing major AMOC transitions occurring across this event (Schmieder *et al.*, 2000; Pena and Goldstein, 2014; Kim *et al.*, 2021). Furthermore, our findings are relevant for better understanding the internal climate responses and feedbacks in a significantly reduced sea ice expected in a global warming scenario.

References

- Bard, E., Rickaby, R.E.M., 2009. Migration of the subtropical front as a modulator of glacial climate. *Nature* 460, 380–383. <https://doi.org/10.1038/nature08189>.
- Barth, A.M., Clark, P.U., Bill, N.S., He, F., Pisias, N.G., 2018. Climate evolution across the Mid-Brunhes Transition. *Climate of the Past* 14, 2071–2087. <https://doi.org/10.5194/cp-14-2071-2018>.
- Beal, L.M., De Ruijter, W.P.M., Biastoch, A., Zahn, R., Cronin, M., Hermes, J., Lutjeharms, J., Quartly, G., Tozuka, T., Baker-Yeboah, S., Bornman, T., Cipollini, P., Dijkstra, H., Hall, I., Park, W., Peeters, F., Penven, P., Ridderinkhof, H., Zinke, J., 2011. On the role of the Agulhas system in ocean circulation and climate. *Nature* 472, 429–436. <https://doi.org/10.1038/nature09983>
- Beal, L.M., Elipot, S., 2016. Broadening not strengthening of the Agulhas Current since the early 1990s. *Nature* 540, 570–573. <https://doi.org/10.1038/nature19853>.
- Becquey, S., Gersonde, R., 2002. Past hydrographic and climatic changes in the Subantarctic Zone of the South Atlantic – The Pleistocene record from ODP Site 1090. *Palaeogeogr Palaeoclimatol Palaeoecol* 182, 221–239. [https://doi.org/10.1016/S0031-0182\(01\)00497-7](https://doi.org/10.1016/S0031-0182(01)00497-7).
- Bell, D.B., Jung, S.J.A., Kroon, D., Lourens, L.J., Hodell, D.A., 2014. Local and regional trends in Plio-Pleistocene $\delta^{18}\text{O}$ records from benthic foraminifera. *Geochemistry, Geophysics, Geosystems* 15, 3304–3321. <https://doi.org/10.1002/2014GC005297>
- Berger, W.H., Wefer, G., 2003. On the dynamics of the ice ages: Stage-11 Paradox, mid-brunhes climate shift, and 100-ky cycle, in: *Geophysical Monograph Series*. pp. 41–59. <https://doi.org/10.1029/137GM04>

- Biastoch, A., Durgadoo, J. V., Morrison, A.K., van Sebille, E., Weijer, W., Griffies, S.M., 2015. Atlantic multi-decadal oscillation covaries with Agulhas leakage. *Nat Commun* 6, 10082. <https://doi.org/10.1038/ncomms10082>
- Billups, K., Vizcaíno, M., Chiarello, J., Kaiser, E., 2020. Reconstructing western boundary current stability in the North Atlantic Ocean for the past 700 kyr from Globorotalia truncatulinoides coiling ratios. *Paleoceanogr Paleoclimatol* 0–3. <https://doi.org/10.1029/2020PA003958>
- Blaauw, M., Christen, J.A., Bennett, K.D., Reimer, P.J., 2018. Double the dates and go for Bayes — Impacts of model choice, dating density and quality on chronologies. *Quat Sci Rev* 188, 58–66. <https://doi.org/10.1016/j.quascirev.2018.03.032>
- Bordbar, M.H., Mohrholz, V., Schmidt, M., 2021. The relation of wind-driven coastal and offshore upwelling in the Benguela Upwelling System. *J Phys Oceanogr* 51, 3117–3133. <https://doi.org/10.1175/JPO-D-20-0297.1>
- Boulila, S., Galbrun, B., Miller, K.G., Pekar, S.F., Browning, J. V., Laskar, J., Wright, J.D., 2011. On the origin of Cenozoic and Mesozoic “third-order” eustatic sequences. *Earth Sci Rev* 109, 94–112. <https://doi.org/10.1016/j.earscirev.2011.09.003>
- Bouttes, N., Paillard, D., Roche, D.M., 2010. Impact of brine-induced stratification on the glacial carbon cycle. *Climate of the Past* 6, 575–589. <https://doi.org/10.5194/cp-6-575-2010>
- Broecker, W.S., 1998. Paleocean circulation during the 1st deglaciation: A bipolar seasaw? *Paleoceanography* 13, 119–121.
- Broecker, W.S., Bond, G., Klas, M., Bonani, G., Wolfli, W., 1990. A salt oscillator in the glacial Atlantic? 1. The concept. *Paleoceanography* 5, 469–477. <https://doi.org/10.1029/PA005i004p00469>
- Buizert, C., Schmittner, A., 2015. Southern Ocean control of glacial AMOC stability and Dansgaard-Oeschger interstadial duration. *Paleoceanography* 30, 1595–1612. <https://doi.org/10.1002/2015PA002795>
- Caley, T., Giraudeau, J., Malaize, B., Rossignol, L., Pierre, C., 2012. Agulhas leakage as a key process in the modes of Quaternary climate changes. *Proceedings of the National Academy of Sciences* 109, 6835–6839. <https://doi.org/10.1073/pnas.1115545109>
- Caley, T., Peeters, F.J.C., Biastoch, A., Rossignol, L., van Sebille, E., Durgadoo, J., Malaizé, B., Giraudeau, J., Arthur, K., Zahn, R., 2014. Quantitative estimate of the paleo-Agulhas leakage. *Geophys Res Lett* 41, 1238–1246. <https://doi.org/10.1002/2014GL059278>
- Candy, I., McClymont, E.L., 2013. Interglacial intensity in the North Atlantic over the last 800 000 years: investigating the complexity of the mid-Brunhes Event. *J Quat Sci* 28, 343–348. <https://doi.org/10.1002/jqs.2632>
- Curry, W.B., Oppo, D.W., 2005. Glacial water mass geometry and the distribution of $\delta^{13}\text{C}$ of ΣCO_2 in the western Atlantic Ocean. *Paleoceanography* 20, 1–12. <https://doi.org/10.1029/2004PA001021>
- de Almeida, F.K., de Mello, R.M., Costa, K.B., Toledo, F.A.L., 2015. The response of deep-water benthic foraminiferal assemblages to changes in paleoproductivity during the Pleistocene (last 769.2 kyr), western South Atlantic Ocean. *Palaeogeogr Palaeoclimatol Palaeoecol* 440, 201–212. <https://doi.org/10.1016/j.palaeo.2015.09.005>
- Diekmann, B., Kuhn, G., 2002. Sedimentary record of the mid-Pleistocene climate transition in the southeastern South Atlantic (ODP Site 1090). *Palaeogeogr Palaeoclimatol Palaeoecol* 182, 241–258. [https://doi.org/10.1016/S0031-0182\(01\)00498-9](https://doi.org/10.1016/S0031-0182(01)00498-9)

- Droxler, A.W., Alley, R.B., Howard, W.R., Poore, R.Z., Burckle, L.H., 2003. Unique and exceptionally long interglacial marine isotope stage 11: Window into Earth warm future climate, in: *Geophysical Monograph Series*. pp. 1–14. <https://doi.org/10.1029/137GM01>
- Duplessy, J.C., Shackleton, N.J., Fairbanks, R.G., Labeyrie, L., Oppo, D., Kallel, N., 1988. Deepwater source variations during the last climatic cycle and their impact on the global deepwater circulation. *Paleoceanography* 3, 343–360. <https://doi.org/10.1029/PA003i003p00343>
- Eide, M., Olsen, A., Ninnemann, U.S., Johannessen, T., 2017. A global ocean climatology of preindustrial and modern ocean $\delta^{13}\text{C}$. *Global Biogeochem Cycles* 31, 515–534. <https://doi.org/10.1002/2016GB005473>
- Ferrari, R., Jansen, M.F., Adkins, J.F., Burke, A., Stewart, A.L., Thompson, A.F., 2014. Antarctic sea ice control on ocean circulation in present and glacial climates. *Proceedings of the National Academy of Sciences* 111, 8753–8758. <https://doi.org/10.1073/pnas.1323922111>
- Flower, B.P., Oppo, D.W., McManus, J.F., Venz, K.A., Hodell, D.A., Cullen, J.L., 2000. North Atlantic Intermediate to Deep Water circulation and chemical stratification during the past 1 Myr. *Paleoceanography* 15, 388–403. <https://doi.org/10.1029/1999PA000430>
- Gordon, A.L., 1986. Interocean exchange of thermocline water. *J Geophys Res* 91, 5037. <https://doi.org/10.1029/JC091iC04p05037>
- Hammer, O., Harper, D., Ryan, P., 2001. PAST: Paleontological Statistics Software Package for Education and Data Analysis. *Palaeontologia Electronica* 4, 1–9.
- Hays, J.D., Imbrie, J., Shackleton, N.J., 1976. Variations in the Earth's Orbit: Pacemaker of the Ice Ages. *Science* (1979) 194, 1121–1132. <https://doi.org/10.1126/science.194.4270.1121>
- Hilgen, F., Zeeden, C., Laskar, J., 2020. Paleoclimate records reveal elusive ~200-kyr eccentricity cycle for the first time. *Glob Planet Change* 194, 103296. <https://doi.org/10.1016/j.gloplacha.2020.103296>
- Hilgen, F.J., Abels, H.A., Kuiper, K.F., Lourens, L.J., Wolthers, M., 2015. Towards a stable astronomical time scale for the Paleocene: Aligning Shatsky Rise with the Zumaia - Walvis Ridge ODP site 1262 composite. *Newsl Stratigr* 48, 91–110. <https://doi.org/10.1127/nos/2014/0054>
- Hodell, D. a., Venz, K. a., Charles, C.D., Ninnemann, U.S., 2003. Pleistocene vertical carbon isotope and carbonate gradients in the South Atlantic sector of the Southern Ocean. *Geochemistry, Geophysics, Geosystems* 4, 1–19. <https://doi.org/10.1029/2002GC000367>
- Hodell, D.A., 1993. Late Pleistocene Paleoceanography of the South Atlantic Sector of the Southern Ocean: Ocean Drilling Program Hole 704A. *Paleoceanography* 8, 47–67. <https://doi.org/10.1029/92PA02774>
- Hodell, D.A., Channell, J.E.T., 2016. Mode transitions in Northern Hemisphere glaciation: co-evolution of millennial and orbital variability in Quaternary climate. *Climate of the Past* 12, 1805–1828. <https://doi.org/10.5194/cp-12-1805-2016>
- Holden, P.B., Edwards, N.R., Wolff, E.W., Valdes, P.J., Singarayer, J.S., 2011. The Mid-Brunhes Event and West Antarctic ice sheet stability. *J Quat Sci* 26, 474–477. <https://doi.org/10.1002/jqs.1525>
- Huang, H., Gao, Y., Ma, C., Jones, M.M., Zeeden, C., Ibarra, D.E., Wu, H., Wang, C., 2021. Organic carbon burial is paced by a ~173-ka obliquity cycle in the middle to high latitudes. *Sci Adv* 7, 1–11. <https://doi.org/10.1126/sciadv.abf9489>

Imbrie, J., Berger, A., Boyle, E.A., Clemens, S.C., Duffy, A., Howard, W.R., Kukla, G., Kutzbach, J., Martinson, D.G., McIntyre, A., Mix, A.C., Molino, B., Morley, J.J., Peterson, L.C., Pisias, N.G., Prell, W.L., Raymo, M.E., Shackleton, N.J., Toggweiler, J.R., 1993. On the structure and origin of major glaciation cycles 2. The 100,000-year cycle. *Paleoceanography* 8, 699–735. <https://doi.org/10.1029/93PA02751>

Imbrie, J., Hays, J.D., Martinson, D.G., McIntyre, A., Mix, A.C., Morley, J.J., Pisias, N.G., Prell and, W.L., Shackleton, N.J., 1984. The orbital theory of pleistocene climate: support from a revised chronology of the marine O180 record. In “Milankovitch and climate.” *Milankovitch and Climate* 269–305.

Jansen, J.H.F., Kuijpers, A., Troelstra, S.R., 1986. A Mid-Brunhes Climatic Event: Long-Term Changes in Global Atmosphere and Ocean Circulation. *Science* (1979) 232, 619–622. <https://doi.org/10.1126/science.232.4750.619>

Jansen, M.F., 2017. Glacial ocean circulation and stratification explained by reduced atmospheric temperature. *Proceedings of the National Academy of Sciences* 114, 45–50. <https://doi.org/10.1073/pnas.1610438113>

Jansen, M.F., Nadeau, L.-P., 2016. The Effect of Southern Ocean Surface Buoyancy Loss on the Deep-Ocean Circulation and Stratification. *J Phys Oceanogr* 46, 3455–3470. <https://doi.org/10.1175/JPO-D-16-0084.1>

Jouzel, J., Masson-Delmotte, V., Cattani, O., Dreyfus, G., Falourd, S., Hoffmann, G., Minster, B., Nouet, J., Barnola, J.M., Chappellaz, J., Fischer, H., Gallet, J.C., Johnsen, S., Leuenberger, M., Loulergue, L., Luethi, D., Oerter, H., Parrenin, F., Raisbeck, G., Raynaud, D., Schilt, A., Schwander, J., Selmo, E., Souchez, R., Spahni, R., Stauffer, B., Steffensen, J.P., Stenni, B., Stocker, T.F., Tison, J.L., Werner, M., Wolff, E.W., 2007. Orbital and Millennial Antarctic Climate Variability over the Past 800,000 Years. *Science* (1979) 317, 793–796. <https://doi.org/10.1126/science.1141038>

Kemp, A.E.S., Grigorov, I., Pearce, R.B., Naveira Garabato, A.C., 2010. Migration of the Antarctic Polar Front through the mid-Pleistocene transition: evidence and climatic implications. *Quat Sci Rev* 29, 1993–2009. <https://doi.org/10.1016/j.quascirev.2010.04.027>

Kim, J., Goldstein, S.L., Pena, L.D., Jaume-Seguí, M., Knudson, K.P., Yehudai, M., Bolge, L., 2021. North Atlantic Deep Water during Pleistocene interglacials and glacials. *Quat Sci Rev* 269, 107146. <https://doi.org/10.1016/j.quascirev.2021.107146>

Kroopnick, P.M., 1985. The distribution of ^{13}C of ΣCO_2 in the world oceans. *Deep Sea Research Part A. Oceanographic Research Papers* 32, 57–84. [https://doi.org/10.1016/0198-0149\(85\)90017-2](https://doi.org/10.1016/0198-0149(85)90017-2)

Lacourse, T., Gajewski, K., 2020. Current practices in building and reporting age-depth models. *Quat Res* 96, 28–38. <https://doi.org/10.1017/qua.2020.47>

Laskar, J., Robutel, P., Joutel, F., Gastineau, M., Correia, A.C.M., Levrard, B., 2004. A long-term numerical solution for the insolation quantities of the Earth. *Astron Astrophys* 428, 261–285. <https://doi.org/10.1051/0004-6361:20041335>

Lea, D.W., 1995. A trace metal perspective on the evolution of Antarctic Circumpolar Deep Water chemistry. *Paleoceanography* 10, 733–747. <https://doi.org/10.1029/95PA01546>

Lessa, D.V.O., Santos, T.P., Venancio, I.M., Santarosa, A.C.A., dos Santos Junior, E.C., Toledo, F.A.L., Costa, K.B., Albuquerque, A.L.S., 2019. Eccentricity-induced expansions of Brazilian coastal upwelling zones. *Glob Planet Change* 179, 33–42. <https://doi.org/10.1016/j.gloplacha.2019.05.002>

- Lisiecki, L.E., Raymo, M.E., 2005. A Pliocene-Pleistocene stack of 57 globally distributed benthic $\delta^{18}\text{O}$ records. *Paleoceanography* 20. <https://doi.org/https://doi.org/10.1029/2004PA001071>
- Lund, D.C., Tessin, A.C., Hoffman, J.L., Schmittner, A., 2015. Southwest Atlantic water mass evolution during the last deglaciation. *Paleoceanography* 30, 477–494. <https://doi.org/10.1002/2014PA002657>
- Lüthi, D., Le Floch, M., Bereiter, B., Blunier, T., Barnola, J.-M., Siegenthaler, U., Raynaud, D., Jouzel, J., Fischer, H., Kawamura, K., Stocker, T.F., 2008. High-resolution carbon dioxide concentration record 650,000–800,000 years before present. *Nature* 453, 379–382. <https://doi.org/10.1038/nature06949>
- Lynch-Stieglitz, J., Adkins, J.F., Curry, W.B., Dokken, T., Hall, I.R., Herguera, J.C., Hirschi, J.J.-M., Ivanova, E. V., Kissel, C., Marchal, O., Marchitto, T.M., McCave, I.N., McManus, J.F., Mulitza, S., Ninnemann, U., Peeters, F., Yu, E.-F., Zahn, R., 2007. Atlantic Meridional Overturning Circulation During the Last Glacial Maximum. *Science* (1979) 316, 66–69. <https://doi.org/10.1126/science.1137127>
- Mackensen, A., Fu'tterer, D.K., Grobe, H., Schmiedl, G., 1993. Benthic foraminiferal assemblages from the eastern South Atlantic Polar Front region between 35° and 57°S: Distribution, ecology and fossilization potential. *Mar Micropaleontol* 22, 33–69. [https://doi.org/10.1016/0377-8398\(93\)90003-G](https://doi.org/10.1016/0377-8398(93)90003-G)
- Marchitto, T.M., Broecker, W.S., 2006. Deep water mass geometry in the glacial Atlantic Ocean: A review of constraints from the paleonutrient proxy Cd/Ca. *Geochemistry, Geophysics, Geosystems* 7. <https://doi.org/10.1029/2006GC001323>
- Marshall, J., Speer, K., 2012. Closure of the meridional overturning circulation through Southern Ocean upwelling. *Nat Geosci* 5, 171–180. <https://doi.org/10.1038/ngeo1391>
- Martin, J.H., 1990. Glacial-interglacial CO₂ change: The Iron Hypothesis. *Paleoceanography* 5, 1–13. <https://doi.org/10.1029/PA005i001p00001>
- Martínez-García, A., Rosell-Melé, A., Geibert, W., Gersonde, R., Masqué, P., Gaspari, V., Barbante, C., 2009. Links between iron supply, marine productivity, sea surface temperature, and CO₂ over the last 1.1 Ma. *Paleoceanography* 24. <https://doi.org/10.1029/2008PA001657>
- Martínez-García, A., Rosell-Melé, A., Jaccard, S.L., Geibert, W., Sigman, D.M., Haug, G.H., 2011. Southern Ocean dust–climate coupling over the past four million years. *Nature* 476, 312–315. <https://doi.org/10.1038/nature10310>
- Marzocchi, A., Jansen, M.F., 2019. Global cooling linked to increased glacial carbon storage via changes in Antarctic sea ice. *Nat Geosci* 12, 1001–1005. <https://doi.org/10.1038/s41561-019-0466-8>
- Mitsui, T., Boers, N., 2022. Machine learning approach reveals strong link between obliquity amplitude increase and the Mid-Brunhes transition. *Quat Sci Rev* 277, 107344. <https://doi.org/10.1016/j.quascirev.2021.107344>
- Mudelsee, M., 2014. *Climate Time Series Analysis, Atmospheric and Oceanographic Sciences Library*. Springer International Publishing, Cham. <https://doi.org/10.1007/978-3-319-04450-7>
- Mudelsee, M., 2000. Ramp function regression: a tool for quantifying climate transitions. *Comput Geosci* 26, 293–307. [https://doi.org/10.1016/S0098-3004\(99\)00141-7](https://doi.org/10.1016/S0098-3004(99)00141-7)

Mudelsee, M., Schulz, M., 1997. The Mid-Pleistocene climate transition: onset of 100 ka cycle lags ice volume build-up by 280 ka. *Earth Planet Sci Lett* 151, 117–123. [https://doi.org/10.1016/S0012-821X\(97\)00114-3](https://doi.org/10.1016/S0012-821X(97)00114-3)

Muglia, J., Schmittner, A., 2021. Carbon isotope constraints on glacial Atlantic meridional overturning: Strength vs depth. *Quat Sci Rev* 257, 106844. <https://doi.org/10.1016/j.quascirev.2021.106844>

Nadeau, L.-P., Ferrari, R., Jansen, M.F., 2019. Antarctic Sea Ice Control on the Depth of North Atlantic Deep Water. *J Clim* 32, 2537–2551. <https://doi.org/10.1175/JCLI-D-18-0519.1>

Oppo, D.W., Horowitz, M., 2000. Glacial deep water geometry: South Atlantic benthic foraminiferal Cd/Ca and $\delta^{13}\text{C}$ evidence. *Paleoceanography* 15, 147–160. <https://doi.org/10.1029/1999PA000436>

Paillard, D., 2021. Climate and Astronomical Cycles, in: Ramstein Gilles and Landais, A. and B.N. and S.P. and G.A. (Ed.), *Paleoclimatology*. Springer International Publishing, Cham, pp. 385–404. https://doi.org/10.1007/978-3-030-24982-3_28

Paillard, D., Labeyrie, L., Yiou, P., 1996. Macintosh Program performs time-series analysis. *Eos, Transactions American Geophysical Union* 77, 379. <https://doi.org/https://doi.org/10.1029/96EO00259>

Paillard, D., Parrenin, F., 2004. The Antarctic ice sheet and the triggering of deglaciations. *Earth Planet Sci Lett* 227, 263–271. <https://doi.org/10.1016/j.epsl.2004.08.023>

Peeters, F.J.C., Acheson, R., Brummer, G.-J.A., de Ruijter, W.P.M., Schneider, R.R., Ganssen, G.M., Ufkes, E., Kroon, D., 2004. Vigorous exchange between the Indian and Atlantic oceans at the end of the past five glacial periods. *Nature* 430, 661–665. <https://doi.org/10.1038/nature02785>

Pena, L.D., Goldstein, S.L., 2014. Thermohaline circulation crisis and impacts during the mid-Pleistocene transition. *Science* (1979) 345, 318–322. <https://doi.org/10.1126/science.1249770>

Peterson, C.D., Lisiecki, L.E., 2018. Deglacial carbon cycle changes observed in a compilation of 127 benthic $\delta^{13}\text{C}$ time series (20–6 ka). *Climate of the Past* 14, 1229–1252. <https://doi.org/10.5194/cp-14-1229-2018>

Petit, J.R., Delmonte, B., 2009. A model for large glacial–interglacial climate-induced changes in dust and sea salt concentrations in deep ice cores (central Antarctica): palaeoclimatic implications and prospects for refining ice core chronologies. *Tellus B: Chemical and Physical Meteorology* 61, 768. <https://doi.org/10.1111/j.1600-0889.2009.00437.x>

Petit, J.R., Jouzel, J., Raynaud, D., Barkov, N.I., Barnola, J.-M., Basile, I., Bender, M., Chappellaz, J., Davis, M., Delaygue, G., Delmotte, M., Kotlyakov, V.M., Legrand, M., Lipenkov, V.Y., Lorius, C., Pépin, L., Ritz, C., Saltzman, E., Stievenard, M., 1999. Climate and atmospheric history of the past 420,000 years from the Vostok ice core, Antarctica. *Nature* 399, 429–436. <https://doi.org/10.1038/20859>

Piola, A.R., Matano, R.P., 2019. Ocean Currents: Atlantic Western Boundary—Brazil Current/Falkland (Malvinas) Current, in: *Encyclopedia of Ocean Sciences*. Elsevier, pp. 414–420. <https://doi.org/10.1016/B978-0-12-409548-9.10541-X>

Pisias, N.G., Moore, T.C., 1981. The evolution of Pleistocene climate: A time series approach. *Earth Planet Sci Lett* 52, 450–458. [https://doi.org/10.1016/0012-821X\(81\)90197-7](https://doi.org/10.1016/0012-821X(81)90197-7)

Rahmstorf, S., 2006. Thermohaline Ocean Circulation, in: *Encyclopedia of Quaternary Science*.

- Raymo, M.E., Oppo, D.W., Curry, W., 1997. The Mid-Pleistocene climate transition: A deep sea carbon isotopic perspective. *Paleoceanography* 12, 546–559. <https://doi.org/10.1029/97PA01019>
- Razik, S., Govin, A., Chiessi, C.M., von Dobeneck, T., 2015. Depositional provinces, dispersal, and origin of terrigenous sediments along the SE South American continental margin. *Mar Geol* 363, 261–272. <https://doi.org/10.1016/j.margeo.2015.03.001>
- Röthlisberger, R., Crosta, X., Abram, N.J., Armand, L., Wolff, E.W., 2010. Potential and limitations of marine and ice core sea ice proxies: an example from the Indian Ocean sector. *Quat Sci Rev* 29, 296–302. <https://doi.org/10.1016/j.quascirev.2009.10.005>
- Röthlisberger, R., Mudelsee, M., Bigler, M., de Angelis, M., Fischer, H., Hansson, M., Lambert, F., Masson-Delmotte, V., Sime, L., Udisti, R., Wolff, E.W., 2008. The Southern Hemisphere at glacial terminations: insights from the Dome C ice core. *Climate of the Past* 4, 345–356. <https://doi.org/10.5194/cp-4-345-2008>
- Sarntheim, M., Erlenkeuser, H., Grafenstein, R. von, Schröder, C., 1984. Stable-isotope stratigraphy for the last 750,000 years: “Meteor” core 13519 from the eastern equatorial Atlantic. *Meteor Forschungsergebnisse: Reihe C, Geologie und Geophysik* 38, 9–24.
- Sarntheim, M., Tiedemann, R., 1989. Toward a High-Resolution Stable Isotope Stratigraphy of the Last 3.4 Million Years: Sites 658 and 659 off Northwest Africa, in: *Proceedings of the Ocean Drilling Program, 108 Scientific Results. Ocean Drilling Program*, pp. 167–185. <https://doi.org/10.2973/odp.proc.sr.108.159.1989>
- Schlitzer, R. (2017). Ocean Data View, odv.awi.de
- Schmieder, F., von Dobeneck, T., Bleil, U., 2000. The Mid-Pleistocene climate transition as documented in the deep South Atlantic Ocean: initiation, interim state and terminal event. *Earth Planet Sci Lett* 179, 539–549. [https://doi.org/10.1016/S0012-821X\(00\)00143-6](https://doi.org/10.1016/S0012-821X(00)00143-6)
- Schmiedl, G., Mackensen, A., 1997. Late Quaternary paleoproductivity and deep water circulation in the eastern South Atlantic Ocean: Evidence from benthic foraminifera. *Palaeoclimatol Palaeoecol* 130, 43–80. [https://doi.org/10.1016/S0031-Palaeogeogr 0182\(96\)00137-X](https://doi.org/10.1016/S0031-Palaeogeogr 0182(96)00137-X)
- Schmittner, A., Lund, D.C., 2015. Early deglacial Atlantic overturning decline and its role in atmospheric CO₂ rise inferred from carbon isotopes ($\delta^{13}\text{C}$). *Climate of the Past* 11, 135–152. <https://doi.org/10.5194/cp-11-135-2015>
- Schulz, M., Mudelsee, M., 2002. REDFIT: estimating red-noise spectra directly from unevenly spaced paleoclimatic time series. *Comput Geosci* 28, 421–426. [https://doi.org/10.1016/S0098-3004\(01\)00044-9](https://doi.org/10.1016/S0098-3004(01)00044-9)
- Siegenthaler, U., Stocker, T.F., Monnin, E., Lüthi, D., Schwander, J., Stauffer, B., Raynaud, D., Barnola, J.-M., Fischer, H., Masson-Delmotte, V., Jouzel, J., 2005. Stable Carbon Cycle - Climate Relationship During the Late Pleistocene. *Science* (1979) 310, 1313–1317. <https://doi.org/10.1126/science.1120130>
- Siegfried, L., Schmidt, M., Mohrholz, V., Pogrzeba, H., Nardini, P., Böttinger, M., Scheuermann, G., 2019. The tropical-subtropical coupling in the Southeast Atlantic from the perspective of the northern Benguela upwelling system. *PLoS One* 14, e0210083. <https://doi.org/10.1371/journal.pone.0210083>
- Sigman, D.M., Boyle, E.A., 2000. Glacial/interglacial variations in atmospheric carbon dioxide. *Nature*. <https://doi.org/10.1038/35038000>

Sigman, D.M., Hain, M.P., Haug, G.H., 2010. The polar ocean and glacial cycles in atmospheric CO₂ concentration. *Nature* 466, 47–55. <https://doi.org/10.1038/nature09149>

Skinner, L.C., Fallon, S., Waelbroeck, C., Michel, E., Barker, S., 2010. Ventilation of the Deep Southern Ocean and Deglacial CO₂ Rise. *Science* (1979) 328, 1147–1151. <https://doi.org/10.1126/science.1183627>

Starr, A., Hall, I.R., Barker, S., Rackow, T., Zhang, X., Hemming, S.R., van der Lubbe, H.J.L., Knorr, G., Berke, M.A., Bigg, G.R., Cartagena-Sierra, A., Jiménez-Espejo, F.J., Gong, X., Gruetzner, J., Lathika, N., LeVay, L.J., Robinson, R.S., Ziegler, M., 2021. Antarctic icebergs reorganize ocean circulation during Pleistocene glacials. *Nature* 589, 236–241. <https://doi.org/10.1038/s41586-020-03094-7>

Stephens, B.B., Keeling, R.F., 2000. The influence of Antarctic sea ice on glacial–interglacial CO₂ variations. *Nature* 404, 171–174. <https://doi.org/10.1038/35004556>

Stramma, L., England, M., 1999. On the water masses and mean circulation of the South Atlantic Ocean. *J Geophys Res Oceans* 104, 20863–20883. <https://doi.org/10.1029/1999JC900139>

Talley, L., 2013. Closure of the Global Overturning Circulation Through the Indian, Pacific, and Southern Oceans: Schematics and Transports. *Oceanography* 26, 80–97. <https://doi.org/10.5670/oceanog.2013.07>

Toggweiler, J.R., 1999. Variation of atmospheric CO₂ by ventilation of the ocean’s deepest water. *Paleoceanography* 14, 571–588. <https://doi.org/10.1029/1999PA900033>

Toggweiler, J.R., Russell, J.L., Carson, S.R., 2006. Midlatitude westerlies, atmospheric CO₂, and climate change during the ice ages. *Paleoceanography* 21. <https://doi.org/10.1029/2005PA001154>

Vázquez Riveiros, N., Waelbroeck, C., Skinner, L., Duplessy, J.-C., McManus, J.F., Kandiano, E.S., Bauch, H.A., 2013. The “MIS 11 paradox” and ocean circulation: Role of millennial scale events. *Earth Planet Sci Lett* 371–372, 258–268. <https://doi.org/10.1016/j.epsl.2013.03.036>

Voigt, I., Cruz, A.P.S., Mulitza, S., Chiessi, C.M., Mackensen, A., Lippold, J., Antz, B., Zabel, M., Zhang, Y., Barbosa, C.F., Tisserand, A.A., 2017. Variability in mid-depth ventilation of the western Atlantic Ocean during the last deglaciation. *Paleoceanography* 32, 948–965. <https://doi.org/10.1002/2017PA003095>

Weijer, W., De Ruijter, W.P.M., Sterl, A., Drijfhout, S.S., 2002. Response of the Atlantic overturning circulation to South Atlantic sources of buoyancy. *Glob Planet Change* 34, 293–311. [https://doi.org/10.1016/S0921-8181\(02\)00121-2](https://doi.org/10.1016/S0921-8181(02)00121-2)

Westerhold, T., Bickert, T., Röhl, U., 2005. Middle to late Miocene oxygen isotope stratigraphy of ODP site 1085 (SE Atlantic): New constrains on Miocene climate variability and sea-level

- fluctuations. *Palaeogeogr Palaeoclimatol Palaeoecol* 217, 205–222. <https://doi.org/10.1016/j.palaeo.2004.12.001>
- Wolff, E.W., Fischer, H., Fundel, F., Ruth, U., Twarloh, B., Littot, G.C., Mulvaney, R., Röthlisberger, R., de Angelis, M., Boutron, C.F., Hansson, M., Jonsell, U., Hutterli, M.A., Lambert, F., Kaufmann, P., Stauffer, B., Stocker, T.F., Steffensen, J.P., Bigler, M., Siggaard-Andersen, M.L., Udisti, R., Becagli, S., Castellano, E., Severi, M., Wagenbach, D., Barbante, C., Gabrielli, P., Gaspari, V., 2006. Southern Ocean sea-ice extent, productivity and iron flux over the past eight glacial cycles. *Nature* 440, 491–496. <https://doi.org/10.1038/nature04614>
- Wolff, E.W., Rankin, A.M., Röthlisberger, R., 2003. An ice core indicator of Antarctic sea ice production? *Geophys Res Lett* 30. <https://doi.org/10.1029/2003GL018454>
- Wu, Z., Yin, Q., Guo, Z., Berger, A., 2020. Hemisphere differences in response of sea surface temperature and sea ice to precession and obliquity. *Glob Planet Change* 192. <https://doi.org/10.1016/j.gloplacha.2020.103223>
- Yin, Q., 2013. Insolation-induced mid-Brunhes transition in Southern Ocean ventilation and deep-ocean temperature. *Nature* 494, 222–225. <https://doi.org/10.1038/nature11790>
- Yin, Q.Z., Berger, A., 2012. Individual contribution of insolation and CO₂ to the interglacial climates of the past 800,000 years. *Clim Dyn* 38, 709–724. <https://doi.org/10.1007/s00382-011-1013-5>
- Yin, Q.Z., Berger, A., 2010. Insolation and CO₂ contribution to the interglacial climate before and after the Mid-Brunhes Event. *Nat Geosci* 3, 243–246. <https://doi.org/10.1038/ngeo771>
- Yu, J., Menviel, L., Jin, Z.D., Thornalley, D.J.R., Barker, S., Marino, G., Rohling, E.J., Cai, Y., Zhang, F., Wang, X., Dai, Y., Chen, P., Broecker, W.S., 2016. Sequestration of carbon in the deep Atlantic during the last glaciation. *Nat Geosci* 9, 319–324. <https://doi.org/10.1038/ngeo2657>
- Zachos, J.C., Kroon, D., Blum, P., *et al.*, 2004. Proceedings of the Ocean Drilling Program, 208 Initial Reports, Proceedings of the Ocean Drilling Program, Initial Reports, Proceedings of the Ocean Drilling Program. *Ocean Drilling Program*. <https://doi.org/10.2973/odp.proc.ir.208.2004>

4.5 Supporting Information

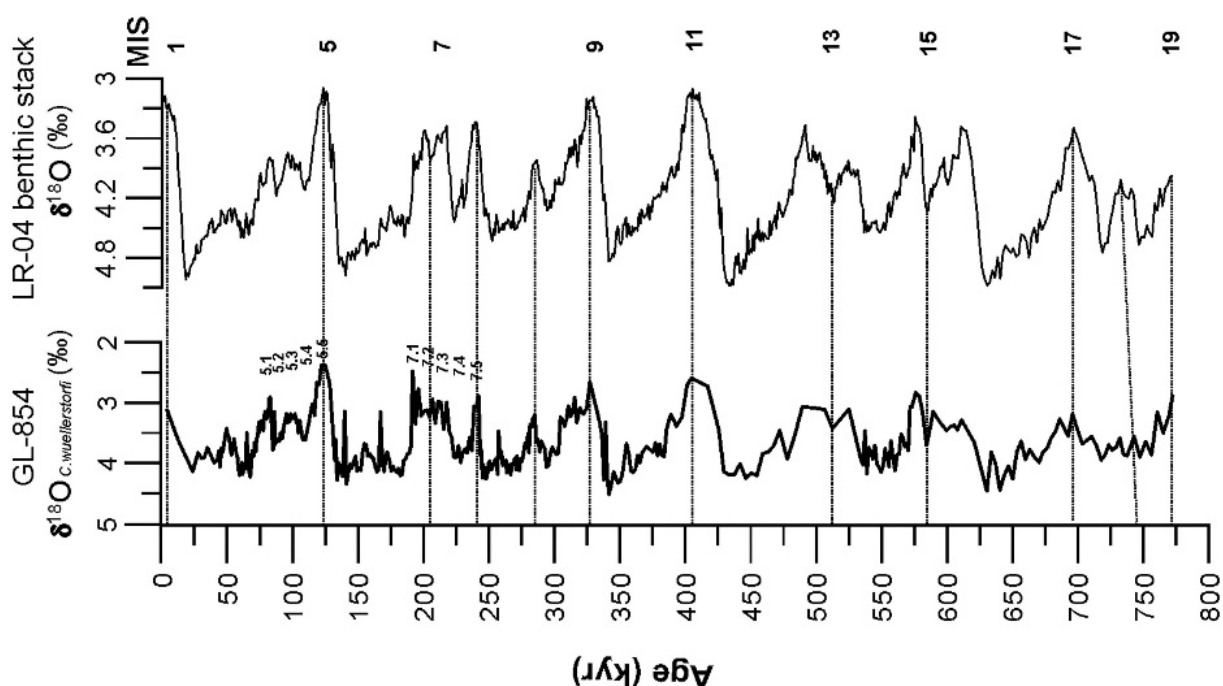
Atlantic $\delta^{13}\text{C}$ Deep-water Seesaw Controlled by Antarctic Sea Ice Over the Last 800 ka

This supporting information contains supplementary figures and tables of the main text of chapter 4.

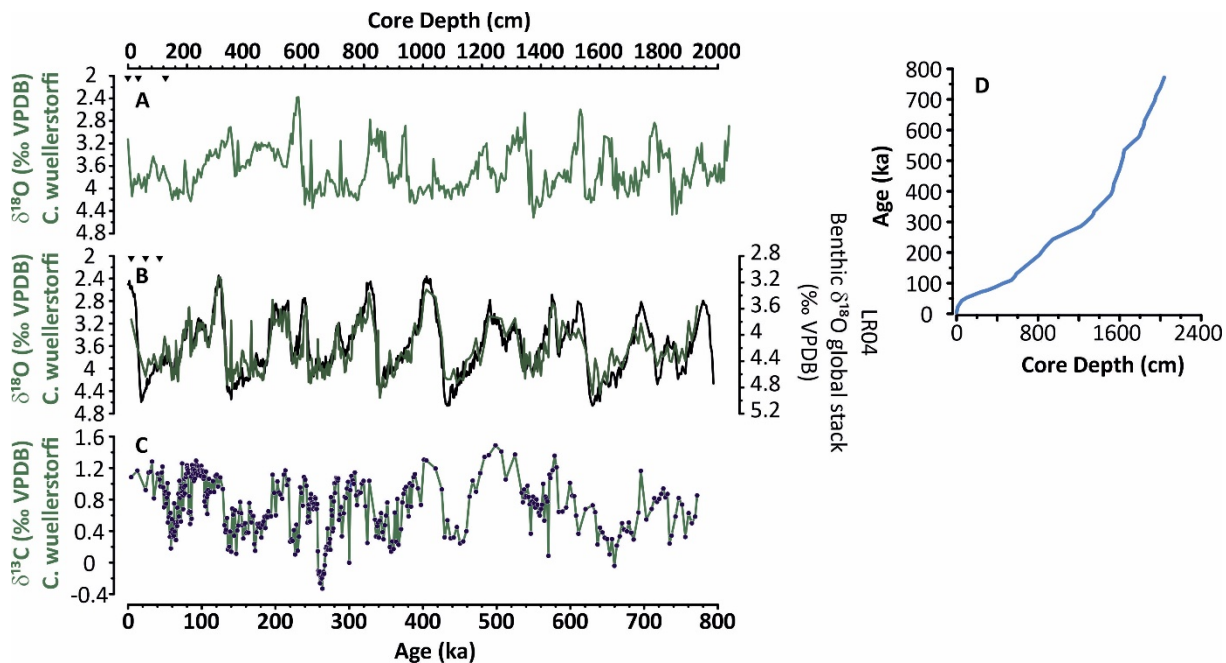
Age model

In the main text we provided all main information regarding the original age model construction for GL-854 core published by de Almeida *et al.* (2015). Chosen tie points and calendar age vs. depth from the visual alignment with benthic foraminifera $\delta^{18}\text{O}$ global stack LR04 (Lisiecki and Raymo, 2005) are indicated in the Supplementary Fig. 1 and 2 (de Almeida *et al.*, 2015).

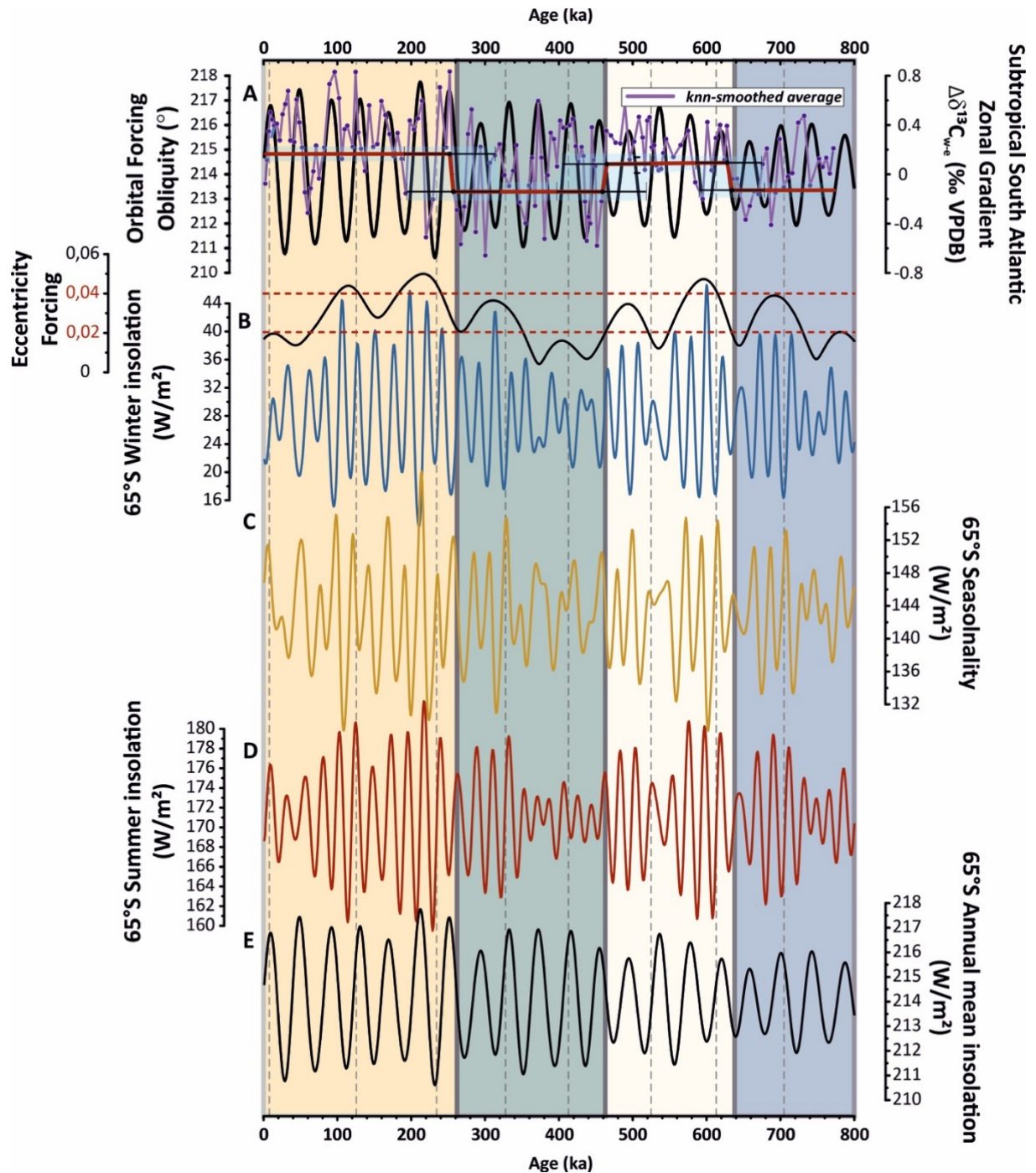
Supplementary Figure 1: Main tie points between core GL-854 and LR04 benthic stack (Lisiecki and Raymo, 2005; de Almeida *et al.*, 2015).



Supplementary Figure 2: Reference curve and age-depth model of core GL-854. Benthic foraminifera (*Cibicoides wuellerstorfi*) A) $\delta^{18}\text{O}$ versus depth, B) $\delta^{18}\text{O}$ and LR04 benthic foraminifera $\delta^{18}\text{O}$ stack LR04 (Lisiecki and Raymo, 2005), C) $\delta^{13}\text{C}$ versus age, and D) age-depth model from de Almeida *et al.* (2015). Triangles represent the calibrated ^{14}C ages.



Supplementary Figure 3: Orbital influence over 65°S insolation across RAMPFIT phases I, II, III, IV. a) $\Delta\delta^{13}\text{C}_{w-e}$ record and obliquity forcing; b) winter; c) seasonality; d) summer, and e) annual mean insolation, which varies in function of a) obliquity (Laskar *et al.*, 2004).



References

- de Almeida, F.K., de Mello, R.M., Costa, K.B., Toledo, F.A.L., 2015. The response of deep-water benthic foraminiferal assemblages to changes in paleoproductivity during the Pleistocene (last 769.2 kyr), western South Atlantic Ocean. *Palaeogeogr Palaeoclimatol Palaeoecol* 440, 201–212. <https://doi.org/10.1016/j.palaeo.2015.09.005>

Laskar, J., Robutel, P., Joutel, F., Gastineau, M., Correia, A.C.M., Levrard, B., 2004. A long-term numerical solution for the insolation quantities of the Earth. *Astron Astrophys* 428, 261–285. <https://doi.org/10.1051/0004-6361:20041335>

Lisiecki, L.E., Raymo, M.E., 2005. A Pliocene-Pleistocene stack of 57 globally distributed benthic $\delta^{18}\text{O}$ records. *Paleoceanography* 20, 1–17. <https://doi.org/10.1029/2004PA001071>

5 PRECESSIONALLY-DRIVEN UPWELLING STRENGTH AT NORTHERN BENGUELA UPWELLING SYSTEM

Anthropogenic greenhouse gas emissions are causing significant disruptions in surface and deep-water circulation and wind patterns (Bronse laer *et al.*, 2018; Cheng *et al.*, 2019; Bronse laer and Zanna, 2020; Rantanen *et al.*, 2022; Li *et al.*, 2023). Climate projections show these changes are expected to persist, significantly altering the global distribution of heat and moisture, which could have severe consequences for the Benguela Upwelling System (BUS) (IPCC, 2022). Bakun (1990) early suggested that global warming would intensify winds favoring upwelling at BUS due to greater thermal contrast and pressure gradients between land and sea (Bakun, 1990; Lu *et al.*, 2007), which has been contradicted by observations (Bakun *et al.*, 2010). The BUS is linked to large-scale atmospheric circulation patterns, driven by an interaction between the southeastern trade winds, the South Atlantic Hadley Cell, the South Atlantic Atmospheric High, and the position of the Intertropical Convergence Zone (ITCZ) (Donohoe *et al.*, 2013; Tim *et al.*, 2016; McGee *et al.*, 2018). Therefore, BUS intensity highly depends on the energy balance between the hemispheres (McGee *et al.*, 2018). CMIP6 models project a clear southward shift of the ITCZ over the eastern Pacific and Atlantic oceans due to regionally contrasting inter-hemispheric energy flows, possibly associated with future reductions in thermohaline circulation (Caesar *et al.*, 2018; IPCC, 2022; Li *et al.*, 2023). Although the rise in global temperatures is a known fact, how it impacts the atmospheric patterns promoting changes at BUS is still uncertain.

BUS is the most biologically productive upwelling region in the world (Carr, 2002; Carr and Kearns, 2003; Blanke *et al.*, 2005; González-Dávila *et al.*, 2009; Santos *et al.*, 2012; Sydeman *et al.*, 2014; Varela *et al.*, 2015, 2018), which refers to the biomass largely produced when the wind-driven Ekman divergence of surface waters induces the vertical mixing of high-nutrient cold South Atlantic Central Waters (SACW) with surface waters (Shannon and Nelson, 1996; Hutchings *et al.*, 2009). The assimilation of CO₂ by increased primary productivity and its transfer to the deep ocean is part of the biological pump, that decreases atmospheric CO₂ concentrations by storing CO₂ as dissolved inorganic carbon (DIC) (Volk and Hoffert, 1985; Emeis *et al.*, 2018). However, when upwelled nutrients are

not fully utilized by biological production, the system becomes an active source of CO₂ to the atmosphere due to enhanced outgassing (Emeis *et al.*, 2018).

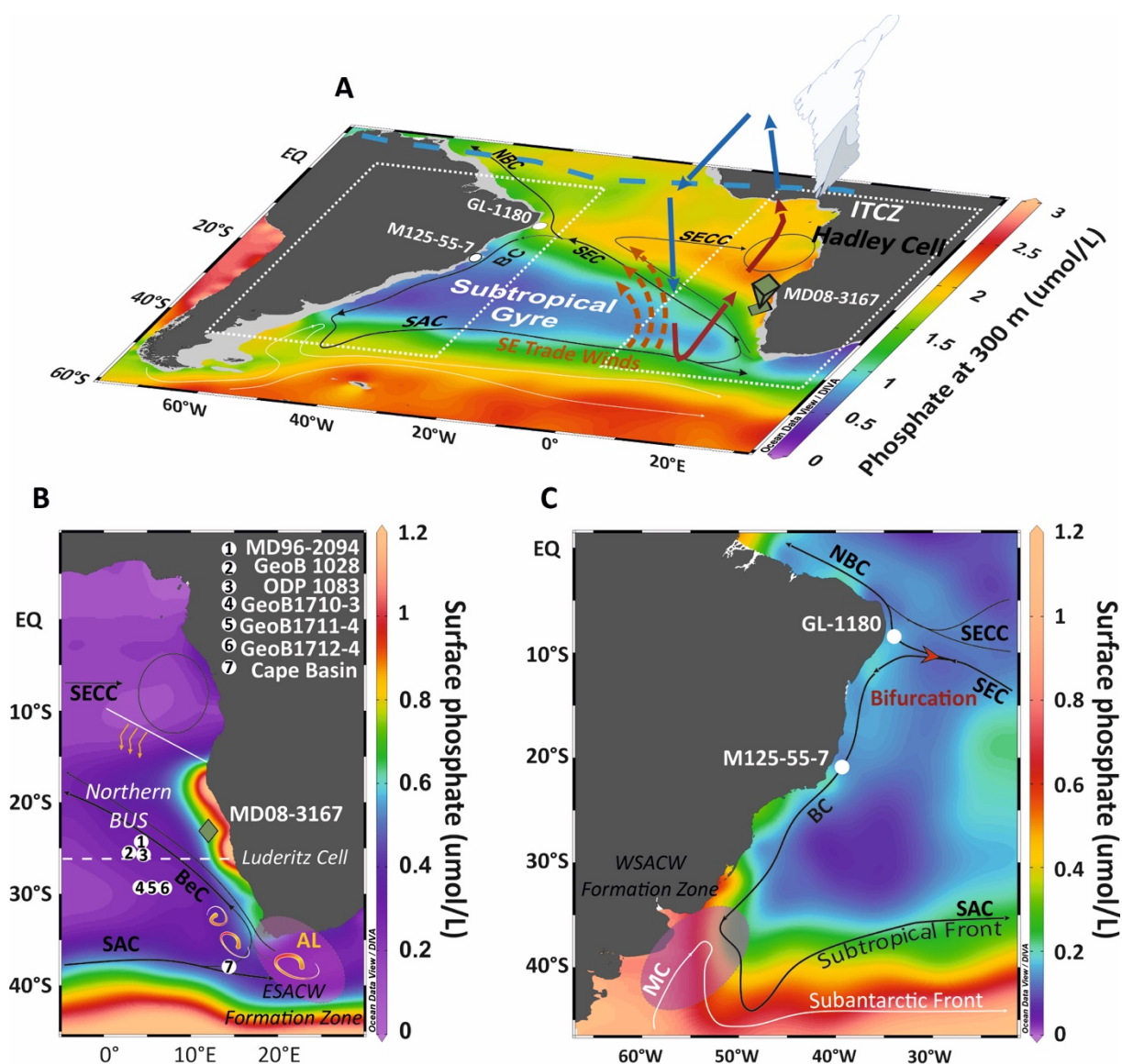
The BUS is divided into two subsystems around the Luderitz Cell region (27°S): (1) southern BUS (SBUS; 25-35 °S), with the seasonal regime and strong upwelling occurring during austral summer (December-February); and (2) northern BUS (NBUS; 17-25°S) with upwelling happening all year long and intensified during austral winter (Fig. 18) (Shannon and Nelson, 1996). The upwelling cells south of 20°S act as an active sink of atmospheric CO₂ (González-Dávila *et al.*, 2009). In the SBUS, there is a great predominance of Eastern SACW (ESACW) that is newly formed when Agulhas Leakage (AL) waters mix in the Cape region with Western SACW (WSACW), formed at Brazil-Malvinas Confluence Zone (BMC), which greatly influence the NBUS (Delaney, 1989; Stramma and England, 1999; Mohrholz *et al.*, 2008; Tim *et al.*, 2018; 2019a, 2019b). Remineralization of organic matter through the long-way transport of WSACW within the Subtropical Gyre (SASG) and the equatorial currents system into the Angola Gyre increases nutrient content and reduces oxygen levels at NBUS, particularly during late austral summer (Mohrholz *et al.*, 2008; Emeis *et al.*, 2018). These waters are advected poleward by the Angola Current, which feeds the NBUS region near the major upwelling cell at Cape Frio (Hutchings *et al.*, 2009).

Studies have been investigating the BUS dynamics across several time scales, particularly concerning wind activity and primary productivity, and through changes in the surface temperature (SST) across several time scales. Present day studies have focused on its oxygen budget (Mohrholz *et al.*, 2008; Schmidt and Eggert, 2016; Ohde and Dadou, 2018), nutrients, primary productivity and CO₂ (Carr, 2002; Carr and Kearns, 2003; González-Dávila *et al.*, 2009; Lamont *et al.*, 2019; Bordbar *et al.*, 2021; Siddiqui *et al.*, 2023), biogeochemical approach (Emeis *et al.*, 2009; Emeis *et al.*, 2018), and from oceanographic modeling (Blanke *et al.*, 2005; Tim *et al.*, 2018, 2019a, 2019b). The link between perturbations in the heat distribution between the hemispheres and the upwelling at BUS has also been investigated in studies from the last glacial to the Holocene (e.g., Kim *et al.*, 2002; Kim *et al.*, 2003; Romero *et al.*, 2003; Farmer *et al.*, 2011; Donohoe *et al.*, 2013; McKay *et al.*, 2016; McGee *et al.*, 2018; Zhao *et al.*, 2019), over the Mid-to-Late Pleistocene (e.g., Little *et al.*, 1997; Kirst *et al.*, 1999; Ufkes *et al.*, 2000; Volbers *et al.*, 2003; Stuut and Lamy, 2004; West *et al.*, 2004; Ufkes and Kroon, 2012), and on longer time scales (e.g., Marlow *et al.*, 2000; Etourneau *et al.*, 2009; Leduc *et al.*, 2014; Petrick *et al.*, 2015). While

some aspects of the findings of these studies are similar, differing conclusions difficult the fully understanding of the dynamics of BUS across different climates. Furthermore, upwelling strength is usually inferred based on local SST or tracking productivity by assessing planktonic foraminifera assemblages, which could lead to misinterpretations since temperature changes could also have been driven by ocean circulation or radiative forcing variations, and assemblages by lateral transport. Therefore, there is a lack of high-resolution long-term records covering the late Pleistocene that can serve as a reliable indicator of BUS variability. Hence it is difficult to fully understand the factors driving BUS, as well as its impacts on the carbon cycle and global climate.

In this work, we aim to investigate the orbital-scale NBUS variability over the last four glacial-interglacial cycles based on the multiproxy study of high-resolution marine sediment core MD08-3167 positioned at the Namibia margin (Fig. 18). We present a 365 ka-long upper ocean stratification reconstruction of the NBUS based on the $\delta^{18}\text{O}$ gradient between planktic foraminifera *Globigerina bulloides* and *Globorotalia inflata* ($\Delta\delta^{18}\text{O}$) as a proxy of upwelling variability and combine it with $\delta^{13}\text{C}$ gradients between the same species ($\Delta\delta^{13}\text{C}_{\text{upper}}$), as well as between *G. inflata* and the benthic foraminifera *Cibicides wuellerstorfi* ($\Delta\delta^{13}\text{C}_{\text{lower}}$) to investigate the potential effects of upwelling changes in the global carbon budget.

Figure 18 - A) South Atlantic upper circulation and atmospheric components: the Intertropical Convergence Zone (ITCZ), trade winds (blue dashed line and orange arrows representation, respectively), and the South Atlantic Hadley Cell (3D blue and red arrows and cloud). Background colors represent interpolated phosphate distribution at 300 m depth (mmol/L) from the World Ocean Atlas 2018 (WOA 18; Garcia *et al.*, 2018) database. Dashed white squares indicate the geographic area referent to B) Eastern South Atlantic (ESA) and C) Western South Atlantic (WSA). Position of sediment core MD08-3167 (green diamond pin, this study) and other marine records discussed in this work (white circles) in A) WSA: GL-1180 (Nascimento *et al.*, 2021); M125-55-7 (Hou *et al.*, 2020); and in B) ESA: MD96-2094 (Stuut *et al.*, 2002); GeoB 1712-4; GeoB 1711-4; GeoB 1710-3 (Little *et al.*, 1997; Volbers *et al.*, 2003; West *et al.*, 2004); GeoB 1028 (Schneider *et al.*, 1995); ODP Site 1083 (West *et al.*, 2004); Cape Basin Record (Peeters *et al.*, 2004). Background colors on B) and C) indicate the phosphate distribution at surface. South Atlantic Central Water (SACW) formation zones are indicated on B) Brazil-Malvinas Confluence (BMC) and C) Agulhas Leakage (AL). The figure was produced using Ocean Data View (Schlitzer, 2021)



5.1 Material and Methods

5.1.1 Sediment core and study area

We investigate the 3524 cm-long Calypso core MD08-3167 (23.3152 °S; 12.3768 °E) retrieved from the continental slope off Namibia margin at 1948 m water depth during IMAGES cruise MD167/RETRO (Waelbroeck *et al.*, 2008). Ten cm³ of sediment were collected every 4 cm between 0-700 cm and every 8 cm through 700 cm to the bottom. The sediment was disaggregated in distilled water in an orbital shaker. Samples were washed over a 63 µm mesh sieve, oven-dried for 24 h at 60 °C, and stored in acrylic flasks. Planktonic foraminifera shells were handpicked using a binocular microscope. Site MD08-3167 was collected in the Southeast Atlantic in the Northern Cape Basin, which is dominated by an eastern boundary current system. The atmospheric circulation is governed by the high-pressure cell of the South Atlantic Atmospheric High, the low-pressure cell over the African continent, and the ITCZ (Tim *et al.*, 2016). This system raises the southeast trade winds, fundamental in governing offshore transport near-surface waters that drive the upwelling activity perennial all year at NBUS (Hutchings *et al.*, 2009).

The Benguela Current (BeC) is an important aspect of the SASG. It flows northward along the eastern boundary and plays a significant role in thermohaline circulation (Garzoli and Matano, 2011). The primary source of water for the BeC is the South Atlantic Current (SAC), which carries subtropical surface waters and receives contributions from the Agulhas Current and Subantarctic Surface Water (Peterson and Stramma, 1991; Shannon and Nelson, 1996; Hutchings *et al.*, 2009). South of Walvis Ridge, the BeC splits into two branches: the Benguela Coastal Current (BCC), which moves northward along the coastline, and the Benguela Oceanic Current (BOC), which flows northwestward (Stramma and Peterson 1989). The BCC meets the warm Angola Current (AC), forming the Angola-Benguela Front (ABF), which moves seasonally between 14°S and 17°S and acts as the northern boundary of the BUS. The northwestward flow of the BCC contributes to the South Equatorial Current (SEC), which is driven by trade winds (Peterson and Stramma, 1991). The SEC flow heads towards the Brazilian margin, where it bifurcates around 10°S and originates two western boundary currents: the southward Brazil Current (BC) and its northward, cross-equatorial counterpart, the North Brazil Current (NBC) (Silveira *et al.*, 2000). The BC and NBC play a key role in the transfer of energy between the southern and northern hemispheres,

determining if South Atlantic upper ocean layers become part of the AMOC continuous northward flow to the North Hemisphere or they recirculate in the South Atlantic subtropical gyre, favoring NBC or BC transport respectively (Peterson and Stramma, 1991; Marcello *et al.*, 2018). The southward flow of BC meets the northeastward extension of the Antarctic Circumpolar Current (ACC) at the BMC (Olson *et al.*, 1988; Silveira *et al.*, 2000). The SAC, which delineates the southern boundary of the SASG, flows towards the east and connects to BeC, closing the upper circulation in the South Atlantic (Peterson and Stramma, 1991; Silveira *et al.*, 2000; Garzoli and Matano, 2011). Roughly every ten years, warm Angola Current water intrudes along the Namibian shelf due to weakened trade winds, a process known as the "Benguela Niño" (Shannon and Nelson, 1996). This intrusion leads to an increase in sea surface temperature on the shelf and a decline in upwelling activity and marine biological productivity in the NBUS.

The BUS dynamics respond to the interaction of many oceanographic features, such as the BeC water sources, the formation of BCC and BOC branches, the presence of ABF, and the impacts of warm AC intrusions and Agulhas Rings from the south (Tim *et al.*, 2018). Large eddies known as Agulhas Rings from AL bring a significant amount of Indian Ocean water to the South Atlantic, affecting the SBUS and more largely the BeC and the Atlantic Ocean (Peeters *et al.*, 2004; Martínez-Méndez *et al.*, 2010; Beal *et al.*, 2011; Garzoli and Matano, 2011; Caley *et al.*, 2014). Increased influence of ESACW from AL region to SBUS promote that the upwelling of more ventilated (younger) waters with low nutrient content, changing the characteristic of upwelled waters and the biological pump (Beal *et al.*, 2011; Tim *et al.*, 2018, 2019b).

5.1.2 Age model

The age model of core MD08-3167 was built using 8 previously published radiocarbon ages measured on *G. bulloides* at the Poznan Radiocarbon Laboratory, Poland (Collins *et al.*, 2013) for the first ca. 700 cm of the core. Radiocarbon ages were recalibrated using the Marine 20 calibration curve (Heaton *et al.*, 2020) without any additional local reservoir effect. The chronology of the lower part of the core is based on graphic alignment between our benthic foraminifera $\delta^{18}\text{O}$ record ($n = 534$) with the global $\delta^{18}\text{O}$ stack LR04 (Lisiecki and Raymo, 2005) with the software QAnalySeries (Kotov and Paelike, 2018), and

the complete age-depth model was built within the software Bacon v. 2.3 to reconstruct Bayesian accumulation histories (Blaauw and Christen, 2011). Error estimations of $\delta^{18}\text{O}$ tie-points consider the mean resolution of the benthic $\delta^{18}\text{O}$ record, the mean resolution of the reference curve, a matching error visually estimated when defining the tie points, and the absolute age error of the time scale used for the reference record. The age model for the sediment core indicates that the core covers between 1.1 and 367 ka BP with a temporal resolution of 0.68 kyr and an average sedimentation rate of 12.3 cm/kyr (Supplementary Fig. 1).

5.1.3 Stable isotopes and gradients

Stable isotopic measurements were performed in at least 3 shells of each of the 4 different foraminifera species: *G. bulloides* ($n = 503$; $\bar{x} = 10$ shells), *G. inflata* ($n = 502$; $\bar{x} = 9.7$ shells), *C. wuellerstorfi* ($n = 429$; $\bar{x} = 4$ shells) and *U. peregrina* ($n = 105$; $\bar{x} = 3$ shells). Planktonic species individuals were picked from a fraction between 250-300 μm , and benthic foraminifera from a fraction between 250-350 μm . The first 700 cm of the MD08-3167 core, planktonic and benthic foraminifera *C. wuellerstorfi* shells were analyzed using a Finnigan Δ^+ and Elementar Isoprime mass spectrometer at the LSCE (Roubi, 2019). The VPDB was calibrated against the NBS-19 standard ($\delta^{18}\text{O} = -2.20\text{‰}$), with an external average reproducibility (1σ) of $\pm 0.05\text{‰}$. The measured NBS-18 standard has a $\delta^{18}\text{O}$ value of $-23.20 \pm 0.20\text{‰}$. Samples between 700 – 3541 cm interval destined to the $\delta^{18}\text{O}$ and $\delta^{13}\text{C}$ measurements were analyzed by Fabien Dewild using a Thermo Finnigan MAT 353 mass spectrometer equipped with a Carbo Kiel IV carbonate device at the *Pôle Spectrométrie Océan (PSO) from Université de Bretagne Occidentale (UBO)*, Plouzané, France. Results were calibrated using the international calibration standards NBS-19 and NBS-18, in which all reported isotopic values are expressed relative to the Vienna Pee-Dee Belemnite (VPDB) scale. The long-term precision of $\delta^{18}\text{O}$ and $\delta^{13}\text{C}$ of the in-house standard (CAMIL-21) is $\pm 0.03\text{‰}$ and $\pm 0.01\text{‰}$ for *G. bulloides*, $\pm 0.03\text{‰}$ and $\pm 0.02\text{‰}$ for *G. inflata*, $\pm 0.03\text{‰}$ and $\pm 0.02\text{‰}$ for *C. wuellerstorfi* and *U. peregrina*.

Uvigerina peregrina precipitates its shell $\delta^{18}\text{O}$ in equilibrium with bottom water, while *C. wuellerstorfi* $\delta^{18}\text{O}$ is shifted by 0.64 ‰. Thus, the *Cibicides wuellerstorfi* $\delta^{18}\text{O}$ record was corrected by a factor of plus 0.64 ‰ and plotted together with *U. peregrina* $\delta^{18}\text{O}$

values to produce a unique and reliable curve for bottom water $\delta^{18}\text{O}$ (Duplessy *et al.*, 1984). On the other hand, only *C. wuellerstorfi* $\delta^{13}\text{C}$ is registered in equilibrium with bottom water $\delta^{13}\text{C}_{\text{DIC}}$, while *U. peregrina* $\delta^{13}\text{C}$ is recorded in equilibrium with porewater $\delta^{13}\text{C}$ (Shackleton, 1974; Duplessy *et al.*, 1984). For this reason, the *U. peregrina* $\delta^{13}\text{C}$ record was not used to compose a high-resolution benthic $\delta^{13}\text{C}$ composite record.

All vertical isotopic gradient calculations were done by subtracting isotopic values of foraminiferal species of the same sample depth without any interpolation method. The $\Delta\delta^{18}\text{O}$ gradient was calculated by subtracting *G. inflata* $\delta^{18}\text{O}$ minus *G. bulloides* $\delta^{18}\text{O}$. $\Delta\delta^{13}\text{C}_{\text{upper}}$ record was calculated by subtracting *G. bulloides* $\delta^{13}\text{C}$ minus *G. inflata* $\delta^{13}\text{C}$, and $\Delta\delta^{13}\text{C}_{\text{lower}}$ by subtracting *G. inflata* $\delta^{13}\text{C}$ minus *C. wuellerstorfi* $\delta^{13}\text{C}$. $\delta^{18}\text{O}$ values registered individually by each species are driven by temperature or salinity changes in the surrounding waters as an on-site water mass density signature that ultimately affects our $\Delta\delta^{18}\text{O}$ record.

5.1.4 Spectral analysis

REDFIT spectral analyses (Schulz and Mudelsee, 2002) were performed on *G. bulloides* and *G. inflata* $\delta^{18}\text{O}$ and in the $\Delta\delta^{18}\text{O}$ records using the software PAST (Hammer *et al.*, 2001) to determine the statistically significant periodicities present in our records. REDFIT allows us to work directly with unevenly spaced data, avoiding the introduction of biases when interpolating time series (Schulz and Mudelsee, 2002). Besides, the $\Delta\delta^{18}\text{O}$ record was calculated based on the same core levels for *G. inflata* and *G. bulloides* $\delta^{18}\text{O}$ records, hence no interpolation is needed.

5.2 Results

5.2.1 Stable isotopes

All stable isotopic records span the last 365 ka, covering the last four glacial terminations (Fig. 19). *Globigerina bulloides* $\delta^{18}\text{O}$ record ($n = 503$) ranges from -0.13 ‰ to 3.49 ‰, with an average of 1.75 ‰ (Fig. 19A). *Globorotalia inflata* $\delta^{18}\text{O}$ record ($n = 502$) ranges from 0.51 ‰ to 3.46 ‰, with an average of 2.03 ‰ (Fig. 19A). Both records display a robust glacial-interglacial pattern, with lower isotopic values during interglacial periods

and higher during glacial periods. Large abrupt increases are consistently observed throughout both records. For instance, in the *G. bulloides* $\delta^{18}\text{O}$ record, the abrupt shift between MIS 5e and the cold interglacial substage MIS 5d shows a shift of 1.8‰ and the transition between MIS 5e and MIS 4 exhibits an abrupt change of 2‰. A similar pattern is observed in the *G. inflata* $\delta^{18}\text{O}$ record, albeit with lower amplitudes, with increases of 0.8‰ during MIS 5d and 1.2‰ during the transition from MIS 5e to MIS 4.

The $\Delta\delta^{18}\text{O}$ record was employed to reconstruct upper ocean stratification over the studied period, with low $\Delta\delta^{18}\text{O}$ values indicating reduced stratification between the surface and thermocline layers, while high values represent increased stratification (Fig. 19B). The $\Delta\delta^{18}\text{O}$ record ($n = 497$) ranges from -1.19 ‰ to 1.36 ‰, with an average of 0.29 ‰. Periods of decreased stratification coincide with the abrupt $\delta^{18}\text{O}$ increases in the individual records.

Globigerina bulloides $\delta^{13}\text{C}$ record ($n = 503$) ranges from -1.70 ‰ to 0.82 ‰, with an average of -0.38 ‰. *Globorotalia inflata* $\delta^{18}\text{O}$ record ($n = 502$) ranges from -0.79 ‰ to 1.04 ‰, with an average of 0.41 ‰ (Fig. 19D). Both records exhibit similar variability, with glacial-interglacial patterns showing lower isotopic values during interglacial periods and higher values during glacial periods. Consistent with their respective $\delta^{18}\text{O}$ record, the $\delta^{13}\text{C}$ for both species also display simultaneous abrupt increases.

The *Cibicides wuellerstorfi* $\delta^{13}\text{C}$ record ($n = 429$) is not continuous throughout the whole core due to intervals where this species was absent. On those levels, *U. peregrina* ($n = 105$) was chosen to compose the benthic $\delta^{18}\text{O}$ record ($n = 534$). $\delta^{13}\text{C}$ results from *U. peregrina* are not used to construct a high-resolution composite record since this species' habitat is placed deeper in the sediment, and its $\delta^{13}\text{C}$ values bias the $\delta^{13}\text{C}_{\text{DIC}}$. *Cibicides wuellerstorfi* $\delta^{13}\text{C}$ record ranges from -0.75 ‰ to 0.80 ‰, with an average of 0.13 ‰. Benthic foraminifera composite $\delta^{18}\text{O}$ record ranges from 2.34 ‰ to 4.62 ‰, with an average of 3.75 ‰. Both records exhibit similar patterns of variation, with higher values during glacial periods and lower values during interglacial periods.

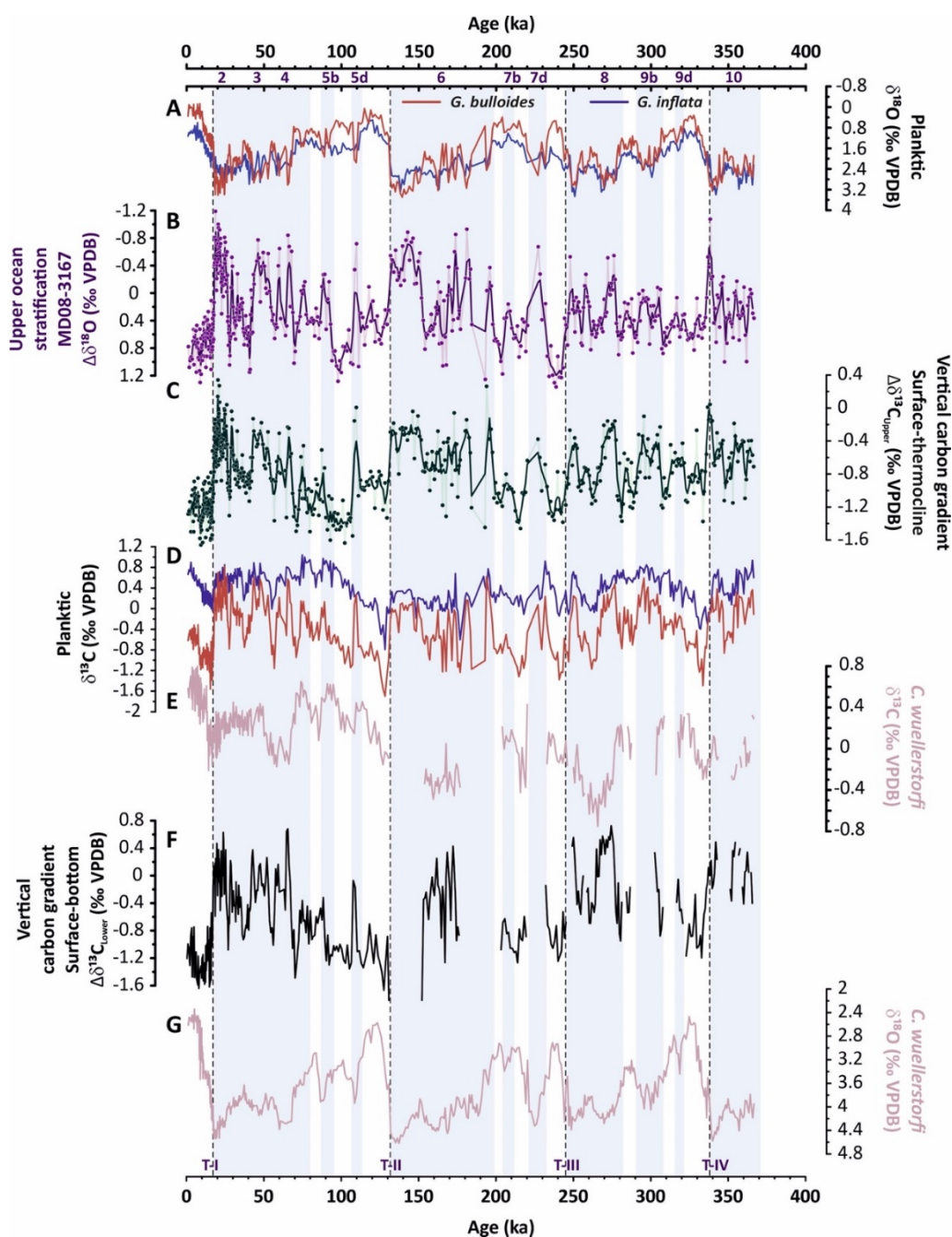
Comparing isotopic records, similar abrupt increasing shifts occurred simultaneously and were documented by independent proxies (i.e., $\delta^{18}\text{O}$ and $\delta^{13}\text{C}$), leading us to presume that they are connected and driven by the same mechanism. These shifts primarily occur during glacial periods and colder substages, as defined based on the benthic foraminifera $\delta^{18}\text{O}$ record.

The $\Delta\delta^{13}\text{C}_{\text{upper}}$ and $\Delta\delta^{13}\text{C}_{\text{lower}}$ records are used to reconstruct vertical carbon transfer between the surface and thermocline, as well as between the thermocline and the benthic layers. High $\Delta\delta^{13}\text{C}_{\text{upper}}$ and $\Delta\delta^{13}\text{C}_{\text{lower}}$ values indicate increased vertical carbon export to the ocean floor, while low values suggest decreased carbon transfer. Both $\Delta\delta^{13}\text{C}_{\text{upper}}$ and $\Delta\delta^{13}\text{C}_{\text{lower}}$ records exhibit similar abrupt shifts on the individual $\delta^{13}\text{C}$ records (Fig. 19C). The $\Delta\delta^{13}\text{C}_{\text{upper}}$ record ($n = 497$) ranges from -1.66 ‰ to 0.34 ‰, with an average of -0.79 ‰. $\Delta\delta^{13}\text{C}_{\text{lower}}$ records ($n = 408$) ranges from -1.67 ‰ to 0.73 ‰, with an average of -0.53 ‰ (Fig. 19F).

5.2.2 Time-series analysis

The results of the REDFIT spectral analysis consistently reveal the presence of the same dominant frequencies within the precession, obliquity, and eccentricity domains for the *G. bulloides* and *G. inflata* $\delta^{18}\text{O}$ records, as well as for the $\Delta\delta^{18}\text{O}$ record. *Globigerina bulloides* $\delta^{18}\text{O}$ exhibits spectral power exceeding 99% within the precession and eccentricity domains and 95% within the obliquity domain. *Globorotalia inflata* $\delta^{18}\text{O}$ exhibits spectral power above 99% on the eccentricity domain, 90% for precession, and 95% for obliquity. The spectral power is particularly pronounced within the eccentricity frequency for both species. Furthermore, the $\Delta\delta^{18}\text{O}$ exhibits spectral power for all three forcing above the 95% confidence level.

Figure 19 - Records from core MD08-3167 located at the Northern Benguela Upwelling System (NBUS). A) *Globigerina bulloides* (red line) and *Globorotalia inflata* (blue line) $\delta^{18}\text{O}$ records (‰ VPDB). B) Upper-ocean stratification record (transparent purple line with circles; $\Delta\delta^{18}\text{O} = \delta^{18}\text{O}_{G.inflata} - \delta^{18}\text{O}_{G.bulloides}$; ‰ VPDB) with three-point running average (solid purple line). C) Upper-vertical $\delta^{13}\text{C}$ gradient between surface and thermocline layers ($\Delta\delta^{13}\text{C}_{\text{upper}} = \delta^{13}\text{C}_{G.bulloides} - \delta^{13}\text{C}_{G.inflata}$; ‰ VPDB; transparent green line with circles) with three-point running average (solid green line). D) *Globigerina bulloides* (red line) and *Globorotalia inflata* (blue line) $\delta^{13}\text{C}$ records (‰ VPDB). E) *Cibicides wuellerstorfi* $\delta^{13}\text{C}$ (pink line; ‰ VPDB). F) Lower-vertical $\delta^{13}\text{C}$ gradient between thermocline and benthic layers ($\Delta\delta^{13}\text{C}_{\text{lower}} = \delta^{13}\text{C}_{G.inflata} - \delta^{13}\text{C}_{C.wuellerstorfi}$; ‰ VPDB; black line). G) Benthic foraminifera $\delta^{18}\text{O}$ composite record composed by *C. wuellerstorfi* (corrected by a factor of plus 0.64 ‰) and *U. peregrina* $\delta^{18}\text{O}$ values (pink line; ‰ VPDB). Vertical blue bars mark glacial periods and cold interglacial substages. Vertical dashed lines mark glacial Terminations. All records are plotted against age (ka)



5.3 Discussion

5.3.1 Upper ocean stratification tracks northern NBUS activity

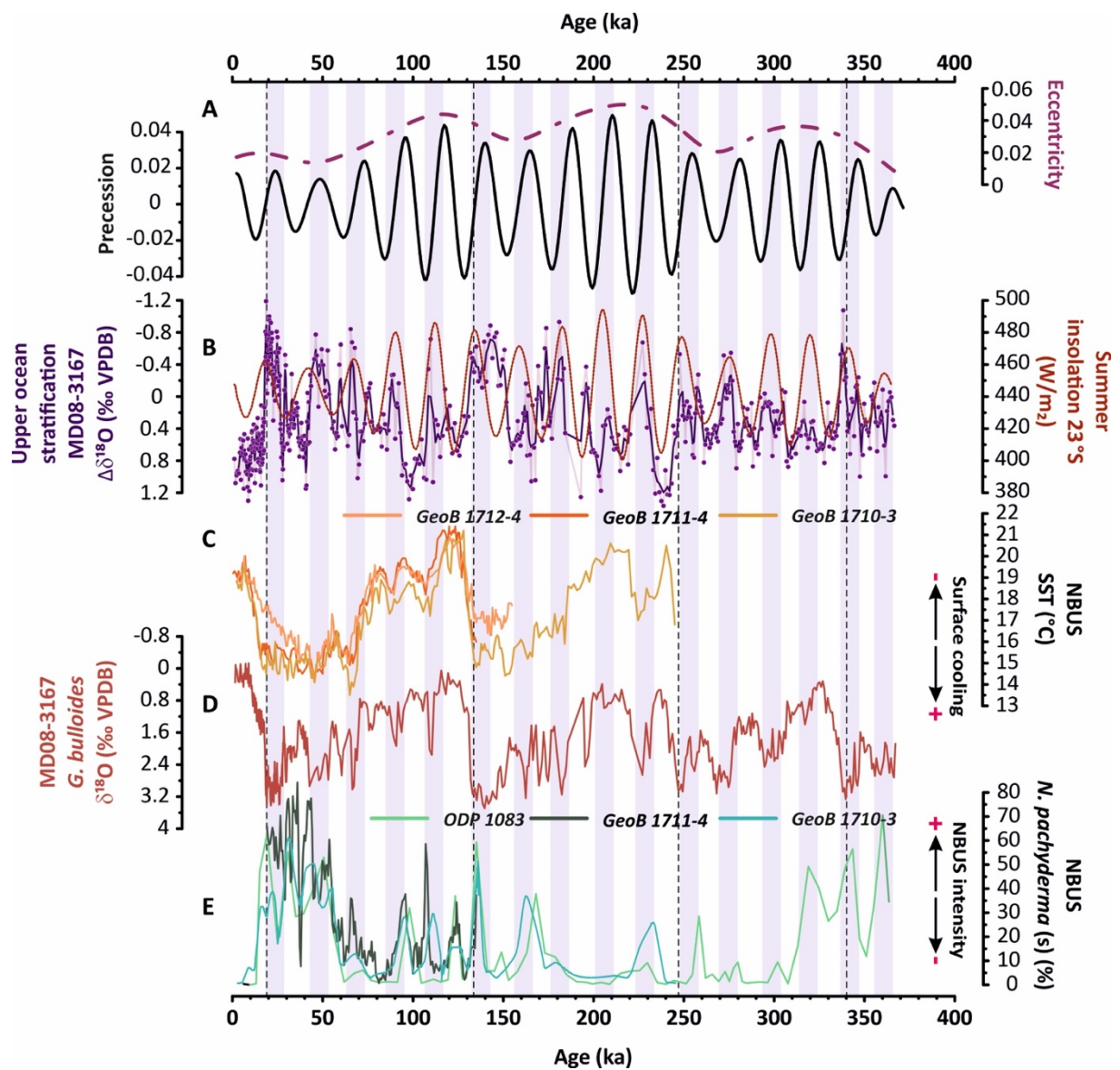
Previous research has demonstrated that utilizing the $\delta^{18}\text{O}$ difference between surface and thermocline foraminiferal species is an effective method for determining the stratification of the upper ocean (Mulitza *et al.*, 1997; Scussolini and Peeters, 2013; Venancio *et al.*, 2018; Nascimento *et al.*, 2021). We applied our $\Delta\delta^{18}\text{O}$ gradient (Fig. 19B) from the MD08-3167 core to track NBUS activity over the last 365 ka. Results show a G-IG variability that suggests greater stratification during interglacial periods. The $\Delta\delta^{18}\text{O}$ systematically decreases during glacial periods and cold substages, showing a reduced stratification corresponding with a rapid increase in *G. bulloides* and *G. inflata* $\delta^{18}\text{O}$ values (Fig. 19A and B). Both isotope records have similar values but *G. inflata* $\delta^{18}\text{O}$ has smaller amplitude and slightly higher values than *G. bulloides* $\delta^{18}\text{O}$ than over the studied period. However, similar periodic $\delta^{18}\text{O}$ decreases during reduced stratification periods approximate thermocline and surface isotopic values, implying a more homogeneous upper ocean at NBUS, likely in response to strengthening wind patterns (Fennel *et al.*, 2012; Bordbar *et al.*, 2021). Wind intensification favors the Ekman pump at the surface, bringing cold SACW waters to the upper ocean layers at this location. Even though $\delta^{18}\text{O}$ might be influenced by other parameters, such as ice volume, temperature, and salinity, similarities between both $\delta^{18}\text{O}$ records led us to assume that the same forcing controls them. SST records from nearby cores GeoB 1712-4, GeoB 1711-4, and GeoB 1710-3 (Fig. 20C) show a systematic SST cooling that matches both increasing $\delta^{18}\text{O}$ and decreasing $\Delta\delta^{18}\text{O}$ values, even though these SST records do not cover all our studied period, which suggest that temperature might be the predominant parameter controlling our $\delta^{18}\text{O}$ records (Fig. 20C; Kirst *et al.*, 1999; Volbers *et al.*, 2003). Other SST records from this region, e.g., GeoB 1028-5 SST at Walvis Ridge, also have a similar pattern. This strongly suggests that cold surface waters could have occurred due to decreased stratification, likely in response to the wind-driven SACW intrusion into the surface (Schneider *et al.*, 1995; Kirst *et al.*, 1999).

Reduced stratification associated with surface cooling at NBUS is related to upwelling activity in response to trade winds intensification (Shannon, 1985). In addition, upwelling intensification would increase the nutrient supply to the surface and enhances primary productivity (Shannon, 1985; Christensen and Giraudeau, 2002). Rapid decreases

in $\Delta\delta^{18}\text{O}$ occur when *N. pachyderma* abundance peaks at ODP Site 1083, GeoB 1711-4, and GeoB 1710-3 are observed (Fig. 20E; Schneider *et al.*, 1995; Little *et al.*, 1997; West *et al.*, 2004). At NBUS, high abundances of this species are connected with eutrophic, nutrient-rich, and cooler surface waters associated with intensified upwelling activity (Little *et al.*, 1997). Timing dissimilarities between *N. pachyderma* abundance and $\Delta\delta^{18}\text{O}$ record might be related to different age model uncertainty and construction methods between the records or possibly lateral transport during foraminifera deposition.

These NBUS records have a precessional frequency suggesting similar orbital controls over our stratification proxy (Schneider *et al.*, 1995; Little *et al.*, 1997; West *et al.*, 2004). Decreased stratification controlled by the upwelling occurs particularly during positive precession periods when Southern Hemisphere summers are intensified (Fig. 20) (Little *et al.*, 1997; West *et al.*, 2004; Paillard, 2021). NBUS intensification would have expanded the coastal upwelling area westward in response to stronger winds, reaching the MD08-3167 site (Little *et al.*, 1997; Volbers *et al.*, 2003; West *et al.*, 2004).

Figure 20 - Precessionally-paced stratification records register NBUS upwelling activity, showing upwelling intensification during austral summer insolation maxima during positive precession periods. A) Eccentricity (purple dashed line) and precession (black line) forcing (Laskar *et al.*, 2004). B) Upper-ocean stratification record (purple line with transparency; $\Delta\delta^{18}\text{O}$; ‰ VPDB) with three-point running average (purple line); and February insolation at 23°S (red dashed line). C) Alkenone-based sea surface temperature records (SST; °C) from GeoB1712-4 (light orange line), GeoB 1711-4 (dark orange line), GeoB 1710-3 (dark yellow line) (Kirst *et al.*, 1999). D) Globigerina bulloides $\delta^{18}\text{O}$ (light red line; ‰ VPDB) from core MD08-3167. E) *Neogloboquadrina pachyderma* abundance records (%) from ODP Site 1083 (light green line; West *et al.*, 2004); GeoB 1711-4 (dark green line; Little *et al.*, 1997); GeoB 1710-3 (neon-like green line; Volbers *et al.*, 2003). Vertical bars highlight periods of upwelling intensification at NBUS following austral summer insolation maxima. Vertical dashed lines mark glacial Terminations. All records are plotted against age (ka)



Spectral analysis performed on *G. bulloides* $\delta^{18}\text{O}$, *G. inflata* $\delta^{18}\text{O}$, and $\Delta\delta^{18}\text{O}$ records shows similar results, with statistically significant spectral power on the precession (23 ka),

obliquity (41 ka), and eccentricity (100 ka) domains within the lowest confidence level of 90% (Fig. 21). Similar dominance by these orbital forcings is also observed in the stratification record from the western tropical South Atlantic, as well as foraminiferal assemblages and SST records from Walvis Ridge (Schneider *et al.*, 1995; Schneider *et al.*, 1996; Chen *et al.*, 2002; West *et al.*, 2004; Nascimento *et al.*, 2021). The precessional pace (up to 95% confidence level) on our isotopic records would explain their similarities and the good agreement of $\Delta\delta^{18}\text{O}$ and summer insolation at 23°S, which is dominated by changes in precession (Fig. 31A and B; Berger and Loutre, 1991). Therefore, it explains all upwelling intensification events indicated in our $\Delta\delta^{18}\text{O}$ record occurring during precession maxima periods during austral summer at perihelium and increased stratification during periods of precession minima during boreal summer at perihelium (Fig. 20).

The strongest orbital power in all the records analyzed is on the eccentricity band, likely related to its modulation of precession amplitude, which is similarly observed in the western African records due to eccentricity-modulated insolation forcing (Chase, 2021). Despite having a strong eccentricity spectral power, our records suggest that low-latitude forcing is the dominant factor in the upwelling activity at NBUS due to the good correlation with summer insolation, also found in other records from southeastern and southernmost Africa (Collins *et al.*, 2011, 2014; Chase, 2021). Obliquity forcing strongly influences mid-to-high latitudes by exercising controls over the meridional temperature gradient that regulates the westerly and trade winds intensity (McCreary and Lu, 1994; Klinger and Marotzke, 2000; Lass and Mohrholz, 2008; Timmermann *et al.*, 2014). Although trade winds are perennial all year at NBUS (Hutchings *et al.*, 2009; Schmidt and Eggert, 2016), at modern conditions, intensification occurs during austral winter season and late summer, increasing the primary productivity at the Namibia margin (Carr, 2002; Carr and Kearns, 2003; Louw *et al.*, 2016; Ohde and Dadou, 2018). Enhanced austral summer insolation during positive precession would have strengthened summer insolation and winter duration, both amplifying the upwelling activity.

Coherently with the asymmetrical inter-hemispheric trade wind dynamic (McGee *et al.*, 2018), Prange and Schulz (2004) argue an antiphase intensity between coastal upwelling zones in northwestern and southwestern Africa. Sedimentation of dust-related particles at the Iberian margin shows strong winds associated with boreal insolation maxima during precession minima episodes in response to intense surface heating and low pressure over the

North African Sahara that contributed to the intensification of western African monsoon (Hodell *et al.*, 2013; Skonieczny *et al.*, 2019). This configuration promotes an opposite effect in the South Atlantic by weakening the trade winds zonality, which decreases the upwelling at NBUS (Schneider and Müller, 1996; West *et al.*, 2004). During precession maxima episodes, weak western African monsoon increased trade wind zonality and induced the upwelling, reducing the stratification and would increase the subtropical-tropical connections (Lass and Mohrholz, 2008; Cabré *et al.*, 2019; Nascimento *et al.*, 2021). Accordingly, wind strength at the southeastern Atlantic shows intensified winds during glacial and positive precession periods, supporting our interpretations (Fig. 31F; Stuut *et al.*, 2002). The enhanced trade wind zonality during positive precession periods increases the subtropical-tropical connections by (1) enhancing the Subtropical Cell that transfers thermocline waters toward tropical regions; and (2) enhancing the BeC that feeds the SEC flowing toward the Brazilian margin (Lass and Mohrholz, 2008; Garzoli and Matano, 2011), piling up waters in the western Tropical South Atlantic that reduced tropical stratification (Nascimento *et al.*, 2021). This low-latitude forcing over subtropical regions would therefore explain a similar stratification pattern observed in the western Tropical Atlantic, which also shows decreased stratification during positive precession (Nascimento *et al.*, 2021). Therefore, we assume that our $\Delta\delta^{18}\text{O}$ record reconstructs a high-resolution NBUS upwelling activity record over the last 365 ka, showing upwelling intensification on the orbital scale following precessionally-driven austral insolation maxima.

Figure 21 - REDFIT spectral analysis (Schulz and Mudelsee, 2002) results performed in MD08-3167 records. A) $\Delta\delta^{18}\text{O}$ record, B) *Globigerina bulloides* $\delta^{18}\text{O}$ record, C) *Globorotalia inflata* $\delta^{18}\text{O}$ record. Results reveal relevant spectral power (Y axes) above the 90% confidence intervals in the precession, obliquity, and eccentricity frequency domains (X axes). Confidence level baselines (green and orange) and significant spectral periodicities are indicated

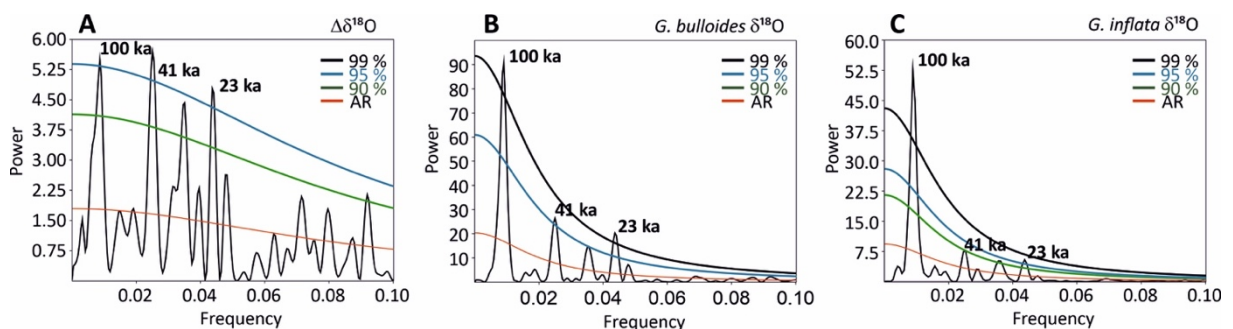
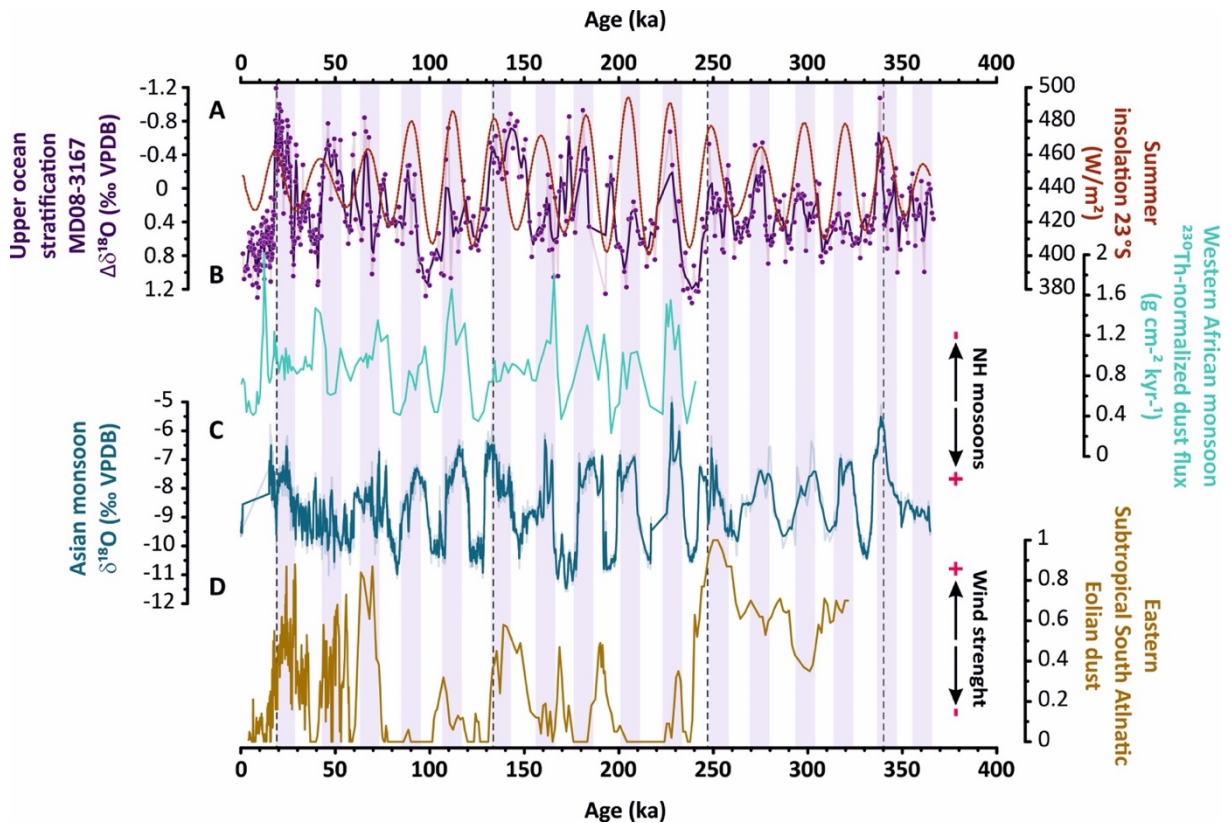


Figure 22 - Trade winds intensification in response to decreased Northern Hemisphere monsoon systems during periods of reduced upper-ocean stratification and related upwelling intensification at NBUS. A) Upper-ocean stratification record (purple line with transparency; $\Delta\delta^{18}\text{O}$; ‰ VPDB) with three-point running average (purple line); and February insolation at 23°S (red dashed line). B) three-point running average ^{230}Th -normalized Sahara dust fluxes from sediment core MD03-2705 (light green line; $\text{g cm}^{-2} \text{ kyr}^{-1}$; Skonieczny *et al.*, 2019). C) Speleothem $\delta^{18}\text{O}$ record of Asian monsoon system (dark green line; ‰ VPDB; Cheng *et al.*, 2016). D) Wind strength proxy from the Eastern subtropical South Atlantic (brown line; Stuuat *et al.*, 2002). Vertical bars highlight periods of upwelling intensification at NBUS following austral summer insolation maxima. Vertical dashed lines mark glacial Terminations. All records are plotted against age (ka)



5.3.2 The mechanism behind precessionally-paced NBUS intensification

The NBUS intensification during austral summer insolation maxima shown by precessionally-paced decreases in our $\Delta\delta^{18}\text{O}$ record responds to the zonally-intensified SE trade winds blowing parallel to the African coast, expanding the coastal upwelling cell offshore. The strength and movement of the SE trade winds are controlled by the South Atlantic Hadley cell and the location of the ITCZ as a result of the asymmetrical atmospheric response to the energy balance between the hemispheres (Marshall *et al.*, 2014). Therefore, the mechanism behind trade winds intensifications during positive precession would demand a northward ITCZ position promoted by vigorous inter-hemispheric heat transport by the AMOC during these periods.

Perturbations on inter-hemispheric energy balance are observed through the expansion of North Atlantic cooling during cold millennial-scale events (a.k.a., stadials) of the last glacial and deglacial period, affecting the South Atlantic atmospheric patterns (Blunier and Brook, 2001; Broecker, 2003; Anderson *et al.*, 2009). The North Atlantic cooling slows deep-water formation, reducing the AMOC transport that traps heat in the South Atlantic, promoting the bipolar seesaw (Broecker, 2003; Barker *et al.*, 2009; Pedro *et al.*, 2018). A warmer South Atlantic due to reduced cross-equatorial heat transport promotes the southward shift of the ITCZ, resulting in the expansion and intensification of the North Atlantic Hadley Cell and related NE trade winds (Peterson, 2000; Broccoli *et al.*, 2006; Marshall *et al.*, 2014; McGee *et al.*, 2014). The opposite pattern is observed during warm interstadial periods (Broecker, 1998; Barker *et al.*, 2009; Pedro *et al.*, 2018). In agreement, proxy-based records show that during stadials, the ITCZ shifted southward, which decreased SE trade winds and the upwelling activity at NBUS (Little *et al.*, 1997; Stuetz *et al.*, 2002; Kim *et al.*, 2003; McGee *et al.*, 2018). The opposite pattern is observed along the northwest African margin in response to the North Atlantic cooling, increasing the NE trade winds and related upwelling activity (Prange and Schulz, 2004; Adkins *et al.*, 2006; Romero *et al.*, 2008; Deplazes *et al.*, 2013; McGee *et al.*, 2013).

Perturbations on inter-hemispheric temperature gradients would also be expected during precession cycles. Following the mechanism proposed during millennial-scale events, enhanced austral summer insolation during positive precession would warm the Southern Hemisphere, resulting in a reduced temperature gradient that would force the ITCZ to move southward (Toggweiler and Lea, 2010). However, this explanation would contradict our findings of increased upwelling activity at NBUS, since the southward ITCZ position would decrease the SE trade winds intensity. We suggest here that the sequence of events happening during precessional cycles, although acting through similar mechanisms than during millennial-scale events, promotes an opposite effect on controlling the cross-equator AMOC fluxes, resulting atmospheric responses, and NBUS upwelling.

During millennial-scale events, deep-water formation in the North Atlantic is constantly suppressed by enhanced meltwater fluxes to the ocean, slowing down the AMOC (McManus *et al.*, 2004). In contrast, Lisiecki *et al.* (2008) used benthic foraminifera $\delta^{13}\text{C}$ records from mid-depths in the Atlantic to show that the deep-water formation rate intensifies during more intense southern summers. They suggest that AMOC is stronger

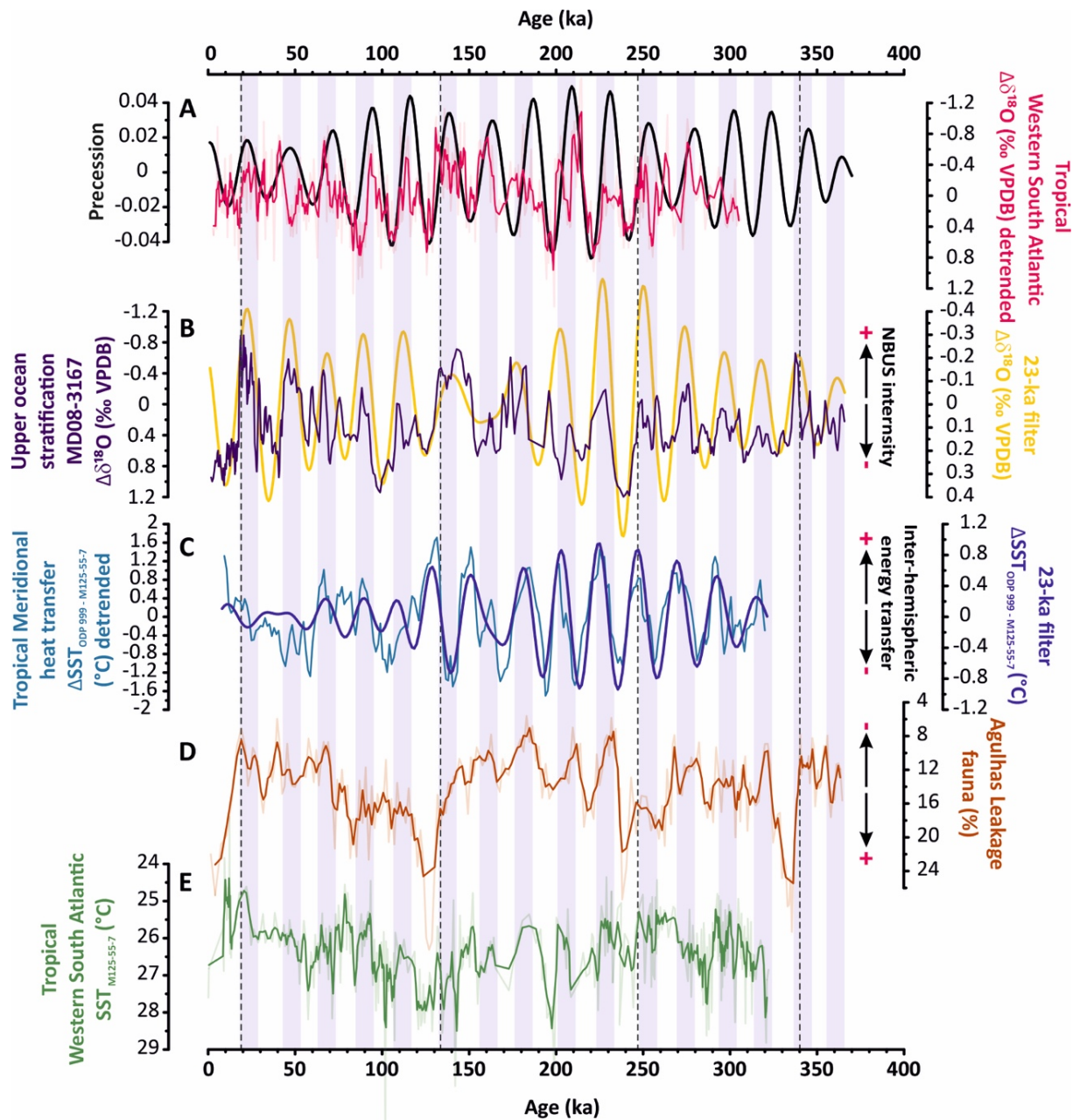
during positive precession periods when North Atlantic is cooler (Lisiecki *et al.*, 2008), which supports the NBUS intensification during this period. We assess the efficiency of the inter-hemispheric energy transfer by calculating the tropical SST gradient between core M125-55-7 located at 20°S in the western tropical South Atlantic and ODP site 999 located at 12°N in the western tropical North Atlantic ($\Delta\text{SST}_{\text{ODP 999-M125-55-7}}$; Fig. 23C) (Schmidt *et al.*, 2006; Hou *et al.*, 2020). Positive values during precession maxima episodes suggest that SST in the tropical western North Atlantic is higher likely in response to the efficient northward heat transfer cooling the western tropical South Atlantic (Fig. 22C and D; Hou *et al.*, 2020). Surface evidence from *G. truncatulinoides* (sinistral) abundance from the western Tropical North Atlantic corroborate our argument by showing intensified cross-equatorial transport during precession maxima (Kaiser *et al.*, 2019). According to Crowley (1992), when large amounts of deep water are formed and exported southward at depths, the upper branch of the AMOC may boost inter-hemispheric transport as a global circulation response. The flow of warm water towards the north helps to balance the deep-water flow. This cools the southern hemisphere and transfers heat from the warmer tropical North Atlantic waters to cooler subpolar regions, operating as the North Atlantic heat piracy during positive precession (Crowley, 1992).

Sediment cores from subantarctic regions and temperature data from Antarctica reveal that warmer southern summers resulted in cooler summer temperatures at South Atlantic high latitudes (Barrows *et al.*, 2007; Kawamura *et al.*, 2007). This corroborates our finding of a stronger AMOC during positive precession periods carrying heat toward North Atlantic but also means the decreased delivery of subtropical warm waters in the southern high latitudes. Therefore, it would also demand a northward position of the South Atlantic Current, the southern branch of the SASG (Peterson and Stramma, 1991; Garzoli and Matano, 2011). A cooling Antarctica may have also pushed the westerlies to a northern position, shifting the ITCZ northward and intensifying SE trade winds during positive precession periods (Toggweiler *et al.*, 2006; Bard and Rickaby, 2009). The northward movements of these atmospheric components promotes a similar shift on the subtropical fronts, closing the gateway for an important source of heat and salt to the SASG by diminishing the Indo-Atlantic exchange through the AL to the South Atlantic (Gordon, 1986; Weijer, 2002; Peeters *et al.*, 2004; Beal *et al.*, 2011). The behavior of the Agulhas Leakage fauna (ALF) from the Cape Basin proposed by Peeters *et al.* (2004) as a proxy for AL

intensity corroborates our interpretations. The ALF record displays a consistent decrease during positive precession periods that is coeval with the decreased SST in the western Tropical Atlantic at 20°S and increased subsurface temperature further north at 8°S, likely in response to intensified heat transfer toward the North Atlantic (Fig. 22D; Hou *et al.*, 2020; Nascimento *et al.*, 2021). A northward SASG also contributes to cool temperatures at high latitudes since warm subtropical waters are delivered far north (Barrows *et al.*, 2007; Kawamura *et al.*, 2007). Hence, the ocean-atmospheric dynamics linked to meridional shifts of the SASG is crucial in exercising control over AMOC states and related NBUS activity.

The proposed mechanism acting through SASG meridional shifts and inter-hemispheric energy transfer during positive precession periods implies that intensified AL occurred during negative precession periods when AMOC was reduced (Fig. 23D). Similar to what has been proposed for modern-like conditions, a possible explanation for this apparent contradiction would be an intensified SASG circulation when the gyre is deflected to the south, likely in response to the increased contribution of the AL to the South Atlantic (Marcello *et al.*, 2023). The SASG would therefore act as a heat reservoir during negative precession that releases its energy to the North Atlantic in response to perturbations on the inter-hemispheric energy balance during positive precession periods (Ballalai *et al.*, 2019). This SASG ocean-atmospheric dynamic allows us to suggest that there is a seesaw pattern between NBUS and AL through the precessional cycles. Pinho *et al.* (2021) suggested that during intense stadials periods in the North Atlantic (a.k.a Heinrich events), the SASG was displaced southward, likely in response to the AMOC slowdown and the related ITCZ dynamic already discussed here. By following the same reasoning, the opposite behavior of the SASG would be expected during positive precession periods, favoring the northward movement of the ITCZ. Therefore, meridional SASG shifts thus plays a key role in controlling the energy transfer across the equator, which is important for maintaining the global energy balance during the precessional cycles.

Figure 23 - Mechanism controlling upwelling intensification at NBUS. A) three-point running average of $\Delta\delta^{18}\text{O}$ (‰ VPDB) record from tropical South Atlantic (pink line; Nascimento *et al.*, 2021) and precession (black line; Laskar *et al.*, 2004). B) three-point running average of $\Delta\delta^{18}\text{O}$ (‰ VPDB) record (dark purple line) and respective 23-ka LOESS filter (yellow line). C) Sea surface temperature (SST) gradient between cores M125-55-7 and ODP Site 999 ($\Delta\text{SST}_{\text{ODP 999} - \text{M125-55-7}}$, blue line; °C), and respective 23-ka LOESS filter (violet line) (Schmidt *et al.*, 2006; Hou *et al.*, 2020). D) Agulhas Leakage fauna record (transparent orange line; Peeters *et al.*, 2004) and respective three-point running average (solid orange line). E) Southern tropical South Atlantic SST from core M125-55-7 (transparent green line; Hou *et al.*, 2020; °C) and respective three-point running average (solid green line). Vertical bars highlight periods of upwelling intensification at NBUS. Vertical dashed lines mark glacial Terminations. All records are plotted against age (ka)



5.3.3 Implications for global atmospheric CO₂

Periods of enhanced upwelling at NBUS would have significantly increased primary productivity observed through a good correlation between our $\Delta\delta^{18}\text{O}$ record and the abundances of *N. pachyderma* species (Fig. 20B and E). Although upwelling regions can be areas of either source or sink of CO₂ to the atmosphere due to ocean-atmosphere gas exchanges, at the present day, the NBUS acts as an atmospheric CO₂ sink since the biological activity exceeds the thermodynamic CO₂ outgassing (González-Dávila *et al.*, 2009; Emeis *et al.*, 2018). Thus, we evaluate if periods of intensified coastal upwelling at NBUS may have had a significant impact on the global carbon cycle by capturing atmospheric CO₂ and storing it in the deep ocean during periods of positive precession.

The $\delta^{13}\text{C}$ vertical profile in the ocean is a useful way to measure the productivity of the upper ocean. ¹²C is preferentially uptaken from the surface waters during photosynthesis, which leaves the surrounding waters more enriched with ¹³C. Therefore, we use vertical $\Delta\delta^{13}\text{C}$ gradients to evaluate the biological pump efficiency associated with upwelling events during positive precession periods. Both *G. bulloides* and *G. inflata* $\delta^{13}\text{C}$ records systematically display increased values in the same periods as the $\Delta\delta^{18}\text{O}$ record (Fig. 19B and D). Although the foraminifera $\delta^{13}\text{C}$ signal from surface layers suffers constant fractionation due to contact with the atmosphere, the amplitude of *G. bulloides* $\delta^{13}\text{C}$ increases during these periods is up to 1 ‰ (Fig 30D). Studies have shown that the isotopic fractionation in surface-dwelling foraminifera species related to CO₂ exchanges may range between 0.4-0.7 ‰ (Duplessy *et al.*, 1988), only partially explaining the amplitude of *G. bulloides* $\delta^{13}\text{C}$ increases. We believe the strong amplitude of these changes is likely also a response to ¹³C-enriched waters in the upper ocean resulting from intensified photosynthesis. Although it is difficult to rule it out, we evaluate the efficiency of the biological pump through our $\Delta\delta^{13}\text{C}$ gradients to avoid misinterpretations. Besides, with this approach, any additional carbon source affecting oceanic $\delta^{13}\text{C}$, such as continental input, can be negligible since it would have affected the whole water column equally. We first assess the carbon transfer from the surface to the thermocline layers by calculating the vertical $\delta^{13}\text{C}$ gradient between *G. bulloides* and *G. inflata* $\delta^{13}\text{C}$ ($\Delta\delta^{13}\text{C}_{\text{upper}}$), then from the thermocline to the deep ocean between *G. inflata* and benthic foraminifera *C. wuellerstorfi* $\delta^{13}\text{C}$ ($\Delta\delta^{13}\text{C}_{\text{lower}}$) (Fig. 24B and C). The $\Delta\delta^{13}\text{C}_{\text{upper}}$ record shows mostly negative values but with drastic increases

concomitant with upwelling-related $\Delta\delta^{18}\text{O}$ decreases (Fig. 24A and B). Thus, surface and thermocline $\delta^{13}\text{C}$ differences are reduced during intensified upwelling at NBUS, which would be coherent with a homogeneous upper layer with enhanced upper ocean primary productivity, supporting our initial hypothesis of upwelling governing both individual $\delta^{13}\text{C}$ records. The partial $\Delta\delta^{13}\text{C}_{\text{lower}}$ record also consistently rises during these periods, which leads us to interpret that during NBUS intensification periods, a great part of the carbon uptaken in the surface is transferred to the bottom.

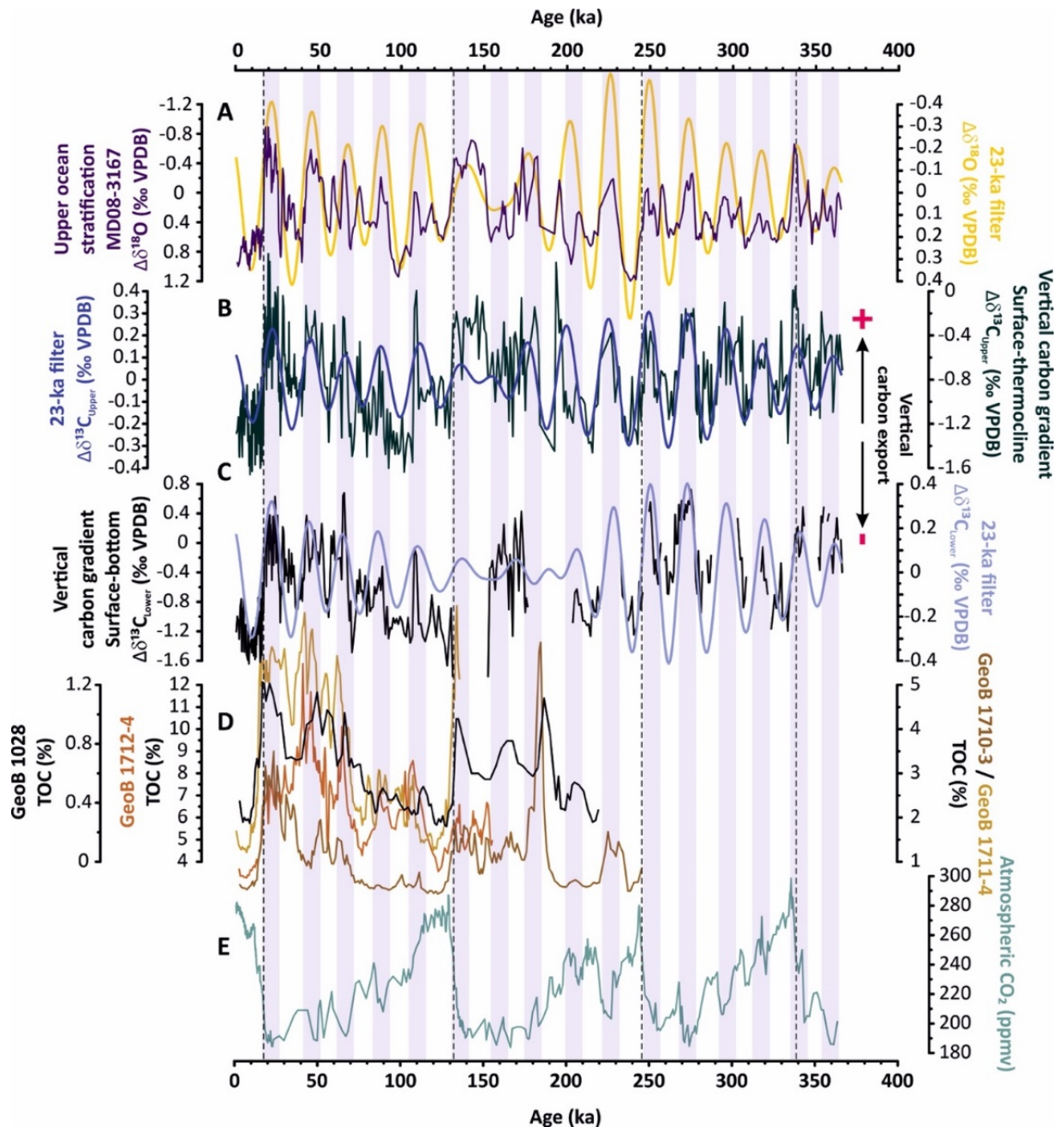
The similarities between $\Delta\delta^{18}\text{O}$, $\Delta\delta^{13}\text{C}_{\text{upper}}$, and $\Delta\delta^{13}\text{C}_{\text{lower}}$ are evidenced by the good match between each of the 23-ka LOESS bandpass filtering applied to these records, corroborating our suspicions of the upwelling controls on both vertical carbon gradients following austral summer insolation during positive precession (Fig. 24A to C). In agreement, Total Organic Carbon (TOC) records from NBUS sites GeoB 1028, GeoB 1712-4, GeoB 1711-4, and GeoB 1710-3 show increased content during periods of intensified upwelling (Fig. 24D; Schneider *et al.*, 1996; Kirst *et al.*, 1999) roughly coeval with our records within the uncertainties of the respective age models.

Increased subtropical-tropical connections due to zonally-intensified trade winds also enhance the SEC and the South Equatorial Counter Current (SECC) that feeds the Angola Gyre, increasing the transport of thermocline waters via Angola Current to NBUS (Lass and Mohrholz, 2008; Mohrholz *et al.*, 2008). During austral summer, less-ventilated (i.e., “older”), hypoxic, nutrient-rich WSACW formed in the Brazil-Malvinas Confluence is delivered to the NBUS until 27°S, whereas during austral winter, the oxygen-rich ESACW formed in the Cape of Good Hope close to AL region is spread northward (Lass and Mohrholz, 2008; Mohrholz *et al.*, 2008; Fennel *et al.*, 2012). We speculate that this seasonal dynamic could be applied to the precessional cycles through our proposed mechanism. During summer insolation maxima, the northward position of the SASG prevented AL waters from entering the South Atlantic, which reduced the contribution of ESACW to NBUS (Lass and Mohrholz, 2008; Tim *et al.*, 2018). Meanwhile, the zonally-intensified trade winds favored intrusions of WSACW to the north of NBUS, feeding the thermocline layers of oxygen-poor and nutrient-rich waters that would have boosted primary productivity during positive precession periods. Therefore, the seesaw pattern between AL and NBUS promoted by SASG dynamics would play an important role also in controlling the properties of the upwelled waters on NBUS, directly impacting the amplitude and efficiency of the biological

pump. Consequently, we expect this change in the source of the SACW upwelled at NBUS to have the potential to amplify the upwelling magnitude, resulting in a significant reduction in atmospheric CO₂ levels.

Indeed, if more carbon has accumulated in the deep ocean during positive precession periods, it would significantly impact global climate by reducing atmospheric CO₂. In agreement, the atmospheric CO₂ record from the European Project for Ice Coring in Antarctica (EPICA) Dome C shows that CO₂ reductions are coeval with inferred intensified upwelling at NBUS (Fig. 24E). Although we are tempted to associate it with the increased efficiency of the NBUS biological pump, it is unlikely that the observed atmospheric CO₂ decrease is solely attributed to NBUS. Our proposed mechanism demands cooler Antarctic temperatures and a northward position of the SASG. This scenario must have shifted westerlies northward far from the Drake Passage latitude, which reduced the upwelling in the Southern Ocean and prevented CO₂ outgassing from deep layers (Toggweiler *et al.*, 2006; Barrows *et al.*, 2007; Kawamura *et al.*, 2007). This ocean-atmospheric dynamic would explain the remarkable match between our both $\Delta\delta^{13}\text{C}$ gradients and the vertical $\Delta\delta^{13}\text{C}$ between South Atlantic Mode Water (SAMW) and Circumpolar Deep Water (CDW) from subantarctic regions where a stronger chemical gradient occurs when atmospheric CO₂ is lower (Ziegler *et al.*, 2013). The low- $\delta^{13}\text{C}$ signal from the Southern Ocean is prevented from being transferred via SAMW northward in response to decreased CDW upwelling close to Antarctica, increasing the vertical $\Delta\delta^{13}\text{C}$ at the southern Agulhas Plateau (Ziegler *et al.*, 2013). Therefore, NBUS intensification (and potential CO₂ sequestration) would act together with reduced upwelling rates in the Southern Ocean, impacting the carbon cycle and the global climate by reducing atmospheric CO₂ during positive precession periods.

Figure 24 - Vertical carbon transfer during upwelling intensification at NBUS based on MD08-3167 isotopic records. A) three-point running average of $\Delta\delta^{18}\text{O}$ (‰ VPDB) record (dark purple line) and respective 23-ka LOESS filter (yellow line). B) Vertical $\delta^{13}\text{C}$ gradient between surface and thermocline layers ($\Delta\delta^{13}\text{C}_{\text{surface-thermocline}}$, dark green line; ‰ VPDB), and respective 23-ka LOESS filter (dark violet line). C) Vertical $\delta^{13}\text{C}$ gradient between thermocline and bottom layers ($\Delta\delta^{13}\text{C}_{\text{thermocline-bottom}}$, black line; ‰ VPDB), and respective 23-ka LOESS filter (light violet line). D) Total organic carbon (TOC) from GeoB 1028, GeoB 1712-4, GeoB 1711-4, and GeoB 1710-3 (‰; dark blue, light brown, dark brown, and gold yellow, respectively; Schneider *et al.*, 1996; Kirst *et al.*, 1999). D) Atmospheric CO_2 record from the European Project for Ice Coring in Antarctica (EPICA) Dome C ice core (ppmv; light green line; Jouzel *et al.*, 2007). Vertical bars highlight periods of upwelling intensification at NBUS following austral summer insolation maxima. Vertical dashed lines mark glacial Terminations. All records are plotted against age (ka)



5.4 Conclusions

This study uses the $\delta^{18}\text{O}$ gradient between *G. bulloides* and *G. inflata* species to reconstruct upper ocean stratification ($\Delta\delta^{18}\text{O}$) at the Northern Benguela Upwelling System (NBUS) over the last 365 ka. Our results show greater stratification during interglacial periods and systematic decreases during glacial periods and cold substages in response to intensified trade winds and increased upwelling activity. Spectral analysis performed on surface and thermocline $\delta^{18}\text{O}$ and $\Delta\delta^{18}\text{O}$ records show similar results with significant power on the precession, obliquity, and eccentricity domains. Upwelling intensifies during austral summer insolation maxima during positive precession periods in response to the expansion and intensification of the South Atlantic Hadley Cell due to a northward position of the ITCZ. We propose a mechanism with intensified inter-hemispheric energy transport by the AMOC during positive precession periods in response to low-latitude forcing. Periods of high austral summer insolation maxima drive the inter-hemispheric gradient by warming the South Atlantic when deep-water formation in the North Atlantic is intensified. The North Atlantic steals heat from the South Atlantic by forcing warm surface waters from the tropical Atlantic to be transferred northward, cooling Antarctica and shifting the SASG and atmospheric components to the north, which closes the AL and promoted zonally-intensified trade winds to increase the upwelling at NBUS. The opposite pattern is observed during negative precession. Enhanced AL increases SASG heat and salt content that is prevented from being transferred northward, making the SASG a heat reservoir during negative precession periods. Therefore, the SASG plays an active role in regulating the inter-hemispheric energy transport and the Indo-Atlantic connection essential for modulating AMOC through precessional cycles. We further suggest that our mechanism implies a seesaw pattern between AL and NBUS activity, which acts as an important mechanism for inter-hemispheric energy transfer.

Increased nutrient supply enhances primary productivity during intensified upwelling periods, increasing the vertical $\delta^{13}\text{C}$ gradient between surface and thermocline, as well as between thermocline and bottom. Concomitant TOC accumulation in nearby sites confirms that the surface biological activity vertically transfers and stores carbon in the deep ocean at NBUS during positive precession periods, coeval with reductions in atmospheric CO_2 . Furthermore, we speculate that zonally-intensified trade winds would have enhanced

the SECC that feeds the Angola Gyre and increased thermocline intrusion of the Angola Current to NBUS. Together with reduced AL, this tropical circulation dynamic would have increased the delivery of nutrient-rich WSACW on the NBUS during positive precession periods, which may have contributed to boosting the upwelling and the efficiency of the biological pump. However, it is unlikely that the upwelling intensification at NBUS by itself would be responsible for the total amplitude of the changes observed on global atmospheric CO₂ variability. We suggest that the added effect of the NBUS biological pump together with reduced upwelling in the Southern Ocean that would prevent CO₂ outgassing to the atmosphere at southern high latitudes, are responsible for significant CO₂ decreases during positive precession periods. The stronger chemical gradient between SAMW and CDW at the southern Agulhas Plateau during these periods supports the hypothesis of more isolated waters in the Southern Ocean during these periods.

The role of precessionally-modulated changes on AMOC cross-hemispheric transport triggers ocean-atmospheric responses in the South Atlantic that shifted the ITCZ northward, intensifying the trade winds and the upwelling activity at NBUS. Our proposed mechanism highlights that basin-wide changes in the South Atlantic dynamic are crucial in modulating the large-scale ocean-atmospheric global patterns seeking to reorganize the energy balance between the hemispheres through precessional cycles. The framework proposed here puts together ocean-atmospheric and deep-water dynamics in the Atlantic acting together to modulate the global climate.

References

- Adkins, J., deMenocal, P., & Eshel, G. (2006). The “African humid period” and the record of marine upwelling from excess ²³⁰Th in Ocean Drilling Program Hole 658C. *Paleoceanography*, 21(4). <https://doi.org/10.1029/2005PA001200>
- Anderson, R. F., Ali, S., Bradtmiller, L. I., Nielsen, S. H. H., Fleisher, M. Q., Anderson, B. E., & Burckle, L. H. (2009). Wind-Driven Upwelling in the Southern Ocean and the Deglacial Rise in Atmospheric CO₂. *Science*, 323(5920), 1443–1448. <https://doi.org/10.1126/science.1167441>
- Bakun, A. (1990). Global Climate Change and Intensification of Coastal Ocean Upwelling. *Science*, 247(4939), 198–201. <https://doi.org/10.1126/science.247.4939.198>
- Bakun, A., Field, D. B., Redondo-Rodriguez, A., & Weeks, S. J. (2010). Greenhouse gas, upwelling-favorable winds, and the future of coastal ocean upwelling ecosystems. *Global Change Biology*, 16(4), 1213–1228. <https://doi.org/10.1111/j.1365-2486.2009.02094.x>

- Ballalai, J. M., Santos, T. P., Lessa, D. O., Venancio, I. M., Chiessi, C. M., Johnstone, H. J. H., Kuhnert, H., Claudio, M. R., Toledo, F., Costa, K. B., & Albuquerque, A. L. S. (2019). Tracking Spread of the Agulhas Leakage Into the Western South Atlantic and Its Northward Transmission During the Last Interglacial. *Paleoceanography and Paleoclimatology*, 2019PA003653. <https://doi.org/10.1029/2019PA003653>
- Bard, E., & Rickaby, R. E. M. (2009). Migration of the subtropical front as a modulator of glacial climate. *Nature*, 460(7253), 380–383. <https://doi.org/10.1038/nature08189>
- Barker, S., Diz, P., Vautravers, M. J., Pike, J., Knorr, G., Hall, I. R., & Broecker, W. S. (2009). Interhemispheric Atlantic seesaw response during the last deglaciation. *Nature*, 457(7233), 1097–1102. <https://doi.org/10.1038/nature07770>
- Barrows, T. T., Juggins, S., De Deckker, P., Calvo, E., & Pelejero, C. (2007). Long-term sea surface temperature and climate change in the Australian-New Zealand region. *Paleoceanography*, 22(2). <https://doi.org/10.1029/2006PA001328>
- Beal, L. M., De Ruijter, W. P. M., Biastoch, A., Zahn, R., Cronin, M., Hermes, J., Lutjeharms, J., Quartly, G., Tozuka, T., Baker-Yeboah, S., Bornman, T., Cipollini, P., Dijkstra, H., Hall, I., Park, W., Peeters, F., Penven, P., Ridderinkhof, H., & Zinke, J. (2011). On the role of the Agulhas system in ocean circulation and climate. *Nature*, 472(7344), 429–436. <https://doi.org/10.1038/nature09983>
- Berger, A., & Loutre, M. F. (1991). Insolation values for the climate of the last 10 million years. *Quaternary Science Reviews*, 10(4), 297–317. [https://doi.org/10.1016/0277-3791\(91\)90033-Q](https://doi.org/10.1016/0277-3791(91)90033-Q)
- Blaauw, M., & Christen, J. A. (2011). Flexible paleoclimate age-depth models using an autoregressive gamma process. *Bayesian Analysis*, 6(3), 457–474. <https://doi.org/10.1214/11-BA618>
- Blanke, B., Speich, S., Bentamy, A., Roy, C., & Sow, B. (2005). Modeling the structure and variability of the southern Benguela upwelling using QuikSCAT wind forcing. *Journal of Geophysical Research: Oceans*, 110(C7). <https://doi.org/10.1029/2004JC002529>
- Blunier, T., & Brook, E. J. (2001). Timing of Millennial-Scale Climate Change in Antarctica and Greenland During the Last Glacial Period. *Science*, 291(5501), 109–112. <https://doi.org/10.1126/science.291.5501.109>
- Bordbar, M. H., Mohrholz, V., & Schmidt, M. (2021). The Relation of Wind-Driven Coastal and Offshore Upwelling in the Benguela Upwelling System. *Journal of Physical Oceanography*, 51(10), 3117–3133. <https://doi.org/10.1175/JPO-D-20-0297.1>
- Broccoli, A. J., Dahl, K. A., & Stouffer, R. J. (2006). Response of the ITCZ to Northern Hemisphere cooling. *Geophysical Research Letters*, 33(1). <https://doi.org/10.1029/2005GL024546>
- Broecker, W. S. (1998). Paleocean circulation during the 1st deglaciation: A bipolar seasaw? *Paleoceanography*, 13(2), 119–121.
- Broecker, W. S. (2003). Does the Trigger for Abrupt Climate Change Reside in the Ocean or in the Atmosphere? *Science*, 300(5625), 1519–1522. <https://doi.org/10.1126/science.1083797>
- Bronselaer, B., Winton, M., Griffies, S. M., Hurlin, W. J., Rodgers, K. B., Sergienko, O. V., Stouffer, R. J., & Russell, J. L. (2018). Change in future climate due to Antarctic meltwater. *Nature*, 564(7734), 53–58. <https://doi.org/10.1038/s41586-018-0712-z>
- Bronselaer, B., & Zanna, L. (2020). Heat and carbon coupling reveals ocean warming due to circulation changes. *Nature*, 584(7820), 227–233. <https://doi.org/10.1038/s41586-020-2573-5>

- Cabré, A., Pelegrí, J. L., & Vallès-Casanova, I. (2019). Subtropical-Tropical Transfer in the South Atlantic Ocean. *Journal of Geophysical Research: Oceans*, *124*(7), 2019JC015160. <https://doi.org/10.1029/2019JC015160>
- Caesar, L., Rahmstorf, S., Robinson, A., Feulner, G., & Saba, V. (2018). Observed fingerprint of a weakening Atlantic Ocean overturning circulation. *Nature*, *556*(7700), 191–196. <https://doi.org/10.1038/s41586-018-0006-5>
- Caley, T., Peeters, F. J. C., Biastoch, A., Rossignol, L., van Sebille, E., Durgadoo, J., Malaizé, B., Giraudeau, J., Arthur, K., & Zahn, R. (2014). Quantitative estimate of the paleo-Agulhas leakage. *Geophysical Research Letters*, *41*(4), 1238–1246. <https://doi.org/10.1002/2014GL059278>
- Carr, M. E., & Kearns, E. J. (2003). Production regimes in four Eastern Boundary Current systems. *Deep-Sea Research Part II: Topical Studies in Oceanography*, *50*(22–26), 3199–3221. <https://doi.org/10.1016/j.dsr2.2003.07.015>
- Carr, M.-E. (2002). Estimation of potential productivity in Eastern Boundary Currents using remote sensing. In *Deep-Sea Research II* (Vol. 49).
- Chase, B. M. (2021). Orbital forcing in southern Africa: Towards a conceptual model for predicting deep time environmental change from an incomplete proxy record. *Quaternary Science Reviews*, *265*, 107050. <https://doi.org/10.1016/j.quascirev.2021.107050>
- Chen, M.-T., Chang, Y.-P., Chang, C.-C., Wang, L.-W., Wang, C.-H., & Yu, E.-F. (2002). Late Quaternary sea-surface temperature variations in the southeast Atlantic: a planktic foraminifer faunal record of the past 600 000 yr (IMAGES II MD962085). *Marine Geology*, *180*(1–4), 163–181. [https://doi.org/10.1016/S0025-3227\(01\)00212-2](https://doi.org/10.1016/S0025-3227(01)00212-2)
- Cheng, H., Edwards, R. L., Sinha, A., Spötl, C., Yi, L., Chen, S., Kelly, M., Kathayat, G., Wang, X., Li, X., Kong, X., Wang, Y., Ning, Y., & Zhang, H. (2016). The Asian monsoon over the past 640,000 years and ice age terminations. *Nature*, *534*(7609), 640–646. <https://doi.org/10.1038/nature18591>
- Cheng, L., Abraham, J., Hausfather, Z., & Trenberth, K. E. (2019). How fast are the oceans warming? In *Science* (Vol. 363, Issue 6423, pp. 128–129). American Association for the Advancement of Science. <https://doi.org/10.1126/science.aav7619>
- Christensen, B. A., & Giraudeau, J. (2002). Neogene and Quaternary evolution of the Benguela upwelling system. *Marine Geology*, *180*(1), 1–2. [https://doi.org/https://doi.org/10.1016/S0025-3227\(01\)00202-X](https://doi.org/https://doi.org/10.1016/S0025-3227(01)00202-X)
- Collins, J. A., Schefuß, E., Govin, A., Mulitza, S., & Tiedemann, R. (2014). Insolation and glacial–interglacial control on southwestern African hydroclimate over the past 140 000 years. *Earth and Planetary Science Letters*, *398*, 1–10. <https://doi.org/10.1016/j.epsl.2014.04.034>
- Collins, J. A., Schefuß, E., Heslop, D., Mulitza, S., Prange, M., Zabel, M., Tjallingii, R., Dokken, T. M., Huang, E., Mackensen, A., Schulz, M., Tian, J., Zarriess, M., & Wefer, G. (2011). Interhemispheric symmetry of the tropical African rainbelt over the past 23,000 years. *Nature Geoscience*, *4*(1), 42–45. <https://doi.org/10.1038/ngeo1039>
- Collins, J. A., Schefuß, E., Mulitza, S., Prange, M., Werner, M., Tharammal, T., Paul, A., & Wefer, G. (2013). Estimating the hydrogen isotopic composition of past precipitation using leaf-waxes from western Africa. *Quaternary Science Reviews*, *65*, 88–101. <https://doi.org/10.1016/j.quascirev.2013.01.007>

- Crowley, T. J. (1992). North Atlantic Deep Water cools the southern hemisphere. *Paleoceanography*, 7(4), 489–497. <https://doi.org/10.1029/92PA01058>
- Delaney, M. L. (1989). Uptake of cadmium into calcite shells by planktonic foraminifera. *Chemical Geology*, 78(2), 159–165. [https://doi.org/10.1016/0009-2541\(89\)90114-9](https://doi.org/10.1016/0009-2541(89)90114-9)
- Deplazes, G., Lückge, A., Peterson, L. C., Timmermann, A., Hamann, Y., Hughen, K. A., Röhl, U., Laj, C., Cane, M. A., Sigman, D. M., & Haug, G. H. (2013). Links between tropical rainfall and North Atlantic climate during the last glacial period. *Nature Geoscience*, 6(3), 213–217. <https://doi.org/10.1038/ngeo1712>
- Donohoe, A., Marshall, J., Ferreira, D., & Mcgee, D. (2013). The relationship between ITCZ location and cross-equatorial atmospheric heat transport: From the seasonal cycle to the last glacial maximum. *Journal of Climate*, 26(11), 3597–3618. <https://doi.org/10.1175/JCLI-D-12-00467.1>
- Duplessy, J. C., Shackleton, N. J., Fairbanks, R. G., Labeyrie, L., Oppo, D., & Kallel, N. (1988). Deepwater source variations during the last climatic cycle and their impact on the global deepwater circulation. *Paleoceanography*, 3(3), 343–360. <https://doi.org/10.1029/PA003i003p00343>
- Emeis, K., Eggert, A., Flohr, A., Lahajnar, N., Nausch, G., Neumann, A., Rixen, T., Schmidt, M., Van der Plas, A., & Wasmund, N. (2018). Biogeochemical processes and turnover rates in the Northern Benguela Upwelling System. *Journal of Marine Systems*, 188, 63–80. <https://doi.org/10.1016/j.jmarsys.2017.10.001>
- Emeis, K.-C., Struck, U., Leipe, T., & Ferdelman, T. G. (2009). Variability in upwelling intensity and nutrient regime in the coastal upwelling system offshore Namibia: results from sediment archives. *International Journal of Earth Sciences*, 98(2), 309–326. <https://doi.org/10.1007/s00531-007-0236-5>
- Etourneau, J., Martinez, P., Blanz, T., & Schneider, R. (2009). Pliocene–Pleistocene variability of upwelling activity, productivity, and nutrient cycling in the Benguela region. *Geology*, 37(10), 871–874. <https://doi.org/10.1130/G25733A.1>
- Farmer, E. J., Chapman, M. R., & Andrews, J. E. (2011). Holocene temperature evolution of the subpolar North Atlantic recorded in the Mg/Ca ratios of surface and thermocline dwelling planktonic foraminifers. *Global and Planetary Change*, 79(3–4), 234–243. <https://doi.org/10.1016/j.gloplacha.2011.02.003>
- Fennel, W., Junker, T., Schmidt, M., & Mohrholz, V. (2012). Response of the Benguela upwelling systems to spatial variations in the wind stress. *Continental Shelf Research*, 45, 65–77. <https://doi.org/10.1016/j.csr.2012.06.004>
- Garcia, H. E., K. Weathers, C. R. Paver, I. Smolyar, T. P. Boyer, R. A. Locarnini, M. M. Zweng, A. V. Mishonov, O. K. Baranova, D. Seidov, and J. R. Reagan, 2018. World Ocean Atlas 2018, Volume 4: Dissolved Inorganic Nutrients (phosphate, nitrate and nitrate+nitrite, silicate). A. Mishonov Technical Ed.; NOAA Atlas NESDIS 84, 35pp.
- Garzoli, S. L., & Matano, R. (2011). The South Atlantic and the Atlantic Meridional Overturning Circulation. *Deep Sea Research Part II: Topical Studies in Oceanography*, 58(17–18), 1837–1847. <https://doi.org/10.1016/j.dsr2.2010.10.063>
- González-Dávila, M., Santana-Casiano, J. M., & Ucha, I. R. (2009). Seasonal variability of fCO₂ in the Angola-Benguela region. *Progress in Oceanography*, 83(1–4), 124–133. <https://doi.org/10.1016/j.pocean.2009.07.033>

Gordon, A. L. (1986). Interoccean exchange of thermocline water. *Journal of Geophysical Research*, *91*(C4), 5037. <https://doi.org/10.1029/JC091iC04p05037>

Hammer, O., Harper, D., & Ryan, P. (2001). PAST: Paleontological Statistics Software Package for Education and Data Analysis. *Palaeontologia Electronica*, *4*, 1–9.

Heaton, T. J., Köhler, P., Butzin, M., Bard, E., Reimer, R. W., Austin, W. E. N., Bronk Ramsey, C., Grootes, P. M., Hughen, K. A., Kromer, B., Reimer, P. J., Adkins, J., Burke, A., Cook, M. S., Olsen, J., & Skinner, L. C. (2020). Marine20—The Marine Radiocarbon Age Calibration Curve (0–55,000 cal BP). *Radiocarbon*, *62*(4), 779–820. <https://doi.org/10.1017/RDC.2020.68>

Hodell, D., Crowhurst, S., Skinner, L., Tzedakis, P. C., Margari, V., Channell, J. E. T., Kamenov, G., Maclachlan, S., & Rothwell, G. (2013). Response of Iberian Margin sediments to orbital and suborbital forcing over the past 420 ka. *Paleoceanography*, *28*(1), 185–199. <https://doi.org/10.1002/palo.20017>

Hou, A., Bahr, A., Schmidt, S., Strebl, C., Albuquerque, A. L., Chiessi, C. M., & Friedrich, O. (2020). Forcing of western tropical South Atlantic sea surface temperature across three glacial-interglacial cycles. *Global and Planetary Change*, *188*, 103150. <https://doi.org/10.1016/j.gloplacha.2020.103150>

Hutchings, L., van der Lingen, C. D., Shannon, L. J., Crawford, R. J. M., Verheye, H. M. S., Bartholomae, C. H., van der Plas, A. K., Louw, D., Kreiner, A., Ostrowski, M., Fidel, Q., Barlow, R. G., Lamont, T., Coetzee, J., Shillington, F., Veitch, J., Currie, J. C., & Monteiro, P. M. S. (2009). The Benguela Current: An ecosystem of four components. *Progress in Oceanography*, *83*(1–4), 15–32. <https://doi.org/10.1016/j.pocean.2009.07.046>

IPCC, 2022: Climate Change 2022: Impacts, Adaptation, and Vulnerability. Contribution of Working Group II to the Sixth Assessment Report of the Intergovernmental Panel on Climate Change [H.-O. Pörtner, D.C. Roberts, M. Tignor, E.S. Poloczanska, K. Mintenbeck, A. Alegria, M. Craig, S. Langsdorf, S. Löschke, V. Möller, A. Okem, B. Rama (eds.)]. Cambridge University Press. Cambridge University Press, Cambridge, UK and New York, NY, USA, 3056 pp., doi:10.1017/9781009325844.

Jouzel, J., Masson-Delmotte, V., Cattani, O., Dreyfus, G., Falourd, S., Hoffmann, G., Minster, B., Nouet, J., Barnola, J. M., Chappellaz, J., Fischer, H., Gallet, J. C., Johnsen, S., Leuenberger, M., Loulergue, L., Luethi, D., Oerter, H., Parrenin, F., Raisbeck, G., ... Wolff, E. W. (2007). Orbital and Millennial Antarctic Climate Variability over the Past 800,000 Years. *Science*, *317*(5839), 793–796. <https://doi.org/10.1126/science.1141038>

Kaiser, E. A., Caldwell, A., & Billups, K. (2019). North Atlantic Upper-Ocean Hydrography During the Mid-Pleistocene Transition Evidenced by Globorotalia truncatulinoides Coiling Ratios. *Paleoceanography and Paleoclimatology*, *34*(4), 658–671. <https://doi.org/10.1029/2018PA003502>

Kawamura, K., Parrenin, F., Lisiecki, L., Uemura, R., Vimeux, F., Severinghaus, J. P., Hutterli, M. A., Nakazawa, T., Aoki, S., Jouzel, J., Raymo, M. E., Matsumoto, K., Nakata, H., Motoyama, H., Fujita, S., Goto-Azuma, K., Fujii, Y., & Watanabe, O. (2007). Northern Hemisphere forcing of climatic cycles in Antarctica over the past 360,000 years. *Nature*, *448*(7156), 912–916. <https://doi.org/10.1038/nature06015>

Kim, J. H., Schneider, R. R., Mulitza, S., & Müller, P. J. (2003). Reconstruction of SE trade-wind intensity based on sea-surface temperature gradients in the Southeast Atlantic over the last 25 kyr. *Geophysical Research Letters*, *30*(22), 3–6. <https://doi.org/10.1029/2003GL017557>

- Kim, J.-H., Schneider, R. R., Müller, P. J., & Wefer, G. (2002). Interhemispheric comparison of deglacial sea-surface temperature patterns in Atlantic eastern boundary currents. *Earth and Planetary Science Letters*, *194*(3–4), 383–393. [https://doi.org/10.1016/S0012-821X\(01\)00545-3](https://doi.org/10.1016/S0012-821X(01)00545-3)
- Kirst, G. J., Schneider, R. R., Müller, P. J., von Storch, I., & Wefer, G. (1999). Late Quaternary Temperature Variability in the Benguela Current System Derived from Alkenones. *Quaternary Research*, *52*(1), 92–103. <https://doi.org/10.1006/qres.1999.2040>
- Klinger, B. A., & Marotzke, J. (2000). Meridional Heat Transport by the Subtropical Cell. *Journal of Physical Oceanography*, *30*(4), 696–705. [https://doi.org/10.1175/1520-0485\(2000\)030<0696:MHTBTS>2.0.CO;2](https://doi.org/10.1175/1520-0485(2000)030<0696:MHTBTS>2.0.CO;2)
- Knorr, G., & Lohmann, G. (2003). Southern Ocean origin for the resumption of Atlantic thermohaline circulation during deglaciation. *Nature*, *424*(6948), 532–536. <https://doi.org/10.1038/nature01855>
- Kotov, S., & Paelike, H. (2018). QAnalySeries - a cross-platform time series tuning and analysis tool. *AGU Fall Meeting Abstracts, 2018*, PP53D-1230.
- Lamont, T., Barlow, R. G., & Brewin, R. J. W. (2019). Long-Term Trends in Phytoplankton Chlorophyll a and Size Structure in the Benguela Upwelling System. *Journal of Geophysical Research: Oceans*, *124*(2), 1170–1195. <https://doi.org/10.1029/2018JC014334>
- Laskar, J., Robutel, P., Joutel, F., Gastineau, M., Correia, A. C. M., & Levrard, B. (2004). A long-term numerical solution for the insolation quantities of the Earth. *Astronomy & Astrophysics*, *428*(1), 261–285. <https://doi.org/10.1051/0004-6361:20041335>
- Lass, H. U., & Mohrholz, V. (2008). On the interaction between the subtropical gyre and the Subtropical Cell on the shelf of the SE Atlantic. *Journal of Marine Systems*, *74*(1–2), 1–43. <https://doi.org/10.1016/j.jmarsys.2007.09.008>
- Leduc, G., Garbe-Schönberg, D., Regenber, M., Contoux, C., Etourneau, J., & Schneider, R. (2014). The late Pliocene Benguela upwelling status revisited by means of multiple temperature proxies. *Geochemistry, Geophysics, Geosystems*, *15*(2), 475–491. <https://doi.org/10.1002/2013GC004940>
- Li, Q., England, M. H., Hogg, A. McC., Rintoul, S. R., & Morrison, A. K. (2023). Abyssal ocean overturning slowdown and warming driven by Antarctic meltwater. *Nature*, *615*(7954), 841–847. <https://doi.org/10.1038/s41586-023-05762-w>
- Lisiecki, L. E., & Raymo, M. E. (2005). A Pliocene-Pleistocene stack of 57 globally distributed benthic $\delta^{18}\text{O}$ records. *Paleoceanography*, *20*(1), 1–17. <https://doi.org/10.1029/2004PA001071>
- Lisiecki, L. E., Raymo, M. E., & Curry, W. B. (2008). Atlantic overturning responses to Late Pleistocene climate forcings. *Nature*, *456*(7218), 85–88. <https://doi.org/10.1038/nature07425>
- Little, M. G., Schneider, R. R., Kroon, D., Price, B., Bickert, T., & Wefer, G. (1997). Rapid palaeoceanographic changes in the Benguela Upwelling System for the last 160,000 years as indicated by abundances of planktonic foraminifera. *Palaeogeography, Palaeoclimatology, Palaeoecology*, *130*(1–4), 135–161. [https://doi.org/10.1016/S0031-0182\(96\)00136-8](https://doi.org/10.1016/S0031-0182(96)00136-8)
- Little, M. G., Schneider, R. R., Kroon, D., Price, B., Summerhayes, C. P., & Segl, M. (1997). Trade wind forcing of upwelling, seasonality, and Heinrich events as a response to sub-Milankovitch climate variability. *Paleoceanography*, *12*(4), 568–576. <https://doi.org/10.1029/97PA00823>

- Louw, D. C., van der Plas, A. K., Mohrholz, V., Wasmund, N., Junker, T., & Eggert, A. (2016). Seasonal and interannual phytoplankton dynamics and forcing mechanisms in the Northern Benguela upwelling system. *Journal of Marine Systems*, *157*, 124–134. <https://doi.org/10.1016/j.jmarsys.2016.01.009>
- Lu, J., Vecchi, G. A., & Reichler, T. (2007). Expansion of the Hadley cell under global warming. *Geophysical Research Letters*, *34*(6). <https://doi.org/10.1029/2006GL028443>
- Marcello, F., Tonelli, M., Ferrero, B., & Wainer, I. (2023). Projected Atlantic overturning slow-down is to be compensated by a strengthened South Atlantic subtropical gyre. *Communications Earth and Environment*, *4*(1). <https://doi.org/10.1038/s43247-023-00750-4>
- Marcello, F., Wainer, I., & Rodrigues, R. R. (2018). South Atlantic Subtropical Gyre Late Twentieth Century Changes. *Journal of Geophysical Research: Oceans*, *123*(8), 5194–5209. <https://doi.org/10.1029/2018JC013815>
- Marlow, J. R., Lange, C. B., Wefer, G., & Rosell-Melé, A. (2000). Upwelling intensification as part of the Pliocene-Pleistocene climate transition. *Science*, *290*(5500), 2288–2291. <https://doi.org/10.1126/science.290.5500.2288>
- Marshall, J., Donohoe, A., Ferreira, D., & McGee, D. (2014). The ocean's role in setting the mean position of the Inter-Tropical Convergence Zone. *Climate Dynamics*, *42*(7–8), 1967–1979. <https://doi.org/10.1007/s00382-013-1767-z>
- Martínez-Méndez, G., Zahn, R., Hall, I. R., Peeters, F. J. C., Pena, L. D., Cacho, I., & Negre, C. (2010). Contrasting multiproxy reconstructions of surface ocean hydrography in the Agulhas Corridor and implications for the Agulhas Leakage during the last 345,000 years. *Paleoceanography*, *25*(4). <https://doi.org/10.1029/2009PA001879>
- McCreary, J. P., & Lu, P. (1994). Interaction between the Subtropical and Equatorial Ocean Circulations: The Subtropical Cell. *Journal of Physical Oceanography*, *24*(2), 466–497. [https://doi.org/10.1175/1520-0485\(1994\)024<0466:IBTSAE>2.0.CO;2](https://doi.org/10.1175/1520-0485(1994)024<0466:IBTSAE>2.0.CO;2)
- McGee, D., deMenocal, P. B., Winckler, G., Stuut, J. B. W., & Bradtmiller, L. I. (2013). The magnitude, timing and abruptness of changes in North African dust deposition over the last 20,000 yr. *Earth and Planetary Science Letters*, *371–372*, 163–176. <https://doi.org/10.1016/j.epsl.2013.03.054>
- McGee, D., Donohoe, A., Marshall, J., & Ferreira, D. (2014). Changes in ITCZ location and cross-equatorial heat transport at the Last Glacial Maximum, Heinrich Stadial 1, and the mid-Holocene. *Earth and Planetary Science Letters*, *390*, 69–79. <https://doi.org/10.1016/j.epsl.2013.12.043>
- McGee, D., Moreno-Chamarro, E., Green, B., Marshall, J., Galbraith, E., & Bradtmiller, L. (2018). Hemispherically asymmetric trade wind changes as signatures of past ITCZ shifts. *Quaternary Science Reviews*, *180*, 214–228. <https://doi.org/10.1016/j.quascirev.2017.11.020>
- McKay, C. L., Filipsson, H. L., Romero, O. E., Stuut, J. B. W., & Björck, S. (2016). The interplay between the surface and bottom water environment within the Benguela Upwelling System over the last 70 ka. *Paleoceanography*, *31*(2), 266–285. <https://doi.org/10.1002/2015PA002792>
- McManus, J. F., Francois, R., Gherardi, J.-M., Keigwin, L. D., & Brown-Leger, S. (2004). Collapse and rapid resumption of Atlantic meridional circulation linked to deglacial climate changes. *Nature*, *428*(6985), 834–837. <https://doi.org/10.1038/nature02494>

- Mohrholz, V., Bartholomae, C. H., van der Plas, A. K., & Lass, H. U. (2008). The seasonal variability of the northern Benguela undercurrent and its relation to the oxygen budget on the shelf. *Continental Shelf Research*, 28(3), 424–441. <https://doi.org/10.1016/j.csr.2007.10.001>
- Mulitza, S., Dürkoop, A., Hale, W., Wefer, G., & Stefan Niebler, H. (1997). Planktonic foraminifera as recorders of past surface-water stratification. *Geology*, 25(4), 335–338. [https://doi.org/10.1130/0091-7613\(1997\)025<0335:PFAROP>2.3.CO;2](https://doi.org/10.1130/0091-7613(1997)025<0335:PFAROP>2.3.CO;2)
- Mulitza, S., Rühlemann, C., Bickert, T., Hale, W., Pätzold, J., & Wefer, G. (1998). Late Quaternary $\delta^{13}\text{C}$ gradients and carbonate accumulation in the western equatorial Atlantic. *Earth and Planetary Science Letters*, 155(3–4), 237–249. [https://doi.org/10.1016/S0012-821X\(98\)00012-0](https://doi.org/10.1016/S0012-821X(98)00012-0)
- Nascimento, R. A., Venancio, I. M., Chiessi, C. M., Ballalai, J. M., Kuhnert, H., Johnstone, H., Santos, T. P., Prange, M., Govin, A., Crivellari, S., Mulitza, S., & Albuquerque, A. L. S. (2021). Tropical Atlantic stratification response to late Quaternary precessional forcing. *Earth and Planetary Science Letters*, 568, 117030. <https://doi.org/10.1016/j.epsl.2021.117030>
- Ohde, T., & Dadou, I. (2018). Seasonal and annual variability of coastal sulphur plumes in the northern Benguela upwelling system. *PLoS ONE*, 13(2). <https://doi.org/10.1371/journal.pone.0192140>
- Olson, D. B., Podestá, G. P., Evans, R. H., & Brown, O. B. (1988). Temporal variations in the separation of Brazil and Malvinas Currents. *Deep Sea Research Part A. Oceanographic Research Papers*, 35(12), 1971–1990. [https://doi.org/10.1016/0198-0149\(88\)90120-3](https://doi.org/10.1016/0198-0149(88)90120-3)
- Paillard, D. (2021). Climate and Astronomical Cycles. In A. and B. N. and S. P. and G. A. Ramstein Gilles and Landais (Ed.), *Paleoclimatology* (pp. 385–404). Springer International Publishing. https://doi.org/10.1007/978-3-030-24982-3_28
- Pedro, J. B., Jochum, M., Buizert, C., He, F., Barker, S., & Rasmussen, S. O. (2018). Beyond the bipolar seesaw: Toward a process understanding of interhemispheric coupling. *Quaternary Science Reviews*, 192, 27–46. <https://doi.org/10.1016/j.quascirev.2018.05.005>
- Peeters, F. J. C., Acheson, R., Brummer, G.-J. A., de Ruijter, W. P. M., Schneider, R. R., Ganssen, G. M., Ufkes, E., & Kroon, D. (2004). Vigorous exchange between the Indian and Atlantic oceans at the end of the past five glacial periods. *Nature*, 430(7000), 661–665. <https://doi.org/10.1038/nature02785>
- Peterson, L. C. (2000). Rapid Changes in the Hydrologic Cycle of the Tropical Atlantic During the Last Glacial. *Science*, 290(5498), 1947–1951. <https://doi.org/10.1126/science.290.5498.1947>
- Peterson, R. G., & Stramma, L. (1991). Upper-level circulation in the South-Atlantic Ocean. *Progress In Oceanography*, 26(1), 1–73. [https://doi.org/10.1016/0079-6611\(91\)90006-8](https://doi.org/10.1016/0079-6611(91)90006-8)
- Petrick, B. F., McClymont, E. L., Marret, F., & van der Meer, M. T. J. (2015). Changing surface water conditions for the last 500 ka in the Southeast Atlantic: Implications for variable influences of Agulhas leakage and Benguela upwelling. *Paleoceanography*, 30(9), 1153–1167. <https://doi.org/10.1002/2015PA002787>
- Pinho, T. M. L., Chiessi, C. M., Portilho-Ramos, R. C., Campos, M. C., Crivellari, S., Nascimento, R. A., Albuquerque, A. L. S., Bahr, A., & Mulitza, S. (2021). Meridional changes in the South Atlantic Subtropical Gyre during Heinrich Stadials. *Scientific Reports*, 11(1), 9419. <https://doi.org/10.1038/s41598-021-88817-0>

- Prange, M., & Schulz, M. (2004). A coastal upwelling seesaw in the Atlantic Ocean as a result of the closure of the Central American Seaway. *Geophysical Research Letters*, 31(17). <https://doi.org/10.1029/2004GL020073>
- Rantanen, M., Karpechko, A. Y., Lipponen, A., Nordling, K., Hyvärinen, O., Ruosteenoja, K., Vihma, T., & Laaksonen, A. (2022). The Arctic has warmed nearly four times faster than the globe since 1979. *Communications Earth and Environment*, 3(1). <https://doi.org/10.1038/s43247-022-00498-3>
- Romero, O. E., Kim, J. H., & Donner, B. (2008). Submillennial-to-millennial variability of diatom production off Mauritania, NW Africa, during the last glacial cycle. *Paleoceanography*, 23(3). <https://doi.org/10.1029/2008PA001601>
- Romero, O., Mollenhauer, G., Schneider, R. R., & Wefer, G. (2003). Oscillations of the siliceous imprint in the central Benguela Upwelling System from MIS 3 through to the early Holocene: the influence of the Southern Ocean. *Journal of Quaternary Science*, 18(8), 733–743. <https://doi.org/10.1002/jqs.789>
- Roubi, A. (2019). Variabilité de l'upwelling du Benguela pendant les derniers 40 000 ans. Université de Bretagne Occidentale, Plouzané, France.
- Santos, F., Gomez-Gesteira, M., deCastro, M., & Alvarez, I. (2012). Differences in coastal and oceanic SST trends due to the strengthening of coastal upwelling along the Benguela current system. *Continental Shelf Research*, 34, 79–86. <https://doi.org/10.1016/j.csr.2011.12.004>
- Schlitzer, R. (2017). Ocean Data View, odv.awi.de
- Schmidt, M., & Eggert, A. (2016). Oxygen cycling in the northern Benguela Upwelling System: Modelling oxygen sources and sinks. *Progress in Oceanography*, 149, 145–173. <https://doi.org/10.1016/j.pocean.2016.09.004>
- Schmidt, M. W., Spero, H. J., & Vautravers, M. J. (2006). Western Caribbean sea surface temperatures during the late Quaternary. *Geochemistry, Geophysics, Geosystems*, 7(2). <https://doi.org/10.1029/2005GC000957>
- Schneider, R., Moller, J., & Ruhland, G. (1995). *Late Quaternary surface circulation in the east equatorial South*. 10(2), 197–219.
- Schneider R. R. and Müller, P. J. and R. G. and M. G. and S. H. and W. G. (1996). Late Quaternary Surface Temperatures and Productivity in the East-Equatorial South Atlantic: Response to Changes in Trade/Monsoon Wind Forcing and Surface Water Advection. In *The South Atlantic: Present and Past Circulation* (pp. 527–551). Springer Berlin Heidelberg. https://doi.org/10.1007/978-3-642-80353-6_27
- Schulz, M., & Mudelsee, M. (2002). REDFIT: estimating red-noise spectra directly from unevenly spaced paleoclimatic time series. *Computers & Geosciences*, 28(3), 421–426. [https://doi.org/10.1016/S0098-3004\(01\)00044-9](https://doi.org/10.1016/S0098-3004(01)00044-9)
- Scussolini, P., & Peeters, F. J. C. (2013). A record of the last 460 thousand years of upper ocean stratification from the central Walvis Ridge, South Atlantic. *Paleoceanography*, 28(3), 426–439. <https://doi.org/10.1002/palo.20041>
- Shannon, L. V. (1985). The Benguela ecosystem. I: Evolution of the Benguela physical features and processes. *Oceanography and Marine Biology*, 23, 105–182.

Shannon, L. V., & Nelson, G. (1996). The Benguela: Large Scale Features and Processes and System Variability. In *The South Atlantic: Present and Past Circulation* (pp. 163–210). Springer Berlin Heidelberg. https://doi.org/10.1007/978-3-642-80353-6_9

Siddiqui, C., Rixen, T., Lahajnar, N., Van der Plas, A. K., Louw, D. C., Lamont, T., & Pillay, K. (2023). Regional and global impact of CO₂ uptake in the Benguela Upwelling System through preformed nutrients. *Nature Communications*, *14*(1). <https://doi.org/10.1038/s41467-023-38208-y>

Silveira, I. C. A. da, Schmidt, A. C. K., Campos, E. J. D., Godoi, S. S. de, & Ikeda, Y. (2000). A corrente do Brasil ao largo da costa leste brasileira. *Revista Brasileira de Oceanografia*, *48*(2), 171–183. <https://doi.org/10.1590/S1413-77392000000200008>

Skonieczny, C., McGee, D., Winckler, G., Bory, A., Bradtmiller, L. I., Kinsley, C. W., Polissar, P. J., De Pol-Holz, R., Rossignol, L., & Malaizé, B. (2019). Monsoon-driven Saharan dust variability over the past 240,000 years. *Science Advances*, *5*(1), 1–9. <https://doi.org/10.1126/sciadv.aav1887>

Stramma, L., & England, M. (1999). On the water masses and mean circulation of the South Atlantic Ocean. *Journal of Geophysical Research: Oceans*, *104*(C9), 20863–20883. <https://doi.org/10.1029/1999JC900139>

Stuut, J.-B. W., & Lamy, F. (2004). Climate variability at the southern boundaries of the Namib (southwestern Africa) and Atacama (northern Chile) coastal deserts during the last 120,000 yr. *Quaternary Research*, *62*(3), 301–309. <https://doi.org/10.1016/j.yqres.2004.08.001>

Stuut, J.-B. W., Prins, M. A., Schneider, R. R., Weltje, G. J., Jansen, J. H. F., & Postma, G. (2002). A 300-kyr record of aridity and wind strength in southwestern Africa: inferences from grain-size distributions of sediments on Walvis Ridge, SE Atlantic. *Marine Geology*, *180*(1–4), 221–233. [https://doi.org/10.1016/S0025-3227\(01\)00215-8](https://doi.org/10.1016/S0025-3227(01)00215-8)

Sydeman, W. J., García-Reyes, M., Schoeman, D. S., Rykaczewski, R. R., Thompson, S. A., Black, B. A., & Bograd, S. J. (2014). Climate change and wind intensification in coastal upwelling ecosystems. *Science*, *345*(6192), 77–80. <https://doi.org/10.1126/science.1251635>

Tim, N., Zorita, E., Emeis, K.-C., Schwarzkopf, F. U., Biastoch, A., & Hünicke, B. (2019a). Analysis of the position and strength of westerlies and trades with implications for Agulhas leakage and South Benguela upwelling. *Earth System Dynamics*, *10*(4), 847–858. <https://doi.org/10.5194/esd-10-847-2019>

Tim, N., Zorita, E., Emeis, K.-C., Schwarzkopf, F. U., Biastoch, A., & Hünicke, B. (2019b). Influence of position and strength of westerlies and trades on Agulhas leakage and South Benguela Upwelling. *Earth System Dynamics Discussions*, *April*, 1–17. <https://doi.org/10.5194/esd-2019-16>

Tim, N., Zorita, E., Hünicke, B., Yi, X., & Emeis, K.-C. (2016). The importance of external climate forcing for the variability and trends of coastal upwelling in past and future climate. *Ocean Science*, *12*(3), 807–823. <https://doi.org/10.5194/os-12-807-2016>

Tim, N., Zorita, E., Schwarzkopf, F. U., Rühls, S., Emeis, K., & Biastoch, A. (2018). The Impact of Agulhas Leakage on the Central Water Masses in the Benguela Upwelling System From A High-Resolution Ocean Simulation. *Journal of Geophysical Research: Oceans*, *123*(12), 9416–9428. <https://doi.org/10.1029/2018JC014218>

Timmermann, A., Friedrich, T., Timm, O. E., Chikamoto, M. O., Abe-Ouchi, A., & Ganopolski, A. (2014). Modeling Obliquity and CO₂ Effects on Southern Hemisphere Climate during the Past 408 ka*. *Journal of Climate*, *27*(5), 1863–1875. <https://doi.org/10.1175/JCLI-D-13-00311.1>

- Toggweiler, J. R., & Lea, D. W. (2010). Temperature differences between the hemispheres and ice age climate variability. *Paleoceanography*, *25*(2). <https://doi.org/10.1029/2009PA001758>
- Toggweiler, J. R., Russell, J. L., & Carson, S. R. (2006). Midlatitude westerlies, atmospheric CO₂, and climate change during the ice ages. *Paleoceanography*, *21*(2). <https://doi.org/10.1029/2005PA001154>
- Ufkes, E., Jansen, J. H. F., & Schneider, R. R. (2000). Anomalous occurrences of *Neogloboquadrina pachyderma* (left) in a 420-ky upwelling record from Walvis Ridge (SE Atlantic). *Marine Micropaleontology*, *40*(1–2), 23–42. [https://doi.org/10.1016/S0377-8398\(00\)00030-X](https://doi.org/10.1016/S0377-8398(00)00030-X)
- Ufkes, E., & Kroon, D. (2012). Sensitivity of south-east Atlantic planktonic foraminifera to mid-Pleistocene climate change. *Palaeontology*, *55*(1), 183–204. <https://doi.org/10.1111/j.1475-4983.2011.01119.x>
- Varela, R., Álvarez, I., Santos, F., DeCastro, M., & Gómez-Gesteira, M. (2015). Has upwelling strengthened along worldwide coasts over 1982–2010? *Scientific Reports*, *5*(1), 10016. <https://doi.org/10.1038/srep10016>
- Varela, R., Lima, F. P., Seabra, R., Meneghesso, C., & Gómez-Gesteira, M. (2018). Coastal warming and wind-driven upwelling: A global analysis. *Science of the Total Environment*, *639*, 1501–1511. <https://doi.org/10.1016/j.scitotenv.2018.05.273>
- Venancio, I. M., Mulitza, S., Govin, A., Santos, T. P., Lessa, D. O., Albuquerque, A. L. S., Chiessi, C. M., Tiedemann, R., Vahlenkamp, M., Bickert, T., & Schulz, M. (2018). Millennial- to Orbital-Scale Responses of Western Equatorial Atlantic Thermocline Depth to Changes in the Trade Wind System Since the Last Interglacial. *Paleoceanography and Paleoclimatology*, *33*(12), 1490–1507. <https://doi.org/10.1029/2018PA003437>
- Volbers, A. N. A., Niebler, H.-S., Giraudeau, J., Schmidt, H., & Henrich, R. (2003). Palaeoceanographic Changes in the Northern Benguela Upwelling System over the last 245.000 Years as Derived from Planktic Foraminifera Assemblages. In *The South Atlantic in the Late Quaternary* (Issue October 2014, pp. 601–622). Springer Berlin Heidelberg. https://doi.org/10.1007/978-3-642-18917-3_26
- Volk, T., & Hoffert, M. I. (1985). Ocean Carbon Pumps: Analysis of Relative Strengths and Efficiencies in Ocean-Driven Atmospheric CO₂ Changes. *American Geophysical Union; Geophysical Monograph*, *32*, 99–110.
- Weijer, W. (2002). Response of the Atlantic overturning circulation to South Atlantic sources of buoyancy. *Global and Planetary Change*, *34*(3–4), 293–311. [https://doi.org/10.1016/S0921-8181\(02\)00121-2](https://doi.org/10.1016/S0921-8181(02)00121-2)
- West, S., Jansen, J. H. F., & Stuut, J. B. (2004). Surface water conditions in the Northern Benguela Region (SE Atlantic) during the last 450 ky reconstructed from assemblages of planktonic foraminifera. *Marine Micropaleontology*, *51*(3–4), 321–344. <https://doi.org/10.1016/j.marmicro.2004.01.004>
- Zhao, X., Dupont, L., Schefuß, E., Granger, R., & Wefer, G. (2019). Late-Holocene oceanic variability in the southern Benguela region driven by interplay of upwelling, fluvial discharge, and Agulhas leakage. *The Holocene*, *29*(2), 219–230. <https://doi.org/10.1177/0959683618810396>
- Ziegler, M., Diz, P., Hall, I. R., & Zahn, R. (2013). Millennial-scale changes in atmospheric CO₂ levels linked to the Southern Ocean carbon isotope gradient and dust flux. *Nature Geoscience*, *6*(6), 457–461. <https://doi.org/10.1038/ngeo1782>

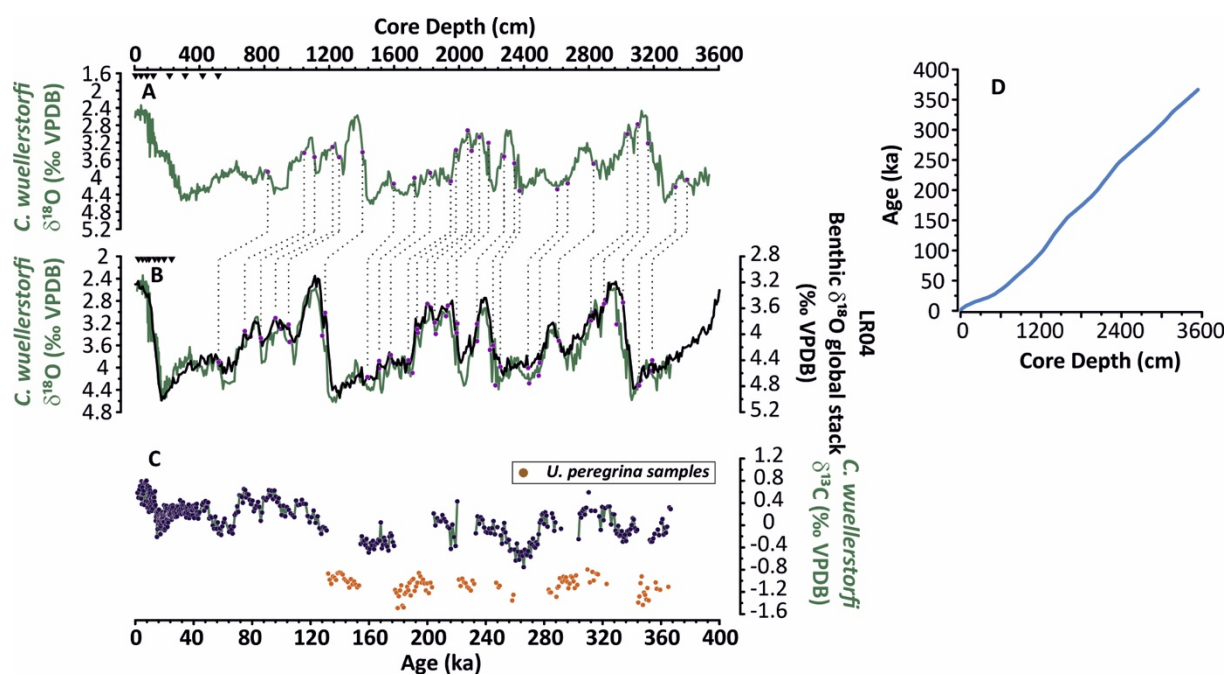
5.5 Supporting Information

Precessionally-driven Upwelling strength at Northern Benguela Upwelling System

This supporting information contains supplementary figures and tables of the main text of chapter 5.

Age model

In the main text, we provided all the information regarding the original age model construction for the MD08-3167 core. Chosen tie points and calendar age vs. depth from the visual alignment with benthic foraminifera $\delta^{18}\text{O}$ global stack LR04 (Lisiecki and Raymo, 2005) are indicated in Supplementary Fig. 1.



Supplementary Figure 1: Reference curve and age-depth model of core MD08-3167. Benthic foraminifera (*Cibicidoides wuellerstorfi*) A) $\delta^{18}\text{O}$ versus depth, B) $\delta^{18}\text{O}$ and LR04 benthic foraminifera $\delta^{18}\text{O}$ stack LR04 (Lisiecki and Raymo, 2005), C) $\delta^{13}\text{C}$ versus age, and D) age-depth model. Triangles represent the calibrated ^{14}C ages.

References

Lisiecki, L.E., Raymo, M.E., 2005. A Pliocene-Pleistocene stack of 57 globally distributed benthic $\delta^{18}\text{O}$ records. *Paleoceanography* 20, 1–17. <https://doi.org/10.1029/2004PA001071>.

6 IMPLEMENTING FORAMINIFERA MG/CA ANALYSIS TECHNIQUE ON IFREMER ICP-MS

As presented in section 3.2.4, the trace elements to calcium (TE/Ca) ratios measured on foraminifera have been widely used in paleoceanography, paleoclimatology, and biogeochemistry areas. Although this kind of analysis has been occasionally performed at IFREMER, no clear protocol existed to analyze foraminifera Mg/Ca in routine. This Chapter aims to provide a protocol for Mg/Ca analysis that will serve as a basis for future implementation of this technique at UFF in Brazil. It is a well-established methodology performed in European laboratories but less common in Brazil, probably due to the high costs and demanding maintenance. I have targeted Mg, Ca, Al, Mn, and Fe elements to be quantified on ThermoFisher Scientific's ELEMENT XR High-resolution Multi-collector ICP-MS at the PSO from IFREMER. Measurements and data treatment were done with the assistance of Yoan Germain, engineering at IFREMER, responsible for conducting measurements on PSO ICP-MS.

We applied the cleaning protocol based on (Barker *et al.*, 2003) and the external calibration method routinely operated at the LSCE for foraminiferal samples. By following the methodology described in this section, it is possible to implement it in other laboratories and ensure good quality measurements producing reliable results.

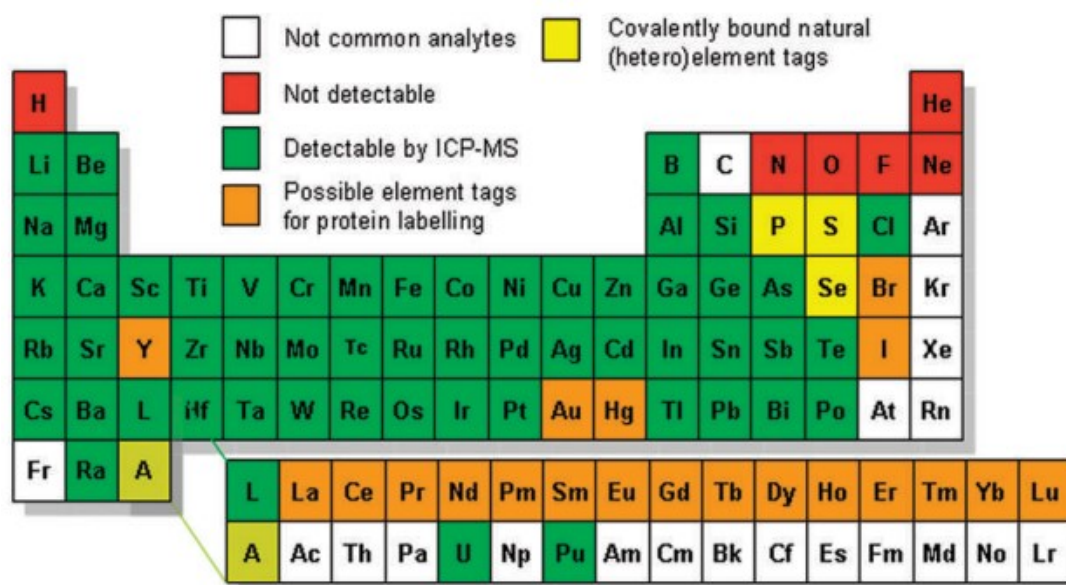
6.1 Elementary analysis on ICP-MS: Foraminifera TE/Ca ratios

Measurements of trace elements in biogenic calcite are used to reconstruct past seawater chemistry and the environmental conditions in which the calcite-producing organism have grown and to infer climate variability across different time scales on geological time (e.g., Katz *et al.*, 2010; Schiebel *et al.*, 2018). Many trace elements can be incorporated into the biogenic calcite during carbonate precipitation, such as Li, B, F, Na, Mg, P, V, Mn, Fe, Cu, Zn, Sr, Cd, Ba, Nd, and U (Lea, 1999), mainly as a result of local oceanographic and sedimentary dynamics. Different proxies have been developed from trace element concentrations normalized by Ca (i.e., TE/Ca ratios), which can be employed for various applications. For many decades, researchers have been studying how trace elements are incorporated in carbonatic organisms (Chave, 1954; Krinsley, 1960). In particular, the Mg/Ca proxy has become a powerful tool for paleoceanographic water column temperature

reconstructions (Duckworth, 1977; Cronblad and Malmgren, 1981; Izuka, 1988; Nürnberg *et al.*, 1996; Elderfield and Ganssen, 2000; Lear *et al.*, 2002), which is currently highly applied in South Atlantic reconstructions (e.g., Vázquez Riveiros *et al.*, 2016; Ballalai *et al.*, 2019; Santos *et al.*, 2017, 2022; Nascimento *et al.*, 2022). Moreover, B/Ca has been used as a proxy for seawater pH (Yu *et al.*, 2007), Na/Ca for seawater calcium concentration (Zhou *et al.*, 2021), I/Ca for upper ocean oxygenation (Lu *et al.*, 2016; Hoogakker *et al.*, 2018), and Sr/Ca also for temperature reconstructions (Cléroux *et al.*, 2008).

TE/Ca measurements are commonly performed in high-resolution analytical instrumentation such as ICP-MS. ICP-MS allows multiple elements to be measured simultaneously in a single analysis allowing both elemental and isotopic measurements in the same instrument (Brenner, 2017), representing a scientific mark in technological advances since its introduction in the 80s. High-resolution (HR) ICP-MS offers a significant advantage in analytical capabilities. Using a sector-field mass spectrometer allows for the physical separation and distinction of an analyte from interferences based on small variations in mass-to-charge ratio. As a result, HR-ICP-MS enables accurate quantification of element (Fig. 25) concentrations and precise determination of isotope ratios across a wide range of elements, regardless of the complexity of the sample matrix. Since, it has become the most versatile element-specific detection technique, with a lower detection limit, reduced instrument size, with improvements in controlling software and maintenance accessibility (Beauchemin, 2008; Pröfrock and Prange, 2012).

Figure 25 - Periodic table highlighting detectable elements by ICP-MS, such as metals, metalloids, semimetals, non-metals, or halogens (modified from Pröfrock and Prange, 2012)



Although ICP-MS also allows measuring solid samples when coupled with specific tools such as laser ablation, in this thesis, foraminifera samples were digested and diluted before analysis. Fig 14 shows a schematic representation of the ICP-MS components (Wilschefski and Baxter, 2019). Samples can be injected into the machine either manually, one by one, or automatically using autosamplers, which is the case of the ICP-MS used at IFREMER. The autosampler pulls the sample through a peristaltic pump to deliver it to a nebulizer, which creates an aerosol entering the sample introduction system and transferring it into the high-temperature argon plasma (Sharp, 1988). Briefly, the introduction system is a spray chamber that stabilizes and filters out the larger aerosol droplets, which is crucial due to the plasma's inefficiency in dissociating large droplets bigger than 10 μm in diameter. The plasma comprises an ionized argon gas free of electrons and positively charged formed at the end of three concentric quartz tubes, commonly known as the torch (Pröfrock and Prange, 2012). The inner tube carries the sample aerosol, around this one passes the auxiliary gas responsible for forming the plasma, and the outer tube is responsible for cooling (Wilschefski and Baxter, 2019). After reaching high temperatures, the plasma vaporizes, atomizes, and ionizes the sample, which is extracted into the interface region passing through two coaxial nickel (or platinum) cones. Ions, photons, and neutral atoms or molecules pass first through the sample cone (~ 1 mm diameter); and secondly through the skimmer cones (~ 0.45 mm diameter) into the ion optics (i.e., electrostatic lenses). The degree of ionization depends on the plasma's temperature and the element's ionization potential. The lens set acts

like a filter preventing atomic species from reaching the detector and focusing the ion beam into the quadrupole mass analyzer, which separates ions according to their mass-charge ratio (m/z) by creating an electric field in the center through which ions pass. These ions are measured at the electron multiplier detector (Wilschefski and Baxter, 2019).

Figure 26 - Schematic representation of an Inductively Coupled Plasma Mass Spectrometry (ICP-MS) (Wilschefski and Baxter, 2019); adapted from Košler and Sylvester (2003)

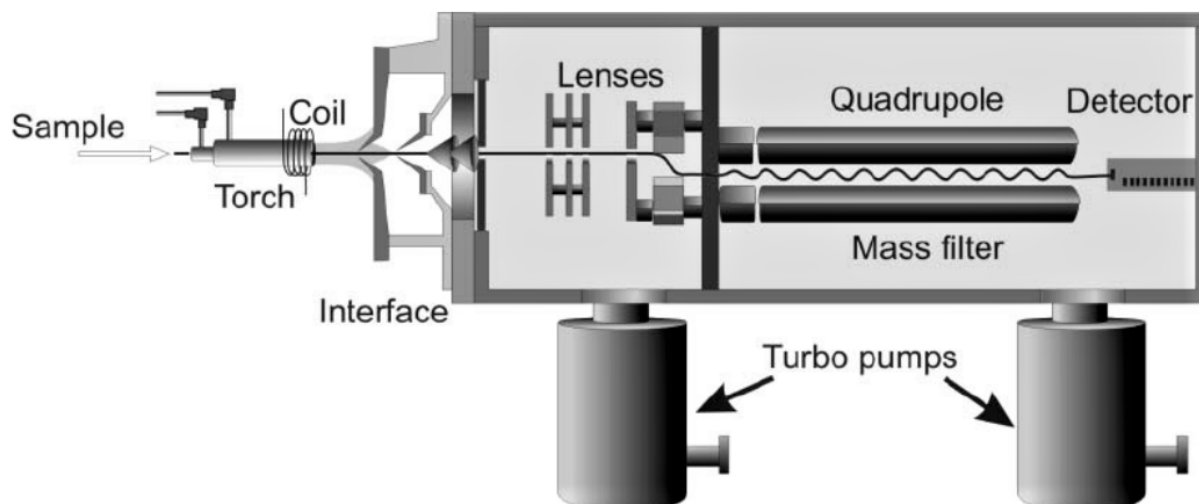
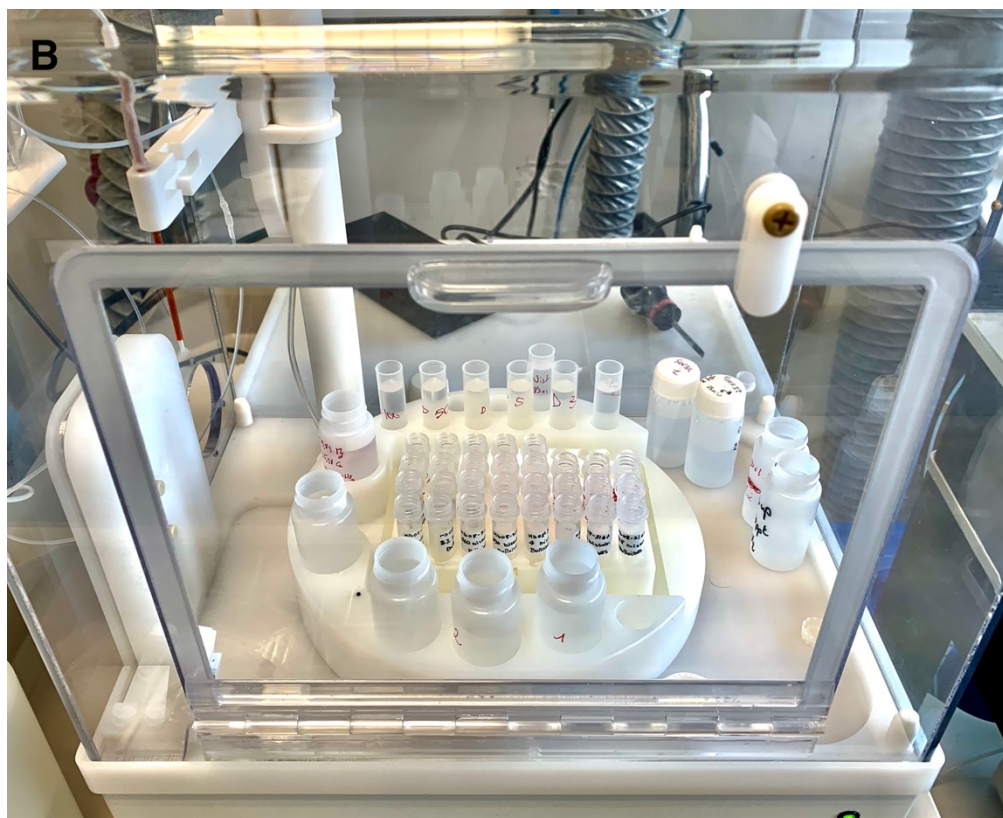


Figure 27 - a) ELEMENT XR High-resolution Multi-collector ICP-MS from the *Pôle Spectrométrie Océan* (PSO) at l'*Institut Français de Recherche pour l'Exploitation de la Mer* (IFREMER). b) ICP-MS autosampler, carrying samples and solutions used for measurements



For most elements, detection limits in ICP-MS are in the nmol/L range, but this also depends on other factors such as instrument operating conditions. The ICP-MS method is susceptible to interferences that can be categorized into spectroscopic and non-spectroscopic, affecting measurements' accuracy and precision. Spectroscopic interferences arise when non-analyte ions have the same m/z as the analyte (Evans and Giglio, 1993; Agatemor and Beauchemin, 2011; Pröfrock and Prange, 2012; Wilschefski and Baxter, 2019). They can be caused by overlapping isotopes of different elements or by forming molecular or polyatomic-ion interferences (Evans and Giglio, 1993). The four types of spectroscopic interferences:

- **Isobaric elements interference:** Occurs when isotopes of different elements have the same mass-to-charge ratio (m/z). These interferences can lead to incorrect identification or quantification of analyte elements (Pröfrock and Prange, 2012).
- **Polyatomic interference:** Arises when molecules or molecular ions are formed in the high-temperature plasma with the same m/z values as the analyte ions. These interferences can be caused due to incomplete atomization, ionization, dissociation, or recombination reaction in the plasma during the extraction of ions into a mass spectrometer (Wilschefski and Baxter, 2019).
- **Double-charged interference:** The ionization energy of argon ensures that most elements will be ionized (i.e., form singly charged ions), but the degree of ionization decreases as the ionization energy of an element becomes closer to that of argon. Therefore, elements with a second ionization potential lower than the first potential ionization of argon will also form a significant fraction of double-charged ions (Linge and Jarvis, 2009; Wilschefski and Baxter, 2019).
- **Tailing interference:** Arises when a spectral line of the analyte overlaps with a line of another element from an adjacent mass, leading to incorrect identification or quantification (Wilschefski and Baxter, 2019).

Non-spectroscopy interferences can be divided into matrix effect or instrument drift (Evans and Giglio, 1993; Agatemor and Beauchemin, 2011; Pröfrock and Prange, 2012; Wilschefski and Baxter, 2019), as described below:

- **Matrix effects:** The presence of matrix effects is a common challenge when using ICP-MS for elemental analysis. They involve analyte signal enhancement

or suppression and signal drift due to properties or constituents of the sample matrix. They can originate from different sources, such as during sample introduction, ion extraction, and transport into the mass spectrometer, depending on the concentration and nature of the sample matrix. A strong matrix effect in measurements biases the signal from samples with respect to the calibration standard solutions (Evans and Giglio, 1993; Linge and Jarvis, 2009; Agatemor and Beauchemin, 2011). Among various factors contributing to matrix effects, the most significant is the space-charge effect due to the electrostatic repulsion between positively-charged ions in the ion beam, which decreases ion transmission efficiency to the detector (Wilschefski and Baxter, 2019).

- **Ion drift:** Another source of interference is due to dissolved solid precipitation in the interface cones, which obstructs and cools the tips of the cones and reduces ion transmission (Agatemor and Beauchemin, 2011).

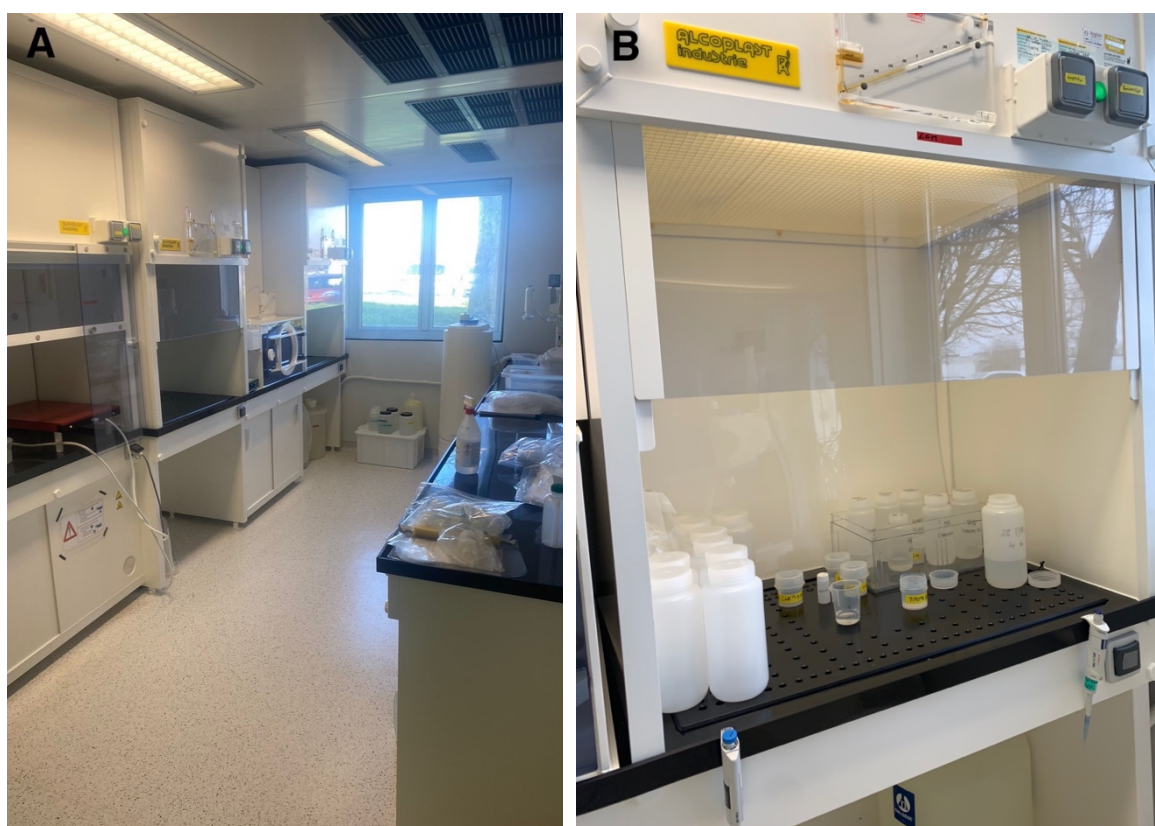
As briefly described in section 3.2.4, Mg/Ca measurements at IFREMER were performed in the planktic foraminifera species *G. inflata* from the MD08-3167 core site. Measurements performed on this matrix are challenging due to the low elementary trace concentrations found in foraminifera shells and the related calcium carbonate matrix effect, which differ from rock and water samples routinely analyzed in the lab and require attention regarding possible sources of contamination. In total, 322 samples from *G. inflata* were measured on ICP-MS element in the Geo-Ocean laboratory at IFREMER, aiming at reconstructing subsurface paleotemperatures in the SE South Atlantic.

6.2 Materials, reagents, and facility structure: Protocol preparation

A significant part of the required materials is used during the cleaning step and the preparation of samples for measurements. These steps are very time-consuming, especially with a high number of samples to be analyzed. For this reason and to avoid cross-contamination when using not-exclusive materials, it is worth organizing a “Mg/Ca-analysis” set with materials, chemical reagents, and prepared solutions before starting the protocol. Samples destined for Mg/Ca analysis are sensitive to contamination, then a clean room laboratory is important to perform the cleaning step (Fig. 28a), preferentially equipped with a laminar flow hood (Fig. 28b). The extensive cleaning procedure based on (Barker *et*

al., 2003) (see next topic for detailed information) was performed in the clean white room *Paléoécologie* at the *Pôle Spectrométrie Océan* (Fig. 28). The clean laboratory has a level of cleanliness defined by the International Organization for Standardization (ISO) and the U.S. Federal Standard 209E is categorized as a class ISO-6, equivalent class 1000, which means that there are more than 1000 particles larger than 0.5 μm in size per cubic foot of air in the room. The air in the clean lab at PSO is also filtered and circulated to minimize the introduction of outside contaminants and is equipped with laminar airflow benches, evaporation stations, extractor hoods, a weighing room, and an ultra-pure water production station.

Figure 28 - a) Clean room laboratory at the *Pôle Spectrométrie Océan* (PSO), IFREMER. b) Laminar flow hood from the clean room where all Mg/Ca cleaning protocol was performed



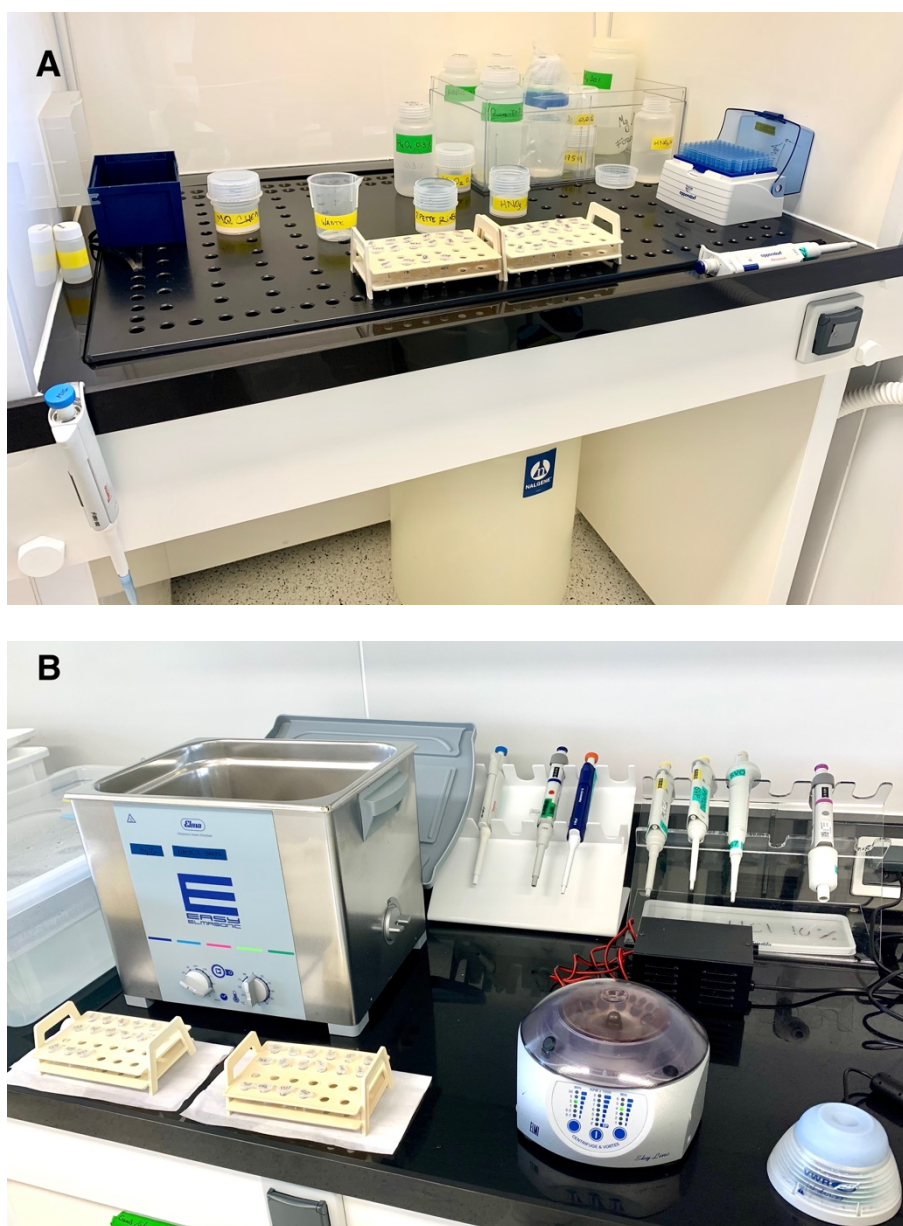
As described in Table 4, I prepared a set of new clean bottles and prepared reagents dedicated to Mg/Ca analysis. To prepare the new bottles, they were cleaned by soaking them in a 10% nitric acid bath for two days. Afterward, they were washed with ultra-pure Milli-Q water and dried inside a laminar airflow bench to prevent any particles from settling inside

the bottle. 500 ml bottles were used to stock a considerable volume of reagents, enough for many samples, while 60 ml beakers with screw caps were destined for everyday use (i.e., pipetting during the cleaning procedure). Bottles were chosen from different materials depending on their intended use. A 5 ml low-density polyethylene (LDPE) bottle was used for methanol since the volume of this reagent used per day of cleaning is small, and storing it for a long time on the available bottles is not recommended. PFA bottles are non-contaminating and made of ultrapure, ultra-chemically resistant material, an excellent choice for high-purity micro samples. If the solutions or reagents for cleaning will be stored for an extended period, PFA bottles are not indicated, and they should be renewed or stored in Teflon bottles. Teflon bottles were used for long-period storage of acid-containing reagents and standards due to their resistance to nearly any chemical, temperature, and process coupled with the properties ideal for solution preservation.

Table 4 - List of the materials used for Mg/Ca analysis

Material	Quantity	Solutions
500ml teflon bottle	4 units	HNO ₃ 10%; HNO ₃ 2%; NIST 8301 and FOREXRB standards
500ml PP bottle	5 units	UHQ H ₂ O (2 units); HNO ₃ 10%; HNO ₃ 0.001 M; HNO ₃ 0.075 M;
250ml PP bottle	1 unit	H ₂ O 0.3%
5ml LDPE bottle	1 unit	Methanol
2.0ml graduated tubes with skirt screw caps (pack of 500)	5 units	Samples
500 uL eppendorff	2 units	-
Eppendorff hack	2 units	-
Micropipettes (200 uL, 1000 uL, 5000 uL)	4 units	-
Microcentrifuge ELMI 12 vial slots	1 unit	-
Lab dancer IKA	1 unit	-
Ultrasonic bath Elmasonic 100H cover	1 unit	-
Nitric acid ultrapure	1L	-
Hydrogen peroxide 30% unstabilised, AnalaR NORMAPUR® for trace analysis	1L	-
Sodium hydroxide 1M in aqueous solution, TitriPUR® Reag. Ph. Eur.	1L	-

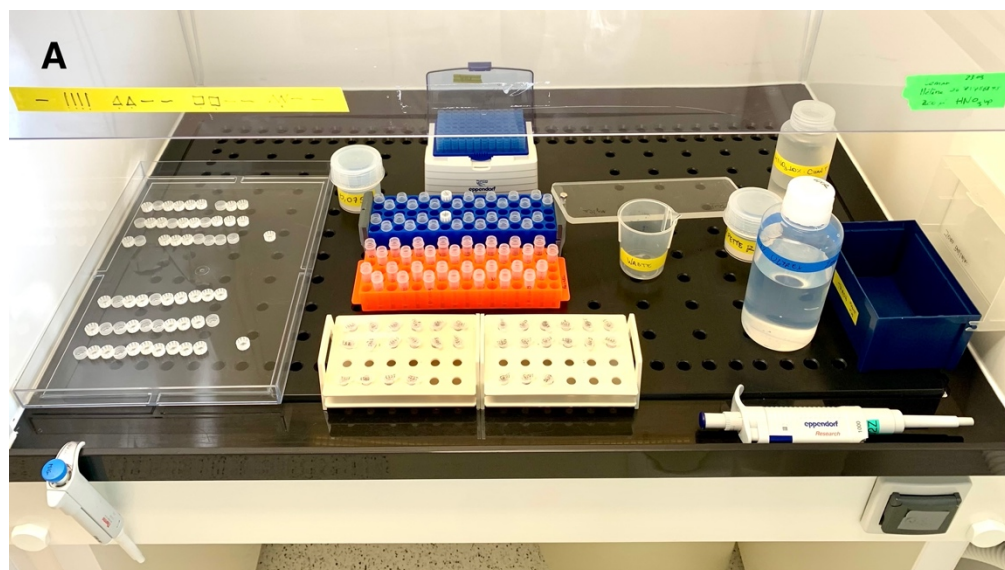
Figure 29 - Equipment needed for routinely cleaning foraminifera samples for Mg/Ca analysis in a clean laboratory, as listed in table 4. a) Set of solutions; b) equipment: ultrasound, microcentrifuge, and lab dancer



After cleaning the samples, dissolution and dilution were performed on the analysis day. I worked with additional sample hacks necessary to prepare sample dilutions during these steps (Fig. 30a). The sample dilutions for the second measurement run were performed in the ICP-MS laboratory (Fig. 30b; see section 6.3 below for details).

Figure 30 - Dilution steps performed on a clean room from PSO. a) dilution preparation for the first measurements run (dilution factor = 5). b) ADS Laminaire sterile hood from the ICP-MS laboratory

where dilutions for the second measurements run, and all standards used for external calibration were prepared



6.2.1 Cleaning protocol

The incorporation of Mg and Ca elements on planktic foraminifera tests depends on the surrounding seawater temperature during calcite growth. However, other factors can influence element concentration, and these interferences must be minimized to provide appropriate *in-situ* temperature estimates. Sample dissolution can affect Mg/Ca

concentration due to loss in magnesian calcite, reducing concentration, which promotes lower-than-real temperature estimations (Dekens *et al.*, 2002; Barker *et al.*, 2003). On the other hand, the presence of clay minerals or organic matter could also cause contamination. This happens because they get adsorbed on foraminiferal shells and increase interferences from Mg ion exchange, and the final Mg/Ca concentration can be either underestimated or overestimated. Different methods for cleaning foraminiferal samples before analysis have been developed to minimize contamination effects (Boyle, 1981; Boyle and Keigwin, 1985; Lea and Boyle, 1991; Rosenthal *et al.*, 2004). Some of the protocols were initially developed for Cd/Ca and Mn/Ca (proxies for nutrient and redox reconstructions, respectively) analyses, i.e., “the Cd cleaning method”, which involves an additional reductive step to remove Mn-Fe-oxide coatings (Boyle and Keigwin, 1985; Boyle and Rosenthal, 1996). Further chemical treatment of samples must be appraised carefully since they may affect trace element chemistry in the primary calcite (Barker *et al.*, 2003; Marr *et al.*, 2013). Therefore, choosing an appropriate cleaning procedure for foraminiferal samples highly depends on which elements of interest are targeted.

Removing silicate contaminants is an essential cleaning step, while oxidative and acid-leaching steps have minor interferences on final concentration estimations. (Barker *et al.*, 2003) performed a study to evaluate the efficiency of different cleaning procedures to determine which cleaning steps are crucial for accurately measuring Mg/Ca in foraminiferal species. They found reductive step may cause partial carbonate dissolution leading to a 10-15% decrease in Mg/Ca ratio. Other chemical-based cleaning techniques can reduce 25% of Mg/Ca values and may have worse effects on estimating low-concentration elements such as Uranium (Barker *et al.*, 2003; Marr *et al.*, 2013). Therefore, to choose additional cleaning steps also depends on which TE/Ca ratio is targeted and the level of contamination of the calcite, associated with the nature of samples, depending on its sedimentological and lithological characteristics from site location (Barker *et al.*, 2003). Hence, regions with high input of clay content would demand the employment of rigorous cleaning procedures.

The cleaning protocol may also undergo adaptations depending on the different measuring analytical instruments. Therefore, each laboratory has adopted its own cleaning and measurement protocols to optimize the measurement routine and improve the quality of results. Most protocols targeting foraminiferal Mg/Ca are based on (Barker *et al.*, 2003).

In this thesis, the implemented cleaning protocol at IFREMER was based on that established by the LSCE (Annex I), itself based on the study by Barker *et al.*, 2003). Each sample, consisting of ~30 planktonic foraminiferal shells, was gently crushed between two glass slides prior to cleaning in (precleaned) Eppendorf vials (see section 3.2.4). Using separate pipette tips for adding and removing reagents and constantly renewing them considerably maximize the cleaning performance, avoiding evident external contamination of samples. The cleaning steps are:

- **Clay removal:** Add 500 μl of UHQ H_2O to the crushed sample. Next, place samples in the ultrasonic bath for 1-2 minutes to improve the desegregation of clays from shell fragments. Remove UHQ H_2O with a pipette, taking care not to accidentally remove any foraminiferal fragment in the bottom on the Eppendorf tube, and, leaving samples with about 10-20 μl of H_2O remaining. This step must be repeated four times to maximize removing contaminants; more repetitions must be added if particulate materials are still visible.
- **Methanol:** Add 250 μl of methanol for further clay removal due to its lower viscosity, which helps dislodge material still attached to the foraminiferal fragments. Ultrasonicate samples for 1-2 minutes and remove methanol. This step must be repeated once again.
- **Remove organic matter:** Add 250 μl of alkali buffered 1% H_2O_2 solution by adding 100 μl H_2O_2 to 10 ml 0.1M NaOH, and close. Place samples in boiling water for 10 minutes to induce oxidation. To set up a boiling bath, you can use an ultrasonic bath with the added benefit of a heating feature. Another option is to use a laboratory heat plate, combined with a glass bowl to prepare a boiling bath. At 2.5 and 7.5 minutes, open vials to release bubbles of gas. At 5 minutes, ultrasonicate samples for a few seconds to dislodge microbubbles that may be attached to the calcite fragments. This step must be repeated once again. Next, rinse samples with UHQ H_2O twice.
- **Removal of coarse-grained silicates:** This step is necessary if silicates were observed in the sample at the binocular microscope after crushing. Transfer each sample to a 1 ml glass micro-beaker, add 100 μl of UHQ H_2O , and quickly transfer to a micro-beaker, avoiding settling. This step must be

repeated 3-4 times to ensure that the entire sample is transferred. Remove the remaining excess H₂O. Manually remove any remaining particles using a fine brush, if necessary, through an inspection on a microscope.

- **Sample transferring:** Transfer the samples to clean vials. It is possible to leave the samples at this point and prepare them for the subsequent steps. However, it is important to ensure enough liquid is left around the foram fragments in the bottom of the tube. The following steps will be conducted on the day of measurements.
- **Weak acid leaching:** This step aims to remove any adsorbed contaminants on the shell fragments. Add 250 µl of 0.001 M HNO₃ to each sample and ultrasonicate for 30 seconds. Remove the acid and quickly rinse samples with UHQ H₂O twice to avoid excessive dissolution.
- **Dissolution:** Add 500 µL of 0.075 M HNO₃ to each sample and ultrasonicate. After wholly dissolved, they should be transferred to clean vials.

6.3 Walking through the analytical steps

A significant part of my thesis was dedicated to improving my technical laboratory skills by implementing the analytical method for Mg/Ca measurements on ICP-MS. It will be helpful later on in my career in order to transfer knowledge between France and Brazil. In the following topics of this section, I describe the performed method divided into pre-, peri-, and post-analysis steps.

6.3.1 Pre-analysis: standard preparations

The ambition of the laboratory in setting a routine methodology for foraminifera Mg/Ca analysis is to be able to incorporate several reliable measurements into the laboratory routine to produce new proxy records that will allow reconstructions of a physical quantity (i.e., ocean temperature), which so far could not be measured in the Geo-Ocean laboratory. A crucial step in the analytical approach is defining a calibration strategy since the measured signal by the ICP-MS detector is reported in units of counts per second (cps), i.e., the number of ions striking the detector every second. External calibration using calibration standards with known element concentrations is used to convert cps data to concentrations, and its preparation is crucial for accurate concentration determination. The relation between cps and

concentration is expected to have linear behavior. The few steps performed will be described below:

(1) choosing a suitable and reliable reference material is vital, preferentially opting for internationally certified standards.

(2) to prepare a high-concentrated stock solution and the dilution factor for desired concentrations for preparing the in-house standard. Creating an in-house standard can be a cost-effective solution to minimize using expensive and limited internationally certified standards. By calibrating the in-house standard against the certified one, it can be used to calibrate samples during measurements, reducing the need for constantly measuring and consuming the certified standard. If needed, a new in-house standard can be created and calibrated against the international one. Properly storing the in-house standard is essential to maintain its stability and concentration. Therefore, storing it on Teflon bottles and refrigerating it is highly recommended. When determining the Mg/Ca target concentrations, we took into account various factors including the geographic location of the samples, the species of foraminifera used, their size, and the regional processes that control the local environmental parameters, such as temperature at the site. I defined the target concentrations for each element measured based on previous studies reported in the literature (de Villiers *et al.*, 2002; Eggins *et al.*, 2003; Hall and Chan, 2004; Yu and Elderfield, 2007; Greaves *et al.*, 2008; Yu *et al.*, 2008; Hönisch *et al.*, 2011; Allen and Hönisch, 2012; Lu *et al.*, 2016; Vázquez Riveiros *et al.*, 2016; Chen *et al.*, 2017; Gray and Evans, 2019; Haynes *et al.*, 2019; Lu *et al.*, 2020; Zhou *et al.*, 2021; Ma *et al.*, 2022).

(3) validate the concentration of the in-house standard in the ICP-MS session by measuring with the used international standard reference material.

(4) Use the in-house standard in ICP-MS measurements as a reference for calibration and to determine the accuracy and precision of the results.

(5) sample measurement sessions comprise repeated measurements of the international standard reference material and in-house standard during each session. If preparing a new in-house standard or international standard dilution is necessary, periodically repeat the validation step to ensure its continued accuracy.

The external calibration for elements Mg/Ca at IFREMER was based on the NIST 8301 international reference standard for boron isotopes in marine carbonate (foraminifera)

(Stewart *et al.*, 2021). The concentrations on NIST 8301 are notified in the standard report (Annex II).

The solution FOREXRB for bracketing method calibration is based on the diluted FOREXR in-house standard. High-purity chemicals and water are needed to prepare the standards to minimize interference by impurities in the ICP-MS analysis. FOREXR was prepared from mono-elementary solutions according to the target elements and respective concentrations of interest (Table 5).

I prepared by weighting the FOREXR stock solution and FOREXRB in-house standard for external calibration during sample measurement sessions and repeated measurements of NIST 8301. Although many elements were measured, our main targets are Mg, Ca, Al, Fe, and Mn elements.

Table 5 - Element ratio concentrations of used standards for the elements of interest in this thesis

Target elements	Target max concentration of FOREXR stock solution	unit	Target max concentration of FOREXRB bracketing solution	unit	NIST 8301 concentrations	unit
Ca	0.04	g/Kg	0.04	g/Kg	51.3	mg/g
Mg/Ca	15	mmol/mol	3	mmol/mol	2.62 ± 0.14	mmol/mol
Al/Ca	0.1	mmol/mol	40	mmol/mol	90.91 ± 16.58	mmol/mol
Mn/Ca	0.1	mmol/mol	40	mmol/mol	49.4 ± 2.14	mmol/mol
Fe/Ca	0.1	mmol/mol	0.05	mmol/mol	25.42 ± 1.69	mmol/mol

6.3.2 The routine of measurements: ICP-MS sessions

On the day of measurements, it is important to have prepared all necessary materials and reagents beforehand. Although a significant part of sample preparation was conducted before analysis day, after cleaning the samples in the clean lab (i.e., white room), the dissolution and dilutions steps must be conducted only on the day of measurements. Each core sample was analyzed two times on each measurement day to determine concentrations precisely. The objective of the first run was to quickly determine Ca intensities present in samples to precisely calculate the dilution factor necessary for normalizing [Ca] samples to

40 ppm to be measured in the second run. During the second run, relatively longer measurement times were used to increase the precision of measurements.

According to the cleaning protocol (Barker *et al.*, 2003), 350 μL of a relatively weak nitric acid (0.075 M) was used to slowly dissolve all foraminifera fragments with an auxiliary lab dancer and ultrasound. This step should be as quick as possible in order to avoid the dissolution of any other remaining lithogenic fraction. Nevertheless, verifying if there are no remaining visible fragments in the sample solution is imperative before dilution.

After dissolving all calcite fragments, sample solutions were centrifuged (10000 rotations/min for 2 minutes) and 300 μL was transferred to new clean vials. During vial transferring, it is crucial to pipet samples carefully to avoid possibly transferring large undissolved particles that might be settled in the bottom, even though this step is done after dissolution. The sample solution was split into two new vials to prepare first- and second-run dilutions. From this point, I worked in the clean lab with two sample racks, one rack for the first run and another for the second. The first rack was destined for the first run, whereas samples were diluted by a factor of 5 by adding 280 μL of HNO_3 2% to 70 μL of raw sample. Sample blanks are not analyzed during the first run, and then they are not diluted.

The remaining 230 μL of each sample were diluted enough to normalize [Ca] to 40 ppm by adding HNO_3 2%, using the Ca intensities obtained on the first run. Normalization calculations follow Eq. 5:

$$V_{\text{HNO}_3} = ((\text{Ca}_{1\text{st}} \times V_{\text{sample}}) / \text{FOREXRB}_{\text{intensities}}) - V_{\text{sample}} \quad (\text{Eq. 5})$$

V_{HNO_3} is the diluent volume necessary to normalize samples to 40 ppm; $\text{Ca}_{1\text{st}}$ is the Ca intensity (in cps) measured in the first run; V_{sample} is the initial volume of sample needed to be diluted prior to the second run (230 μL); $\text{FOREXRB}_{\text{intensities}}$ is the normalization calculated by the averaged intensity of several measurements of FOREXRB (about 15 per session with [Ca] = 40 ppm) analyzed in the first run.

The second run was thus performed after calculating the nitric acid necessary to normalize all samples to 40 ppm and dilute them. Due to IPC-MS collector limitations, the minimum volume of samples was 300 μL , and all sample blanks were diluted by 2.

6.3.3 Post-analysis: data treatment

After measurements, the output file from the ICP-MS needs to be “cleaned” for the following correction steps; it is essential to have a clean, well-organized file to avoid mistakes in formula propagation and to help the posterior data analysis. I defined color codes for each sample type to break up the sequence of measurements in each session. The color system is shown in Table 6.

Table 6 - Example of a table used to apply all post-analysis corrections. Elements were organized following their resolution range (i.e., low resolution (LR), medium resolution (MR), and high resolution (HR)). Color codes were determined for each sample in the sequence of measurements on the ICP-MS session. Yellow: machine blanks; blue: FOREXRB in-house standard; green: NIST 8301 (Forams) international standard; red: NIST 8301 dilutions; no fill: foraminifera samples, identified by core name, sp, and depth

Measurements sequence	Isotope	Medium-resolution (MR)				
		Mg ²⁴ (MR)	Ca ⁴⁴ (MR)	Al ²⁷ (MR)	Mn ⁵⁵ (MR)	Fe ⁵⁶ (MR)
Blank133	Intensity AVG [cps]	675.2	1390.5	252.1	22.9	229.2
FOREXRB1	Intensity AVG [cps]	854697.8	27588592.6	59849.0	111241.5	119305.8
NIST D030	Intensity AVG [cps]	720956.2	28158457.4	39922.9	75224.6	34755.9
NIST D031	Intensity AVG [cps]	753342.2	28539779.8	41195.0	77237.2	38744.0
FOREXRD500	Intensity AVG [cps]	91894.7	29314757.6	6784.3	3500.5	17303.6
FOREXRB2	Intensity AVG [cps]	898352.2	29217429.9	63002.2	118311.2	125831.6
BLANK028	Intensity AVG [cps]	697.5	1382.2	226.4	17.4	265.8
FOREXRB3	Intensity AVG [cps]	891324.8	29531217.6	63060.6	116160.3	122900.4
FOREXRD500b	Intensity AVG [cps]	93986.5	29505811.8	6668.9	3608.3	17423.0
NIST033E	Intensity AVG [cps]	757841.0	29046149.7	41107.3	79205.6	36661.4
FOREXRB4	Intensity AVG [cps]	874148.7	28193169.1	61536.2	115470.0	120960.0
BLANK029	Intensity AVG [cps]	727.3	1401.7	266.7	13.9	380.8
FOREXRB5	Intensity AVG [cps]	864627.0	28418452.9	60143.1	115916.6	120515.4
3167-GI-909	Intensity AVG [cps]	359209.8	20949126.6	19791.9	8013.8	145547.5
3167-GI-914	Intensity AVG [cps]	320290.3	21356321.6	10387.8	9545.0	148115.5
NIST036E	Intensity AVG [cps]	734802.5	28049697.7	39921.5	76237.3	36222.5
3167-GI-925	Intensity AVG [cps]	286385.6	20863963.9	16945.4	9280.0	137175.1
3167-GI-933	Intensity AVG [cps]	263276.5	20789190.8	13944.2	7946.3	220758.0
FOREXRB6	Intensity AVG [cps]	845033.8	27910181.8	59331.9	112420.8	118476.5
Blank058	Intensity AVG [cps]	666.2	1273.7	239.6	22.9	305.0
FOREXRB7	Intensity AVG [cps]	858445.8	27594844.2	59957.0	111781.8	118902.4
3167-GI-941	Intensity AVG [cps]	256449.0	21894586.5	20555.5	7712.6	162198.2
3167-GI-949	Intensity AVG [cps]	311640.8	21270092.9	19303.6	10474.0	310300.9
FOREXRD500064	Intensity AVG [cps]	88801.5	28023589.8	6695.3	3385.8	16332.1
3167-GI-957	Intensity AVG [cps]	364658.8	21875599.6	19497.7	19126.2	79108.7
3167-GI-965	Intensity AVG [cps]	406137.3	24132783.5	17638.1	22297.5	230696.0
FOREXRB8	Intensity AVG [cps]	847749.7	27833490.4	58588.8	111769.3	117801.6

Blank059	Intensity AVG [cps]	597.4	1275.8	239.6	21.5	216.7
FOREXRB9	Intensity AVG [cps]	833161.5	27326460.6	58289.8	109791.0	115409.9
3167-GI-973	Intensity AVG [cps]	379015.3	23348792.3	34706.8	23359.9	665513.8
3167-GI-981	Intensity AVG [cps]	394676.4	23111842.3	15107.5	17398.9	52260.3
FOREXRD10066	Intensity AVG [cps]	429784.8	28602032.6	8641.7	16156.5	29406.9
3167-GI-989	Intensity AVG [cps]	392458.4	23281000.4	16338.2	16077.9	294528.4
3167-GI-997	Intensity AVG [cps]	376995.6	22984400.5	16240.1	19409.4	92677.5
FOREXRB10	Intensity AVG [cps]	816473.7	26861563.6	57288.5	107743.5	114399.1
Blank060	Intensity AVG [cps]	555.6	1191.7	257.6	22.9	220.0
FOREXRB11	Intensity AVG [cps]	839344.0	26942634.0	58217.7	108894.3	116272.6
3167-GI-1005	Intensity AVG [cps]	336655.0	22071960.3	6938.7	15320.4	48101.9
3167-GI-1013	Intensity AVG [cps]	365165.1	23440507.0	9236.2	14159.6	38924.3
FOREXRD500065	Intensity AVG [cps]	85562.8	27320185.0	6349.7	3403.8	16027.3
3167-GI-1021	Intensity AVG [cps]	363183.1	21956330.2	10581.2	14359.9	28540.2
3167-GI-1029	Intensity AVG [cps]	369260.8	23042304.2	14135.1	12953.5	24767.2
FOREXRB12	Intensity AVG [cps]	810510.7	27172379.5	58036.7	109717.4	114915.5
Blank	Intensity AVG [cps]	535.5	1130.5	254.9	28.5	226.7
FOREXRB13	Intensity AVG [cps]	804635.2	26486430.9	56057.1	106927.0	111841.5
3167-GI-1037	Intensity AVG [cps]	370083.0	22738189.3	9607.5	12973.6	35948.0
3167-GI-1045	Intensity AVG [cps]	396071.4	22821602.0	8617.3	14295.1	26113.3
NIST037E	Intensity AVG [cps]	681817.4	26320586.5	36793.3	70993.8	32148.9
3167-GI-1053	Intensity AVG [cps]	417383.2	22784774.8	10123.6	14164.5	29279.9
3167-GI-1061	Intensity AVG [cps]	349188.6	22482418.9	8839.3	14346.0	32380.4
FOREXRB14	Intensity AVG [cps]	775302.8	25355418.2	54870.7	102319.4	108873.7
Blank061	Intensity AVG [cps]	539.7	1175.7	211.8	25.7	250.8
FOREXRB15	Intensity AVG [cps]	798596.8	26542787.3	56879.4	105465.0	110463.6
3167-GI-1069	Intensity AVG [cps]	513804.8	33976571.2	11702.3	20614.5	31071.5
3167-GI-1077	Intensity AVG [cps]	516452.5	33542003.0	9440.7	24997.3	38385.5
FOREXRB16	Intensity AVG [cps]	803229.3	25971799.3	56699.4	105814.3	110832.2
Blank032	Intensity AVG [cps]	530.7	1136.8	225.7	20.8	222.5
FOREXRB17	Intensity AVG [cps]	786059.5	26154421.5	55430.4	105655.6	111851.1
3167-GI-1085	Intensity AVG [cps]	441781.8	25954543.0	7980.3	20101.1	80217.2
3167-GI-1093	Intensity AVG [cps]	846851.8	50177370.5	9638.2	36398.4	40636.4
FOREXRB18	Intensity AVG [cps]	803279.7	26559499.6	57246.9	106317.6	113482.8
3167-GI-1101	Intensity AVG [cps]	393357.8	23580015.3	6088.3	14729.1	17683.5
3167-GI-1109	Intensity AVG [cps]	383820.1	22981570.3	7342.7	16047.3	22057.9
FOREXRB22	Intensity AVG [cps]	807335.3	26374210.2	55634.5	107888.6	112568.6
3167-GI-1117	Intensity AVG [cps]	344180.0	23456731.3	7858.6	11979.1	16349.5
3167-GI-1125	Intensity AVG [cps]	71.5	436.8	55.6	2.1	82.5
FOREXRB19	Intensity AVG [cps]	780958.0	25644936.7	54489.4	104448.5	111254.2
3167-GI-1133	Intensity AVG [cps]	348525.8	23319143.8	6582.7	12051.4	13355.6
3167-GI-1141	Intensity AVG [cps]	329704.8	23668761.6	9053.3	13352.8	17364.5
Blank033	Intensity AVG [cps]	524.4	1094.4	228.5	16.7	213.3
FOREXRB20	Intensity AVG [cps]	774773.3	25632017.7	54582.4	103450.8	108991.4
3167-GI-1149	Intensity AVG [cps]	373613.5	23623718.8	5787.3	15845.6	23130.0

3167-GI-1157	Intensity AVG [cps]	460326.3	26629246.5	17440.7	18674.8	76132.0
FOREXRB21	Intensity AVG [cps]	762295.2	25524601.7	54353.6	102981.8	108510.9
B04	Intensity AVG [cps]	3821.0	16098.7	3055.5	154.2	4183.2
B07	Intensity AVG [cps]	10748.1	85046.3	4694.9	450.0	3639.2
Blank034	Intensity AVG [cps]	483.4	935.2	229.2	13.9	187.5
FOREXRB23	Intensity AVG [cps]	759469.7	25219623.6	53699.8	100819.8	104988.5
NIST038E	Intensity AVG [cps]	647991.3	24874769.9	34715.2	67836.2	30585.3

A sample-specific dilution factor was applied to each foraminiferal sample that needed correction for. Real dilution factor (RDF) corrections were applied to each diluted sample and standard. No correction was applied for blanks and undiluted samples. The dilution factor applied to foraminifera samples is based on the calculated dilutions prior to the second run. For stock solution dilutions or NIST 8301, It was estimated conservatively by considering the weight of each compound added to make the new solution. It is calculated as described in Eq. 6:

$$\text{RDF}_{\text{correction}} = \text{Weight}_{\text{HNO}_3} / \text{Weight}_{\text{solution}} \quad (\text{Eq. 6})$$

$\text{RDF}_{\text{correction}}$ is the real dilution factor based on the weight of the reagents composing a solution; $\text{Weight}_{\text{HNO}_3}$ is the weight of the diluent; $\text{Weight}_{\text{solution}}$ is the weight of the "mother solution" that was diluted.

After intense long operational periods, i.e., with a high number of samples per day and/or after a sequence of multiple days of measurement, it is possible that ICP-MS present instabilities that could promote the decrease of the measured intensity counts. To track and correct possible machine-sourced deviations, Yoan Germain uses nitric acid 2 % spiked with indium (In) routinely as a default diluent for samples and standards, as well as for the machine blanks measured on ICP-MS from IFREMER. In natural samples, In concentrations is very little or rather none, so its concentration should be constant before and after measurements since the unique source of this element would come from the diluent. Therefore, In intensities are used to track possible drifts in the measurements. Evaluating the measured machine blank intensities following each analysis session allows us to check if measurement intensities are artificially decaying and calculate a correction factor to "adjust" element concentrations for a potential drift. The In-correction factor is calculated relative to an average of a few measurements of machine blanks at the beginning of each session, as described in Eq. 7:

$$I_{\text{c-factor}} = I_{\text{measured}} / I_{\text{blank}} \quad (\text{Eq. 7})$$

$I_{\text{c-factor}}$ is the I_{n} correction factor for machine-drift measurement correction; I_{measured} is the intensity of the sample to be corrected; and I_{blank} is the average intensity of few I_{n} measurements of machine blanks used for bracketing correction.

Even though, by verifying I_{n} values from blanks, it is possible to track deviations on each ICP-MS session and identify potential untrustable machine blanks that resulted from intern contamination or machine instabilities. Therefore, machine blanks are crucial reference values used in the following data correction step. Blank measurements and corrections were performed between blocks of standards and foraminifera samples, and the correction applied considering the two nearest blanks (i.e., from the beginning and end of the block) chosen around what is being measured (i.e., machine blanks, international reference material, in-house standard, and different dilutions, or foraminifera samples). It was calculated by subtracting the averaged value between the two nearest reliable measured machine blank values, which means that they did not deviate due to machine stabilities or did not present traces of contamination (i.e., not-aberrant values that should be nearly constant among them), applied individually for each measured element. It is calculated as described in Eq. 8:

$$E_{\text{blank-corrected}} = E_{\text{measured}} - (E_{\text{blank1}} + E_{\text{blank2}}/2) \quad (\text{Eq. 8})$$

$E_{\text{blank-corrected}}$ is the measured intensity of an element corrected with machine blanks; E_{measured} is the measured intensity of an element; E_{blank1} and E_{blank2} are machine blank intensities of an element measured between "blocks" of sample measurements.

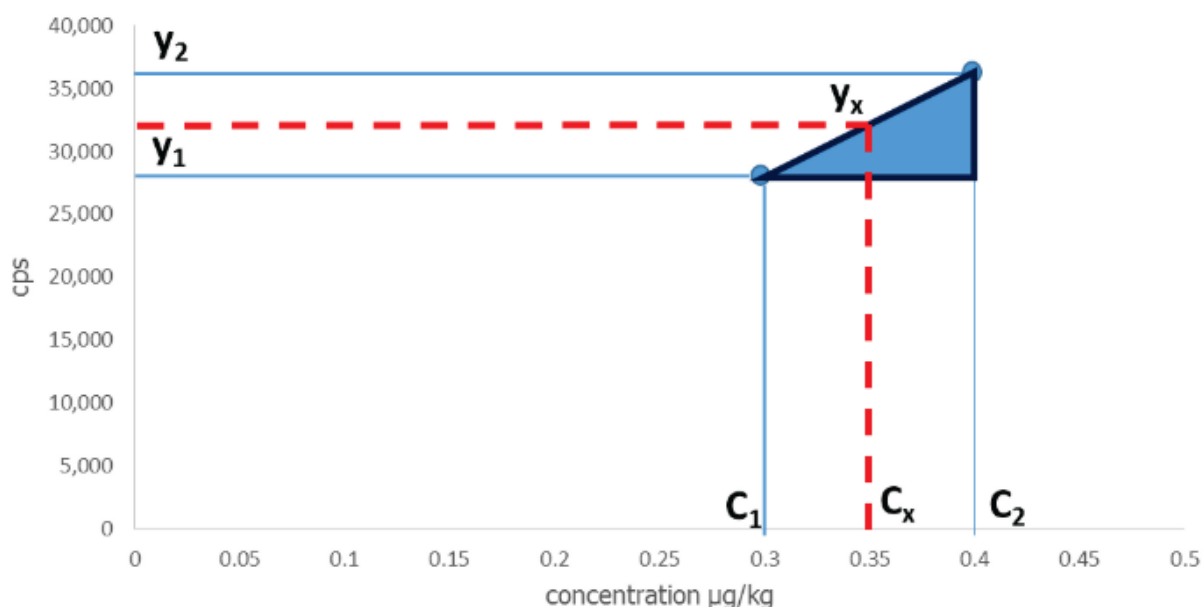
After correcting all measurements, I refined the results by removing elements not present in NIST 8301 composition; hence, their concentrations could not be determined on the scope of this thesis. Therefore, as mentioned earlier in this section, I attend to report the ^{24}Mg , ^{44}Ca , ^{27}Al , ^{55}Mn , and ^{56}Fe measurements.

6.3.4 Determination of element concentrations

The following steps are dedicated to determining element concentrations using the bracketing method. The bracketing method provides a way to increase the accuracy of ICP-MS measurements by accounting for instrument drift and other sources of measurement

error. By bracketing the unknown sample with known reference materials, the method helps to reduce the impact of these sources of error, such as calibration bias, and to improve the precision and accuracy of the results (Ketrin *et al.*, 2017). This external calibration is based on a "bracket" with standard measurements before and after the unknown sample. This allows to linearly calculate the relation between measured cps intensities and concentrations as a calibration curve (Fig. 31). The concentration of the unknown sample can be determined by reporting the signal intensity through the calibration curve. The calibration accuracy can be validated by comparing the calculated concentrations with the true concentrations of the reference materials. I implemented this method by calibrating FOREXRB with NIST 8301 known values (measured cps against known concentrations) and then FOREXRB standard to construct a two-point standard calibration curve. FOREXRB was measured before and after a group of samples, and NIST 8301 was constantly measured throughout the sessions. An average of 7 measurements were performed on the NIST 8301 standard and 20 on the FOREXRB on every session on ICP-MS.

Figure 31 - Schematic example of bracketing method concentration determination calculated from the two known concentration standards (modified from Ketrin *et al.*, 2017). C_1 and Y_1 represent the concentration and intensity of standard 1; same for C_2 and Y_2 but relative to standard 2; C_x and Y_x are the concentration and intensity of the analyte in the sample. The analyte concentration C_x is determined from linear interpolation between two known intensities-concentration values of the standards (i.e., the hypotenuse line on the blue triangle)



From this point, I calculated the statistics of measured standards and determined sample concentrations directly from $TE/^{44}Ca$ ratios (in intensities cps/cps) individually for each ICP-MS session. After calculating the ratios, I separated foraminifera samples from the

standards. Each kind of standard was grouped to calculate the descriptive statistics of standards to evaluate the precision and reproducibility of the measurements from every session.

Table 7 - Example of a) NIST 8301 international reference material and b) FOREXRB in-house standard statistics calculations routinely done on each ICP-MS measurement session. The mean and standard deviation of the standard measurement intensities for each TE/Ca ratio of interest were used to determine FOREXRB concentrations and sample concentrations (i.e., in mmol/mol)

A

NIST 8301 reported values:

Ratios	Mg/Ca	Al/Ca	Mn/Ca	Fe/Ca
Units	mmol/mol	mmol/mol	mmol/mol	mmol/mol
Concentration	2.62	90.91	49.40	25.42
STD	0.14	16.58	2.14	1.69

NIST 8301 measured intensities:

Sample name	Mg/Ca	Al/Ca	Mn/Ca	Fe/Ca
Units	cps/cps	cps/cps	cps/cps	cps/cps
NIST D030	0.02558	0.00141	0.00267	0.00123
NIST D031	0.02637	0.00144	0.00271	0.00135
NIST033E	0.02607	0.00141	0.00273	0.00125
NIST036E	0.02617	0.00141	0.00272	0.00128
NIST037E	0.02589	0.00139	0.00270	0.00121
NIST038E	0.02603	0.00139	0.00273	0.00122

NIST 8301 session statistics:

Statistics	Mg/Ca	Al/Ca	Mn/Ca	Fe/Ca
Units	cps/cps	cps/cps	cps/cps	cps/cps
Ave	0.02602	0.00141	0.00271	0.00126
STD	0.00027	0.00002	0.00002	0.00005
RSD%	1.0	1.3	0.8	3.1

B**FORERXB specified (true) ratio concentrations:**

Ratios	Mg/Ca	Al/Ca	Mn/Ca	Fe/Ca
Units	mmol/mol	mmol/mol	mmol/mol	mmol/mol
Concentration	3.07	146.92	69.53	63.48

FORERXB measured intensities:

Sample name	Mg/Ca	Al/Ca	Mn/Ca	Fe/Ca
Units	cps/cps	cps/cps	cps/cps	cps/cps
FOREXRB1	0.03096	0.00216	0.00403	0.00432
FOREXRB2	0.03073	0.00215	0.00405	0.00430
FOREXRB3	0.03016	0.00213	0.00393	0.00415
FOREXRB4	0.03098	0.00217	0.00410	0.00428
FOREXRB5	0.03040	0.00211	0.00408	0.00423
FOREXRB6	0.03025	0.00212	0.00403	0.00423
FOREXRB7	0.03109	0.00216	0.00405	0.00430
FOREXRB8	0.03044	0.00210	0.00402	0.00422
FOREXRB9	0.03047	0.00212	0.00402	0.00422
FOREXRB10	0.03038	0.00212	0.00401	0.00425
FOREXRB11	0.03113	0.00215	0.00404	0.00431
FOREXRB12	0.02981	0.00213	0.00404	0.00422
FOREXRB13	0.03036	0.00211	0.00404	0.00421
FOREXRB14	0.03056	0.00215	0.00403	0.00428
FOREXRB15	0.03007	0.00213	0.00397	0.00415
FOREXRB16	0.03091	0.00217	0.00407	0.00426
FOREXRB17	0.03004	0.00211	0.00404	0.00427
FOREXRB18	0.03023	0.00215	0.00400	0.00426
FOREXRB22	0.03059	0.00210	0.00409	0.00426
FOREXRB19	0.03043	0.00212	0.00407	0.00433
FOREXRB20	0.03021	0.00212	0.00404	0.00424
FOREXRB21	0.02985	0.00212	0.00403	0.00424
FOREXRB23	0.03010	0.00212	0.00400	0.00416

FORERXB session statistics:

Statistics	Mg/Ca	Al/Ca	Mn/Ca	Fe/Ca
Units	cps/cps	cps/cps	cps/cps	cps/cps
Ave	0.03044	0.00213	0.00403	0.00425
STD	0.00038	0.00002	0.00004	0.00005
RSD%	1.3	1.1	0.9	1.2

The following steps are dedicated to determining standards and sample concentrations calibrated from measured intensities and known standard concentrations. It

is necessary to consider the theoretical TE/Ca concentrations content in NIST 8301 (NIST_{theoretical concentration}), which is relative to the specific ratio concentrations reported in the international reference material report (Annex II), and the volume of each mono-elementary solution and HNO₃ added during FOREXRB solution preparation. By using the averaged intensity of the NIST 8301 measurements and knowing the reported theoretical concentrations, it is possible to determine the real measured concentration for FOREXRB during the session. The relation between these variables follows Eq. 9:

$$\text{FOREXRB}_{\text{true concentration}} = (\text{FOREXRB}_{\text{measured}} * \text{NIST}_{\text{theoretical concentration}} / \text{NIST}_{\text{measured}} \quad (\text{Eq. 9})$$

FOREXRB_{true concentration} is the FOREXRB "true" concentration calculated with the bracketing method; FOREXRB_{measured} is the FOREXRB measured intensity during the session (in cps/cps); NIST_{theoretical concentration} is the NIST ratio value for the determined ratio reported in the international standard reference material report; NIST_{measured} is the intensity of NIST measured during the session (in cps/cps).

Ratio concentrations from foraminifera samples were determined by considering the measured element ratio intensities (cps/cps) from samples, FOREXRB measured intensities (cps/cps), and previously calculated FOREXRB true concentration (mmol/mol), as described in Eq. 10:

$$\text{Sample}_{\text{true concentration}} = (\text{Sample}_{\text{measured}} * \text{FOREXRB}_{\text{true concentration}} / \text{FOREXRB}_{\text{measured}}. \quad (\text{Eq. 10})$$

Sample_{true concentration} is the calculated "true" concentration of samples calculated with the bracketing method; Sample_{measured} is the measured sample intensity during the session (in cps/cps). Note that FOREXRB theoretical values are not used for sample "true" concentration determination but for calculating the precision of FOREXRB "true" concentration determination.

It is crucial to mention that the data treatment and following measurement quality evaluation must be carefully conducted to provide an accurate final ratio concentration of samples. In this regard, aberrant ratio intensities before true concentration calculations can often be explained by an equivocal value considered in the equations during the raw-data correction steps, so results must be carefully inspected.

Beyond calculation mistakes, aberrant ratio intensities could also be caused by the matrix effect. The machine blanks can reveal matrix effects or unperceived inner-machine interferences during the measurements. It is essential to build a logical sequence of measurements with repeated analyzes of many blanks and standards throughout each session. Besides, routinely periodic maintenance, particularly cleaning or changing the ICP-MS cones, and often verifying the operational parameters to track the machine's stability is paramount to assure quality data.

6.4 Measurement results

High discrepancies between determined NIST 8301 and FOREXRB concentrations (i.e., calculated from the bracketing method) and their theoretical values (i.e., calculated by the weight of solvents/species during standard solution preparation) might occur due to inaccurate determination of initial standard element concentrations or to possible machine interferences during the measurements. Systematic deviations identified in the overall standard measurement statistics might reflex machine drifts variabilities throughout different sessions. The uncertainties associated with the measurements were evaluated through the repeated analysis of standard solutions and replicate samples. The standard solutions were measured repeatedly throughout the analysis to evaluate the instrumental drift and correct for any systematic errors. The replicate samples were analyzed multiple times to assess the precision of the measurements. The reported uncertainties can be used to evaluate the reliability of the measurements and to compare the results with other studies.

The external reproducibility of the measurements was determined by calculating measurement statistics of 75 NIST 8301 and 234 measurements of FOREXRB throughout 12 sessions on ICP-MS. On each analysis day, an average of 6 NIST 8301 and 20 FOREXRB measurements were performed. The percentage difference between the measurement means and theoretical values are 2.4 % and 3.8 %, respectively, from NIST 8301 and FOREXRB. Complementary to the SD, another method used to report analytical uncertainty on element measurements is to use the relative standard deviation (%RSD) of replicate measurements (Blum and Bergquist, 2007). %RSD is calculated by dividing the standard deviation of the replicate measurements by the mean of the measurements and multiplying by 100. SD

provides information about the variability of the replicate measurements, and %RSD allows for comparing precision between different studies (Table 8).

Table 8 - Standard statistics for a) NIST 8301 and b) FOREXRB

A

NIST 8301	Mg/Ca	Al/Ca	Mn/Ca	Fe/Ca
<u>Units</u>	<u>cps/cps</u>	<u>cps/cps</u>	<u>cps/cps</u>	<u>cps/cps</u>
Measurement mean	0.02732	0.00154	0.00271	0.00130
1 SD	0.00118	0.00016	0.00008	0.00013
RSD %	4.3	10.4	2.9	9.8
<u>Units</u>	<u>mmol/mol</u>	<u>μmol/mol</u>	<u>μmol/mol</u>	<u>μmol/mol</u>
Measurement mean	2.68	102.6	47.19	19.98
1 SD	0.07	8.7	0.91	2.2
RSD %	2.58	8.52	1.92	10.96
% diff	2.393	12.858	-4.480	-21.387

B

FOREXRB	Mg/Ca	Al/Ca	Mn/Ca	Fe/Ca
<u>Units</u>	<u>cps/cps</u>	<u>cps/cps</u>	<u>cps/cps</u>	<u>cps/cps</u>
Measurement mean	0.03074	0.00219	0.00396	0.00416
1 SD	0.00300	0.00016	0.00038	0.00013
RSD %	9.8	7.2	9.5	3.1
<u>Units</u>	<u>mmol/mol</u>	<u>μmol/mol</u>	<u>μmol/mol</u>	<u>μmol/mol</u>
Measurement mean	2.949	129.377	72.180	81.239
1 SD	0.288	9.339	6.891	2.545
RSD %	9.8	7.2	9.5	3.1
% diff	3.8	11.9	-3.8	-28.0

The uncertainties associated with the NIST 8301 measurements were determined to be ± 0.07 mmol/mol (1 SD) and 2.58 % RSD for Mg/Ca. The FOREXRB measurements had an uncertainty of ± 0.29 mmol/mol (1 SD) and 9.8 % for Mg/Ca. The average Mg/Ca measurement on foraminifera samples was 1.46 ± 0.29 mmol/mol ($n = 300$, 1 SD) (Table 9).

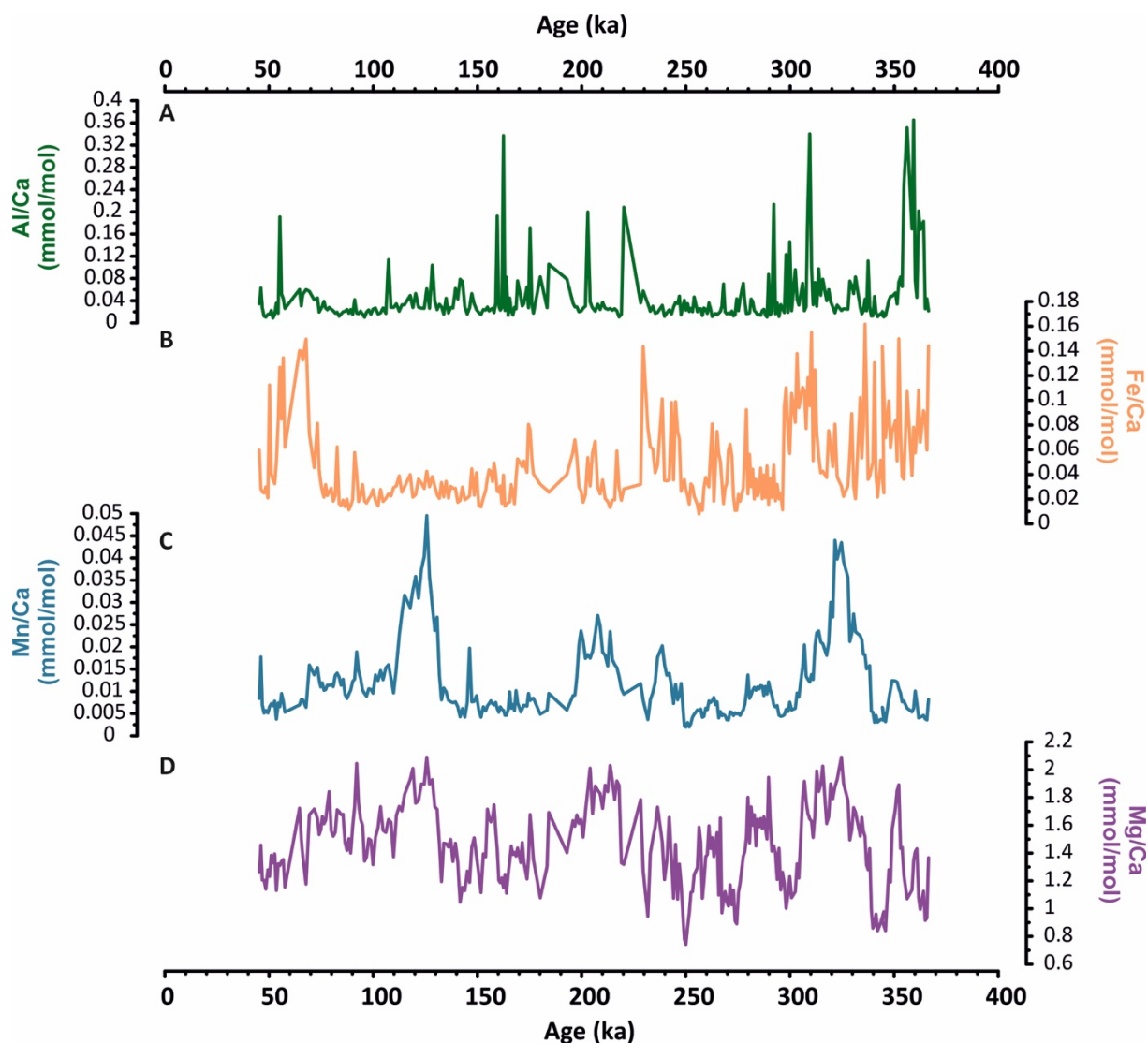
Table 9 - Sample measurements statistics: minimum, maximum, mean, standard deviation. Different from raw data presented for NIST 8301 and FOREXRB, all ratios are reported in mmol/mol since these ratios a commonly reported on this unit

Foraminiferal samples	Mg/Ca	Al/Ca	Mn/Ca	Fe/Ca
Units	mmol/mol	mmol/mol	mmol/mol	mmol/mol
Min	0.742	0.009	0.002	0.008
Max	2.091	0.365	0.050	0.162
Measurement mean	1.457	0.044	0.012	0.047
1 SD	0.287	0.053	0.008	0.033

6.5 Tracking contamination: Evaluating the efficacy of the cleaning protocol

One crucial post-analysis verification for Mg/Ca paleotemperature reconstructions is the evaluation of the presence of contamination in the analyzed samples, which could compromise the reliability of the measured results. For this reason, Al/Ca, Fe/Ca, and Mn/Ca ratios (here, TE/Ca_{contaminants}) are used as fingerprints to track contamination and evaluate the efficiency of the performed cleaning protocol in removing clay particles, Mn-coatings or organic matter. Clay minerals represent a significant fraction of marine sediments, and their effects on Mg/Ca vary among samples and depend on site locations. Samples with low Mg/Ca content are more sensitive to contamination, even in small amounts, compared to those with high Mg/Ca values. For example, samples from cold regions with low Mg/Ca concentrations (<2 mmol/mol) are more likely to suffer strong interferences by silicate than those from warm locations (i.e., with expected higher Mg/Ca). Thus, the relationship between Mg/Ca and TE/Ca_{contaminants} ratios will highlight potential traces of contamination in our measurements (Fig. 32).

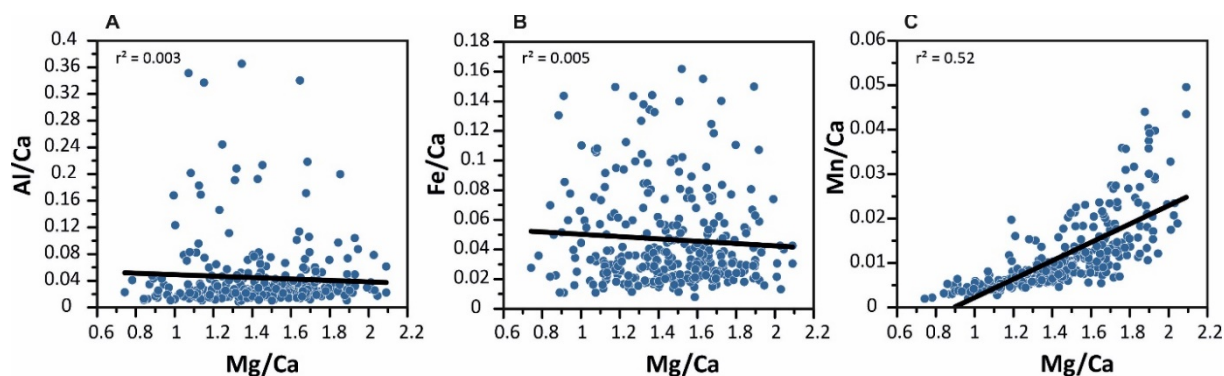
Figure 32 - *Globorotalia inflata* TE/Ca ratios from core MD08-3167 used for tracking contamination (TE/Ca_{contaminants}) in the measured samples. a) Al/Ca ratio. b) Mn/Ca ratio. c) Fe/Ca ratio. d) XRF Ti/Ca used as a reference of detrital material presence at the site. e) Benthic $\delta^{18}\text{O}$ (permil, VPDB) as a time reference. All curves plotted against age (ka)



Maximum contaminant accepted concentrations are between 0.3 – 0.5 mmol/mol for Al/Ca, and about 0.1 mmol/mol for Fe/Ca and Mn/Ca (Barker *et al.*, 2003; Lea *et al.*, 2005; Kuhnert *et al.*, 2014). Our measured *G. inflata* samples present an average of Al/Ca = 0.04 mmol/mol, Fe/Ca = 0.05 mmol/mol, and Mn/Ca = 0.01 mmol/mol. All TE/Ca_{contaminants} concentration averages are predominantly below commonly accepted limits reported in the literature. A way to inspect contamination is to examine the covariance between measured TE/Ca_{contaminants} and Mg/Ca. Significantly low covariances are observed with Al/Ca ($r^2 = 0.003$) and Fe/Ca ($r^2 = 0.005$), and although there is a level of correlation with Mn/Ca ($r^2 = 0.52$), averaged concentration shows it is negligible and do not represent any sign of

contamination (Fig. 33). Samples with drastically higher concentrations of all these elements than the reported limits were removed from the final Mg/Ca results of the MD08-3167 site ($n = 22$). Weldeab *et al.* (2006) observed that changes in the amount and composition of terrigenous input to the ocean floor are related to the presence of authigenic phases (Mn-Fe-oxides, pyrite, and secondary minerals such as ferric oxy-hydroxides). Predominant soil types close to the Namibia region are acrisol, plinthosol, and ferralsol, susceptible to intensive weathering (Govin *et al.*, 2012). They are generally enriched in Fe and Al (Moore and Dennen, 1970; Middelburg *et al.*, 1988; Driessen *et al.*, 2001; Govin *et al.*, 2012), and the delivery of these elements to the site may explain the slightly higher Fe/Ca values found in these samples throughout our measurements compared to those stipulated by Barker *et al.* (2003). Therefore, periods of enhanced terrigenous contributions to the MD08-3167 site may impact our TE/Ca_{contaminants} variability.

Figure 33 - Evaluation of contaminant contribution to Mg/Ca values based on TE/Ca ratios. a) Al/Ca vs. Mg/Ca, $r^2 = 0.003$. b) Mn/Ca vs. Mg/Ca, $r^2 = 0.005$. c) Fe/Ca vs. Mg/Ca, $r^2 = 0.52$. Al/Ca and Fe/Ca present extremely low r^2 , indicating a negligible correlation with Mg/Ca data. However, Mn/Ca correlates with Mg/Ca ($r^2=0.52$). Although this correlation seems relevant, the average value of Mn/Ca values lets us assume they are negligible since absolute values are lower than described in the literature showing no contamination



However, a few samples ($n = 16$) have been found to have Fe/Ca values slightly above 0.1 mmol/mol (and < 1.6 mmol/mol) but without any indication of another contamination trace (i.e., seen through lower Al/Ca and Mn/Ca concentrations). Other studies found TE/Ca_{contaminants} values slightly elevated in comparison with Barker *et al.*, (2003) (e.g., Groeneveld *et al.*, 2008; Steinke *et al.*, 2010; Vázquez Riveiros *et al.*, 2016), but they also could not find a strong Fe correlation between these ratios and Mg/Ca. The Mg/Ca values of these samples with higher Fe/Ca did not exhibit any abnormal absolute values compared with the surrounding data points. Instead, they showed coherent values consistent with the overall variability of the dataset, with similar Mg/Ca concentration to a surrounding

sample with lower than 1 mmol/mol Fe/Ca. Besides, the calculated correlation between Mg/Ca and Fe/Ca is extremely weak ($r^2 = 0.02$), suggesting that even with slightly higher Fe/Ca concentrations, Mg/Ca absolute values are unaffected. Therefore, since it promotes no changes in the final Mg/Ca curve and does not compromise these individual-level measurements, it was decided to keep those samples ($n = 16$). Alternatively, studies have considered adding a reductive step to the cleaning protocol for Mg/Ca measurements to remove oxide coatings and reduce the potential of Fe–Mn-oxyhydroxides contamination in the samples (Martin and Lea, 2002; Barker *et al.*, 2003; Weldeab *et al.*, 2006). While it is widely acknowledged that the removal of Fe and Mn phases can effectively eliminate high-Mg contaminants, uncertainties remain regarding the extent of the impact on Mg/Ca concentrations. It has been noted that this process may lead to decreased Mg/Ca concentrations and introduce a bias of up to 0.6°C when converted to temperature (Barker *et al.*, 2003; Rosenthal *et al.*, 2004). Our examination indicates no prior reason to consider including an additional reductive step in the protocol and suggests that our final Mg/Ca results are reliable and contaminant-free.

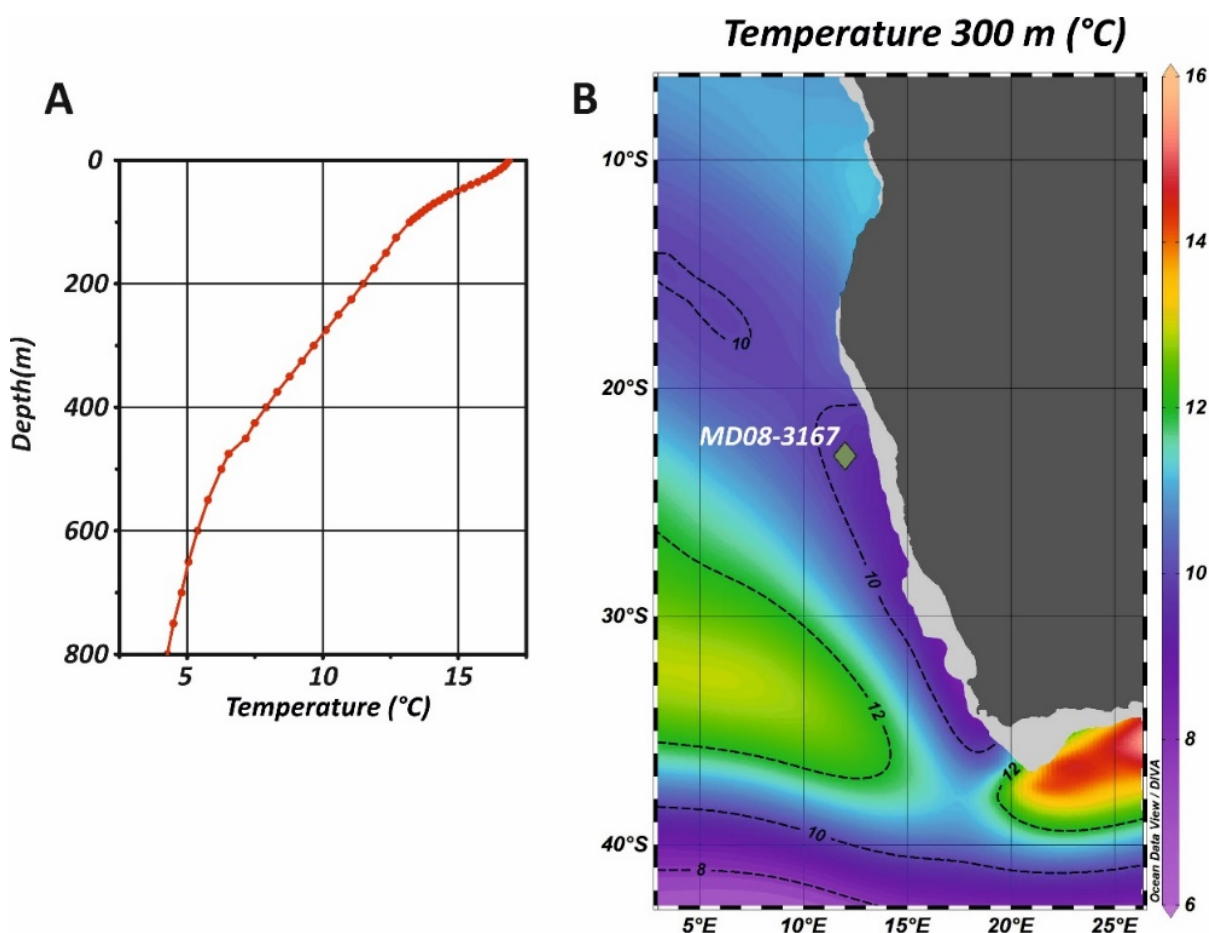
6.6 Evaluation of Mg/Ca-temperature equations

Choosing an appropriate calibration equation is crucial to reconstruct past ocean temperatures accurately. The proper calibration equation is selected based on the foraminifera species of interest. Different species have different calibration equations due to particular shell chemistry and growth rates. A vast number of calibrations have been proposed to transform Mg/Ca concentrations to temperature, usually derived from culture experiments (Lea *et al.*, 1999), sediment traps (Anand *et al.*, 2003), or core-top (surface sediment) studies (Groeneveld and Chiessi, 2011). Several calibrations are available (e.g., Elderfield and Ganssen, 2000; Anand *et al.*, 2003; Cléroux *et al.*, 2008; 2013; Groeneveld and Chiessi, 2011; Gray and Evans, 2019), in which species-specific and regionally constrained equations would provide more accurate paleotemperature reconstructions (Cléroux *et al.*, 2008; 2013; Groeneveld and Chiessi, 2011).

The appropriateness of a given calibration equation to a particular dataset can be validated by comparing the Mg/Ca-reconstructed temperatures to present-day seawater temperatures in the study site at the calcification depth. *Globorotalia inflata* species calcify

their tests between 200 – 600 m water depths, with a maximum peak abundance of around 250 m, which makes it a key species representing the permanent thermocline in the South Atlantic (Groeneveld and Chiessi, 2011). The local annual mean temperature at these depths on northern BUS, close to the MD08-3107 location, was extracted from WOA 2018 database (Locarnini *et al.*, 2018). The thermocline at our site is positioned between 125 – 800 m, with temperatures between $\sim 13 - 3^{\circ}\text{C}$; *G. inflata* calcification depth is known to occur all year around within a temperature range of $\sim 12 - 5^{\circ}\text{C}$ (Fig. 34a; Lončarić *et al.*, 2006; Cléroux *et al.*, 2007; Groeneveld and Chiessi, 2011; Locarnini *et al.*, 2018). I selected eight commonly used Mg/Ca-temperature equations developed specifically for *G. inflata* species to evaluate which one better reconstructs thermocline temperatures at the MD08-3167 site (Table 10).

Figure 34 - Annual mean temperature conditions at site MD08-3167 a) Vertical temperature profile and b) temperature at 300m in the Namibia margin. Data from both plots are from the World Ocean Atlas 2018 (WOA18) database (Locarnini *et al.*, 2018). All temperature values are reported in $^{\circ}\text{C}$



According to the oxygen isotope values measured on core top samples of *G. inflata*, calcification occurs across a broad spectrum of water depths in the southeastern Atlantic close to the MD08-3167 site, with an apparent mean depth around 250 m (Lončarić *et al.*,

2006). Estimated interglacial temperatures would be expected to be 10 – 12.5°C, with a mean value of 11°C (Fig. 34a). Equations number 1, 2, 3, and 4 (Anand *et al.*, 2003; Cléroux *et al.*, 2008; Farmer *et al.*, 2010) produced unrealistic warm thermocline temperatures, with interglacial temperatures reaching maximum values above 20°C that are unrealistic to our site, probably because they were developed based in the North Atlantic data and to cover a temperature range higher than found at present day close to the southeastern Atlantic (Table 10; Fig. 34a). Equations 5 and 6 (Elderfield and Ganssen, 2000; Groeneveld and Chiessi, 2011) are very similar and generate slightly higher than expected interglacial temperatures above 14°C, and equation 6 generates cooler temperatures than equation 5, reaching below 2°C. Equations based on core tops collected from the North Atlantic may not represent the South Atlantic. This is probably an additional factor explaining out-range temperatures generated from equations 1, 2, 3, 4, and 5. Although equations 5 and 6 produced similar results in which absolute values are mostly comprised of the expected range, only the equation from Groeneveld and Chiessi (2011) was developed from top cores from the South Atlantic. Equation 6 would be, in theory, the most suitable equation to fit our data because it was South Atlantic constrained. Therefore, equations 1 to 5 are unlikely to reconstruct proper thermocline temperatures at the Namibia margin.

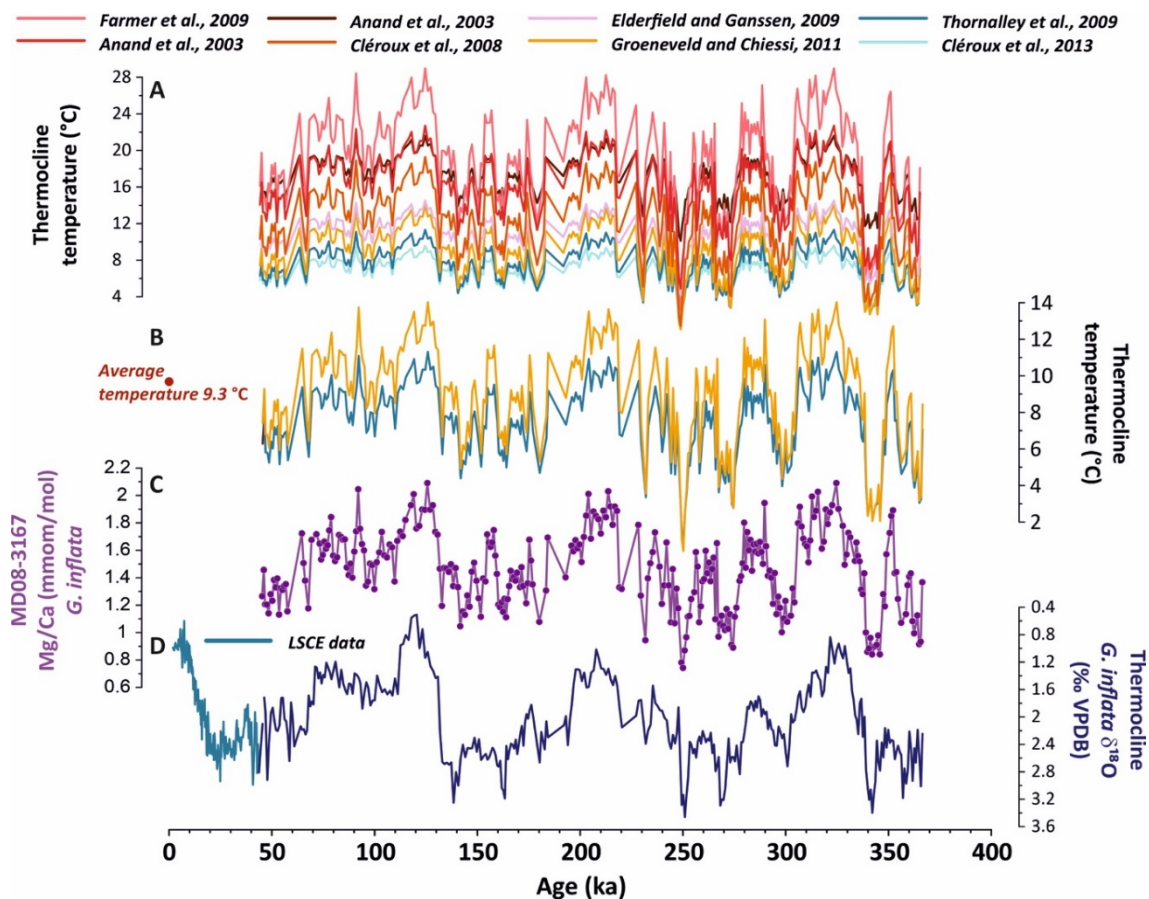
Table 10 - List of Mg/Ca-temperature equations specifically developed for *G. inflata* species evaluated in this thesis

N	Reference	Method	G. inflata Size fraction (mm)	Mg/Ca = B*exp(A*T)		Temperature range	Region
				Equation	r ²		
1	Farmer <i>et al.</i> , 2010	Core top	350-500	Mg/Ca = 0.916 (± 0.07) * exp (0.039 (± 0.006) * T)	0.52	15-21	Subpolar North Atlantic
2	Anand <i>et al.</i> , 2003	Sediment trap	350-500	Mg/Ca = 0.56 (± 0.16) * exp (0.058 (± 0.015) * T)	0.74		North Atlantic
3	Anand <i>et al.</i> , 2003	Sediment trap	350-500	Mg/Ca = 0.299 (± 0.005) * exp (0.090 * T)	0.55	15-21	North Atlantic
4	Cléroux <i>et al.</i> , 2008	Core top	250-315	Mg/Ca = 0.71 (± 0.06) * exp (0.06 (± 0.006) * T)	0.72	10.5-17.9	North Atlantic
5	Elderfield and Ganssen, 2000	Core top	n.a.	Mg/Ca = 0.49 (± 0.008) * exp (0.1 * T)	n.a.	7.5-15	North Atlantic
6	Groeneveld and Chiessi, 2011	Core top	250-315	Mg/Ca = 0.72 (+ 0.045; - 0.042)* exp (0.076 (±0.006) * T)	0.81	3.1-16.5	South Atlantic North Atlantic to tropical South Atlantic
7	Thornalley <i>et al.</i> , 2009	Core top	300-355	Mg/Ca = 0.675 * exp (0.1 * T)	n.a.		Subpolar North Atlantic
8	Cléroux <i>et al.</i> , 2013	Core top	250-315	Mg/Ca = 0.585 (± 0.050) * exp (0.133 (± 0.032) * T)	0.71		Subpolar North Atlantic

Overall, equations 7 and 8 produced very similar absolute temperature values, especially during glacial periods, but with slightly lower interglacial temperatures generated by Cléroux *et al.* (2013). Although equation 8 included South Atlantic core-top samples for *G. inflata*, Cléroux *et al.* (2013) argue that the lower pre-exponential constant obtained in their analysis compared to other calibrations, was likely due to their use of a different cleaning procedure than described in Barker *et al.* (2003). Therefore, although this equation yields temperature estimates that fit the water column observations, it might not be directly comparable with our data. Although equation 7 from Thornalley *et al.* (2009) is also based on North Atlantic core tops, they applied the protocol from Barker *et al.* (2003). The resulting temperatures are reasonably comprised of the expected thermocline temperature range.

In summary, similarly to previous studies reconstructing thermocline temperatures from *G. inflata* (Haarmann *et al.*, 2011), equations 6 and 7 are probably the most indicated equations to fit our Mg/Ca data since it is difficult to rule out if equation 6 is finally producing unrealistic interglacial temperatures (Fig 23b; Thornalley *et al.*, 2009; Groeneveld and Chiessi, 2011). Another factor to consider is the state of encrustation of the specimens being used. It has been observed that *G. inflata* with thicker crusts exhibits consistently lower Mg/Ca ratios, highlighting the importance of accurately determining a well-defined and narrow encrustation state (Groeneveld and Chiessi, 2011a). Most of the *G. inflata* shells from the MD08-3167 core were picked free of incrustation when keeping the minimum of 8 individuals per level was feasible. Since we do not have any information on the encrustation state of the specimens used to define equation 7, and since equation 6 is the one that was proposed by using sedimentary material from the South Atlantic, thus, equation 6 from Groeneveld and Chiessi (2011) seems the best for our Mg/Ca data from Southeastern Atlantic.

Figure 35 - Evaluation of Mg/Ca-temperature equations developed for *G. inflata* (Table 10). a) Comparison of reconstructed thermocline temperature from the eight different equations (°C). b) Reconstructed thermocline temperature (°C) equations from Thornalley *et al.* (2009) and Groeneveld and Chiessi (2011), which are the most plausible equations for the MD08-3167 site. c) Mg/Ca record (mmol/mol) and d) $\delta^{18}\text{O}$ (permil, VPDB) from MD08-3167 core



Temperature variability reconstructed based on Groeneveld and Chiessi (2011) displays a temperature range of approximately 14°C to 0.4°C, with an average of 9.3°C over the last ca. 400 ka. The results show that the mean G-IG amplitude of the record is 1.04 mmol/mol, corresponding to a mean temperature of 4.8°C. The largest amplitude was found during Termination IV, with Mg/Ca increasing 1.2 mmol/mol from MIS 10 to MIS 9, or 6.7°C. These findings suggest that the region experienced significant temperature variability during the last 400 ka, with well-imprinted G-IG cycles and superimposed millennial scale changes. The average annual mean temperature of the record is coherent with the mean thermocline temperature expected at 250 m. Authors applying the same equation to *G. inflata* in the South Atlantic also found similar results (Haarmann *et al.*, 2011; Rackebrandt *et al.*, 2011). While the temperature record derived from *G. inflata* by Rackebrandt *et al.* (2011), that uses the same Mg/Ca-temperature calibration as our study spans a time range outside of our study period, approximately 375-775 ka, it is noteworthy that they also observed a comparable G-IG

amplitude. Mg/Ca record displays a systematic decrease in concentration concomitant with increasing *G. inflata* $\delta^{18}\text{O}$ values, which is also shown in *G. bulloides* $\delta^{18}\text{O}$ record (see discussion in Chapter 5 and 6). This leads us to assume that thermocline cooling can explain a significant part of the factors influencing $\delta^{18}\text{O}$ of these isotopic increases. This is an interesting feature of the temperature record that has undoubtedly the potential to be explored in future publications derived from the results of this thesis. A similar pattern is also observed on isotopic records from the MD08-3167 core, which is the basis of discussions in Chapter 5.

6.7 Conclusions and perspectives

I have established an Mg/Ca protocol to analyze carbonate samples using an ICP-MS at IFREMER. Measurements were performed in the species *G. inflata* to reconstruct thermocline temperature variability over the last ca. 400 ka in the Northern Benguela Upwelling System (NBUS). External calibration was performed using a bracketing method with NIST 8301 and FOREXRB in-house standards to account for measurement uncertainties. The use of these standards allowed us to transform your intensities in concentrations. The accuracy and precision of our measurements were within acceptable limits. The external reproducibility of our measurements was assessed by multiple standard measurements, which have a %RSD average of 2.6% and 9.8%, respectively, for NIST 8301 and FOREXRB.

The Mg/Ca ratios in core MD08-3167 ranged from 0.7 mmol/mol (at ca. 250 ka) to 2.09 mmol/mol (at ca. 325 ka), which, after calibration with the equation 6 (Groeneveld and Chiessi, 2011) correspond to temperatures of 0.4°C and 14°C, respectively, with an average of 1.5 mmol/mol that corresponds to a temperature of 9.3°C. The mean G-IG amplitude of the record is 1.04 mmol/mol, corresponding to a mean temperature of 4.8°C, of which the largest amplitude of 1.2 mmol/mol (6.7 °C) was found during Termination IV, which corresponds to 6.7°C.

The temperature record spanning the last ca. 365 ka shows a systematic thermocline cooling concomitant with increased excursions on $\delta^{18}\text{O}$ over this period, which indicate that the temperature greatly influences planktic $\delta^{18}\text{O}$ value at this depth. These sharp thermocline coolings could be attributed to various factors, including changes in the intensity of upwelling and wind stress over time (see Chapter 5). Our results highlight the importance of foraminifera Mg/Ca measurements in reconstructing past thermocline temperature changes contributing to a

better understanding of the mechanisms driving past oceanographic and climate variability in the NBUS. Moreover, our findings suggest that external forcing significantly impacted thermocline, including changes in ocean currents and wind patterns with important implications for the carbon cycle.

Implementing the Mg/Ca technique at IFREMER has significantly contributed to my development as a researcher and to the future of my career, opening up new avenues for exploration and collaboration within the scientific community. I have gained expertise in an analytical technique that is widely utilized in the fields of Paleoceanography and Paleoclimatology. The future prospects of further exploration, expanded temporal coverage, and inter-laboratory collaborations hold immense potential for career development and further advancements in understanding climatic system. Furthermore, it promoted an opportunity for the advancement of an analytical technique, making Geo-Ocean and IFREMER one of the laboratories in France performing elementary analysis applied to foraminifera calcite. The addition of this technique contributes to the strong, well-established sedimentological background of the laboratory by providing additional paleoceanographic tools (e.g., other TE/Ca ratios) and adding a paleoclimatological approach to the current investigations. Besides, it increases the possibility of future collaboration with other laboratories from IFREMER, such as the *Laboratoire d'Océanographie Physique et Spatiale* (LOPS), with the potential of integrating observational oceanographic in situ measurements to a paleoceanographic and geochemistry approach. Combining present and past oceanographic information will bring relevant insights into the role of the ocean in the regulation and evolution of the climate, which is the main subject of one of the working groups from LOPS.

Implementing this technique represents a significant step forward for technology transferring between LSCE and IFREMER and future implementation in the recently purchased ICP-OES dedicated to carbonate samples at LOOP. After instituting this in Brazil, the method will be validated, and foraminiferal samples already picked from the GL-854 core will be analyzed. It will generate new temperature records from surface and thermocline layers over the past ca. 800 ka, a unique record at the subtropical region of this nature covering this time range at the Brazilian margin. This will allow me to explore the thermal gradient in future investigations, comparing western and eastern South Atlantic and vertical energy fluxes. Complementary as a future step, constructing inter-laboratory calibrations will strengthen collaboration between the involved research groups and possible future works, including researchers and students, producing novel reliable TE/Ca records.

7 CONCLUSIONS AND FUTURE STEPS

The general objective of this thesis was to investigate the role of orbital forcing in driving paleoceanographic processes hosted by the South Atlantic and their influence on global climate through the regulation of atmospheric CO₂ levels over the last 800 ka. I have examined two sediment cores from significant locations in the subtropical region at the edges of the SASG to produce almost 3000 new datapoints for reconstructing the properties of the surface, thermocline, and benthic ocean layers. My focus was to study significant paleoceanographic processes from both surface and deep-water perspectives. I examined how these two perspectives come together, are interconnected, and influence the climate system as a whole. To achieve this goal, I proposed three different lines of investigation based on (1) long-term deep-water dynamics; (2) investigations on ocean-atmospheric dynamics related to the BUS, and (3) Mg/Ca-based thermocline temperature reconstruction from the BUS. By examining surface-to-deep water column processes, I have gained valuable insights into ocean-atmospheric dynamics and how these processes respond to orbital forcing and are intimately connected to different AMOC states on their respective time scales, as well as their impact on the carbon cycle and contribution to driving the global climate.

I investigated deep-water processes and mechanisms by analyzing a benthic foraminiferal $\delta^{13}\text{C}$ record from WSA sediment core GL-854 over the last 800 ka, elucidating NADW and AABW variability and their influence on different AMOC states. In this manuscript under review on the Global and Planetary Changes, we have explored the zonal benthic foraminifera gradient between the DWBC and the DEBC to reconstruct NADW variability in the South Atlantic basin. Fluctuations in the $\Delta\delta^{13}\text{C}_{\text{w-e}}$ record respond to the proportion of NADW and AABW at 2200 m depth in the South Atlantic, where an increase (decrease) implies increased influence of NADW (AABW). Trend estimations revealed an oscillatory behavior between weak and strong AMOC modes, highlighting the sensitivity of $\Delta\delta^{13}\text{C}_{\text{w-e}}$ to vertical movements of the NADW-AABW boundary. Another key finding was the significant role of Antarctic sea-ice extent variability in driving the deep-water seesaw dynamic and controlling the AMOC. More or less sea-ice coverage has a direct impact on brine rejection, controlling AABW formation and the distribution of $\delta^{13}\text{C}$ in the Atlantic. Expansion and contractions of sea ice establish different AMOC phases, suggesting that a vigorous AMOC state demands reduced Southern Ocean sea ice on the orbital scale.

We uncovered compelling evidence regarding the contributions of very low- $\delta^{13}\text{C}$ glacial AABW signal to depths near 2200 m between MIS 12 and MIS 8, revealing a sensibility to strong glacial deep-water masses influence to both $\delta^{13}\text{C}$ records. We observed a notable increase in the $\Delta\delta^{13}\text{C}_{\text{w-e}}$ from ca. 300 ka on, indicating an enhanced southward penetration of NADW likely influenced by the intensified G-IG amplitude of AMOC following the MBT. We also found that ocean-atmospheric dynamics related to our sea ice mechanism increased the influence of AL waters in the South Atlantic after the MBT, which would have contributed to higher-amplitude G-IG cycles. These discoveries provide valuable insights into the complex interplay between deep-water circulation, AMOC variations, and the transition between climates. Orbital forcing, specifically the combined effects of obliquity and eccentricity, plays a crucial role in regulating the sea ice extent by controlling different insolation configurations at high latitudes South Atlantic. Hence, the AMOC plays the role of effectively propagating the influence of orbital effects on the climate through modulations in Atlantic deep-water formation. The connections between deep-water circulation, sea-ice and ocean-atmospheric dynamics, and AMOC variations in the South Atlantic bring light to climate change across the MBT. The connections between these factors also provide insights into the controls exerted by the South Atlantic on deep-water circulation, which may contribute to the ambiguous MBT signal in North Atlantic climate records. In conclusion, our study highlights the significant role of the South Atlantic in modulating deep-water circulation and AMOC variations.

I further investigated how ocean-atmospheric processes respond to orbital forcing from surface observations. I have reconstructed the upwelling activity at NBUS and investigated its impacts on carbon cycling on the orbital scale over the past 365 ka. By analyzing the $\delta^{18}\text{O}$ gradient between *G. bulloides* and *G. inflata* species, I reconstructed a stratification record that responds to changes in trade wind intensity and resulting upwelling. Our records showed that greater stratification occurred during interglacial periods and decreased stratification during glacial periods and cold substages, associated with intense austral summer insolation. This is attributed to the expansion and intensification of the South Atlantic Hadley Cell, driven by a northward position of the ITCZ in response to vigorous inter-hemispheric energy transport performed by the AMOC during positive precession phases. The North Atlantic, extracting heat from the South Atlantic during intense austral summers when enhanced deep-water formation in the North Atlantic and cooler Antarctica temperatures pushed the SASG northward and favored cross-equatorial energy transport. The mechanism proposed in this study suggests a seesaw pattern between the AL and NBUS activity, making the SASG a great heat reservoir

during negative precession phases, which could be a precondition for stronger AMOC during positive precession periods. These basin-wide changes in the South Atlantic paleoceanographic dynamics play a crucial role in modulating large-scale ocean-atmospheric patterns and reorganizing the energy balance between the hemispheres throughout precessional cycles.

The vertical $\delta^{13}\text{C}$ gradient between the surface, thermocline, and bottom waters in the NBUS reflects enhanced carbon transfer and an efficient biological pump during intensified upwelling likely in response to more efficient transport of matter between surface and deep layers and to primary productivity. The efficient upwelling-driven carbon storage in the deep ocean at NBUS, combined with reduced upwelling in the Southern Ocean due to the northward SASG that prevents CO_2 outgassing at southern high latitudes during positive precession phases, contributed to reductions in global atmospheric CO_2 . The results shown in Chapter 5 focuses therefore on the surface processes and sheds light on the ocean-atmospheric dynamics and carbon cycling on a global scale driven by low-latitude forcing and precessional cycles in the South Atlantic.

Throughout my research period at IFREMER (2021-2022), I have successfully developed and implemented a Mg/Ca analysis protocol using an ICP-MS to analyze carbonate samples. By applying this method to foraminifera species *G. inflata*, I have reconstructed thermocline temperature variability in the NBUS over the last 365 ka. Using external calibration with the bracketing method using NIST 8301 and in-house standards helped reduce measurement uncertainties and improve the reliability of our data. The accuracy and precision of the measurements were within acceptable limits. The Mg/Ca values from core MD08-3167 show a range of values from 0.7 mmol/mol (at 250 ka) to 2.09 mmol/mol (at 325 ka); calibrating these ratios using the equation proposed by Groeneveld and Chiessi (2011) corresponds to temperatures range between 0.4°C and 14°C . I found that thermocline cooling coincided with increased positive excursions in $\delta^{18}\text{O}$, suggesting a strong influence of temperature on planktic $\delta^{18}\text{O}$ values at this site. The observed sharp thermocline coolings can be attributed to various factors, including changes in upwelling intensity and wind stress over time. This study adds to the growing evidence of the potential of foraminifera Mg/Ca measurements provide to geo- and environmental-sciences laboratories as an additional tool, broadening our understanding of climate variability through a paleoceanography perspective. Chapter 6 presents the successful implementation of this technique and represents a relevant aspect of my thesis linked to the international technology transfer between the involved laboratories, and has contributed to my personal growth as a researcher. Besides, it will potentially strengthen international

collaborations and add to the number of laboratories that use this technique, increasing the production of new records.

Overall, the findings of this thesis provide a comprehensive understanding of the orbitally-induced paleoceanographic changes in the subtropical South Atlantic and their implications for global climate. Integrating surface and deep-water perspectives, along with examining ocean-atmospheric dynamics and carbon cycling, has shed light on the intricate connections and feedback mechanisms that exercise controls in the AMOC variability with implications for the atmospheric CO₂. This research contributes to the broader scientific understanding of long-term climate variability and highlights the importance of the South Atlantic region in global climate, which is crucial for improving climate models and future climatic projections.

7.1 Future Steps

In light of the significant findings presented in my thesis on the role of orbital forcing in driving paleoceanographic processes in the South Atlantic, there are several promising avenues for future research. By addressing remaining knowledge gaps and advancing our understanding of these processes, we can further contribute to the broader scientific understanding of long-term paleoclimatic and paleoceanographic variability in the South Atlantic. Besides, I didn't explore all records generated from this thesis, which is extremely important in the near future in producing the afterward scientific articles investigating different subjects raised from the discussion conducted on this thesis.

Regarding investigating deep-water variability in the South Atlantic, producing additional proxies measured on foraminifera species from GL-854 and MD08-3167 would be very interesting. For example, producing a long-term sortable silt record would be valuable to evaluate if our interpretations based on different configurations of deep-water production between NADW and AABW in producing different AMOC modes are correlated with changes in bottom water velocity. This approach would allow us to investigate the relation between deep-water production, ventilation, and intensity on longer time scales. Another interesting possibility would be to produce ϵNd records (i.e., a proxy for water mass tracer) from both South Atlantic margins to reconstruct changes in deep-water masses based on the end-members from NADW and AABW. In addition, another interesting aspect related to bottom waters would

be to evaluate the impact of increased carbon burial on benthic species. For example, it has been observed that when a great amount of organic matter is delivered to the bottom, *C. wuellerstorfi* disappears, and these favorable conditions increase *U. peregrina* species' abundance. Our benthic foraminiferal stable isotope records from NBUS seem to follow this pattern, in which *C. wuellerstorfi* is absent specifically during periods of intense upwelling and carbon transfer to the bottom (Chapter 5). Based on XRF element ratios such as Mn/Fe, Mn/Al, or Br/Ti, for example (Ziegler *et al.*, 2008; Govin *et al.*, 2012), it is possible to investigate changes in oxygenation and redox conditions at NBUS, whereas is expected to follow the upwelling activity (Chapter 5).

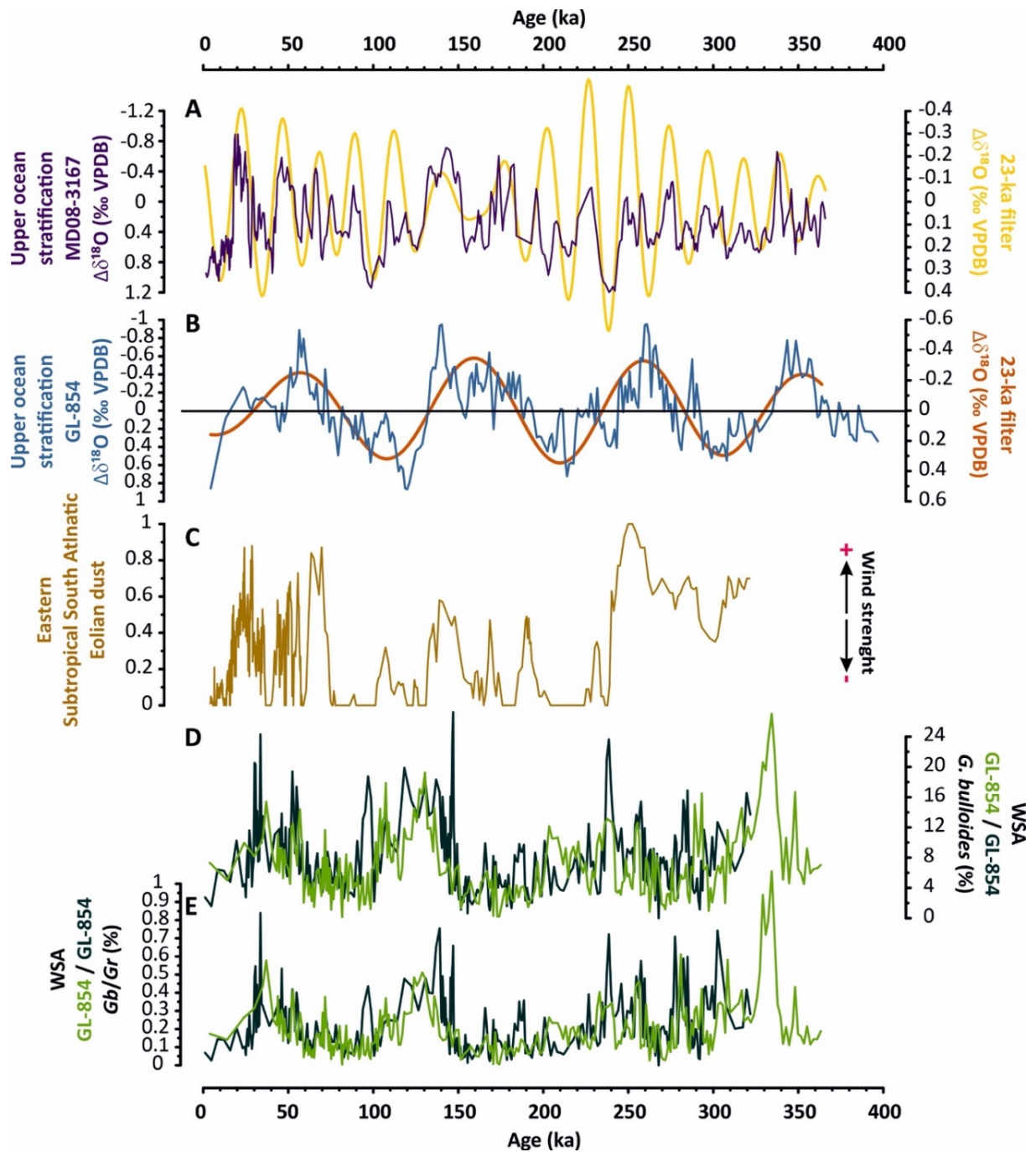
Specifically for evaluating upper-ocean productivity and the efficiency of the biological pump, which is also useful for interpreting benthic foraminiferal responses as mentioned above, would be to produce TOC records from GL-854 and MD08-3167 cores. TOC record from MD08-3167 would be interesting to measure to quantify the amount of carbon being buried at NBUS in response to the reconstructed upwelling activity from Chapter 5. In addition, recent studies have investigated barium incorporation on planktic foraminifera to evaluate the implementation of Ba/Ca measured on ICP as a direct proxy for reconstructing marine productivity (Fehrenbacher *et al.*, 2018; Fritz-Endres *et al.*, 2022; Richey *et al.*, 2022). I would like to explore this interesting approach by measuring Ba/Ca ratio concentrations on *G. inflata* species to reconstruct upwelling activity and compare it to the stratification record at NBUS.

While it is commonly understood that the upwelling cells on the eastern boundary are stronger, it is important to note that upwelling cells can also be found in the western boundary currents. The Cabo Frio upwelling cell located at the pathway of the BC at the Brazilian margin has a different seasonal behavior compared with the NBUS, intensifying in the austral summer (Campos *et al.*, 2000; Castelao and Barth, 2006). Previous research from Lessa *et al.* (2017) shows that upwelling activity at Cabo Frio expands and intensifies during interglacial periods such as MIS 5 and, in longer time scales over the Late Pleistocene, eccentricity pace the upwelling intensification (Lessa *et al.*, 2019). Although orbital forcings drive eastern and western upwelling regimes, their intensification periods occur in opposite phases, likely acting as a zonal seesaw pattern. This leads to the conclusion that they follow different mechanisms.

As a preliminary investigation for my next manuscript comparing both upwelling regimes over the last 365 ka, I reconstructed the upper-ocean stratification from the GL-854 based on the $\delta^{18}\text{O}$ gradient between *G. inflata* and *Globigerinoides ruber* ($\Delta\delta^{18}\text{O} = \delta^{18}\text{O}_{G. inflata}$

- $\delta^{18}\text{O}_{G. ruber}$; Fig. 36B), similar to the NBUS reconstruction from Chapter 5. Interestingly, periods of stratification decreases in GL-854 are associated with increasing *G. bulloides* abundances from GL-854 and nearby cores, indicating enhanced surface nutrient content that is associated with the offshore expansion of the Cabo Frio upwelling cell (Fig. 36D) (Lessa *et al.*, 2019). This pattern is also observed in the ratio between *G. bulloides* and *G. ruber* relative abundances (*Gb/Gr* ratio), which indicates changes in surface oceanographic conditions. Increased *Gb/Gr* ratios are expected when cold, nutrient-rich waters reach the Santos Basin associated with the upwelling intensification (Fig. 36E) (Lessa *et al.*, 2017). By comparing GL-854 and MD08-3167, it will be possible to elucidate the difference between driven mechanisms operating both eastern and western South Atlantic upwelling cells, the role of the SASG meridional shifts, now from observations from its western boundary, and the relation with different AMOC modes, and their impact on global climate.

Figure 36 - Comparison between eastern and western upper-ocean stratification records. A) MD08-3167 three-point running average of $\Delta\delta^{18}\text{O}$ (‰ VPDB) record (dark purple line) and respective 23-ka LOESS filter (yellow line). B) GL-854 upper-ocean stratification record (blue line; $\Delta\delta^{18}\text{O}$; ‰ VPDB) and respective 100-ka LOESS filter (dark orange line). C) Wind strength proxy from the Eastern subtropical South Atlantic (brown line; Stuetz *et al.*, 2002). D) GL-854 (light green line) and GL-852 (dark green line) *G. bulloides* relative abundance (%; Lessa *et al.*, 2019). E) GL-854 (light green line) and GL-852 (dark green line) relative abundance ratio between *G. bulloides* and *Globigerinoides ruber* (*Gb/Gr*) species (Lessa *et al.*, 2019)



REFERENCES

- Adam, O., Schneider, T., & Bischoff, T. (2016). Seasonal and Interannual Variations of the Energy Flux Equator and ITCZ. Part I: Zonally Averaged ITCZ Position. *Journal of Climate*, *29*. <https://doi.org/10.1175/jcli-d-15-0512.1>
- Adegbe, A. T., Schneider, R. R., Röhl, U., & Wefer, G. (2003). Glacial millennial-scale fluctuations in central African precipitation recorded in terrigenous sediment supply and freshwater signals offshore Cameroon. *Palaeogeography, Palaeoclimatology, Palaeoecology*, *197*(3–4), 323–333. [https://doi.org/10.1016/S0031-0182\(03\)00474-7](https://doi.org/10.1016/S0031-0182(03)00474-7).
- Adkins, J. F., McIntyre, K., & Schrag, D. P. (2002). The Salinity, Temperature, and $\delta^{18}\text{O}$ of the Glacial Deep Ocean. *Science*, *298*(November), 1769–1773. <https://doi.org/10.1126/science.1076252>.
- Agatemor, C., & Beauchemin, D. (2011). Matrix effects in inductively coupled plasma mass spectrometry: A review. *Analytica Chimica Acta*, *706*(1), 66–83. <https://doi.org/10.1016/j.aca.2011.08.027>.
- Alifu, H., Hirabayashi, Y., Imada, Y., & Shiogama, H. (2022). Enhancement of river flooding due to global warming. *Scientific Reports*, *12*(1). <https://doi.org/10.1038/s41598-022-25182-6>.
- Allen, K. A., & Hönisch, B. (2012). The planktic foraminiferal B/Ca proxy for seawater carbonate chemistry: A critical evaluation. *Earth and Planetary Science Letters*, *345–348*, 203–211. <https://doi.org/10.1016/j.epsl.2012.06.012>.
- Al-Sabouni, N., Kucera, M., & Schmidt, D. N. (2007). Vertical niche separation control of diversity and size disparity in planktonic foraminifera. *Marine Micropaleontology*, *63*(1–2), 75–90. <https://doi.org/10.1016/j.marmicro.2006.11.002>.
- Anand, P., Elderfield, H., & Conte, M. H. (2003). Calibration of Mg/Ca thermometry in planktonic foraminifera from a sediment trap time series. *Paleoceanography*, *18*(2). <https://doi.org/10.1029/2002PA000846>.
- Anderson, R. F., Ali, S., Bradtmiller, L. I., Nielsen, S. H. H., Fleisher, M. Q., Anderson, B. E., & Burckle, L. H. (2009). Wind-Driven Upwelling in the Southern Ocean and the Deglacial Rise in Atmospheric CO₂. *Science*, *323*(5920), 1443–1448. <https://doi.org/10.1126/science.1167441>.
- Arz, H. W., Pätzold, J., & Wefer, G. (1999). Climatic changes during the last deglaciation recorded in sediment cores from the northeastern Brazilian Continental Margin. *Geo-Marine Letters*, *19*(3), 209–218. <https://doi.org/10.1007/s003670050111>.
- Ballalai, J. M., Santos, T. P., Lessa, D. O., Venancio, I. M., Chiessi, C. M., Johnstone, H. J. H., Kuhnert, H., Claudio, M. R., Toledo, F., Costa, K. B., & Albuquerque, A. L. S. (2019). Tracking Spread of the Agulhas Leakage Into the Western South Atlantic and Its Northward Transmission During the Last Interglacial. *Paleoceanography and Paleoclimatology*, 2019PA003653. <https://doi.org/10.1029/2019PA003653>.
- Bard, E. (1988). Correction of accelerator mass spectrometry ^{14}C ages measured in planktonic foraminifera: Paleoceanographic implications. *Paleoceanography*, *3*(6), 635–645. <https://doi.org/10.1029/PA003i006p00635>.
- Barker, S., Diz, P., Vautravers, M. J., Pike, J., Knorr, G., Hall, I. R., & Broecker, W. S. (2009). Interhemispheric Atlantic seesaw response during the last deglaciation. *Nature*, *457*(7233), 1097–1102. <https://doi.org/10.1038/nature07770>.

- Barker, S., Greaves, M., & Elderfield, H. (2003). A study of cleaning procedures used for foraminiferal Mg/Ca paleothermometry. *Geochemistry, Geophysics, Geosystems*, 4(9), 1–20. <https://doi.org/10.1029/2003GC000559>.
- Bé, A. W. H. (1977). *An ecological, zoogeographic and taxonomic review of recent planktonic foraminifera*.
- Beauchemin, D. (2008). Inductively Coupled Plasma Mass Spectrometry. *Analytical Chemistry*, 80(12), 4455–4486. <https://doi.org/10.1021/ac8006945>.
- Beniston, M., & Stephenson, D. B. (2004). Extreme climatic events and their evolution under changing climatic conditions. *Global and Planetary Change*, 44(1–4), 1–9. <https://doi.org/10.1016/j.gloplacha.2004.06.001>.
- Berger, A., & Loutre, M. F. (2006). Glaciation, causes | Milankovitch theory and paleoclimate. *Encyclopedia of Quaternary Science, 1856*, 1017–1022. <https://doi.org/10.1016/B0-44-452747-8/00013-2>.
- Blaauw, M., & Christen, J. A. (2011). Flexible paleoclimate age-depth models using an autoregressive gamma process. *Bayesian Analysis*, 6(3), 457–474. <https://doi.org/10.1214/11-BA618>.
- Blaauw, M., Christen, J. A., Bennett, K. D., & Reimer, P. J. (2018). Double the dates and go for Bayes — Impacts of model choice, dating density and quality on chronologies. *Quaternary Science Reviews*, 188, 58–66. <https://doi.org/10.1016/j.quascirev.2018.03.032>.
- Blum, J. D., & Bergquist, B. A. (2007). Reporting of variations in the natural isotopic composition of mercury. *Analytical and Bioanalytical Chemistry*, 388(2), 353–359. <https://doi.org/10.1007/s00216-007-1236-9>.
- Bouttes, N., Paillard, D., & Roche, D. M. (2010). Impact of brine-induced stratification on the glacial carbon cycle. *Climate of the Past*, 6(5), 575–589. <https://doi.org/10.5194/cp-6-575-2010>.
- Boyle, E. A. (1981). Cadmium, zinc, copper, and barium in foraminifera tests. *Earth and Planetary Science Letters*, 53(1), 11–35. [https://doi.org/10.1016/0012-821X\(81\)90022-4](https://doi.org/10.1016/0012-821X(81)90022-4).
- Boyle, E. A., & Keigwin, L. D. (1985). Comparison of Atlantic and Pacific paleochemical records for the last 215,000 years: changes in deep ocean circulation and chemical inventories. *Earth and Planetary Science Letters*, 76(1–2), 135–150. [https://doi.org/10.1016/0012-821X\(85\)90154-2](https://doi.org/10.1016/0012-821X(85)90154-2).
- Boyle, E., & Rosenthal, Y. (1996). Chemical Hydrography of the South Atlantic During the Last Glacial Maximum: Cd vs. $\delta^{13}\text{C}$. In *The South Atlantic* (pp. 423–443). Springer Berlin Heidelberg. https://doi.org/10.1007/978-3-642-80353-6_23.
- Brenner, I. (Joe). (2017). Inductively Coupled Plasma Mass Spectrometry Applications. In J. C. Lindon, G. E. Tranter, & D. W. Koppenaal (Eds.), *Encyclopedia of Spectroscopy and Spectrometry (Third Edition)* (Third Edit, pp. 229–235). Academic Press. <https://doi.org/https://doi.org/10.1016/B978-0-12-803224-4.00057-1>.
- Broccoli, A. J., Dahl, K. A., & Stouffer, R. J. (2006). Response of the ITCZ to Northern Hemisphere cooling. *Geophysical Research Letters*, 33(1). <https://doi.org/10.1029/2005GL024546>.
- Broecker, W. S. (2003). Does the Trigger for Abrupt Climate Change Reside in the Ocean or in the Atmosphere? *Science*, 300(5625), 1519–1522. <https://doi.org/10.1126/science.1083797>.

- Butzin, M., Prange, M., & Lohmann, G. (2005). Radiocarbon simulations for the glacial ocean: The effects of wind stress, Southern Ocean sea ice and Heinrich events. *Earth and Planetary Science Letters*, 235(1–2), 45–61. <https://doi.org/10.1016/j.epsl.2005.03.003>.
- Caesar, L., McCarthy, G. D., Thornalley, D. J. R., Cahill, N., & Rahmstorf, S. (2021). Current Atlantic Meridional Overturning Circulation weakest in last millennium. *Nature Geoscience*. <https://doi.org/10.1038/s41561-021-00699-z>.
- Caesar, L., Rahmstorf, S., Robinson, A., Feulner, G., & Saba, V. (2018). Observed fingerprint of a weakening Atlantic Ocean overturning circulation. *Nature*, 556(7700), 191–196. <https://doi.org/10.1038/s41586-018-0006-5>.
- Campos, E. J. D., Velhote, D., & da Silveira, I. C. A. (2000). Shelf break upwelling driven by Brazil Current Cyclonic Meanders. *Geophysical Research Letters*, 27(6), 751–754. <https://doi.org/10.1029/1999GL010502>.
- Carr, M. E., & Kearns, E. J. (2003). Production regimes in four Eastern Boundary Current systems. *Deep-Sea Research Part II: Topical Studies in Oceanography*, 50(22–26), 3199–3221. <https://doi.org/10.1016/j.dsr2.2003.07.015>.
- Carr, M.-E. (2002). Estimation of potential productivity in Eastern Boundary Currents using remote sensing. In *Deep-Sea Research II* (Vol. 49).
- Castelao, R. M., & Barth, J. A. (2006). Upwelling around Cabo Frio, Brazil: The importance of wind stress curl. *Geophysical Research Letters*, 33(3), L03602. <https://doi.org/10.1029/2005GL025182>.
- Chave, K. E. (1954). Aspects of the Biogeochemistry of Magnesium 1. Calcareous Marine Organisms. *The Journal of Geology*, 62(3), 266–283. <https://doi.org/10.1086/626162>.
- Chen, P., Yu, J., & Jin, Z. (2017). An evaluation of benthic foraminiferal U/Ca and U/Mn proxies for deep ocean carbonate chemistry and redox conditions. *Geochemistry, Geophysics, Geosystems*, 18(2), 617–630. <https://doi.org/10.1002/2016GC006730>.
- Chiessi, C. M., Mulitza, S., Paul, A., Pätzold, J., Groeneveld, J., & Wefer, G. (2008). South Atlantic interocean exchange as the trigger for the Bølling warm event. *Geology*, 36(12), 919. <https://doi.org/10.1130/G24979A.1>.
- Cléroux, C., Cortijo, E., Anand, P., Labeyrie, L., Bassinot, F., Caillon, N., & Duplessy, J.-C. C. (2008). Mg/Ca and Sr/Ca ratios in planktonic foraminifera: Proxies for upper water column temperature reconstruction. *Paleoceanography*, 23(3). <https://doi.org/10.1029/2007PA001505>.
- Cléroux, C., Cortijo, E., Duplessy, J.-C., & Zahn, R. (2007). Deep-dwelling foraminifera as thermocline temperature recorders. *Geochemistry, Geophysics, Geosystems*, 8(4). <https://doi.org/10.1029/2006GC001474>.
- Cléroux, C., DeMenocal, P., Arbuszewski, J., & Linsley, B. (2013). Reconstructing the upper water column thermal structure in the Atlantic Ocean. *Paleoceanography*, 28(3), 503–516. <https://doi.org/10.1002/palo.20050>.
- Collins, J. A., Schefuß, E., Govin, A., Mulitza, S., & Tiedemann, R. (2014). Insolation and glacial–interglacial control on southwestern African hydroclimate over the past 140 000 years. *Earth and Planetary Science Letters*, 398, 1–10. <https://doi.org/10.1016/j.epsl.2014.04.034>.

Carbon Cycle and the Global Deep Water Circulation. *Quaternary Research*, 21(2), 225–243. [https://doi.org/10.1016/0033-5894\(84\)90099-1](https://doi.org/10.1016/0033-5894(84)90099-1).

Eggins, S., De Deckker, P., & Marshall, J. (2003). Mg/Ca variation in planktonic foraminifera tests: implications for reconstructing palaeo-seawater temperature and habitat migration. *Earth and Planetary Science Letters*, 212(3–4), 291–306. [https://doi.org/10.1016/S0012-821X\(03\)00283-8](https://doi.org/10.1016/S0012-821X(03)00283-8).

Elderfield, H., & Ganssen, G. (2000). Past temperature and $\delta^{18}\text{O}$ of surface ocean waters inferred from foraminiferal Mg/Ca ratios. *Nature*, 405(6785), 442–445. <https://doi.org/10.1038/35013033>.

Emeis, K.-C., Struck, U., Leipe, T., & Ferdelman, T. G. (2009). Variability in upwelling intensity and nutrient regime in the coastal upwelling system offshore Namibia: results from sediment archives. *International Journal of Earth Sciences*, 98(2), 309–326. <https://doi.org/10.1007/s00531-007-0236-5>.

Emiliani, C. (1955). Pleistocene Temperatures. *The Journal of Geology*, 63(6), 538–578. <https://doi.org/10.1086/626295>.

Evans, E. H., & Giglio, J. J. (1993). Interferences in inductively coupled plasma mass spectrometry. A review. *Journal of Analytical Atomic Spectrometry*, 8(1), 1. <https://doi.org/10.1039/ja9930800001>.

Fairbanks, R. G., Mortlock, R. A., Chiu, T. C., Cao, L., Kaplan, A., Guilderson, T. P., Fairbanks, T. W., Bloom, A. L., Grootes, P. M., & Nadeau, M. J. (2005). Radiocarbon calibration curve spanning 0 to 50,000 years BP based on paired $^{230}\text{Th}/^{234}\text{U}/^{238}\text{U}$ and ^{14}C dates on pristine corals. *Quaternary Science Reviews*, 24(16–17), 1781–1796. <https://doi.org/10.1016/j.quascirev.2005.04.007>.

Farmer, E. J., Chapman, M. R., & Andrews, J. E. (2010). North Atlantic Globorotalia inflata coretop Mg/Ca calibrations and temperature reconstructions over Termination I. *IOP Conference Series: Earth and Environmental Science*, 9, 012019. <https://doi.org/10.1088/1755-1315/9/1/012019>.

Fasullo, J. T., & Trenberth, K. E. (2008). The Annual Cycle of the Energy Budget. Part II: Meridional Structures and Poleward Transports. *Journal of Climate*, 21(10), 2313–2325. <https://doi.org/10.1175/2007JCLI1936.1>.

Fehrenbacher, J. S., Russell, A. D., Davis, C. V., Spero, H. J., Chu, E., & Hönisch, B. (2018). Ba/Ca ratios in the non-spinose planktic foraminifer *Neogloboquadrina dutertrei*: Evidence for an organic aggregate microhabitat. *Geochimica et Cosmochimica Acta*, 236, 361–372. <https://doi.org/https://doi.org/10.1016/j.gca.2018.03.008>.

Ferrari, R., Jansen, M. F., Adkins, J. F., Burke, A., Stewart, A. L., & Thompson, A. F. (2014). Antarctic sea ice control on ocean circulation in present and glacial climates. *Proceedings of the National Academy of Sciences*, 111(24), 8753–8758. <https://doi.org/10.1073/pnas.1323922111>.

Fontanier, C., Jorissen, F. J., Licari, L., Alexandre, A., Anschutz, P., & Carbonel, P. (2002). Live benthic foraminiferal faunas from the Bay of Biscay: faunal density, composition, and microhabitats. *Deep Sea Research Part I: Oceanographic Research Papers*, 49(4), 751–785. [https://doi.org/10.1016/S0967-0637\(01\)00078-4](https://doi.org/10.1016/S0967-0637(01)00078-4).

Fritz-Endres, T., Fehrenbacher, J. S., Russell, A. D., & Cynar, H. (2022). Increased Productivity in the Equatorial Pacific During the Deglaciation Inferred From the Ba/Ca Ratios of Non-Spinose Planktic Foraminifera. *Paleoceanography and Paleoclimatology*, 37(12), e2022PA004506. <https://doi.org/https://doi.org/10.1029/2022PA004506>.

- Garzoli, S. L., Baringer, M. O., Dong, S., Perez, R. C., & Yao, Q. (2013). South Atlantic meridional fluxes. *Deep Sea Research Part I: Oceanographic Research Papers*, 71, 21–32. <https://doi.org/10.1016/j.dsr.2012.09.003>.
- Garzoli, S. L., & Matano, R. (2011). The South Atlantic and the Atlantic Meridional Overturning Circulation. *Deep Sea Research Part II: Topical Studies in Oceanography*, 58(17–18), 1837–1847. <https://doi.org/10.1016/j.dsr2.2010.10.063>.
- Gilbert, E., & Kittel, C. (2021). Surface Melt and Runoff on Antarctic Ice Shelves at 1.5°C, 2°C, and 4°C of Future Warming. *Geophysical Research Letters*, 48(8), 1–9. <https://doi.org/10.1029/2020GL091733>.
- Giraudeau, J. (1993). Planktonic foraminiferal assemblages in surface sediments from the southwest African continental margin. *Marine Geology*, 110(1–2), 47–62. [https://doi.org/10.1016/0025-3227\(93\)90104-4](https://doi.org/10.1016/0025-3227(93)90104-4).
- Goni, G. J., Bringas, F., & DiNezio, P. N. (2011). Observed low frequency variability of the Brazil Current front. *Journal of Geophysical Research*, 116(C10), C10037. <https://doi.org/10.1029/2011JC007198>.
- Gooday, A. J. (2003). *Benthic foraminifera (protista) as tools in deep-water palaeoceanography: Environmental influences on faunal characteristics* (Vol. 46, pp. 1–90). Academic Press. [https://doi.org/10.1016/S0065-2881\(03\)46002-1](https://doi.org/10.1016/S0065-2881(03)46002-1).
- Govin, A., Holzwarth, U., Heslop, D., Ford Keeling, L., Zabel, M., Mulitza, S., Collins, J. A., & Chiessi, C. M. (2012). Distribution of major elements in Atlantic surface sediments (36°N–49°S): Imprint of terrigenous input and continental weathering. *Geochemistry, Geophysics, Geosystems*, 13(1). <https://doi.org/10.1029/2011GC003785>.
- Gray, W. R., & Evans, D. (2019). Nonthermal Influences on Mg/Ca in Planktonic Foraminifera: A Review of Culture Studies and Application to the Last Glacial Maximum. *Paleoceanography and Paleoclimatology*, 34(3), 306–315. <https://doi.org/10.1029/2018PA003517>.
- Greaves, M., Caillon, N., Rebaubier, H., Bartoli, G., Bohaty, S., Cacho, I., Clarke, L., Cooper, M., Daunt, C., Delaney, M., DeMenocal, P., Dutton, A., Eggins, S., Elderfield, H., Garbe-Schoenberg, D., Goddard, E., Green, D., Groeneveld, J., Hastings, D., ... Wilson, P. A. (2008). Interlaboratory comparison study of calibration standards for foraminiferal Mg/Ca thermometry. *Geochemistry, Geophysics, Geosystems*, 9(8). <https://doi.org/10.1029/2008GC001974>.
- Groeneveld, J., & Chiessi, C. M. (2011). Mg/Ca of *Globorotalia inflata* as a recorder of permanent thermocline temperatures in the South Atlantic. *Paleoceanography*, 26(2), 1–12. <https://doi.org/10.1029/2010PA001940>.
- Groeneveld, J., Nürnberg, D., Tiedemann, R., Reichert, G.-J., Steph, S., Reuning, L., Crudeli, D., & Mason, P. (2008). Foraminiferal Mg/Ca increase in the Caribbean during the Pliocene: Western Atlantic Warm Pool formation, salinity influence, or diagenetic overprint? *Geochemistry, Geophysics, Geosystems*, 9(1). <https://doi.org/10.1029/2006GC001564>.
- Haarmann, T., Hathorne, E. C., Mohtadi, M., Groeneveld, J., Kölling, M., & Bickert, T. (2011). Mg/Ca ratios of single planktonic foraminifer shells and the potential to reconstruct the thermal seasonality of the water column. *Paleoceanography*, 26(3). <https://doi.org/10.1029/2010PA002091>.

Hall, J. M., & Chan, L. H. (2004). Li/Ca in multiple species of benthic and planktonic foraminifera: Thermocline, latitudinal, and glacial-interglacial variation. *Geochimica et Cosmochimica Acta*, 68(3), 529–545. [https://doi.org/10.1016/S0016-7037\(00\)00451-4](https://doi.org/10.1016/S0016-7037(00)00451-4).

Haynes, L. L., Hönisch, B., Holland, K., Rosenthal, Y., & Eggins, S. M. (2019). Evaluating the planktic foraminiferal B/Ca proxy for application to deep time paleoceanography. *Earth and Planetary Science Letters*, 528, 115824. <https://doi.org/10.1016/j.epsl.2019.115824>.

Heaton, T. J., Köhler, P., Butzin, M., Bard, E., Reimer, R. W., Austin, W. E. N., Bronk Ramsey, C., Grootes, P. M., Hughen, K. A., Kromer, B., Reimer, P. J., Adkins, J., Burke, A., Cook, M. S., Olsen, J., & Skinner, L. C. (2020). Marine20—The Marine Radiocarbon Age Calibration Curve (0–55,000 cal BP). *Radiocarbon*, 62(4), 779–820. <https://doi.org/10.1017/RDC.2020.68>.

Henry, L. G., McManus, J. F., Curry, W. B., Roberts, N. L., Piotrowski, A. M., & Keigwin, L. D. (2016). North Atlantic ocean circulation and abrupt climate change during the last glaciation. *Science*, 353(6298), 470–474. <https://doi.org/10.1126/science.aaf5529>.

Hönisch, B., Allen, K. A., Russell, A. D., Eggins, S. M., Bijma, J., Spero, H. J., Lea, D. W., & Yu, J. (2011). Planktic foraminifera as recorders of seawater Ba/Ca. *Marine Micropaleontology*, 79(1–2), 52–57. <https://doi.org/10.1016/j.marmicro.2011.01.003>.

Hoogakker, B. A. A., Lu, Z., Umling, N., Jones, L., Zhou, X., Rickaby, R. E. M., Thunell, R., Cartapanis, O., & Galbraith, E. (2018). Glacial expansion of oxygen-depleted seawater in the eastern tropical Pacific. *Nature*, 562(7727), 410–413. <https://doi.org/10.1038/s41586-018-0589-x>.

Hou, A., Bahr, A., Chiessi, C. M., Jaeschke, A., Albuquerque, A. L. S., Pross, J., Koutsodendris, A., & Friedrich, O. (2022). Obliquity influence on low-latitude coastal precipitation in eastern Brazil during the past ~850 kyr. *Paleoceanography and Paleoclimatology*. <https://doi.org/10.1029/2021PA004238>.

Hutchings, L., van der Lingen, C. D., Shannon, L. J., Crawford, R. J. M., Verheye, H. M. S., Bartholomae, C. H., van der Plas, A. K., Louw, D., Kreiner, A., Ostrowski, M., Fidel, Q., Barlow, R. G., Lamont, T., Coetzee, J., Shillington, F., Veitch, J., Currie, J. C., & Monteiro, P. M. S. (2009). The Benguela Current: An ecosystem of four components. *Progress in Oceanography*, 83(1–4), 15–32. <https://doi.org/10.1016/j.pocean.2009.07.046>.

Huybers, P. (2009). Antarctica's Orbital Beat. *Science*, 325(5944), 1085–1086. <https://doi.org/10.1126/science.1176186>.

Huybers, P., & Wunsch, C. (2005). Obliquity pacing of the late Pleistocene glacial terminations. *Nature*, 434(7032), 491–494. <https://doi.org/10.1038/nature03401>.

Imbrie, J., Berger, A., Boyle, E. A., Clemens, S. C., Duffy, A., Howard, W. R., Kukla, G., Kutzbach, J., Martinson, D. G., McIntyre, A., Mix, A. C., Molino, B., Morley, J. J., Peterson, L. C., Pisias, N. G., Prell, W. L., Raymo, M. E., Shackleton, N. J., & Toggweiler, J. R. (1993). On the structure and origin of major glaciation cycles 2. The 100,000-year cycle. *Paleoceanography*, 8(6), 699–735. <https://doi.org/10.1029/93PA02751>.

Imbrie, J., Boyle, E. A., Clemens, S. C., Duffy, A., Howard, W. R., Kukla, G., Kutzbach, J., Martinson, D. G., McIntyre, A., Mix, A. C., Molino, B., Morley, J. J., Peterson, L. C., Pisias, N. G., Prell, W. L., Raymo, M. E., Shackleton, N. J., & Toggweiler, J. R. (1992). On the Structure and Origin of Major Glaciation Cycles 1. Linear Responses to Milankovitch Forcing. *Paleoceanography*, 7(6), 701–738. <https://doi.org/10.1029/92PA02253>.

Imbrie, J., Hays, J. D., Martinson, D. G., McIntyre, A., Mix, A. C., Morley, J. J., Pisias, N. G., Prell and, W. L., & Shackleton, N. J. (1984). The orbital theory of pleistocene climate: support from a revised chronology of the marine O180 record. In “Milankovitch and climate.” *Milankovitch and Climate*, January, 269–305.

IPCC, 2022: Climate Change 2022: Impacts, Adaptation, and Vulnerability. Contribution of Working Group II to the Sixth Assessment Report of the Intergovernmental Panel on Climate Change [H.-O. Pörtner, D.C. Roberts, M. Tignor, E.S. Poloczanska, K. Mintenbeck, A. Alegría, M. Craig, S. Langsdorf, S. Löschke, V. Möller, A. Okem, B. Rama (eds.)]. Cambridge University Press. Cambridge University Press, Cambridge, UK and New York, NY, USA, 3056 pp., doi:10.1017/9781009325844.

Irvali, N., Ninnemann, U. S., Kleiven, H. K. F., Galaasen, E. V., Morley, A., & Rosenthal, Y. (2016). Evidence for regional cooling, frontal advances, and East Greenland Ice Sheet changes during the demise of the last interglacial. *Quaternary Science Reviews*, 150, 184–199. <https://doi.org/10.1016/j.quascirev.2016.08.029>.

Izuka, S. K. (1988). Relationship of magnesium and other minor elements in tests of *Cassidulina subglobosa* and *C. oriangulata* to physical oceanic properties. *The Journal of Foraminiferal Research*, 18(2), 151–157. <https://doi.org/10.2113/gsjfr.18.2.151>.

Jansen, M. F. (2017). Glacial ocean circulation and stratification explained by reduced atmospheric temperature. *Proceedings of the National Academy of Sciences*, 114(1), 45–50. <https://doi.org/10.1073/pnas.1610438113>.

Jansen, M. F., & Nadeau, L.-P. (2016). The Effect of Southern Ocean Surface Buoyancy Loss on the Deep-Ocean Circulation and Stratification. *Journal of Physical Oceanography*, 46(11), 3455–3470. <https://doi.org/10.1175/JPO-D-16-0084.1>.

Johns, W., Lee, T., & Beardsley, R. (1998). Annual cycle and variability of the North Brazil Current. *Journal of Physical*, 103–128.

Katz, M. E., Cramer, B. S., Franzese, A., Honisch, B., Miller, K. G., Rosenthal, Y., & Wright, J. D. (2010). Traditional and emerging geochemical proxies in foraminifera. *The Journal of Foraminiferal Research*, 40(2), 165–192. <https://doi.org/10.2113/gsjfr.40.2.165>.

Ketrin, R., Handayani, E. M., & Komalasari, I. (2017). Bracketing method with certified reference materials for high precision and accuracy determination of trace cadmium in drinking water by Inductively Coupled Plasma - Mass Spectrometry. *AIP Conference Proceedings*, 1803, 020058. <https://doi.org/10.1063/1.4973185>.

Kim, J. H., Schneider, R. R., Mulitza, S., & Müller, P. J. (2003). Reconstruction of SE trade-wind intensity based on sea-surface temperature gradients in the Southeast Atlantic over the last 25 kyr. *Geophysical Research Letters*, 30(22), 3–6. <https://doi.org/10.1029/2003GL017557>.

Košler, J., & Sylvester, P. J. (2003). 9. Present Trends and the Future of Zircon in Geochronology: Laser Ablation ICPMS. In *Zircon* (pp. 243–276). De Gruyter. <https://doi.org/10.1515/9781501509322-012>.

Kotov, S., & Paelike, H. (2018). QAnalySeries - a cross-platform time series tuning and analysis tool. *AGU Fall Meeting Abstracts, 2018*, PP53D-1230.

Krinsley, D. (1960). Trace Elements in the Tests of Planktonic Foraminifera. *Micropaleontology*, 6(3), 297. <https://doi.org/10.2307/1484237>.

- Kroopnick, P. M. (1985). The distribution of ^{13}C of ΣCO_2 in the world oceans. *Deep Sea Research Part A. Oceanographic Research Papers*, 32(1), 57–84. [https://doi.org/10.1016/0198-0149\(85\)90017-2](https://doi.org/10.1016/0198-0149(85)90017-2).
- Kucera, M. (2007). Chapter Six Planktonic Foraminifera as Tracers of Past Oceanic Environments. In *Developments in Marine Geology* (Vol. 1, Issue 07, pp. 213–262). [https://doi.org/10.1016/S1572-5480\(07\)01011-1](https://doi.org/10.1016/S1572-5480(07)01011-1).
- Kucera, M., Rosell-Melé, A., Schneider, R., Waelbroeck, C., & Weinelt, M. (2005). Multiproxy approach for the reconstruction of the glacial ocean surface (MARGO). *Quaternary Science Reviews*, 24(7–9), 813–819. <https://doi.org/10.1016/j.quascirev.2004.07.017>.
- Kuhnert, H., Kuhlmann, H., Mohtadi, M., Meggers, H., Baumann, K., & Pätzold, J. (2014). Holocene tropical western Indian Ocean sea surface temperatures in covariation with climatic changes in the Indonesian region. *Paleoceanography*, 29(5), 423–437. <https://doi.org/10.1002/2013PA002555>.
- Lacourse, T., & Gajewski, K. (2020). Current practices in building and reporting age-depth models. *Quaternary Research*, 96(May), 28–38. <https://doi.org/10.1017/qua.2020.47>.
- Lea, D. W. (1995). A trace metal perspective on the evolution of Antarctic Circumpolar Deep Water chemistry. *Paleoceanography*, 10(4), 733–747. <https://doi.org/10.1029/95PA01546>.
- Lea, D. W. (1999). Trace elements in foraminiferal calcite. In *Modern Foraminifera* (pp. 259–277). Springer Netherlands. https://doi.org/10.1007/0-306-48104-9_15.
- Lea, D. W., & Boyle, E. A. (1991). Barium in planktonic foraminifera. *Geochimica et Cosmochimica Acta*, 55(11), 3321–3331. [https://doi.org/10.1016/0016-7037\(91\)90491-M](https://doi.org/10.1016/0016-7037(91)90491-M).
- Lea, D. W., Mashiotto, T. A., & Spero, H. J. (1999). Controls on magnesium and strontium uptake in planktonic foraminifera determined by live culturing. *Geochimica et Cosmochimica Acta*, 63(16), 2369–2379. [https://doi.org/10.1016/S0016-7037\(99\)00197-0](https://doi.org/10.1016/S0016-7037(99)00197-0).
- Lea, D. W., Pak, D. K., & Paradis, G. (2005). Influence of volcanic shards on foraminiferal Mg/Ca in a core from the Galápagos region. *Geochemistry, Geophysics, Geosystems*, 6(11). <https://doi.org/10.1029/2005GC000970>.
- Lear, C. H., Rosenthal, Y., & Slowey, N. (2002). Benthic foraminiferal Mg/Ca-paleothermometry: a revised core-top calibration. *Geochimica et Cosmochimica Acta*, 66(19), 3375–3387. [https://doi.org/10.1016/S0016-7037\(02\)00941-9](https://doi.org/10.1016/S0016-7037(02)00941-9).
- Lee, S. Y., Chiang, J. C. H., Matsumoto, K., & Tokos, K. S. (2011). *Southern Ocean wind response to North Atlantic cooling and the rise in atmospheric CO₂: Modeling perspective and paleoceanographic implications*. 26, 1–16. <https://doi.org/10.1029/2010PA002004>.
- Lessa, D. V. O., Santos, T. P., Venancio, I. M., & Albuquerque, A. L. S. (2017). Offshore expansion of the Brazilian coastal upwelling zones during Marine Isotope Stage 5. *Global and Planetary Change*, 158, 13–20. <https://doi.org/10.1016/j.gloplacha.2017.09.006>.
- Lessa, D. V. O., Santos, T. P., Venancio, I. M., Santarosa, A. C. A., dos Santos Junior, E. C., Toledo, F. A. L., Costa, K. B., & Albuquerque, A. L. S. (2019). Eccentricity-induced expansions of Brazilian coastal upwelling zones. *Global and Planetary Change*, 179(May), 33–42. <https://doi.org/10.1016/j.gloplacha.2019.05.002>.

- Lessa, D. V. O., Venancio, I. M., dos Santos, T. P., Belem, A. L., Turcq, B. J., Sifeddine, A., & Albuquerque, A. L. S. (2016). Holocene oscillations of Southwest Atlantic shelf circulation based on planktonic foraminifera from an upwelling system (off Cabo Frio, Southeastern Brazil). *The Holocene*, 26(8), 1175–1187. <https://doi.org/10.1177/0959683616638433>.
- Li, Q., England, M. H., Hogg, A. McC., Rintoul, S. R., & Morrison, A. K. (2023). Abyssal ocean overturning slowdown and warming driven by Antarctic meltwater. *Nature*, 615(7954), 841–847. <https://doi.org/10.1038/s41586-023-05762-w>.
- Linge, K. L., & Jarvis, K. E. (2009). Quadrupole ICP-MS: Introduction to Instrumentation, Measurement Techniques and Analytical Capabilities. *Geostandards and Geoanalytical Research*, 33(4), 445–467. <https://doi.org/10.1111/j.1751-908X.2009.00039.x>.
- Lisiecki, L. E., & Raymo, M. E. (2005). A Pliocene-Pleistocene stack of 57 globally distributed benthic $\delta^{18}\text{O}$ records. *Paleoceanography*, 20(1), 1–17. <https://doi.org/10.1029/2004PA001071>.
- Little, M. G., Schneider, R. R., Kroon, D., Price, B., Bickert, T., & Wefer, G. (1997). Rapid palaeoceanographic changes in the Benguela Upwelling System for the last 160,000 years as indicated by abundances of planktonic foraminifera. *Palaeogeography, Palaeoclimatology, Palaeoecology*, 130(1–4), 135–161. [https://doi.org/10.1016/S0031-0182\(96\)00136-8](https://doi.org/10.1016/S0031-0182(96)00136-8).
- Liu, F., Lu, J., Luo, Y., Huang, Y., & Song, F. (2020). On the oceanic origin for the enhanced seasonal cycle of SST in the midlatitudes under global warming. *Journal of Climate*, 33(19), 8401–8413. <https://doi.org/10.1175/JCLI-D-20-0114.1>.
- Liu, W., Fedorov, A. V., Xie, S.-P., & Hu, S. (2020). Climate impacts of a weakened Atlantic Meridional Overturning Circulation in a warming climate. *Science Advances*, 6(26), eaaz4876. <https://doi.org/10.1126/sciadv.aaz4876>.
- Locarnini, R. A., Mishonov, A. V., Baranova, O. K., Boyer, T. P., Zweng, M. M., Garcia, H. E., Reagan, J. R., Seidov, D., Weathers, K. W., Paver, C. R., & Smolyar, I. V. (2018). *World Ocean Atlas 2018, Volume 1 Temperature* (Vol. 1). <http://www.nodc.noaa.gov/OC5/indprod.html>.
- Lončarić, N., Peeters, F. J. C., Kroon, D., & Brummer, G. J. A. (2006). Oxygen isotope ecology of recent planktic foraminifera at the central Walvis Ridge (SE Atlantic). *Paleoceanography*, 21(3), 1–18. <https://doi.org/10.1029/2005PA001207>.
- Lu, W., Dickson, A. J., Thomas, E., Rickaby, R. E. M., Chapman, P., & Lu, Z. (2020). Refining the planktic foraminiferal I/Ca proxy: Results from the Southeast Atlantic Ocean. *Geochimica et Cosmochimica Acta*, 287, 318–327. <https://doi.org/10.1016/j.gca.2019.10.025>.
- Lu, Z., Hoogakker, B. A. A., Hillenbrand, C.-D., Zhou, X., Thomas, E., Gutchess, K. M., Lu, W., Jones, L., & Rickaby, R. E. M. (2016). Oxygen depletion recorded in upper waters of the glacial Southern Ocean. *Nature Communications*, 7(1), 11146. <https://doi.org/10.1038/ncomms11146>.
- Lüthi, D., Le Floch, M., Bereiter, B., Blunier, T., Barnola, J.-M., Siegenthaler, U., Raynaud, D., Jouzel, J., Fischer, H., Kawamura, K., & Stocker, T. F. (2008). High-resolution carbon dioxide concentration record 650,000–800,000 years before present. *Nature*, 453(7193), 379–382. <https://doi.org/10.1038/nature06949>.
- Lutze, G. F., & Thiel, H. (1989). Epibenthic foraminifera from elevated microhabitats; *Cibicidoides wuellerstorfi* and *Planulina ariminensis*. *The Journal of Foraminiferal Research*, 19(2), 153–158. <https://doi.org/10.2113/gsjfr.19.2.153>.

- Lynch-Stieglitz, J., Adkins, J. F., Curry, W. B., Dokken, T., Hall, I. R., Herguera, J. C., Hirschi, J. J.-M., Ivanova, E. V., Kissel, C., Marchal, O., Marchitto, T. M., McCave, I. N., McManus, J. F., Mulitza, S., Ninnemann, U., Peeters, F., Yu, E.-F., & Zahn, R. (2007). Atlantic Meridional Overturning Circulation During the Last Glacial Maximum. *Science*, *316*(5821), 66–69. <https://doi.org/10.1126/science.1137127>.
- Lynch-Stieglitz, J., Stocker, T. F., Broecker, W. S., & Fairbanks, R. G. (1995). The influence of air-sea exchange on the isotopic composition of oceanic carbon: Observations and modeling. *Global Biogeochemical Cycles*, *9*(4), 653–665. <https://doi.org/10.1029/95GB02574>.
- Ma, R., S epulcre, S., Licari, L., Haurine, F., Bassinot, F., Yu, Z., & Colin, C. (2022). Changes in productivity and intermediate circulation in the northern Indian Ocean since the last deglaciation: new insights from benthic foraminiferal Cd/Ca records and benthic assemblage analyses. *Climate of the Past*, *18*(8), 1757–1774. <https://doi.org/10.5194/cp-18-1757-2022>.
- Mackensen, A., F utterer, D. K., Grobe, H., & Schmiedl, G. (1993). Benthic foraminiferal assemblages from the eastern South Atlantic Polar Front region between 35  and 57 S: Distribution, ecology and fossilization potential. *Marine Micropaleontology*, *22*(1–2), 33–69. [https://doi.org/10.1016/0377-8398\(93\)90003-G](https://doi.org/10.1016/0377-8398(93)90003-G).
- Mackensen, A., & Schmiedl, G. (2019). Stable carbon isotopes in paleoceanography: atmosphere, oceans, and sediments. *Earth-Science Reviews*, *197*(December 2018), 102893. <https://doi.org/10.1016/j.earscirev.2019.102893>.
- Marcello, F., Wainer, I., & Rodrigues, R. R. (2018). South Atlantic Subtropical Gyre Late Twentieth Century Changes. *Journal of Geophysical Research: Oceans*, *123*(8), 5194–5209. <https://doi.org/10.1029/2018JC013815>.
- Marengo, J. A., Tomasella, J., Soares, W. R., Alves, L. M., & Nobre, C. A. (2012). Extreme climatic events in the Amazon basin. *Theoretical and Applied Climatology*, *107*(1–2), 73–85. <https://doi.org/10.1007/s00704-011-0465-1>.
- Marr, J. P., Bostock, H. C., Carter, L., Bolton, A., & Smith, E. (2013). Differential effects of cleaning procedures on the trace element chemistry of planktonic foraminifera. *Chemical Geology*, *351*, 310–323. <https://doi.org/10.1016/j.chemgeo.2013.05.019>.
- Marshall, J., Donohoe, A., Ferreira, D., & McGee, D. (2014). The ocean’s role in setting the mean position of the Inter-Tropical Convergence Zone. *Climate Dynamics*, *42*(7–8), 1967–1979. <https://doi.org/10.1007/s00382-013-1767-z>.
- Marshall, J., & Speer, K. (2012). Closure of the meridional overturning circulation through Southern Ocean upwelling. *Nature Geoscience*, *5*(3), 171–180. <https://doi.org/10.1038/ngeo1391>.
- Martin, P. A., & Lea, D. W. (2002). A simple evaluation of cleaning procedures on fossil benthic foraminiferal Mg/Ca. *Geochemistry, Geophysics, Geosystems*, *3*(10), 1–8. <https://doi.org/10.1029/2001GC000280>.
- Marzocchi, A., & Jansen, M. F. (2019). Global cooling linked to increased glacial carbon storage via changes in Antarctic sea ice. *Nature Geoscience*, *12*(12), 1001–1005. <https://doi.org/10.1038/s41561-019-0466-8>.
- McGee, D., Moreno-Chamarro, E., Green, B., Marshall, J., Galbraith, E., & Bradtmiller, L. (2018). Hemispherically asymmetric trade wind changes as signatures of past ITCZ shifts. *Quaternary Science Reviews*, *180*, 214–228. <https://doi.org/10.1016/j.quascirev.2017.11.020>.

Middelburg, J. J., van der Weijden, C. H., & Woittiez, J. R. W. (1988). Chemical processes affecting the mobility of major, minor and trace elements during weathering of granitic rocks. *Chemical Geology*, 68(3–4), 253–273. [https://doi.org/10.1016/0009-2541\(88\)90025-3](https://doi.org/10.1016/0009-2541(88)90025-3).

Mitsui, T., & Boers, N. (2022). Machine learning approach reveals strong link between obliquity amplitude increase and the Mid-Brunhes transition. *Quaternary Science Reviews*, 277, 107344. <https://doi.org/10.1016/j.quascirev.2021.107344>.

Mitsui, T., Tzedakis, P. C., & Wolff, E. W. (2022). *Insolation evolution and ice volume legacies determine interglacial and glacial intensity*. l(May).

Moore, B. R., & Dennen, W. H. (1970). A Geochemical Trend in Silicon-Aluminum-Iron Ratios and the Classification of Clastic Sediments. *SEPM Journal of Sedimentary Research*, Vol. 40(4), 1147–1152. <https://doi.org/10.1306/74D72153-2B21-11D7-8648000102C1865D>.

Morey, A. E., Mix, A. C., & Pisias, N. G. (2005). Planktonic foraminiferal assemblages preserved in surface sediments correspond to multiple environment variables. *Quaternary Science Reviews*, 24(7–9), 925–950. <https://doi.org/10.1016/j.quascirev.2003.09.011>.

Mulitza, S., Prange, M., Stuut, J.-B., Zabel, M., von Dobeneck, T., Itambi, A. C., Nizou, J., Schulz, M., & Wefer, G. (2008). Sahel megadroughts triggered by glacial slowdowns of Atlantic meridional overturning. *Paleoceanography*, 23(4). <https://doi.org/10.1029/2008PA001637>.

Murray, J. W. (2006). *Ecology and Applications of Benthic Foraminifera*. Cambridge University Press. <https://doi.org/10.1017/CBO9780511535529>.

Nascimento, R. A., Shimizu, M. H., Venancio, I. M., Chiessi, C. M., Kuhnert, H., Johnstone, H., Govin, A., Lessa, D., Ballalai, J. M., Piacsek, P., Mulitza, S., & Albuquerque, A. L. S. (2022). Warmer western tropical South Atlantic during the Last Interglacial relative to the current interglacial period. *Global and Planetary Change*, 95(14), 103889. <https://doi.org/10.1016/j.gloplacha.2022.103889>.

Nascimento, R. A., Venancio, I. M., Chiessi, C. M., Ballalai, J. M., Kuhnert, H., Johnstone, H., Santos, T. P., Prange, M., Govin, A., Crivellari, S., Mulitza, S., & Albuquerque, A. L. S. (2021). Tropical Atlantic stratification response to late Quaternary precessional forcing. *Earth and Planetary Science Letters*, 568, 117030. <https://doi.org/10.1016/j.epsl.2021.117030>.

National Oceanic and Atmospheric Administration (NOAA). (2022). Global Monitoring Laboratory - Carbon Cycle Greenhouse Gases. Retrieved from <https://www.esrl.noaa.gov/gmd/ccgg/>.

Nürnberg, D., Bijma, J., & Hemleben, C. (1996). Assessing the reliability of magnesium in foraminiferal calcite as a proxy for water mass temperatures. *Geochimica et Cosmochimica Acta*, 60(5), 803–814. [https://doi.org/10.1016/0016-7037\(95\)00446-7](https://doi.org/10.1016/0016-7037(95)00446-7).

Olson, D. B., Podestá, G. P., Evans, R. H., & Brown, O. B. (1988). Temporal variations in the separation of Brazil and Malvinas Currents. *Deep Sea Research Part A. Oceanographic Research Papers*, 35(12), 1971–1990. [https://doi.org/10.1016/0198-0149\(88\)90120-3](https://doi.org/10.1016/0198-0149(88)90120-3).

Orbigny, A. D. d'. (1826). Tableau méthodique de la classe des Céphalopodes. *Annales Des Sciences Naturelles*.

Orbigny, A. D. d'. (1839). Foraminifères des îles Canaries. *Histoire Naturelle Des Iles Canaries*, 2(2), 120–146.

Paillard, D. (2021). Climate and Astronomical Cycles. In A. and B. N. and S. P. and G. A. Ramstein Gilles and Landais (Ed.), *Paleoclimatology* (pp. 385–404). Springer International Publishing. https://doi.org/10.1007/978-3-030-24982-3_28.

Paillard, D., Labeyrie, L., & Yiou, P. (1996). Macintosh Program performs time-series analysis. *Eos, Transactions American Geophysical Union*, 77(39), 379. <https://doi.org/https://doi.org/10.1029/96EO00259>.

Pedro, J. B., Jochum, M., Buizert, C., He, F., Barker, S., & Rasmussen, S. O. (2018). Beyond the bipolar seesaw: Toward a process understanding of interhemispheric coupling. *Quaternary Science Reviews*, 192, 27–46. <https://doi.org/10.1016/j.quascirev.2018.05.005>.

Peterson, L. C. (2000). Rapid Changes in the Hydrologic Cycle of the Tropical Atlantic During the Last Glacial. *Science*, 290(5498), 1947–1951. <https://doi.org/10.1126/science.290.5498.1947>.

Peterson, R. G., & Stramma, L. (1991). Upper-level circulation in the South-Atlantic Ocean. *Progress In Oceanography*, 26(1), 1–73. [https://doi.org/10.1016/0079-6611\(91\)90006-8](https://doi.org/10.1016/0079-6611(91)90006-8).

Petit, J. R., Jouzel, J., Raynaud, D., Barkov, N. I., Barnola, J.-M., Basile, I., Bender, M., Chappellaz, J., Davis, M., Delaygue, G., Delmotte, M., Kotlyakov, V. M., Legrand, M., Lipenkov, V. Y., Lorius, C., Pépin, L., Ritz, C., Saltzman, E., & Stievenard, M. (1999). Climate and atmospheric history of the past 420,000 years from the Vostok ice core, Antarctica. *Nature*, 399(6735), 429–436. <https://doi.org/10.1038/20859>.

Planton, S., Déqué, M., Chauvin, F., & Terray, L. (2008). Expected impacts of climate change on extreme climate events. *Comptes Rendus - Geoscience*, 340(9–10), 564–574. <https://doi.org/10.1016/j.crte.2008.07.009>.

Portilho-Ramos, R. da C., Ferreira, F., Calado, L., Frontalini, F., & de Toledo, M. B. (2015). Variability of the upwelling system in the southeastern Brazilian margin for the last 110,000years. *Global and Planetary Change*, 135, 179–189. <https://doi.org/10.1016/j.gloplacha.2015.11.003>.

Pröfrock, D., & Prange, A. (2012). Inductively Coupled Plasma–Mass Spectrometry (ICP-MS) for Quantitative Analysis in Environmental and Life Sciences: A Review of Challenges, Solutions, and Trends. *Applied Spectroscopy*, 66(8), 843–868. <https://doi.org/10.1366/12-06681>.

Purich, A., & England, M. H. (2023). Projected Impacts of Antarctic Meltwater Anomalies over the Twenty-First Century. *Journal of Climate*, 36(8), 2703–2719. <https://doi.org/https://doi.org/10.1175/JCLI-D-22-0457.1>.

Rackebrandt, N., Kuhnert, H., Groeneveld, J., & Bickert, T. (2011). Persisting maximum Agulhas leakage during MIS 14 indicated by massive *Ethmodiscus* oozes in the subtropical South Atlantic. *Paleoceanography*, 26(3). <https://doi.org/10.1029/2010PA001990>.

Rahmstorf, S. (2006). Thermohaline Ocean Circulation. In *Encyclopedia of Quaternary Science*. Rantanen, M., Karpechko, A. Y., Lipponen, A., Nordling, K., Hyvärinen, O., Ruosteenoja, K., Vihma, T., & Laaksonen, A. (2022). The Arctic has warmed nearly four times faster than the globe since 1979. *Communications Earth and Environment*, 3(1). <https://doi.org/10.1038/s43247-022-00498-3>.

Ravelo, A. C., & Hillaire-Marcel, C. (2007). *The Use of Oxygen and Carbon Isotopes of Foraminifera in Paleoceanography* (Vol. 1, Issue 07, pp. 735–764). [https://doi.org/10.1016/S1572-5480\(07\)01023-8](https://doi.org/10.1016/S1572-5480(07)01023-8).

- Regenberg, M., Steph, S., Nürnberg, D., Tiedemann, R., & Garbe-Schönberg, D. (2009). Calibrating Mg/Ca ratios of multiple planktonic foraminiferal species with $\delta^{18}\text{O}$ -calcification temperatures: Paleothermometry for the upper water column. *Earth and Planetary Science Letters*, 278(3–4), 324–336. <https://doi.org/10.1016/j.epsl.2008.12.019>.
- Reimer, P. J., Bard, E., Bayliss, A., Beck, J. W., Blackwell, P. G., Ramsey, C. B., Buck, C. E., Cheng, H., Edwards, R. L., Friedrich, M., Grootes, P. M., Guilderson, T. P., Haflidason, H., Hajdas, I., Hatté, C., Heaton, T. J., Hoffmann, D. L., Hogg, A. G., Hughen, K. A., ... van der Plicht, J. (2013). IntCal13 and Marine13 Radiocarbon Age Calibration Curves 0–50,000 Years cal BP. *Radiocarbon*, 55(04), 1869–1887. https://doi.org/10.2458/azu_js_rc.55.16947.
- Richey, J. N., Fehrenbacher, J. S., Reynolds, C. E., Davis, C. V., & Spero, H. J. (2022). Barium enrichment in the non-spinose planktic foraminifer, *Globorotalia truncatulinoides*. *Geochimica et Cosmochimica Acta*, 333, 184–199. <https://doi.org/https://doi.org/10.1016/j.gca.2022.07.006>.
- Richter, T. O., van der Gaast, S., Koster, B., Vaars, A., Gieles, R., de Stigter, H. C., De Haas, H., & van Weering, T. C. E. (2006). The Avaatech XRF Core Scanner: technical description and applications to NE Atlantic sediments. *Geological Society, London, Special Publications*, 267(1), 39–50. <https://doi.org/10.1144/GSL.SP.2006.267.01.03>.
- Riechers, K., Mitsui, T., Boers, N., & Ghil, M. (2021). *Orbital Insolation Variations, Intrinsic Climate Variability, and Quaternary Glaciations*. *October*, 1–34. <https://doi.org/10.5194/cp-2021-136>.
- Rodrigues, R. R., Rothstein, L. M., & Wimbush, M. (2007). Seasonal Variability of the South Equatorial Current Bifurcation in the Atlantic Ocean: A Numerical Study. *Journal of Physical Oceanography*, 37(1), 16–30. <https://doi.org/10.1175/JPO2983.1>.
- Rosenthal, Y. (2007). Chapter Nineteen Elemental Proxies for Reconstructing Cenozoic Seawater Paleotemperatures from Calcareous Fossils. In *Developments in Marine Geology* (Vol. 1, Issue 07, pp. 765–797). [https://doi.org/10.1016/S1572-5480\(07\)01024-X](https://doi.org/10.1016/S1572-5480(07)01024-X).
- Rosenthal, Y., Perron-Cashman, S., Lear, C. H., Bard, E., Barker, S., Billups, K., Bryan, M., Delaney, M. L., DeMenocal, P. B., Dwyer, G. S., Elderfield, H., German, C. R., Greaves, M., Lea, D. W., Marchitto, T. M., Pak, D. K., Paradis, G. L., Russell, A. D., Schneider, R. R., ... Wilson, P. A. (2004). Interlaboratory comparison study of Mg/Ca and Sr/Ca measurements in planktonic foraminifera for paleoceanographic research. *Geochemistry, Geophysics, Geosystems*, 5(4). <https://doi.org/10.1029/2003GC000650>.
- Roubi, A. (2019). Variabilité de l'upwelling du Benguela pendant les derniers 40 000 ans. Université de Bretagne Occidentale, Plouzané, France.
- Santos, T. P., Lessa, D. O., Venancio, I. M., Chiessi, C. M., Mulitza, S., Kuhnert, H., Govin, A., Machado, T., Costa, K. B., Toledo, F., Dias, B. B., & Albuquerque, A. L. S. (2017). Prolonged warming of the Brazil Current precedes deglaciations. *Earth and Planetary Science Letters*, 463(April), 1–12. <https://doi.org/10.1016/j.epsl.2017.01.014>.
- Santos, T. P., Shimizu, M. H., Nascimento, R. A., Venancio, I. M., Campos, M. C., Portilho-Ramos, R. C., Ballalai, J. M., Lessa, D. O., Crivellari, S., Nagai, R. H., Chiessi, C. M., Kuhnert, H., Bahr, A., & Albuquerque, A. L. S. (2022). A data-model perspective on the Brazilian margin surface warming from the Last Glacial Maximum to the Holocene. *Quaternary Science Reviews*, 286, 107557. <https://doi.org/10.1016/j.quascirev.2022.107557>.

Schiebel, R., Bijma, J., & Hemleben, C. (1997). Population dynamics of the planktic foraminifer *Globigerina bulloides* from the eastern North Atlantic. *Deep Sea Research Part I: Oceanographic Research Papers*, 44(9–10), 1701–1713. [https://doi.org/10.1016/S0967-0637\(97\)00036-8](https://doi.org/10.1016/S0967-0637(97)00036-8).

Schiebel, R., & Hemleben, C. (2017). *Planktic Foraminifers in the Modern Ocean*. Springer Berlin Heidelberg. <https://doi.org/10.1007/978-3-662-50297-6>.

Schiebel, R., Smart, S. M., Jentzen, A., Jonkers, L., Morard, R., Meilland, J., Michel, E., Coxall, H. K., Hull, P. M., de Garidel-Thoron, T., Aze, T., Quillévéré, F., Ren, H., Sigman, D. M., Vonhof, H. B., Martínez-García, A., Kučera, M., Bijma, J., Spero, H. J., & Haug, G. H. (2018). Advances in planktonic foraminifer research: New perspectives for paleoceanography. *Revue de Micropaléontologie*, 61(3–4), 113–138. <https://doi.org/10.1016/j.revmic.2018.10.001>.

Schiebel, R., Zeltner, A., Treppke, U. F., Waniek, J. J., Bollmann, J., Rixen, T., & Hemleben, C. (2004). Distribution of diatoms, coccolithophores and planktic foraminifers along a trophic gradient during SW monsoon in the Arabian Sea. *Marine Micropaleontology*, 51(3–4), 345–371. <https://doi.org/10.1016/j.marmicro.2004.02.001>.

Schlitzer, R. (2017). Ocean Data View, odv.awi.de

Schmidt, M. W., Spero, H. J., & Lea, D. W. (2004). Links between salinity variation in the Caribbean and North Atlantic thermohaline circulation. *Nature*, 428(6979), 160–163. <https://doi.org/10.1038/nature02346>.

Schneider R. R. and Müller, P. J. and R. G. and M. G. and S. H. and W. G. (1996). Late Quaternary Surface Temperatures and Productivity in the East-Equatorial South Atlantic: Response to Changes in Trade/Monsoon Wind Forcing and Surface Water Advection. In *The South Atlantic: Present and Past Circulation* (pp. 527–551). Springer Berlin Heidelberg. https://doi.org/10.1007/978-3-642-80353-6_27.

Sen Gupta, B. K. (2003). *Modern Foraminifera*. Springer Netherlands. <https://doi.org/10.1007/0-306-48104-9>.

Shackleton, N. J. (1974). Attainment of isotopic equilibrium between ocean water and the benthonic foraminifera geus *Uvigerina*: Isotopic changes in the ocean during the last glacial. *Colloques Internationaux Du C.N.R.S.*, 219, 203–210.

Shakun, J. D., Clark, P. U., He, F., Marcott, S. A., Mix, A. C., Liu, Z., Otto-Bliesner, B., Schmittner, A., & Bard, E. (2012). Global warming preceded by increasing carbon dioxide concentrations during the last deglaciation. *Nature*, 484(7392), 49–54. <https://doi.org/10.1038/nature10915>.

Shannon, L. V. (1985). The Benguela ecosystem. I: Evolution of the Benguela physical features and processes. *Oceanography and Marine Biology*, 23, 105–182.

Sharp, B. L. (1988). Pneumatic nebulisers and spray chambers for inductively coupled plasma spectrometry. A review. Part 1. Nebulisers. *Journal of Analytical Atomic Spectrometry*, 3(5), 613. <https://doi.org/10.1039/ja9880300613>.

Siegenthaler, U., Stocker, T. F., Monnin, E., Lüthi, D., Schwander, J., Stauffer, B., Raynaud, D., Barnola, J.-M., Fischer, H., Masson-Delmotte, V., & Jouzel, J. (2005). Stable Carbon Cycle - Climate Relationship During the Late Pleistocene. *Science*, 310(5752), 1313–1317. <https://doi.org/10.1126/science.1120130>.

- Sigman, D. M., & Boyle, E. A. (2000). Glacial/interglacial variations in atmospheric carbon dioxide. *Nature*, *407*(6806), 859–869. <https://doi.org/10.1098/rsta.2013.0054>.
- Silveira, I. C. A. da, Schmidt, A. C. K., Campos, E. J. D., Godoi, S. S. de, & Ikeda, Y. (2000). A corrente do Brasil ao largo da costa leste brasileira. *Revista Brasileira de Oceanografia*, *48*(2), 171–183. <https://doi.org/10.1590/S1413-77392000000200008>.
- Spindler, M., Hernleben, C., Bayer, U., Bé, A., & Anderson, O. (1979). Lunar Periodicity of Reproduction in the Planktonic Foraminifer *Hastigerina pelagica*. *Marine Ecology Progress Series*, *1*(September 1977), 61–64. <https://doi.org/10.3354/meps001061>.
- Spratt, R. M., & Lisiecki, L. E. (2016). A Late Pleistocene sea level stack. *Climate of the Past*, *12*(4), 1079–1092. <https://doi.org/10.5194/cp-12-1079-2016>.
- Steinke, S., Groeneveld, J., Johnstone, H., & Rendle-Bühning, R. (2010). East Asian summer monsoon weakening after 7.5Ma: Evidence from combined planktonic foraminifera Mg/Ca and $\delta^{18}\text{O}$ (ODP Site 1146; northern South China Sea). *Palaeogeography, Palaeoclimatology, Palaeoecology*, *289*(1–4), 33–43. <https://doi.org/10.1016/j.palaeo.2010.02.007>.
- Steph, S., Regenberg, M., Tiedemann, R., Mulitza, S., & Nürnberg, D. (2009). Stable isotopes of planktonic foraminifera from tropical Atlantic/Caribbean core-tops: Implications for reconstructing upper ocean stratification. *Marine Micropaleontology*, *71*(1–2), 1–19. <https://doi.org/10.1016/j.marmicro.2008.12.004>.
- Stephens, B. B., & Keeling, R. F. (2000). The influence of Antarctic sea ice on glacial–interglacial CO_2 variations. *Nature*, *404*(6774), 171–174. <https://doi.org/10.1038/35004556>.
- Stewart, J. A., Christopher, S. J., Kucklick, J. R., Bordier, L., Chalk, T. B., Dapoigny, A., Douville, E., Foster, G. L., Gray, W. R., Greenop, R., Gutjahr, M., Hemsing, F., Henahan, M. J., Holdship, P., Hsieh, Y., Kolevica, A., Lin, Y., Mawbey, E. M., Rae, J. W. B., ... Day, R. D. (2021). NIST RM 8301 Boron Isotopes in Marine Carbonate (Simulated Coral and Foraminifera Solutions): Inter-laboratory $\delta^{11}\text{B}$ and Trace Element Ratio Value Assignment. *Geostandards and Geoanalytical Research*, *45*(1), 77–96. <https://doi.org/10.1111/ggr.12363>.
- Stocker, T. F. (1998). The Seesaw Effect. *Science*, *282*(5386), 61–62. <https://doi.org/10.1126/science.282.5386.61>.
- Stuut, J.-B. W., Prins, M. A., Schneider, R. R., Weltje, G. J., Jansen, J. H. F., & Postma, G. (2002). A 300-kyr record of aridity and wind strength in southwestern Africa: inferences from grain-size distributions of sediments on Walvis Ridge, SE Atlantic. *Marine Geology*, *180*(1–4), 221–233. [https://doi.org/10.1016/S0025-3227\(01\)00215-8](https://doi.org/10.1016/S0025-3227(01)00215-8).
- Thornalley, D. J. R., Elderfield, H., & McCave, I. N. (2009). Holocene oscillations in temperature and salinity of the surface subpolar North Atlantic. *Nature*, *457*(7230), 711–714. <https://doi.org/10.1038/nature07717>.
- Thornalley, D. J. R., Oppo, D. W., Ortega, P., Robson, J. I., Brierley, C. M., Davis, R., Hall, I. R., Moffa-Sanchez, P., Rose, N. L., Spooner, P. T., Yashayaev, I., & Keigwin, L. D. (2018). Anomalously weak Labrador Sea convection and Atlantic overturning during the past 150 years. *Nature*, *556*(7700), 227–230. <https://doi.org/10.1038/s41586-018-0007-4>.
- Timmermann, A., Timm, O., Stott, L., & Menviel, L. (2009). The roles of CO_2 and orbital forcing in driving Southern Hemispheric temperature variations during the last 21 000 Yr. *Journal of Climate*, *22*(7), 1626–1640. <https://doi.org/10.1175/2008JCLI2161.1>.

- Tjallingii, R. (2007). *Application and quality of X-Ray fluorescence core scanning in reconstructing late Pleistocene NW African continental margin sedimentation patterns and paleoclimate variations*.
- Toggweiler, J. R., & Lea, D. W. (2010). Temperature differences between the hemispheres and ice age climate variability. *Paleoceanography*, *25*(2). <https://doi.org/10.1029/2009PA001758>.
- Toggweiler, J. R., Russell, J. L., & Carson, S. R. (2006). Midlatitude westerlies, atmospheric CO₂, and climate change during the ice ages. *Paleoceanography*, *21*(2). <https://doi.org/10.1029/2005PA001154>.
- Toggweiler, J. R., & Samuels, B. (1995). Effect of drake passage on the global thermohaline circulation. *Deep Sea Research Part I: Oceanographic Research Papers*, *42*(4), 477–500. [https://doi.org/10.1016/0967-0637\(95\)00012-U](https://doi.org/10.1016/0967-0637(95)00012-U).
- Vázquez Riveiros, N., Govin, A., Waelbroeck, C., Mackensen, A., Michel, E., Moreira, S., Bouinot, T., Caillon, N., Orgun, A., & Brandon, M. (2016). Mg/Ca thermometry in planktic foraminifera: Improving paleotemperature estimations for *G. bulloides* and *N. pachyderma* left. *Geochemistry, Geophysics, Geosystems*, *17*(4), 1249–1264. <https://doi.org/10.1002/2015GC006234>.
- Volbers, A. N. A., Niebler, H.-S., Giraudeau, J., Schmidt, H., & Henrich, R. (2003). Palaeoceanographic Changes in the Northern Benguela Upwelling System over the last 245.000 Years as Derived from Planktic Foraminifera Assemblages. In *The South Atlantic in the Late Quaternary* (Issue October 2014, pp. 601–622). Springer Berlin Heidelberg. https://doi.org/10.1007/978-3-642-18917-3_26.
- Waelbroeck, C., Labeyrie, L., Michel, E., Duplessy, J. C., McManus, J. F., Lambeck, K., Balbon, E., & Labracherie, M. (2002). Sea-level and deep water temperature changes derived from benthic foraminifera isotopic records. *Quaternary Science Reviews*, *21*(1–3), 295–305. [https://doi.org/10.1016/S0277-3791\(01\)00101-9](https://doi.org/10.1016/S0277-3791(01)00101-9).
- Waelbroeck, C., Lougheed, B. C., Vazquez Riveiros, N., Missiaen, L., Pedro, J., Dokken, T., Hajdas, I., Wacker, L., Abbott, P., Dumoulin, J. P., Thil, F., Eynaud, F., Rossignol, L., Fersi, W., Albuquerque, A. L., Arz, H., Austin, W. E. N., Came, R., Carlson, A. E., ... Ziegler, M. (2019). Consistently dated Atlantic sediment cores over the last 40 thousand years. *Scientific Data*, *6*(1), 165. <https://doi.org/10.1038/s41597-019-0173-8>.
- Wang, X., Auler, A. S., Edwards, R. L., Cheng, H., Cristalli, P. S., Smart, P. L., Richards, D. A., & Shen, C.-C. (2004). Wet periods in northeastern Brazil over the past 210 kyr linked to distant climate anomalies. *Nature*, *432*(7018), 740–743. <https://doi.org/10.1038/nature03067>.
- Weldeab, S., Schneider, R. R., & Kölling, M. (2006). Comparison of foraminiferal cleaning procedures for Mg/Ca paleothermometry on core material deposited under varying terrigenous-input and bottom water conditions. *Geochemistry, Geophysics, Geosystems*, *7*(4). <https://doi.org/10.1029/2005GC000990>.
- West, S., Jansen, J. H. F., & Stuut, J. B. (2004). Surface water conditions in the Northern Benguela Region (SE Atlantic) during the last 450 ky reconstructed from assemblages of planktonic foraminifera. *Marine Micropaleontology*, *51*(3–4), 321–344. <https://doi.org/10.1016/j.marmicro.2004.01.004>.
- Wilschefschi, S., & Baxter, M. (2019). Inductively Coupled Plasma Mass Spectrometry: Introduction to Analytical Aspects. *Clinical Biochemist Reviews*, *40*(3), 115–133. <https://doi.org/10.33176/AACB-19-00024>.
- Wolff, E. W., Barbante, C., Becagli, S., Bigler, M., Boutron, C. F., Castellano, E., de Angelis, M., Federer, U., Fischer, H., Fundel, F., Hansson, M., Hutterli, M., Jonsell, U., Karlin, T., Kaufmann, P.,

- Lambert, F., Littot, G. C., Mulvaney, R., Röthlisberger, R., ... Wegner, A. (2010). Changes in environment over the last 800,000 years from chemical analysis of the EPICA Dome C ice core. *Quaternary Science Reviews*, 29(1–2), 285–295. <https://doi.org/10.1016/j.quascirev.2009.06.013>.
- Wolff, E. W., Fischer, H., Fundel, F., Ruth, U., Twarloh, B., Littot, G. C., Mulvaney, R., Röthlisberger, R., de Angelis, M., Boutron, C. F., Hansson, M., Jonsell, U., Hutterli, M. A., Lambert, F., Kaufmann, P., Stauffer, B., Stocker, T. F., Steffensen, J. P., Bigler, M., ... Gaspari, V. (2006). Southern Ocean sea-ice extent, productivity and iron flux over the past eight glacial cycles. *Nature*, 440(7083), 491–496. <https://doi.org/10.1038/nature04614>.
- WoRMS Editorial Board (2023). World Register of Marine Species. Available from <https://www.marinespecies.org> at VLIZ. Accessed 2023-06-04. doi:10.14284/170.
- Wu, Z., Yin, Q., Guo, Z., & Berger, A. (2020). Hemisphere differences in response of sea surface temperature and sea ice to precession and obliquity. *Global and Planetary Change*, 192. <https://doi.org/10.1016/j.gloplacha.2020.103223>.
- Yin, Q. (2013). Insolation-induced mid-Brunhes transition in Southern Ocean ventilation and deep-ocean temperature. *Nature*, 494(7436), 222–225. <https://doi.org/10.1038/nature11790>.
- Yin, Q. Z., & Berger, A. (2012). Individual contribution of insolation and CO₂ to the interglacial climates of the past 800,000 years. *Climate Dynamics*, 38(3–4), 709–724. <https://doi.org/10.1007/s00382-011-1013-5>.
- Yu, J., & Elderfield, H. (2007). Benthic foraminiferal B/Ca ratios reflect deep water carbonate saturation state. *Earth and Planetary Science Letters*, 258(1–2), 73–86. <https://doi.org/10.1016/j.epsl.2007.03.025>.
- Yu, J., Elderfield, H., & Hönisch, B. (2007). B/Ca in planktonic foraminifera as a proxy for surface seawater pH. *Paleoceanography*, 22(2). <https://doi.org/10.1029/2006PA001347>.
- Yu, J., Elderfield, H., Jin, Z., & Booth, L. (2008). A strong temperature effect on U/Ca in planktonic foraminiferal carbonates. *Geochimica et Cosmochimica Acta*, 72(20), 4988–5000. <https://doi.org/10.1016/j.gca.2008.07.011>.
- Zhou, X., Rosenthal, Y., Haynes, L., Si, W., Evans, D., Huang, K.-F., Hönisch, B., & Erez, J. (2021). Planktic foraminiferal Na/Ca: A potential proxy for seawater calcium concentration. *Geochimica et Cosmochimica Acta*, 305, 306–322. <https://doi.org/10.1016/j.gca.2021.04.012>.
- Ziegler, M., Jilbert, T., de Lange, G. J., Lourens, L. J., & Reichert, G.-J. (2008). Bromine counts from XRF scanning as an estimate of the marine organic carbon content of sediment cores. *Geochemistry, Geophysics, Geosystems*, 9(5), n/a-n/a. <https://doi.org/10.1029/2007GC001932>

Annex A

LSCE
Equipe Paléocéen

<p>Protocole de préparation des échantillons pour la mesure des rapports Mg/Ca et Sr/Ca dans les foraminifères</p>
--

15/02/08

1 .	Protocole de nettoyage	2
1.1.	Pesée des forams	2
1.2.	Crushing	2
1.3.	Extraction des argiles	3
1.4.	Extraction de la matière organique	4
1.5.	Attaque à l'acide faible	4
1.6.	Dissolution	4
		5
2.	Préparation des réactifs	6
3.	Nettoyage des micro tubes de 0,5 ml	7

<p>POUR CE PROTOCOLE, PREVOIR UN NOMBRE DE MICRO TUBES <u>PROPRES SUFFISANT</u> I.E. 4 FOIS LE NOMBRE (D'ECHANTILLONS + UN BLANC)</p>

EX : pour 15 échantillons + 1 blanc, il faut laver $4 * (15+1) = 64$ micro tubes

1. Protocole de nettoyage

Ce protocole s'inspire largement de celui utilisé à Cambridge. Il est écrit pour des échantillons de type G. bulloides, froid (Mg/Ca < 2mmol/mol). Il préconise l'utilisation de tube "nonrelargueur" de Mg avant les étapes impliquant de l'acide.

Il est important de noter que ce protocole pourra varier en fonction de chaque espèce.

(E. G. pour échantillons à fort Mg/Ca avec peu d'argiles, il sera possible de raccourcir quelques étapes, alors que pour des échantillons froids contenant des IRD il faudra être plus rigoureux.)

Il faut compter 4 heures pour la totalité du protocole pour 24 échantillons et bien entraîné.

1.1. Pesée des forams

- 1) Transférer les forams à l'aide d'un pinceau fin et sec dans une capsule inox (à manipuler avec une pince coudée).
- 2) Peser les échantillons en utilisant la microbalance qui se trouve dans la salle "bino".
- 3) Enregistrer le poids des forams (attention de bien soustraire le poids de la capsule). Transférer les forams sur une plaque en verre sur laquelle aura été déposé au préalable une goutte d'eau.

Il est très important de précisément compter le nombre d'individus pesés par échantillon. un comptage incorrect de 1 sur 20 représente 50 d'erreur sur la pesée.

1.2. Crushing

L'objectif de cette étape est d'ouvrir les loges des forams afin de facilement vider l'intérieur des loges au cours des étapes de nettoyages qui suivront. Pour cela, il faut écraser l'échantillon délicatement entre deux plaques de verre. ATTENTION : trop écraser l'échantillon résultera de la perte d'échantillon au cours du nettoyage.

- 1) Déposer une goutte d'eau sur les forams préalablement déposés sur la plaque de verre.
- 2) Déposer la seconde plaque sur la première et exercer une pression pour permettre l'ouverture des chambres (des loges).
ASTUCE : 2 tours de scotch sur chaque extrémité de la plaque de verre supérieure permettent un crushing efficace.
- 3) Relever la plaque de verre supérieure et regrouper tous les fragments sur la plaque inférieure.
- 4) Avec un pinceau humide, transférer les fragments dans un ptube de 0,5mL.

1.3. Extraction des argiles

Pour cette étape, il est conseillé de traiter les échantillons un par un afin d'optimiser l'efficacité du nettoyage.

Taper les vtubes sur la paille pour bien faire descendre les morceaux de forams au fond.

- 1) Introduire 500pL d'eau I.JHQ dans chaque micro tube afin de mettre en suspension la matière organique (les bulles d'air présentes au fond du tube peuvent être retirées en tapotant la base du tube de l'ongle ou en utilisant la centrifugeuse).
- 2) Attendre 30 secondes pour permettre aux carbonates de sédimenter dans le fond.
- 3) À l'aide d'une pipette 500pL, aspirer l'eau au-dessus de l'échantillon.

Après ces étapes, tous les tubes doivent contenir environ 10 à 20À- d'eau.

- 4) Passer les échantillons aux ultrasons de 30" à 2 minutes. (Ceci permet la séparation des argiles toujours présentes à la surface des tests).

Des argiles en suspension apparaissent sous la forme d'un résidu laiteux juste au-dessus de l'échantillon.

- 5) Avec une pipette de 500pL, ajouter de l'eau ultra pure dans chaque tube (pour agiter l'échantillon et mettre en suspension des argiles toujours fixées).
- 6) Attendre que l'échantillon se soit redéposé au fond du tube. Cette étape prendra quelques secondes (assez de temps pour que les carbonates aient le temps de se redéposer au fond). Après cette étape, la partie de l'échantillon restante sera principalement contaminée par des particules silicatées.
- 7) Retirer (aspirer) l'eau au-dessus de l'échantillon contenant les argiles.
- 8) Renouveler les étapes de (4) à (7), 4 fois. Répéter encore si des argiles en suspension sont toujours visibles après passage aux ultrasons.

Après ces étapes de nettoyage à l'eau, on utilisera l'éthanol qui permet de mettre en suspension les argiles les plus récalcitrantes. La faible viscosité de l'éthanol permet de détacher le matériel toujours attaché aux tests de carbonates.

- 9) Introduire 250pL d'éthanol à chaque échantillon.
- 10) Passer 2 minutes aux ultrasons.
- 11 Utiliser le vortex (lab dancer) pour mettre en suspension les argiles.
- 12) Attendre quelques secondes (30") que l'échantillon repose au fond du tube et retirer l' éthanol.
- 13) Répéter les étapes 9 à 12, 1 fois.
- 14) Répéter les étapes 5 à 7 afin d'enlever l'éthanol, 2 fois.

1.4. Extraction de la matière organique

- 1) Ajouter 250pL 'H2O2 à 0,3% (*) à chaque tube. Fermer les capsules des tubes hermétiquement, et les sécuriser, entre le rack plexiglas et son couvercle afin d'éviter que les tubes s'ouvrent lorsqu'ils seront sous pression.
- 2) Placer le porte échantillons dans un bain d'eau bouillante pendant 10 minutes (se servir d'un chronomètre). À 2'30" et à 7'30", retirer, et secouer ou taper le porte échantillons contre la paille, pour enlever les bulles de condensation. À 5 minutes, passer les échantillons 30 secondes aux ultrasons puis les remettre dans le bain d'eau bouillante après les avoir débarrassés des bulles d'air formées. (Retirer les bulles permet de maintenir le contact entre le réactif et l'échantillon).
- 3) À la fin des 10 minutes, utiliser la centrifugeuse pendant 1 minute à 10000tr/min, pour enlever les bulles et faire déposer les forams au fond. Retirer l'eau oxygénée à l'aide d'une pipette.
- 4) Répéter les étapes 1 à 3.
- 5) Rincer les échantillons à l'eau ultra pure 2 fois en veillant à rincer le bouchon (avec une pipette de 500vL).

(*) Préparée à partir de NaOH à 0.1M (100pL d'H2O2 30% dans 10mL de NaOH 0.1M)

[→ Am: silicate removal + change of val.]

1.5. Attaque à l'acide faible

Un acide dilué est utilisé afin de retirer des contaminants incorporés aux fragments de test.

- 1) Ajouter 250pL d'HN03 0.001M à chaque échantillon.
- 2) Passer 30 secondes aux ultrasons.
- 3) Retirer rapidement l'acide.
- 4) Ajouter avec une pipette de 500vL de l'eau UHQ rapidement afin d'éviter une dissolution excessive des carbonates. 5) Retirer le surplus d'eau.

- 5) Répéter les étapes 4 et
5. 7) Retirer le maximum d'eau.

¹À la fin de cette étape, les échantillons peuvent être stockés en attendant l'analyse. Ils seront dissous et dilués le même jour que leur analyse.

1.6. Dissolution

Afin d'assurer des dilutions précises, il est important que tous les volumes soient précisément pipetés à partir de cette étape.

- 1) Ajoute 350pL 'HN03 0.075M.
- 2) Passer que ques instants aux u trasons en fonction des échantillons (vérifier que les échantillons sont bien dissous). Au cours de cette étape, tapoter les échantillons contre la paillasse afin de faire s'échapper les bulles de CO₂ et de permettre à la dissolution de se faire correctement.
- 3) Dès que la production de CO₂ cesse, secouer l'échantillon pour mélanger.
- 4) Centrifuger les échantillons (10000 tour(min pendant ? minutes) pour déposer au fond les petites particules de silices toujours présentes.
- 5) Transférer 300À- de la solution dans un tube propre, en laissant 50 au fond de l' ancien tube.

Si l'acide de dissolution reste dans un échantillon contenant des silicates ou du matériel non carbonaté pour plus de temps nécessaire à la dissolution des carbonates, il y a un fort risque de contamination par relargage d' élément dans la solution. Il faut donc passer à la mesure ICP immédiatement après cette étape.

1.7. Dilution

Après nettoyage et dissolution, 20 foraminifères planctoniques doivent donner une concentration de Ca comprise entre 100 et 200 ppm, en fonction de l' espèce de forams et de la fraction d' échantillon perdue au cours du nettoyage.

La méthode pour la mesure de Mg/Ca et Sr/Ca en utilisant un ICP-AES Vista-Pro requiert, pour une précision et une Justesse optimales, des solutions contenant une concentration connue de Ca comprise entre 60 et 100 ppm, et utilise une solution de N350À- par analyse.

Deux runs pour chaque échantillon sont nécessaires. Un 1er run pour déterminer la concentration en Ca de l'échantillon et un 2nd run à une concentration optimum de Ca pour la détermination des rapports Mg/Ca et Sr/Ca.

Pour les échantillons contenus dans 300pL d¹HN03 à 0,075M après centrifugation, une dilution d¹un facteur 5 doit être faite avant le 1er run, suivie par une dilution du reste de l'échantillon en fonction de la concentration de Ca désirée.

- 1) Préparer une série de tubes propres pour la dilution
- 2) Ajouter 280pL d' à 0,075M à chaque tube
(Ou 250pL pour une dilution de facteur 3 si on a ajouté 500pL au départ). 3)
Ajouter 70gL d' échantillon afin d'obtenir une dilution de facteur 5 (Ou ajouter 125pL d'échantillon pour une dilution de facteur 3).

Si dilution /5 il reste 230yL d'échantillon pour le 2nd run

(Si dilution / 3 il reste 325pL d' échantillon pour le 2nd run)

un pipetage précis des volumes est nécessaire afin d'assurer une estimation correcte de fa concentration en Ca et des dilutions effectuées avant le 2nd run.

2. Préparation des réactifs

Préparation de l'acide 10% pour vaissell

ATTENTION : mettre en route l'extraction de la hotte.

-Remplir la bouteille prévue pour la préparation du 10⁰/0 (sous la hotte) avec d' H2O UHQ jusqu'à la marque (850mL).

-Prendre la flacon de 125mL avec 2 traits de jauge à 50 et 100mL marqués au feutre.

-Verser 100ml d'HN03 (69⁰/0) (sous la hotte) dans la bouteille de préparation. -Verser 50ml d'HN03 (6970) (sous la hotte) dans la bouteille de préparation.

Rinçage des pointes

Acide (10⁰/0, HN03) 3 fois

H2O Elga UHQ 3 fois

Extraction des argiles

H2O Elga UHQ

Éthanol

Oxidant (pour extraire la matière organique)

On veut du H2O2 0,3⁰/0

250 PL de solution est nécessaire par échantillon

Une préparation du réactif doit être réalisée pour chaque série d' échantillons

Préparation à partir de H2O2 30⁰/0 w/v et NaOH O.IM.

A Préparation du NaOH 0,1M

-Mettre un peu d' eau UHQ dans une fiole de 50 mL.

-Ajouter 500pL de NaOH (30⁰/0) dans la fiole.

-Compléter au trait de jauge avec de I¹ eau UHQ.

Préparation du H2O2 0,3⁰/0

-Sortir la bouteille du frigo avant pour atteindre la T⁰ ambiante avant utilisation.

-Prendre le flacon au bouchon orange.

-Mettre 100pL d' H2O2 30⁰/0 w/v (pipeter dans petite fiole relais de 5 mL). -Compléter à 10ml avec NaOH (O,IM).

Préparation du HN03 0,1M

-Utiliser comme acide de départ le HN03 65 % (15M) distillé ou Normatom ultra pur de Norbert Franck.

-Prendre la bouteille sous l'hôte prévue pour préparation.

-Remplir d' eau jusqu'à la marque H20. -Ajouter 6,67 mL d' HN03 (6570).

② Préparation du HNO_3 0,001M pour leaching

À partir du HN03 0,1M.

-Mettre une peu d' eau UHQ dans fiole de 25 mL.

-Ajouter 250 d'acide 0,1M.

-Compléter avec de l' eau UHQ jusqu'à 25 mL.

75mL d'acide à 0,1M dans 1 fiole de 100mL.

Utiliser 1 fiole de 25mL d'eau UHQ transvaser dans fiole de 100mL et compléter jusqu'au trait de jauge avec HN03 à 0,1M.

3. Nettoyage des micro tubes de 0,5 ml

1) Préparer un bain d' acide dans les récipients cylindriques Nalgène avec couvercle blanc. 2) Mettre de l'acide avec un compte-gouttes dans chacun des tubes (et dans chaque couvercle) en s'assurant qu'il ne reste pas de bulles d'air dedans. Puis les plonger dans un bain d'acide à 10 % avec leurs couvercles ouverts.

3) Fermer le récipient cylindrique et laisser 24 heures.

4) Retirer l'acide de chaque tube : ouvrir le couvercle et verser l'acide dans un nouveau récipient identique pour récupérer l'acide. Refermer le couvercle, agiter le récipient pour se débarrasser de l'acide encore présent au fond des tubes, rouvrir et retirer l'acide une nouvelle fois. 6) Rincer trois fois avec de l'eau Elga la totalité du récipient en agitant pour chaque rinçage. 7) Faire un dernier rinçage avec de l'eau Elga en prenant cette fois les tubes individuellement. 8) Faire sécher les micro tubes à l' étuve.

Annex B



National Institute of Standards & Technology

Report of Investigation

Reference Material 8301

Boron Isotopes in Marine Carbonate (Simulated Coral and Foraminifera Solutions)

This Reference Material (RM) is intended for use in developing and evaluating methods for measuring relative differences in boron (B) isotope-number ratios, $R(^{11}\text{B}/^{10}\text{B})$. It is specifically designed to evaluate B isotope-number ratio measurements normalized to SRM 951 (hereafter designated as $\delta^{11}\text{B}_{\text{SRM951}}$ or simply $\delta^{11}\text{B}$ measurements) in marine carbonate samples [1]. Even though the $\delta^{11}\text{B}$ values are reported as reference and not certified values [2], the use of RM 8301 will serve as an effective harmonization standard to improve the comparability of data among different laboratories.

A unit of RM 8301 consists of three vials each of two simulated solutions, labeled as RM 8301 (Coral) and RM 8301 (Foram), each containing approximately 4 mL of a gravimetrically prepared solution with a nominal 50 mg/g mass fraction of calcium in approximately 3 mol/L nitric acid in water. The synthetic materials have been designed to reflect typical $\delta^{11}\text{B}$ values and trace element content of authentic coral skeleton and foraminiferal test (invertebrate shell) samples (hence the “Coral” or “Foram” designations in RM 8301).

Expiration of Value Assignment: RM 8301 is valid, within the measurement uncertainty specified, until **31 July 2030**, provided this RM is handled and stored in accordance with instructions given in this Report of Investigation (see “Instructions for Storage and Use”). The reference values are nullified if the RM is damaged, contaminated, or otherwise modified.

Reference Values: Reference values and expanded uncertainties for $\delta^{11}\text{B}_{\text{SRM951}}$ are shown in Table 1. These values were determined from inter-laboratory study data using the DerSimonian-Laird analysis method within the NIST Consensus Builder [3].

Table 1. Reference Values^(a) and Expanded Uncertainty Estimates for the Relative B Isotope-Number Ratio Differences of RM 8301 (Coral) and RM 8301 (Foram) solutions

RM Solution	Reference Value	Expanded Uncertainty
	$10^3 \delta^{11}\text{B}_{\text{SRM951}}^{(b)}$	$10^3 \delta^{11}\text{B}_{\text{SRM951}}^{(b)}$
8301 (Coral)	+24.17	± 0.18
8301 (Foram)	+14.51	± 0.17

^(a) A reference value is a non-certified value that is the best estimate of the true value; however, the value may reflect only the measurement precision and may not include all sources of uncertainty [2].

^(b) The $\delta^{11}\text{B}$ value is expressed as $x \pm 2u(x)$, where x is a mean value and $u(x)$ is its associated standard uncertainty. While the best estimate of the delta value lies within the interval $x \pm 2u(x)$ with approximately 95 % confidence, this interval may not include the true value.

Relative Differences in Isotope-Number Ratio Values: The difference in the measured isotope-number ratio of boron isotopes in a sample p , $R(^{11}\text{B}/^{10}\text{B})_p = [N(^{11}\text{B})_p/N(^{10}\text{B})_p]$ is reported as a $\delta^{11}\text{B}$ value [1]. The relative difference in isotope-number ratios for boron is referenced to SRM 951 where:

$$\delta^{11}\text{B} = [R(^{11}\text{B}/^{10}\text{B})_{\text{sample}} / R(^{11}\text{B}/^{10}\text{B})_{\text{SRM951}}] - 1$$

SRM951 refers to the boron SRM 951 delta scale, which is defined by assigning a $\delta^{11}\text{B}$ value of 0 ‰ to SRM 951 [1], where the symbol ‰ is part per thousand and is equal to 0.001.

Carlos A. Gonzalez, Chief
Chemical Sciences Division

Gaithersburg, MD 20899
Report Issue Date: 06 January 2021
RM 8301

Steven J. Choquette, Director
Office of Reference Materials

Page 1 of 5

Maintenance of RM: NIST will monitor this RM over the period of its validity. If substantive technical changes occur that affect the value assignment before the expiration of this report, NIST will notify the purchaser. Registration (see attached sheet or register online) will facilitate notification.

Technical aspects involved in the design, manufacture, and issuance of this RM were coordinated by S. Christopher of the NIST Chemical Sciences Division and J. Stewart and R. Day, formerly of NIST.

Statistical analyses were performed by B. Toman of the NIST Statistical Engineering Division.

Design and coordination of the inter-laboratory comparison exercise were performed by J. Stewart and R. Day. The institutions listed in Table 2 provided the $\delta^{11}\text{B}_{\text{SRM951}}$ data used to assign the reference values in Table 1 and/or the supplemental elemental data for RM 8301 listed in Appendix A.

Boron measurements at NIST were provided by J. Stewart and R. Day. Material bottling was performed by C. Davis, R. Day, D. Ellisor, J. Hoguet, A. Moors, J. Ness, R. Pugh, and J. Stewart.

Support aspects involved in the issuance of this RM were coordinated through the NIST Office of Reference Materials.

INSTRUCTIONS FOR STORAGE AND USE

CAUTION: This RM contains an acidic solution sealed in screw top plastic vials. All appropriate safety precautions should be taken during opening and handling. This includes the use of gloves and other appropriate personal protective equipment.

STORAGE: Unopened vials should be stored under normal laboratory conditions in an upright position inside the original packaging supplied by NIST.

USE: The amount of material in each individual vial of RM 8301 (Coral) or RM 8301 (Foram) far exceeds the amount typically needed for boron isotope ratio mass spectrometry. NIST recommends opening the vials individually when needed and aliquoting the opened solutions into pre-cleaned secondary containers for subsequent dilution. This will minimize the potential for contamination and allow for cross-checking. Also, by tightly resealing the secondary containers with paraffin film, the potential for the solutions to undergo isotopic fractionation will be minimized.

Table 2. Laboratories Contributing $\delta^{11}\text{B}$ Data and/or Mole Fraction (Element/Ca Ratio) Data for RM 8301

Institution	Location
Department of Earth Sciences, National Cheng Kung University	Tainan, Taiwan
GEOMAR Helmholtz Center for Ocean Research Kiel	Kiel, Germany
Laboratoire des Sciences du Climat et de l'Environnement	Paris, France
National Institute of Standards and Technology	Charleston, SC, USA
University of Bristol	Bristol, United Kingdom
University of Oxford	Oxford, United Kingdom
University of Southampton	Southampton, United Kingdom
University of St. Andrews, STAig Laboratory	St. Andrews, Scotland
Yale University Metal Geochemistry Centre	New Haven, CT, USA

MATERIAL SOURCE, PREPARATION AND ANALYSIS⁽¹⁾

Material Source and Preparation: The simulated solutions comprising RM 8301 (Coral) and RM 8301 (Foram), were prepared at NIST by gravimetric addition and blending of acidified solutions of single element standards, NIST SRM 951a *Boric Acid Isotopic Standard* [4] and an enriched (>99 %) elemental ¹¹B spike to separate 20 L volumes of two different acidified calcium carbonate source solutions. The synthetically created solutions are representative of the expected trace element content, together with a $\delta^{11}\text{B}_{\text{SRM951}}$ value within the natural range found in authentic coral or foraminifera samples. Supplemental mass fraction data for boron and calcium, and mole fraction data (element/Ca ratios) for various elements in the RM 8301 (Coral) and RM 8301 (Foram) solutions are listed in Appendix A to provide additional information about the solution matrixes. The boron mass fraction values in Appendix A can be used to estimate the amount of solution required for B isotope purification and analysis methods.

Homogeneity Testing: The inter-laboratory study for $\delta^{11}\text{B}$ showed good agreement (<0.03 ‰ difference) for twenty-seven vials of RM 8301 (Coral) at a 10 μL typical aliquot size, and RM 8301 (Foram) at a 50 μL typical aliquot size, that were randomly selected from across the entire production batch. Shapiro-Wilk and *F*-Tests on vials measured from the first and last quartiles of the production batch suggested that the data were normally distributed and of similar variance ($p>0.05$). Parametric two-sample t-tests applied revealed no statistically significant difference ($p>0.05$) between mean $\delta^{11}\text{B}_{\text{SRM951}}$ values for either RM 8301 solution.

Analytical Methods: The $\delta^{11}\text{B}$ reference values for RM 8301 are based on an inter-laboratory study using multi-collector inductively coupled plasma mass spectrometry (MC-ICP-MS), of which NIST was one of the participants. Most laboratories (including NIST) employed anion exchange chromatography using a boron-chelating resin (Amberlite IRA743) [5] to eliminate matrix effects prior to MC-ICP-MS analysis. The matrix separations were performed after buffering the samples of RM 8301 to an approximate pH of 5 using a sodium acetate-acetic acid buffer. The buffered samples were loaded onto the resin, followed by column washing. Boron was then eluted with nitric acid. One laboratory performed micro-sublimation [6] prior to MC-ICP-MS. All laboratories calibrated their multi-collector instruments using a standard-sample bracketing approach with NIST SRM 951 *Boric Acid* or SRM 951a *Boric Acid Isotopic Standard*. Additional boron isotopic RM materials with published $\delta^{11}\text{B}_{\text{SRM951}}$ values were processed and measured concurrently with the RM 8301 samples to verify that the measurements were in control [7].

Additional Resource: Fuller details on the production, analysis, and statistical evaluation of RM 8301 are provided in [7].

NOTICE TO USERS

NIST strives to maintain a RM inventory supply but cannot guarantee the continued or continuous supply of any specific RM or SRM. Accordingly, NIST encourages the use of this RM as a primary benchmark for the quality and accuracy of the user's in-house reference materials and working standards. As a benchmark, this RM should be used to validate the more routinely used isotopic reference materials present in a laboratory. Comparisons between this RM and in-house reference materials or working measurement standards should take place at intervals appropriate to the conservation of the RM and the stability of the relevant in-house materials. For further guidance on how this approach can be implemented, contact NIST by email at srms@nist.gov.

(1) Certain commercial equipment, instruments or materials are identified in this certificate to adequately specify the experimental procedures. Such identification does not imply recommendation or endorsement by the National Institute of Standards and Technology, nor does it imply that the materials or equipment identified are necessarily the best available for the purpose.

REFERENCES

- [1] Brand, W.A.; Coplen, T.B.; Vogl, J.; Rosner, M.; Prohaska, T.; *Assessment of International Reference Materials for Isotope-Ratio Analysis (IUPAC Technical Report)*; Pure Appl. Chem., Vol. 86(3), pp 425–467 (2014).
- [2] Beauchamp, C.R.; Camara, J.E.; Carney, J.; Choquette, S.J.; Cole, K.D.; DeRose, P.C.; Duerwer, D.L.; Epstein, M.S.; Kline, M.C.; Lippa, K.A.; Lucon, E.; Phinney, K.W.; Polakoski, M.; Possolo, A.; Sharpless, K.E.; Sieber, J.R.; Toman B.; Winchester M.R.; Windover, D.; *Metrological Tools for the Reference Materials and Reference Instruments of the NIST Material Measurement Laboratory*; NIST Special Publication 260–136; U.S. Government Printing Office: Washington, D.C. (2020); available at <https://nvlpubs.nist.gov/nistpubs/SpecialPublications/NIST.SP.260-136-2020.pdf> (accessed Jan 2021).
- [3] Koepke, A.; Lafarge, T.; Possolo, A.; Toman, B.; *NIST Consensus Builder User's Manual* (2017); available at <https://consensus.nist.gov> (accessed Jan 2021).
- [4] SRM 951a; *Boric Acid Isotopic Standard*; National Institute of Standards and Technology; U.S. Department of Commerce: Gaithersburg, MD (29 August 2011); available at: <https://www-s.nist.gov/srmors/certificates/951A.pdf> (accessed Jan 2021).
- [5] Kiss, E.; *Ion-exchange Separation and Spectrophotometric Determination of Boron in Geological Materials*; Analytica Chimica Acta, Vol. 211, pp. 243–256 (1988).
- [6] Liu, Y.; Aciego, S.; Wanamaker, A.; Sell, B.; *A High-Throughput System for Boron Microsublimation and Isotope Analysis by Total Evaporation Thermal Ionization Mass Spectrometry*; Rapid Comm. in Mass Spectrom., Vol 27, pp. 1705–1714 (2013).
- [7] Stewart, J.A.; Christopher, S.J.; Kucklick, J.R.; Bordier, L.; Chalk, T.B.; Dapoigny, A.; Douville, E.; Foster, G.L.; Gray, W.R.; Greenop, R.; Gutjahr, M.; Hemsing, F.; Henehan, M.J.; Holdship, P.; Hsieh, Y.; Kolevica, A.; Lin, Y.; Mawbey, E.M.; Rae, J.W.B.; Robinson, L.F.; Shuttleworth, R.; You, C.; Zhang, S.; Day, R.D.; *NIST RM 8301 Boron Isotopes in Marine Carbonate (Simulated Coral and Foraminifera Solutions): Inter-laboratory $\delta^{11}\text{B}$ and Trace Element Ratio Value Assignment*; Geostandards and Geoanalytical Research; available at <https://doi.org/10.1111/ggr.12363> (accessed Jan 2021).

Users of this RM should ensure that the Report of Investigation in their possession is current. This can be accomplished by contacting the SRM Program: telephone (301) 975-2200; e-mail srminfo@nist.gov; or via the Internet at <https://www.nist.gov/srm>.

Appendix A

Supplemental data for RM 8301 were collected from the inter-laboratory test for $\delta^{11}\text{B}$ [7]. These data provide complementary information about the material, which may be useful to the RM user. However, the data in Table 3 are not certified and should not be used for calibration, validation, or establishing metrological traceability.

Table 3. Non-Certified Values for RM 8301 Boron Isotopes in Marine carbonate (Simulated Coral and Foraminifera Solutions), reported in units of mass fraction for boron and calcium, or mole fraction for element/calcium ratios

Constituent	RM 8301 (Coral)	RM 8301 (Foram)	Units
Boron	7.1	1.9	mg/kg
Calcium	49.7	51.3	mg/g
Al/Ca	48.1	90.9	$\mu\text{mol/mol}$
B/Ca	528.1	138.9	$\mu\text{mol/mol}$
Ba/Ca	5.9	3.9	$\mu\text{mol/mol}$
Cd/Ca	0.2	0.6	$\mu\text{mol/mol}$
Fe/Ca	15.4	25.4	$\mu\text{mol/mol}$
Li/Ca	5.4	9.0	$\mu\text{mol/mol}$
Mg/Ca	4.1	2.6	mmol/mol
Mn/Ca	2.6	49.4	$\mu\text{mol/mol}$
Na/Ca	20.0	3.1	mmol/mol
Nd/Ca	0.2	5.1	$\mu\text{mol/mol}$
Sr/Ca	8.1	1.3	mmol/mol
U/Ca	828.9	68.7	nmol/mol



CUSTOMER REGISTRATION AND SATISFACTION REPORT CARD
FOR NIST STANDARD REFERENCE MATERIALS

To be notified of any updates or developments of a product, please register your Standard Reference Material (SRM).

We also invite you to rate our services. Information provided by you is very valuable to our continued efforts to enhance our features and content of our measurement services.

You can complete and return this card.

Please Print

Instead, submit an online product survey, customer service survey and/or registration. Go to <https://www.nist.gov/srm/registration-and-surveys>.

Visit us at
<http://www.nist.gov/srm>

Thank you.

PURCHASE INFORMATION		
SRM/RM Number:		
Date Shipped:		
NIST Division:		
NIST Sales Order Number: Example (0800000)		
Customer Purchase Order Number:		
Lot Number:		
Serial Number:		
Purchased directly from NIST?	Yes <input type="checkbox"/>	No <input type="checkbox"/>
CUSTOMER INFORMATION		
User First Name:		
User Surname:		
Organization/Company:		
Address:		
Address (continued):		
City, State/Province:	City:	State/Province:
Country, Postal Code:	Country:	Postal Code:
E-mail:		
Phone:		
Fax:		

Best Method of Contact: Email Phone Fax

Do NOT cut.

Fold, staple, and mail.

Do NOT cut.

Please rate your SRM purchasing experience and product by checking the appropriate box in the table below.

Category	Question	Excellent	Very Good	Good	Fair*	Poor*	N/A
Website	Navigation and usability of the SRM web site						
	Web presentation of SRM product information						
	Overall website experience						
Order Placement	SRM availability for purchase						
	Ease with getting in touch with SRM Sales and Customer Service						
	Response time with your request for a quote or order						
Order Fulfillment	Overall experience with order placement (via online, email, phone, or fax)						
	Once the order for available items was placed, timeliness of delivery						
	Carrier treatment of shipment						
Product	Packaging of SRM(s)						
	SRM Certificate or Report of Investigation information						
	Material Safety Data sheet or SRM Exemption Letter information						
	Overall SRM Quality						
	Overall SRM Value						
How could NIST serve you better in the future?							
*Let us know why any score was Fair or Poor.							
What is the intended use of this SRM to your work?							
Other comments?							
How did you hear about NIST Standard Reference Materials?							
<input type="checkbox"/> Advertisement <input type="checkbox"/> Catalog/Brochure <input type="checkbox"/> Colleague <input type="checkbox"/> Exhibit/Meeting <input type="checkbox"/> Web <input type="checkbox"/> Repeat Customer							

Approved by Office of Management and Budget (OMB) for public information collection until 31 August 2024.

OMB Control No.: 0693-0031



NO POSTAGE
NECESSARY
IF MAILED
IN THE
UNITED STATES



BUSINESS REPLY MAIL
FIRST CLASS MAIL PERMIT NO. 11 GAITHERSBURG, MD

POSTAGE WILL BE PAID BY THE ADDRESSEE

NATIONAL INSTITUTE OF STANDARDS AND TECHNOLOGY
OFFICE OF REFERENCE MATERIALS, MS 2300
PO BOX 7139
GAITHERSBURG MD 20898-7139



Titre : Changements paléocéanographiques induits par l'orbite dans l'Atlantique Sud subtropical pour le climat mondial au cours des 800 000 dernières années

Mots clés : Circulation Méridienne de l'Atlantique; cycles orbitaux; Gyre Subtropical de l'Atlantique Sud; transfert de chaleur inter-hémisphérique; contrôles de l'Atlantique Sud sur le climat; analyses de Mg/Ca.

Résumé : La activité anthropiques ont remodelé le climat de la Terre en augmentant le CO₂ atmosphérique et le réchauffement climatique, souvent lié au ralentissement de la circulation méridionale de renversement de l'Atlantique (AMOC). L'AMOC redistribue la chaleur et le carbone via le gyre subtropical de l'Atlantique Sud (SASG), agissant avec la zone de convergence intertropicale (ITCZ), poursuivant l'équilibre énergétique mondial. Les variations orbitales peuvent induire des changements climatiques à long terme par des changements d'insolation. Cette thèse étudie les influences orbitales sur la paléocéanographie subtropicale de l'Atlantique Sud sur 800 ka, en analysant les foraminifères benthiques et planctiques $\delta^{18}\text{O}$, $\delta^{13}\text{C}$ des carottes GL-854 et MD08-3167 et la température Mg/Ca de la thermocline de MD08-3167. Ce cadre dévoile les processus et les contrôles des eaux profondes et de l'atmosphère océanique à l'échelle orbitale sur le système d'upwelling de Benguela (BUS), explorant les liens de l'AMOC avec le climat mondial.

Les chapitres 1 à 3 fixent les objectifs, les méthodes et les résultats. Le chapitre 4 explore la dynamique des eaux profondes à 770 ka, dans laquelle quatre modes AMOC contrôlés par les changements induits orbitalement dans la glace de mer de l'Antarctique sont proposés. Le cadre fourni relie les dynamiques des eaux profondes, de la glace de mer et de l'atmosphère océanique, façonnant le climat du Pléistocène supérieur. Le chapitre 5 traite de 365 ka de variabilité BUS. La formation intensifiée des eaux profondes de l'Atlantique Nord pendant les périodes de précession positive améliore le transfert d'énergie interhémisphérique, déplaçant la SASG et la ZCIT vers le nord, stimulant ainsi la remontée d'eau. Le mécanisme contrôlant le BUS relie l'intensité de l'AMOC et les modèles atmosphériques globaux à la baisse du CO₂ atmosphérique. Le chapitre 6 présente le protocole Mg/Ca réalisé sur ICP-MS à l'IFREMER. La fusion des perspectives en eaux de surface et en eaux profondes vise à clarifier les mécanismes contrôlant l'AMOC pour le climat global.

Title : Orbitally-Induced Paleoceanographic Changes in Subtropical South Atlantic for the Global Climate over the Last 800,000 Years

Keywords : Atlantic Meridional Overturning Circulation; orbital cycles; South Atlantic Subtropical Gyre, inter-hemispheric heat transfer; South Atlantic controls on climate, Mg/Ca analysis.

Abstract : Anthropogenic activity has reshaped Earth's climate by increasing atmospheric CO₂ and global warming, often linked to an Atlantic Meridional Overturning Circulation (AMOC) slowdown. The AMOC redistributes heat and carbon via the South Atlantic Subtropical Gyre (SASG), acting with the Intertropical Convergence Zone (ITCZ), pursuing global energy equilibrium. Orbital variations can induce long-term climate shifts through insolation changes. This thesis investigates orbital influences on subtropical South Atlantic paleoceanography over 800 ka, analyzing benthic and planktic foraminifera $\delta^{18}\text{O}$, $\delta^{13}\text{C}$ from GL-854 and MD08-3167 cores and thermocline Mg/Ca temperature from MD08-3167. This framework unveils orbital-scale deep-water and ocean-atmosphere processes and controls on the Benguela Upwelling System (BUS), exploring AMOC's connections to climate.

Chapters 1 to 3 set objectives, methods, and results. Chapter 4 explores 770 ka deep-water dynamics, where four AMOC modes controlled by orbitally-induced changes in Antarctic sea ice are proposed. The provided framework connects deep water, sea-ice, and ocean-atmosphere dynamics, shaping the Late Pleistocene climate. Chapter 5 discusses 365 ka of BUS variability. Intensified North Atlantic deep-water formation during positive precession periods enhances inter-hemispheric energy transfer, shifting SASG and ITCZ northwards, boosting upwelling. The mechanism controlling BUS connects AMOC intensity and global atmospheric patterns to atmospheric CO₂ decline. Chapter 6 outlines Mg/Ca protocol performed on ICP-MS at IFREMER. Merging both surface and deep water perspectives seeks to clarify mechanisms controlling AMOC for the global climate.

Título : Mudanças paleoceanográficas induzidas orbitalmente no Atlântico Sul subtropical para o clima global nos últimos 800.000 anos

Palavras-chave : Circulação de Revolvimento Meridional do Atlântico; ciclos orbitais; Giro subtropical do Atlântico Sul; transferência de calor inter-hemisférica; controles do Atlântico Sul no clima, análise de Mg/Ca.

Résumé : As emissões antropogênicas remodelaram o clima da Terra, aumentando o CO₂ atmosférico e o aquecimento global, muitas vezes associados a redução da Circulação de Revolvimento Meridional do Atlântico (AMOC). A AMOC redistribui calor e carbono através do Giro Subtropical do Atlântico Sul (SASG), agindo em conjunto com a Zona de Convergência Intertropical (ITCZ), buscando o equilíbrio energético global. As variações orbitais podem causar alterações climáticas a longo prazo, através de alterações de insolação. Esta tese investiga as influências orbitais na paleoceanografia do Atlântico Sul subtropical nos últimos 800 ka, analisando $\delta^{18}\text{O}$, $\delta^{13}\text{C}$ em foraminíferos bentônicos e planctônicos dos testemunhos GL-854 e MD08-3167, e a temperatura da termoclina através de Mg/Ca no MD08-3167. Esta estrutura revela processos e controles em escala orbital de águas profundas e oceano-atmosféricas no Sistema de Ressurgência de Benguela (BUS), explorando as conexões da AMOC com o clima.

Os capítulos de 1 a 3 apresentam objetivos, métodos e resultados. O Capítulo 4 explora a dinâmica de águas profundas de 770 ka, onde são propostos quatro modos AMOC controlados por mudanças induzidas orbitalmente no gelo marinho da Antártida. O mecanismo conecta a dinâmica das águas profundas, do gelo marinho e da atmosfera oceânica, moldando o clima do Pleistoceno tardio. O Capítulo 5 discute 365 ka de variabilidade do BUS. A formação intensificada de águas profundas no Atlântico Norte durante os períodos de precessão positiva aumenta a transferência inter-hemisférica de energia, deslocando o SASG e a ITCZ para norte, intensificando a ressurgência. O mecanismo que controla o BUS conecta a intensidade da AMOC e os padrões atmosféricos globais ao declínio do CO₂ atmosférico. O Capítulo 6 descreve o protocolo Mg/Ca realizado em ICP-MS no IFREMER. A fusão das perspectivas de águas superficiais e profundas busca esclarecer os mecanismos que controlam a AMOC para o clima global.